
UNIVERSITY OF BIRMINGHAM

# PARTICULATE MATTER EMISSIONS CHARACTERISTICS, DYNAMICS AND CONTROL IN COMPRESSION IGNITION ENGINES

**By**

**Aawishkar. U. Dharmadhikari**

**A thesis submitted to**
**The University of Birmingham**
**for the degree of**
**DOCTOR OF PHILOSOPHY**

Department of Mechanical Engineering
The University of Birmingham
March 2020

# Abstract

Combustion engines' exhaust emissions have impacted the environment with greenhouse gas emissions on a large scale and this will reach a global catastrophe limit in the coming decades. It has been an important issue of consideration for many years and substituting fossil fuels to decarbonise the environment has been of utmost importance. With the increase in knowledge and research to understand and control particulate matter emissions, the fundamental research still holds unanswered questions.

The study carried out in the following thesis is primarily focussed on the particulate matter's inception, evolution, control and its characterisation from a compression ignition engine. The thesis proceeds with the initial study on the evolution and course of particulate matter inside the exhaust tailpipe using a zero-dimensional numerical model. The model aims to investigate the nucleation of water and sulphuric acid from the engine out, and its impact on the particulate matter as it is transported autonomously along a 3.5-metre exhaust pipe. The research is also concerned with explaining the effects of exhaust temperatures on particulate matter and gas emissions, by characterising them into size, mass, and concentrations at consecutive testing positions. The simulated and analysed data are used for a comparative analysis with empirical results acquired from similar exhaust temperature and particulate matter conditions that were confirmed as the assumptions were established.

Further, the research is based on an empirical investigation of particulate matter evolution and the impact of the external cooling of an exhaust tailpipe. The cooling was produced using copper coil tube windings with a decreasing pitch along the length of the pipe and supplied with an ice water and antifreeze mixture solution. The external cooling of the

exhaust tailpipe was an important parameter to study the effects of external cooling on the particulate matter flowing through the internal space of the tailpipe. The evolution of the particulates and the impact of the reduction in temperature gradient provided agreeable results. The objective was achieved in understanding and contributing to the knowledge of particulate behaviour inside the tailpipe under various engine operating conditions.

In consideration of the previous studies mentioned above, it is critical to research the control of particulate matter and gas emissions at this stage. Hence, a diesel particulate filter is equipped as an exhaust after-treatment system for the abatement and oxidation of toxic gases and particulate matter. A catalyst is developed to be coated on the filter substrate with a novel nano-fibrous morphology using a rare-earth metal catalyst. The conceptualisation of the research was to investigate the morphological effects on particle trapping and the oxygenated catalytic effect on soot burn at low exhaust temperatures. Tests were performed at laboratory scale and test bench scale, where the filter substrate was coated with the catalyst; and the results acquired depicted an increased filtration efficiency consistent at 95–99%, and a high oxidation and continuous regeneration rate at reduced local exhaust temperatures, contributing to overall lower back pressure on the particulate filter and engine. Finally, the thesis provides details of the research findings and conclusions to provide a valuable contribution to the knowledge of exhaust emissions' characteristics and their control.

# ACKNOWLEDGEMENTS

I would like to sincerely thank my supervisor Professor Hongming Xu, for his continuous advice, encouragement, and guidance during my study and for giving me the opportunity to study and work under his supervision. He has been a very huge support in the last four years of my research and helped me in providing all the resources required for my research work. I would like to also thank Professor Akbar. G. and Dr. Raya. A. D for their support, progress review comments, and advice every year during my course. Many thanks to Carl Hingley, Jack Garrod and Kevan Charlesworth for helping me during my experiments and proactively supporting me during that time. I would like to also thank Professor Yusong Yu, for guiding me and participating in valuable discussions regarding the particle growth model.

I would like to specially thank the most important people in my life, my mother (Mrs. Smita Dharmadhikari), my father (Mr. Ulhas Dharmadhikari) and my grandfather (Mr. Prabhakar Dharmadhikari) who have given me unconditional love, motivation, and support during this journey and helped me emotionally at every stage. I would also like to especially thank my fiancée Miss Deboshree Ghosh, who has been very strong, patient and has always been by my side during difficult times. I hope to make you all proud of my work.

I would like to show my sincere gratitude to Dr. Soheil Zeraati Rezaei, for his consistent support, guidance, mentoring, and advice during my Ph.D. and also because of whom I was able to pursue my research work. I would also like to thank my very dear friends and colleagues, Mr. Lewis Parry and Dr. Omid Doustdar who have been very strong, supportive and gave me motivation during the ups and downs in my study, social and personal life. Mr.

Parry's experience and skill sets on the engine and other technical aspects have educated me in many ways during each stage. A special thanks to Dr. Manju. D. Tanwar for providing me with utmost guidance during one of my experimental work on particulate filters and catalysis effects. Many thanks to my close friends Dr. Amrit. B. Sahu, Dr. Mandar Badve and Dr. Anand Jadhav, who have consistently motivated me during the research work and gave appropriate suggestions regarding many aspects whenever asked. I would like to also thank Mrs Janet Hingley, as this thesis was copy-edited for conventions of language, grammar and spelling by Janet's proofreading Service.

I would like to finally thank all my colleagues from the FPS group: Haoye Liu, Carlo Coratella, Quan Zhou, Ziyang Li, Ji Li, Olalere Rafiu Kayode, Yunfan Zhang, Bin Shuai, and Yinglong He for their support during the course. A special thanks to Mr Pankaj Golani, who however is no longer with us, but continues to inspire me by his sheer dedication and passion towards contributing knowledge to the automotive industry.

*I dedicate this Ph.D. Thesis*

*to my mother, father, grandfather*

*and Deboshree*

# Table of Contents

# List of abbreviations

| | |
|---|---|
| AM | Accumulation mode |
| AMC | Accumulation mode concentration |
| AMCMD | Accumulation mode count median diameter |
| AMM | Accumulation mode mass |
| BEV | Battery electric vehicles |
| BTDC | Before top dead centre |
| BMEP | Brake mean effective pressure |
| BET | Break even temperature |
| $CO_2$ | Carbon dioxide |
| CO | Carbon monoxide |
| CO (L) | Carbon monoxide –Low |
| C-DPF | Catalysed diesel particulate filter |
| cpsi | Cells per square inch |
| CLD | Chemi-luminescence detection |
| CNT | Classical nucleation theory |
| CRDI | Common rail direct injection |
| CI | Compression ignition |
| CMD | Count mean diameter |
| CAD | Crank angle in degrees |
| DPF | Diesel particulate filter |
| DPM | Diesel particulate matter |
| ECU | Engine control unit |
| EGR | Exhaust gas recirculation |
| ETP | Exhaust tail pipe |
| FSN | Filter smoke number |
| FID | Flame ionization detection |
| FSC | Fuel sulphur content |
| GPF | Gasoline particulate filter |
| GMD | Geometric mean diameter |
| HRR | Heat-release rate |
| HCCI | Homogeneous charge compression ignition |

| | |
|---|---|
| HEV | Hybrid electric vehicles |
| HC | Hydrocarbons |
| OH | Hydroxide |
| IQ | Injection quantity |
| IT | Injection timing |
| ICE | Internal combustion engine |
| J | Joules |
| kHz | kilo Hertz |
| λ | Lambda |
| LTC | Low temperature combustion |
| MPD | Magneto-pneumatic detection |
| MFB | Mass fraction burn |
| MS | Mass spectrometry |
| MPa | Mega Pascal |
| nm | nanometre |
| NI | National instruments |
| $N_2$ | Nitrogen |
| $NO_2$ | Nitrogen dioxide |
| NO | Nitrogen monoxide |
| $NO_X$ | Nitrogen oxide |
| NDIR | Non-dispersive infrared |
| NM | Nucleation mode |
| NMC | Nucleation mode concentration |
| NMCMD | Nucleation mode count median diameter |
| NMM | Nucleation mode mass |
| OD | Outer diameter |
| $O_2$ | Oxygen |
| PDL | Particle dynamics lab |
| PGM | Particle growth model |
| PSD | Particle size distribution |
| PI | Positive ignition |
| KOH | Potassium hydroxide |
| PDR | Pre-determined dilution ratio |

| | |
|---|---|
| PCCI | Premixed charge compression ignition |
| PT | Pressure transducer |
| RH | Relative humidity |
| SEM | Scanning electron microscopy |
| SCR | Selective catalytic reduction |
| SOFs | Soluble organic fractions |
| TGA | Thermal gravimetric analysis |
| TC | Thermocouple |
| THC | Total hydrocarbon |
| TNC | Total number concentration |
| UDF | User defined function |
| UI | User interface |
| VGT | Variable geometry turbine |
| VNT | Variable nozzle turbine |
| $H_2O$ | Water |

# List of equation abbreviations

| | |
|---|---|
| $\bar{c}_i$ | Particle thermal speed |
| $C_{ci}$ | Slip correction factor |
| $C_{diffusion}$ | Diffusion coefficient |
| $D_{chamber}$ | Chamber diameter |
| $d_{H2O}/d_{H2SO4}$ | Mean droplet diameter of $H_2O/H_2SO_4$ |
| $D_i/D_j$ | Particle diameter of coagulation regime |
| $d_{nucleation}$ | Diameter of nucleated particle |
| $H_2O_{mass}$ | Vapour molecular mass of $H_2O$ |
| $H_2SO_{4mass}$ | Vapour molecular mass of $H_2SO_4$ |
| i | Number of nucleating species |
| J | Nucleation rate |
| $k_B$ | Boltzmann constant |
| $Kn_{H2O}/Kn_{H2SO4}$ | Knudsen number for $H_2O/H_2SO_4$ |

| | |
|---|---|
| $Kn_{i,j}$ | Knudsen number |
| $m_p^*$ | Mass of critical cluster |
| $N_{ie}$ | Equilibrium molecular concentration |
| $\mathcal{N}_{total}$ | Number of molecules in critical cluster |
| $P_d$ | Particle diffusivity |
| $P_{SA}$ | Saturation vapour pressure of sulphuric acid |
| $P_{water}$ | Saturation vapour pressure of water |
| r* | Radius of critical nucleus |
| Re | Reynolds number |
| RH | Relative humidity |
| $R_{H2O/H2SO4}$ | Condensation rate ($H_2O$ and $H_2SO_4$) |
| $R_{lossH2O}/R_{lossH2SO4}$ | Loss of material |
| $R_n$ | Nucleation rate |
| $r_{nucleation}$ | Radius of nucleated particle |
| S | Vapour saturation ratio |
| $SA_{conc}$ | Total gas phase concentration of $H_2SO_4$ |
| Sc | Schmidt number |
| Sh | Sherwood number |
| T | Gas temperature |
| $T_{abs}$ | Absolute temperature |
| $T_{pc}$ | Pseudocritical temperature |
| $U_{ex}$ | Exhaust gas velocity |
| $w_i$ | Molecular weight |
| $Z^*$ | Mole fraction of $H_2SO_4$ |
| $\beta$ | Collision frequency |
| $\Gamma$ | Activity coefficients |
| $\Delta G^*$ | Nucleation barrier |
| $\lambda_{pi}, \lambda_{pj}$ | Particle mean free path |
| $\xi$ | Mass fraction of gaseous species |
| $\rho_g$ | Gas density |
| $\rho_i$ | Liquid density |
| $\sigma$ | Surface tension coefficient |

# List of Figures

# List of Tables

# List of conferences and publications

1. Aawishkar Dharmadhikari (2017), Diesel particulate filter – A clean environment strategy, **Research Poster Conference 2017, University of Birmingham, UK**
2. Aawishkar Dharmadhikari (2018), Particulate matter reduction using catalysed diesel particulate filter (CDPF), **UnICEG, Thermal management and exhaust aftertreatment, University of Nottingham, UK**
3. Aawishkar Dharmadhikari, Yusong Yu, Haoye Liu, Hongming Xu (2018), Soot formation and particulate characteristics in the cylinder of a gasoline direct injection (GDI) engine using particle growth model (PGM), **Cambridge Particle Meeting, Cambridge University, UK**
4. Aawishkar Dharmadhikari, Lewis Parry, Yusong Yu, Hongming Xu (2019), Particle Growth Model (PGM), **Submitted for final corrections to co-authors**
5. Aawishkar Dharmadhikari, Lewis Parry, Soheil Zeraati Rezaei, Hongming Xu (2019), Gas and particulate emission dynamics in a PCCI engine equipped with cooled exhaust tail pipe, **Submitted for final corrections to co-authors**
6. Manju. D. Tanwar, Soheil Zeraati Rezaei, Aawishkar Dharmadhikari, Lewis Parry, Hongming Xu (2019), Loose contact catalyst coated diesel particulate filter (DPF), **Submitted for final corrections to co-authors**
7. Lewis Parry, Soheil Zeraati Rezaei, Aawishkar Dharmadhikari, Hongming Xu (2019), Taguchi-DOE Analysis of 2-Methylfuran and Diesel Blend Performance in a Compression Ignition Engine, **Submitted to co-authors for corrections**

# CHAPTER 1

# INTRODUCTION

Internal combustion engines serve the purpose of converting chemical energy in fossil fuels to mechanical power and channelizing it to various applications. The mixture of fuel and air inside these combustion vessels provides a high energy output due to burning or oxidation. Quantities supplied from the intake to by-products from the exhaust sides are the primary considerations for any combustion vessel. Nevertheless, combustion by-products play a significant role in air pollution, releasing an extensive amount of particulate and gaseous emissions. [1] The important question remains, as to how these harmful emissions can be reduced and controlled, and further increasing the air quality. Internal combustion engines (ICE) date back to 1876 when the first spark ignition (SI) engine was developed by Otto, and in 1892 Diesel invented a compression ignition (CI) engine, [1] Since then, advancements in the research of combustion engines have been a part of the core research and applications for vibrant power and energy applications.

Fuel-led IC engines have consistently shown high engine efficiency and low fuel consumption over a couple of decades, but also raise the question of the environmental and health effects because of their fuel combusted primary and secondary exhaust emissions. Due to the stringent emission regulations imposed on research and the commercial industries, and furthermore, the motivation to reduce these toxic emissions substantially, a large amount of research, knowledge, and development is being put into the after-treatment of these exhaust emissions. Spark ignition (SI) and compression ignition (CI) engines, have distinctive working principles and characteristics but provide a similarly positive and negative output, higher power and toxic gas/PM emissions respectively. For a diesel fuelled engine, the load on the engine is

controlled through the fuel quantity injected and the injection timing that further results in high pressure for combustion. Whereas, gasoline fuelled engines require a pre-mixed air and fuel mixture, further regulated and introduced inside the combustion chamber, where the balance between the heterogeneous air-fuel mixture entering and the spark timing is controlled for combustion. Hence, the series of combustion events for SI and CI engines leads to different particulate and gas emissions for diesel and gasoline fuelled engines.

## 1.1 Compression ignition (CI) engine fundamentals

For a generic compression ignition (CI) engine, the air is introduced independently through the manifold, and the fuel is injected through a common rail fuel injection system using injectors, comprised of a low-pressure and high-pressure pump for the fuel supply. Combustion air introduced inside the chamber blends with the injected fuel to form a heterogeneous or homogeneous mixture. During the compression stroke, the piston moving upwards compresses the air-fuel mixture, increasing the in-cylinder temperature and pressure until the mixture reaches an ignition degree. Further to a certain ignition delay period, the combustion process initiates and it further rests until the combustion phase retards to complete or incomplete combustion of the air-fuel mixture. The in-cylinder pressure reaches its peak during the combustion phase, which adds to the increase in heat release rates as well. The by-products (gas and particulate matter) from the combustion are released from the exhaust valve, through to exhaust after-treatment systems like oxidation catalysts and particulate filters. [1] Figure 1.1 given below shows the change in heat release and pressure inside the cylinder during the combustion phase for a pilot (20%) and main (80%) fuel injection quantities, which are analysed from one of the experimentations done in the chapters further.

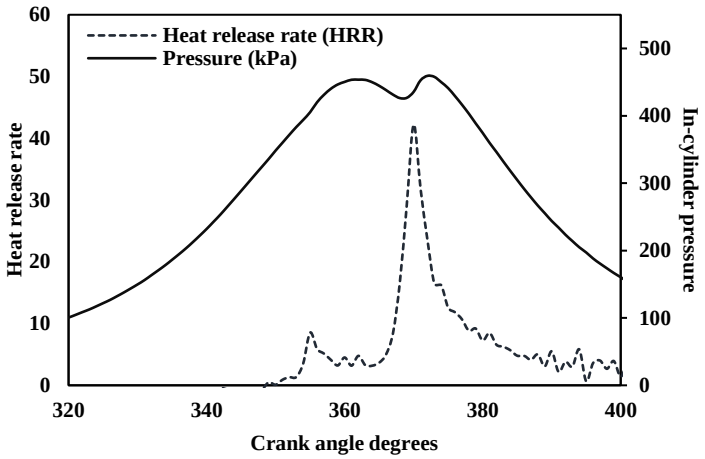


**Figure 1.1 – Split injection strategy – In-cylinder heat release rate and pressure**

The primary toxic emissions from diesel fuel burn are namely oxides of nitrogen ($NO_X$), carbon monoxides (CO), hydrocarbons (HC) and particulate matter (PM). Among these, nitrogen oxides have always been a primary concern for lean mixture and low-temperature combustion, producing higher levels of $NO_X$ fumes. Whereas, the concern about particulate matter (PM) arises during higher in-cylinder temperatures producing low $NO_X$ levels, but incurring too high PM concentrations. This is a common challenging phenomenon known as the $NO_X$-PM trade-off, observed for CI engines; whereas CO and HC levels reside at lower bands of concentration compared to $NO_X$ and PM, but are still considered to be harmful gases and aid the greenhouse effect.

While it is critical to abate these in-cylinder and after-exhaust emissions, developments in CI engine technology have increased majorly in the last couple of decades with increasing pressure by regulatory bodies to reduce them to appropriate limits. With the introduction of after-treatment systems like the diesel oxidation catalyst (DOC) – with its primary function as an oxidising agent; the diesel particulate filter (DPF) – used as a particulate filter and with

regeneration for burning accumulated PM inside channels; and selective catalytic reduction (SCR) – a $NO_X$ reduction technique using ammonia as a reducing agent, these emission limits have been possible to achieve. Various design considerations and fuelling strategies have also been developed for reduced fuel consumption, an increase in thermal efficiency and reducing in-cylinder gas and particulate emissions.

## 1.2 Vehicle emissions and regulations

Unregulated and uncontrolled pollutants have been emitted from coal industries, motor vehicles, and other pollutant producing industries since the early 1900s. In Los Angeles, the term introduced as "smog", initially noted as a nose and eye irritation air pollutant was discovered. From the great smog of London in 1952, and to date, the 2013 East China smog and the 2017 great smog of Delhi, the attention of researchers and regulatory bodies has been consistently focussed on reducing the motor vehicles and industries which are producing harmful and toxic pollutants. Due to these air pollution disasters for both humans and the natural world, governments and regulatory bodies have put rigorous pressure on sustaining the emission limits and purifying air quality. Even after enforcing these regulations, the air quality has not increased to its highest margin as it was before industrialisation. The major reason for these air pollution disasters was the pollutants' formation and dissipation into the atmosphere; caused by fossil fuel burning, other carbon compounds and emission producing methodologies, combining with dry weather and low wind speeds to create a heavy condensed land cloud consisting of life-threatening chemicals.

Exhaust emissions from an internal combustion engine (ICE) comprise complex and toxic compounds that affect human health and the environment on a large scale. [1-6] The by-

products emitted from complete or incomplete combustion are forced out of an exhaust tailpipe to ambient atmospheric conditions. Oxides of nitrogen ($NO_X$), hydrocarbons (HCs), carbon monoxide (CO) and particulate matter (PM) are the important emitted gas emissions that are required to be reduced.

### 1.2.1 Total hydrocarbons (THC)

Exhaust gases comprised of organic and inorganic elements bear a certain percentage of hydrocarbons (HCs). The resulting exhaust composition of unburned fuel is primarily hydrocarbon (HC) which is assigned in terms of total hydrocarbons' (THCs) concentration in percentage and these can be classified in reactive and nonreactive elements. These reactive elemental THCs aid in combining with other chemical elements in ambient air to give smog. Some THCs are characterised as physiologically inert, nonreactive, and not assisting in smog formation. [1, 7, 8] They can be categorised as reactive and non-reactive compounds like methane and non-methane HC. The fundamental reasoning of HC formation depends on aromatics' and olefins' content in fuel structures. High ratios of these compounds ordinarily produce high concentrations of reactive and non-reactive HCs (largely reactive). Other reasons for THC production are majorly dependent on the engine operating conditions, where partial combustion efficiency determines the THC output, proved as incomplete combustion in the chamber. [1, 9]

### 1.2.2 Oxides of carbon (CO and $CO_2$)

Production of oxides of carbon (CO and $CO_2$) is principally done by controlling air/fuel ratios, where carbon monoxide (CO) is further produced with transmutation and breakdown of carbon dioxide ($CO_2$). A higher significance is given to CO produced in SI engines than in CI

engines, as the A/F ratio occurs frequently near to its stoichiometry at part and full load. Whereas for a partial and full load in diesel engines, the mixture introduced for combustion is a lean mixture, thus producing low CO levels. [1, 7, 8] For the hydrocarbon combustion mechanism, the formation of CO is a primary reaction step, given as:

$$(R^{HC})H \rightarrow (R^{HC}) \rightarrow (R^{HC})O_2 \rightarrow (R^{HC})CHO \rightarrow (R^{HC})CO \rightarrow CO \quad (1)$$

where $R^{HC}$ represents a radical of hydrocarbon. An increase in the concentration of CO to the maximum value is observed in the flame zone at a rapid rate and reduced further forming to $CO_2$ at lower rates. The general reaction for the oxidation of CO is given as:

$$CO + OH \rightarrow CO_2 + H \quad (2)$$

With CI engines having higher efficiency and lower fuel consumption, it denotes to prove that the $CO_2$ production at the exhaust is less compared to SI engine exhaust $CO_2$. [1]

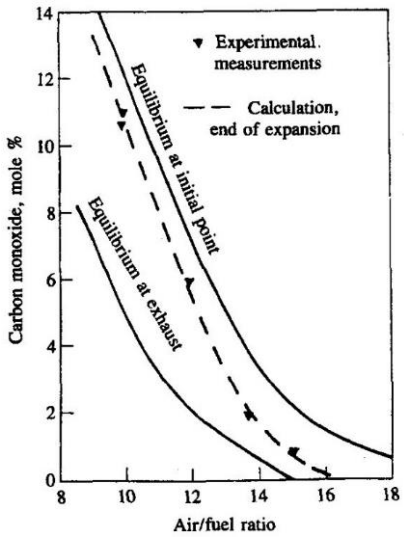


**Figure 1.2 - Predicted CO concentration at the end of the expansion stroke, compared with measured exhaust concentrations, as a function of the A/F ratio. Equilibrium level at top centre combustion and exhaust conditions also shown. [1, 10]**

### 1.2.3 Nitrous oxides ($NO_X$)

Oxides of nitrogen comprise a combination of nitrogen oxide (NO) and nitrogen dioxide ($NO_2$). The production of nitrogen oxide (NO) usually takes place in the presence of oxygen with atmospheric nitrogen where NO is the paramount contributor to overall $NO_X$. Kinetics of nitrogen oxide (NO) formation was first suggested by Zeldovich, and hence it was summarised as the Zeldovich mechanism. [1] The primary reaction mechanism added by Zeldovich and Lavoie for NO formation from an individual nitrogen molecular state was given as;

$$N + O_2 \leftrightarrow NO + O \quad (3)$$

$$O + N_2 \leftrightarrow NO + N \quad (4)$$

$$N + OH \leftrightarrow NO + H \quad (5)$$

On the other hand, nitrogen dioxides ($NO_2$) comprised in total $NO_X$ concentration reside in the range 10–30% of composition as shown in Figure 1.3. Inside the flame zone, species conversion from NO to $NO_2$ is carried out rapidly in the presence of hydroperoxyl ($HO_2$), and without sub-sequential allaying of $NO_2$, conversion to NO takes place given as [1]:

$$NO + HO_2 \rightarrow NO_2 + OH \quad (6)$$

$$NO_2 + O \rightarrow NO + O_2 \quad (7)$$

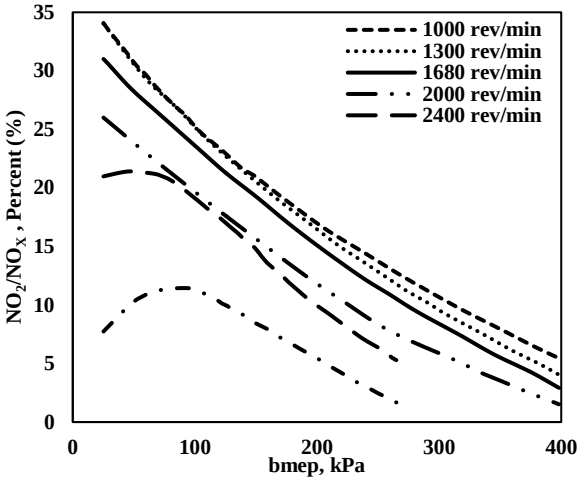


**Figure 1.3 - $NO_2$ present in $NO_X$ in diesel exhaust as a function of speed and load [1]**

### 1.2.4 Particulate matter (PM) emissions

Particulate matter (PM) emissions cover both solid and liquid particles with a diverse composition of these particles. The transportation industry is largely responsible for PM concentration percentages in air pollution worldwide. [8] Fuel operated vehicles produce a large number of toxic particulates that contain carcinogens. Carbonaceous materials like soot are produced from fuel pyrolysis during engine combustion, and result in unburnt and organic compounds like hydrocarbons. The particle formation takes place majorly in oxygen-deficient domains, where the inception of particulates is established. Organic compounds reside and absorb in soot, forming a particulate. The particulate matter size and concentration is dependent on the PM sampling systems and engine exhaust compositions. The PM size is generally monitored from 1 nm to 1000 nm in many particulate analysing devices. The PM size measured is subdivided into nucleation, accumulation and coarse modes that define the particle size range and corresponding concentrations at any given testing position. For diesel particulate matter (DPM), the size of particulates ranges between 20 and 50 nm (nucleation mode residence) and PM concentration is widely spread over 1 nm to 1000 nm.

### 1.2.5 Vehicle testing and worldwide regulated emissions

The regulatory body for emission limits categorised gasoline and diesel engine tailpipe particulate and gas emissions in three categories based on their applications: light-duty, heavy-duty and off-road heavy-duty vehicles. The Euro VI emission limits for light-duty vehicles as provided in Commission Regulation (EC) No 595/2009 (amending Regulation (EC) No 715/2007 and 692/2008) for positive ignition (PI)/spark ignition (SI) and compression ignition (CI) engines, is given in Table 1.1 below for gas emissions (CO, HC and $NO_X$) and particulate matter (PM) emissions. In May 2011, Commission Regulation (EC) 582/2011 (amending Regulation (EC) No 595/2009) was finalised and published the emission limits for Worldwide Harmonised Steady and Transient state cycle (WHSC and WHTC) Euro VI heavy-duty vehicles, setting the PM and gas emission limits as shown in Table 1.2.

**Table 1.1 - Euro 6 emission limits for light-duty and commercial vehicles (Commission Regulation (EC) No 595/2009)**

| | **Emission limits** | | | | | | |
|---|---|---|---|---|---|---|---|
| | Mass of carbon monoxide (CO) | Mass of total hydrocarbon (THC) | Mass of oxides of nitrogen ($NO_X$) | Mass of non-methane hydrocarbons (NMHC) | Combined mass of THC and $NO_X$ | Particulate matter mass (PM) | Number of particles |
| | (mg/km) | (mg/km) | (mg/km) | (mg/km) | (mg/km) | (mg/km) | (#/km) |
| **Positive ignition (PI)** | 1000 | 100 | 60 | 68 | - | 5.0 | $6.0 * 10^{11}$ |
| **Compression ignition (CI)** | 500 | - | 80 | - | 170 | 5.0 | $6.0 * 10^{11}$ |

**Table 1.2 - Euro 6 emission limits for heavy-duty vehicles (Commission Regulation (EC) No 582/2011)**

| | Emission limits | | | | | |
|---|---|---|---|---|---|---|
| | Carbon monoxide (CO) | Total hydrocarbon (THC) | Oxides of nitrogen ($NO_X$) | Ammonia ($NH_3$) | Particulate matter mass (PM) | Number of particles |
| | (mg/kWh) | (mg/kWh) | (mg/kWh) | (ppm) | (mg/kWh) | (#/kWh) |
| **WHTC (PI)** | 4000 | - | 460 | 10 | 10 | |
| **WHTC (CI)** | 4000 | 160 | 460 | 10 | 10 | $6.0*10^{11}$ |
| **WHSC (CI)** | 1500 | 130 | 400 | 10 | 10 | $8.0*10^{11}$ |

## 1.3 Advancements in combustion technologies

Combustion of a diesel engine is established to be inhomogeneous, as the air and fuel mixture causes a large amount of gas and particulate emissions. Advanced technologies introduced in the discipline of engine and fuel performance with emission reduction have shown promising results. Introducing low-temperature combustion (LTC), homogeneous charge compression ignition (HCCI), and premixed charge compression ignition (PCCI) has shown a significant reduction in the soot and $NO_X$ emissions, with decreased equivalence ratios and local temperatures for diesel combustion. [11, 12]

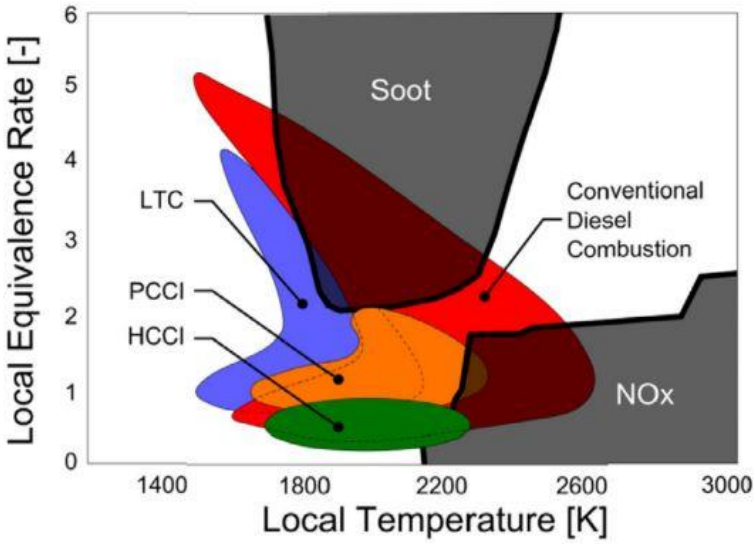


**Figure 1.4 - LTC, PCCI, HCCI and conventional engine combustion regimes for soot and NOX as a function of local equivalence ratios and temperatures [12]**

Reducing emissions using injection strategies and recirculating exhaust gases through the intake manifold shows a significant reduction in engine noise and emissions. To achieve a sound atomisation and a minimal emission level, it is essential to balance a considerable amount of exhaust gas recirculation (EGR), appropriate fuel injection timing and quantities, and corresponding injection pressure. [1] Methodologies like multiple injection strategies using pilot, main and post injections have proven to reduce $NO_X$ and engine noise substantially but also increase the particulate number concentrations. Advanced injection strategies include three to five injections inside the combustion chamber, with various quantities and timings providing high engine performance and low emission levels. Another method using the introduction of various quantities of EGR shows an increase in engine performance and combustion efficiency, but with increased PM and reduced $NO_X$; and it is essential to balance the trade-off.

To achieve LTC for diesel fuel PCCI engines have been used in light-duty vehicle applications. As previously mentioned, with the balanced introduction of considerable injection

strategies and EGR control, PCCI combustion can be achieved for LTC. The combinations are used to achieve a near homogenous in-cylinder combustion flame and significantly decrease the emissions due to a homogenous mixture of air and fuel. A comparative analysis carried out by [12, 13] observed that CO and HC levels are lower for PCCI than HCCI; whereas, $NO_X$ and soot emissions show higher levels for HCCI.

## 1.4 Alternate powertrain technologies

The transportation industry supplies more than 90% of power using liquefied fuels, and it will continue to be in existence for many generations to come. Based on some researched statistics, it is conceived that two-thirds of the worldwide diesel-operated vehicle sales will be cut down by the year 2025. The transition from diesel and gasoline operated vehicles has already begun towards bio-fuels (e.g. organic waste), and also towards power transmission to wheels using battery operated motors. The increasing fear of natural disasters due to emissions is already established in many media-related articles, and researchers have reinforced this, marking it as a critical time for everyone to act towards climate control and decarbonisation.

The scientific concern in using alternative fuels has been incremented to avoid the use of fossil fuels that result in harmful greenhouse gas emissions and the scarceness associated with the excessive use of fossil fuels. Alternative fuel resources and power generation techniques have been under consideration for some decades and have progressed to a wide scale of production and applications. Among many alternative fuel resources, biodiesel fuels and blended fuels have intrigued researchers and it is claimed they have equivalent efficiency, an assuring reduction in $NO_X$ emissions and power output like diesel fuel. [14-18]

The abatement of emissions has also been carried out during recent years using alternative powertrain systems. Vehicles using battery electric, hybrid electric, plug-in hybrid electric and fuel cell electric are some of the major alternative powertrains in concept or being commercialised.

Battery electric vehicles use a battery powered motor for vehicle propulsion. Various batteries are being produced for battery electric vehicles (BEV) and hybrid electric vehicle (HEV) to increase the performance and longevity of the vehicles without charging. [18, 19] Battery materials used in some BEVs and HEVs are lead-acid, nickel-cadmium, nickel-metal hydride, lithium-ion and many more. Due to the higher accessibility and lower monetary value of lead-acid batteries, they are widely used in EVs.

A schematic of a BEV and a HEV is given in Figure 5, demonstrating the power transmission in electric vehicles. A hybrid electric vehicle (HEV) uses both a conventional internal combustion engine (ICE) and an electric motor for vehicle propulsion. The HEV uses the power output from the ICE (diesel or gasoline) to regenerate or recharge the on-board battery without any plug-in factor, and either a parallel/series or both integrated configuration is used. [18]

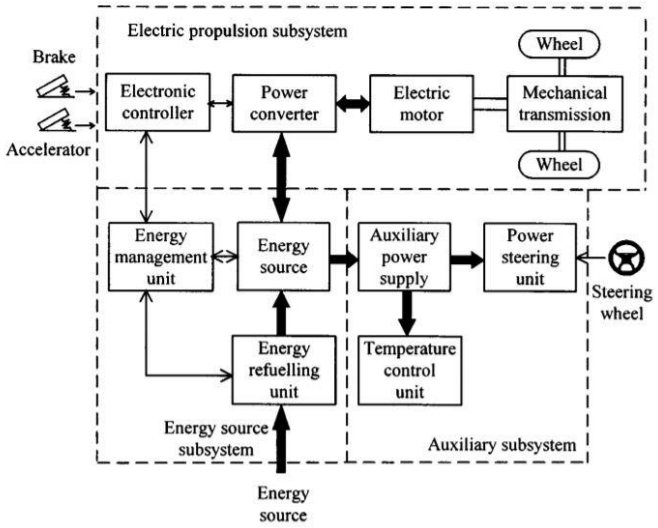


**Figure 1.5 - Electrical elements of a BEV system (left) [19]**

On the other hand, plug-in hybrid electric vehicles (PHEVs) work on a similar concept as HEVs by using both the ICE and EVs' powertrain strategy. The important difference between them is the PHEVs start-up and propulsion are done using electric power, hence the sizing of these batteries is larger compared to other HEVs. [20, 21] A large amount of these vehicle fleets have been seen in recent times and are reducing the urban area emissions transiting to rural localities. In the context of BEVs and PHEVs, the power generation on the grid and supplies to these vehicles through charging stations should be done using renewable resources by industries to provide a cleaner energy source.

## 1.5 Research objectives

The aim of the following research is to investigate particulate matter dynamics and gas-particulate interaction inside diesel exhaust pipes, using experimental and modelling approach; and furthermore, to implement a non-noble metal catalyst with a novel catalyst morphology to investigate the particle filtration and achieve diesel particulate matter oxidation/reduction at low temperatures (< 500 ºC). The research is distributed into multiple objectives to provide the novelty, investigation, and validation of these approaches. Some of the specific objectives are mentioned below:

1. To develop a numerical particulate growth model (PGM), investigating the $H_2O$-$H_2SO_4$ binary nucleation and its impact on particle inception and growth, assisted by gas-to-particulate interaction and the evolution of particulate matter along the length of an exhaust tailpipe, depending on temperature gradient and dilution of exhaust gases. The boundary conditions for the mathematical model is to be produced using test bench experimentation as a baseline test for various engine operating conditions.
2. Develop a conceptual strategy to externally cool a diesel exhaust tailpipe and reduce the temperature gradient to investigate particulate matter and gas emission dynamics and characteristics inside the tailpipe. Primary investigations focus on the diesel particulate matter (DPM) size, concentration, and mass along the length of the tailpipe.
3. Provide design considerations of an exhaust system to be used in the development of a novel catalyst using PM characterisation for variant temperature and exhaust pipe lengths.
4. To develop a rare-earth metal catalyst with a novel catalyst morphology to be coated on a diesel particulate filter (DPF); and investigate the mechanical filtration and gas species conversion efficiencies during passive regeneration of a catalysed diesel particulate filter (C-DPF) on a laboratory scale and test bench scale experimentation.

## 1.6 Thesis outline

To achieve the objectives mentioned earlier, the research is spread through the thesis in different chapters providing an elaboration of achieving these objectives. The chapters include the background literature, research methodology, results acquired and the conclusions made. The chapters are outlined below.

### 1.6.1 Chapter 2 – Literature Review

The chapter is focussed on the review of background knowledge and investigation of previous concepts applied, in relation to the recent case-studies and research performed. Initially, the fundamental background of in-cylinder gas and particulate matter emissions formation processes is thoroughly studied. Afterward, an overview of diesel after-treatment fundamentals and developments are studied to provide information on the advancements in research of particulate filter substrates under catalysed and non-catalysed conditions for emissions abatement. In addition, model developments for diesel particulate filter pressure drop and soot oxidation models are reviewed as well. Finally, an approach towards soot modelling over the past decades and its advancements are studied in detail.

### 1.6.2 Chapter 3 – Experimental systems and setup

To achieve the aim and objectives above mentioned, an experimental test bench and instrumentation are distinctly mentioned in this chapter. Experimental test bench and instrumentation used on the compression ignition engine testing is mentioned and in addition to the conceptualisation of novel cooling exhaust tailpipe strategy for diesel engine and catalysed diesel particulate filter. Measurement instrumentation for temperature, pressure, gas and particulate matter is mentioned, giving the uncertainty and sensitivity of them. A review

of uncertainty of instrumentation and equipment is also provided in this chapter. The methodology used for data analysis for all the results is provided in final section of the chapter.

### 1.6.3 Chapter 4 – Simulation of particle inception and growth using particle growth model

The chapter establishes the particle growth model (PGM) and its sub-models used for simulation purpose, and simulation results recorded from the model based on the initial boundary conditions acquired of a CI engine baseline experimentation, equipped with a exhaust tail pipe. The physical and dynamical processes incurred in the engine exhaust along the length of 3.5 meter exhaust pipe and the contribution of particulate to particulate interaction and nucleation of water and sulphuric acid are researched thoroughly. The model is investigated for particulate matter (PM) size and concentration variations that are comparable with the experimental baseline testing.

### 1.6.4 Chapter 5 – Particulate and gas emission dynamics in cooled and non-cooled exhaust tail pipe

This chapter is focussed on the investigation of particle dynamics inside the exhaust pipe, using a split injection strategy and variable engine loads on a conventional diesel combustion (CDC) engine, and a monotonous decrease in the exhaust gas temperature with external cooling of the tailpipe, as mentioned in Chapter 3. The results are based on the comparative analysis through baseline testing in the absence of the external cooling of the tailpipe, giving an in-depth understanding of the impact of exhaust gas temperatures on particulate matter and gaseous emissions. Further, the model established in chapter 4 is used for validation of exhaust pipe cooling results.

### 1.6.5 Chapter 6 – Design considerations of exhaust systems for compression ignition engines

The following chapter discusses the coupling between the particulate matter dynamics inside an exhaust tail pipe and the necessity of particle filtration in order to meet the emission limits imposed by regulatory bodies. The chapter provides a brief theory, simulation and recommendations on the requirement and design considerations to be made for high efficiency exhaust system and the effect of PM processes and exhaust gas temperature using established PGM in chapter 4.

### 1.6.6 Chapter 7 – Experimental investigation of nanofiber catalyst on diesel particulate filter

The development of a novel catalyst morphology for a non-noble metal catalyst as mentioned in Chapter 3 is presented in this chapter; in order to investigate the lab-scale and full-scale catalyst coated on a diesel particulate filter (DPF). The results acquired are provided as a series of lab-scale and full-scale particulate filter experimentation, achieving passive regeneration with low oxidation/reduction of temperature and low backpressure. The validation of this study is done by using a non-catalysed DPF using the same engine test bench.

### 1.6.7 Chapter 8 – Conclusions and Future Work

The final chapter notes the conclusions from the above experimentation and simulations done during the research. Each results chapter depicts its own conclusions based on the data analysed. This chapter further provides an insight into recommendations to carry forward the research done in this thesis.

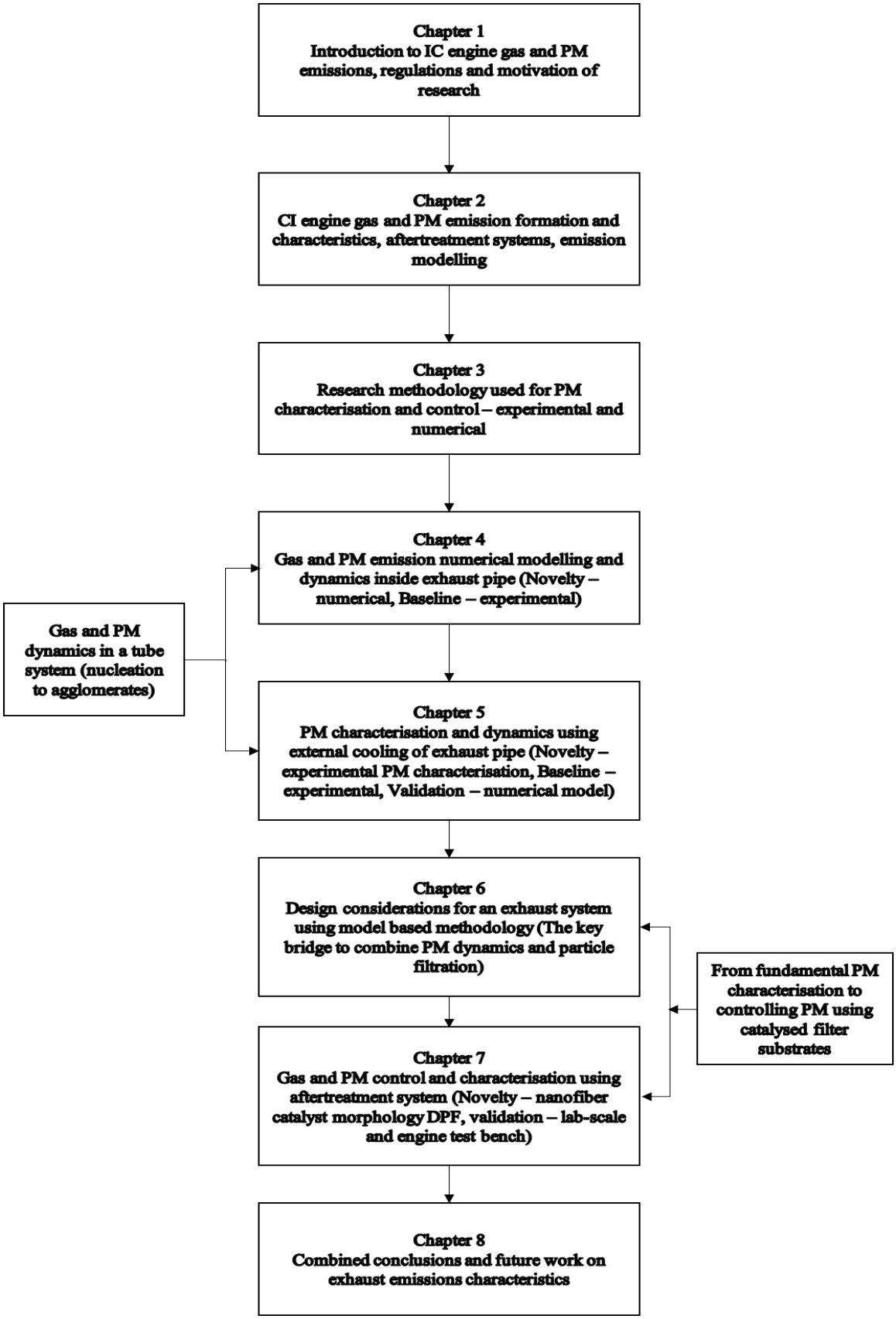


**Figure 1.6 - Flowchart of thesis chapters**

## 1.7 Research novelty

The research work carried out in the following thesis deals with three major novelties focussed on exhaust gas and particulate matter dynamics and its control. The investigation of particle dynamics is done using empirical and numerical methods, where particulate matter is characterised considering physical and chemical parameters like exhaust gas temperature, the critical temperature of the gaseous emissions for vapour condensation/ nucleus formation and the interaction of gas-to-particulate and particulate-to-particulate emissions inside an exhaust tail pipe. A novel methodology is used in the empirical investigation of particulate matter dynamics along the length of the exhaust pipe. Copper coil windings with variable pitch are used in the experimentation, to externally cool the exhaust tail pipe and reducing the spatial temperature inside the exhaust pipe. The numerical model and method used in the research take physical and chemical characteristics of the data acquired from baseline experimentation as initial boundary conditions. The model provides detailed information and knowledge of the particle evolution and the contribution of gaseous species inside the exhaust pipe at different lengths.

The control of particulate matter and conversion of gaseous species is performed using an aftertreatment system equipped on the engine. The diesel particulate filter used in the experimental setup is coated with a catalyst of a novel morphology as nanofibers. The nanofibers having an irregular and tangled morphology are implemented to trap particulate matter for higher filtration efficiency and the excessive oxygen radicals comprised in the catalyst aided in low temperature oxidation of trapped particulate matter. Investigation of catalyst robustness is performed using laboratory scale methods, investigating the carbon combustion with and without the catalysts and also have also been tested on a diesel engine test bench.

# CHAPTER 2

# LITERATURE REVIEW

The chapter is focussed on the background literature considered for the following experimental and modelling approach for this Ph.D. thesis. As the experimentation is executed on a modern compression ignition (CI) engine, fundamental studies carried out earlier on in-cylinder gas, soot, and particulate matter (PM) emission formation are described, with the recent instrumentation advancements included to investigate the characteristics of these gas and particulate matter emissions. The effect of variant engine parameters on gas and PM characteristics is also addressed in the literature background. Further, after-treatment strategies for the control of engine exhausts are explained, focussing on particle filtration and the performance of a diesel particulate filter (DPF). Types of catalysts and their morphologies coated on these after-treatment systems are demonstrated to provide an in-depth understanding and foundation for further research carried out. Later, the chapter progresses with a thorough review of different emission models that have been used previously for gas and PM emission characterisation. Finally, the chapter concludes with the summary of literature background covered and follows to research methodologies and set-ups.

## 2.1 IC engine in-cylinder and after-exhaust emissions

Universally, engine emissions are categorised in two parts: gas and particulate matter (PM) emissions. Particulate matter (PM) consists of ultra-fine and fine nanometre sized solid and liquid particles that range from 1 nm to 1000nm. Whereas, gas emissions comprise of numerous toxic and harmful gases, prominently unburned hydrocarbons (HC), oxides of carbon (CO and $CO_2$) and nitrogen oxides ($NO_x$). [22-24]

These emissions hold toxic and carcinogenic characteristics that can affect the human health leading to severe conditions. To understand its effects and what they mean to environmental impacts, it is important to study its structure and behaviour, and develop control techniques to decrease the health and environmental effects caused.

### 2.1.1 Diesel particulate matter (DPM) formation

Particulate matter is a mixture of condensed solid and liquid particles, containing two categories of organic fraction: soluble and insoluble. Solid particles are categorised as soot and liquid as soluble organic fractions (SOFs), such as polycyclic aromatic hydrocarbons (PAHs), aldehydes, paraffin, and alkanes. These combine together to form particulates that differ in size from nanometre (nm) to micrometre (μm). [1, 9, 22, 24]

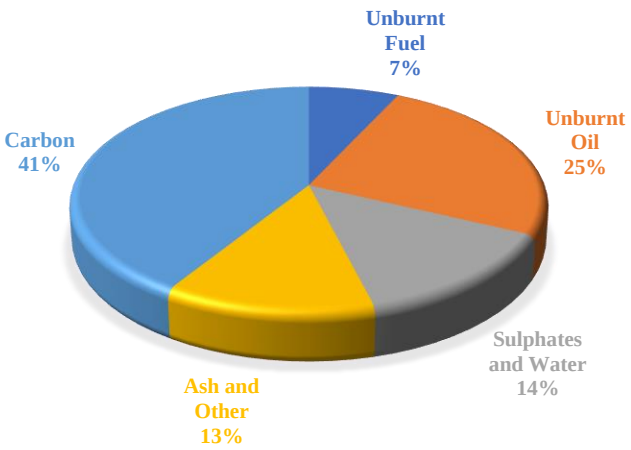


**Figure 2.1 - Composition of particulates in a heavy-duty vehicle exhaust [25]**

Particulate size ($D_P$) is assumed spherical and generally measured from 1 nm to 10000 nm diameter. These particulates are characterised in three size categories depending on the particle diameter as nucleation mode (NM) – (< 50 nm); accumulation mode (AM) – (50–1000 nm); and coarse mode (> 1000 nm), which is a common practice to be measured in terms of size irrespective of their particle nature (solid or liquid). [22, 24, 25] Figure 2.2 shows the graphical representation of these modes. In recent decades, concerns regarding nucleation and accumulation modes are more due to their tendency to penetrate the human body through the skin as the particle sizes vary in nanometres.

The formation of PM undergoes many physical and chemical processes from fuel pyrolysis to agglomerates. Figure 2.3 shows the processes involved in the formation of PM agglomerates: 1) fuel pyrolysis; 2) nucleation; 3) surface growth; and 4) agglomeration.

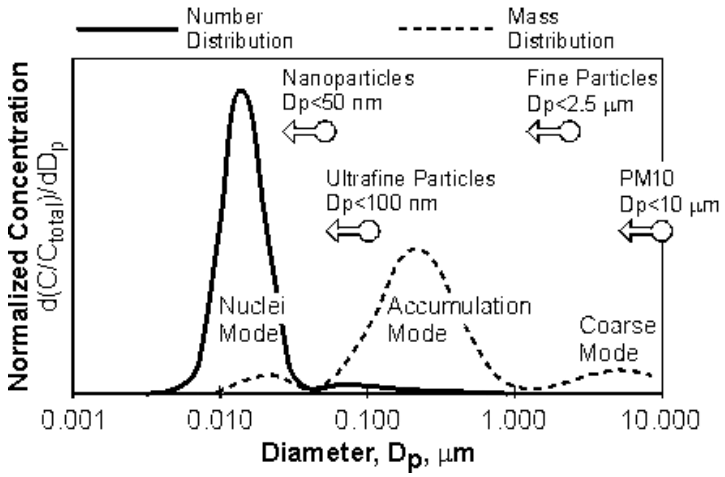


**Figure 2.2 - Particulate size distributions [25]**

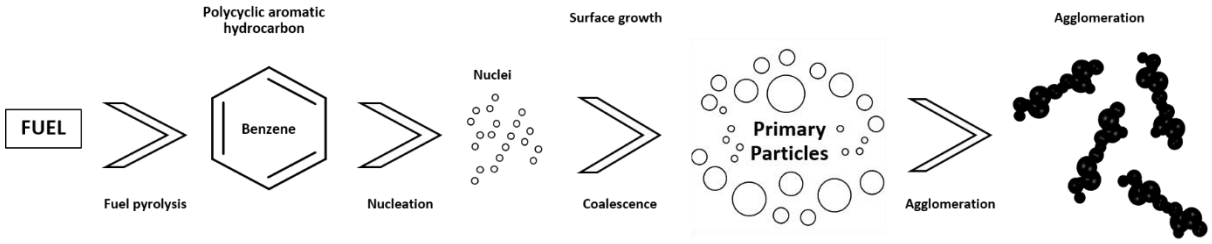


**Figure 2.3 - Physical processes for particulate formation [22, 24]**

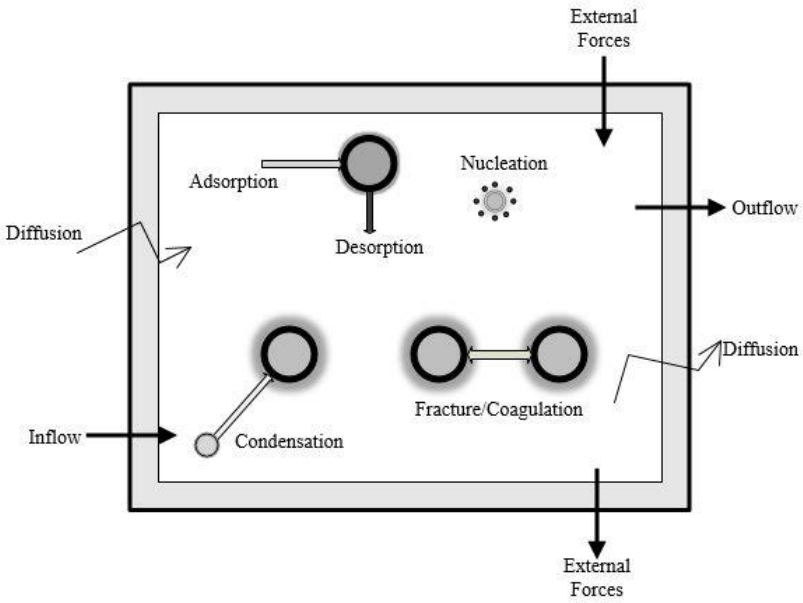


**Figure 2.4 - Particulate interaction and physical processes**

From fuel chain pyrolysis to the formation of agglomerates, particulate formation is closely dependent on many physical factors and engine operations; such as the amount of fuel injected, low or high combustion temperature and pressure during the power stroke, and most importantly, fuel structure. Diesel fuel structure consists of carbon and hydrogen chains ranging from $C_{10}H_{20}$ to $C_{15}H_{28}$ which comprise a lower volatility grade and require a high compression ratio for complete combustion. Whereas, gasoline fuel structure has a smaller chain structure consisting of n-octane and it is comprised of $C_8H_{18}$ chains which contain high volatility characteristics and require a spark to commence combustion inside the chamber. Particulate formation in both fuels undergoes a similar process, but their particulate sizes and concentrations differ on a larger scale. Due to the volatility of gasoline exhaust emissions, PM formed from octane chains is dominated more by nucleation mode (< 50 nm) particle concentration than accumulation and coarse mode (> 50 nm) collectively. Whereas for high hydrocarbon chains of diesel fuel, the PM consists of an irregular distribution of nucleation and accumulation mode particles that change depending on the engine operating conditions. [22, 24-26]

Fuel injected in the combustion chamber with a mixture of air undergoes oxidation during the combustion stage; where hydrocarbon chains under the influence of a high temperature and in the presence of oxygen, form gas species. At fuel-rich regions and low oxidation temperatures, the process of pyrolysis is carried out; it collapses hydrocarbon (HC) chains into smaller components and incepts a soot nuclei or precursors for soot build-up by surface growth. Rising in-cylinder temperatures increase the oxidation and pyrolysis rates which present faster oxidation rates than pyrolysis. Fuel pyrolysis produces fundamentally similar species for diesel and gasoline fuels with variations in species volume of polycyclic aromatic hydrocarbons (PAHs), polyunsaturated hydrocarbons, acetylenes, and poly-

acetylenes. Heavier molecules stimulate a radical pool size as stated by [27], with an addition given where pyrolysis produced a higher amount of radicals. [28] Stated that the primary by-products of fuel pyrolysis in laminar diffusion flames were ethylene, acetylene, methane, benzene, and propylene. In addition, [29] reported on the oxidation of acetylene in the presence of a sufficient amount of O and OH. The report also suggested that due to radicals like O, $O_2$, and OH, pyrolysis can induce higher rates, as the mechanism involves bonding to free radicals forming complex chemical compound species.

Further to pyrolysis, the inception of soot particles progresses from gas-phase reacting species. The process of forming a soot nucleus from gas-phase reactants is called the nucleation process which takes place in fuel-rich regions and oxygen-deficient regions. It is stated by [9, 22, 24, 26] that increasing radical binding to hydrocarbons and aliphatic compounds, form heavier aromatics inducing soot inception. Importantly, the formed nuclei does not accomodate to the total soot mass at this stage, but it has considerably a significant effect at later stages. Due to its potential for an increase in the surface growth, mass addition to the soot nuclei is strongly supported. The nucleation procedure typically is not observed in the primary stages of combustion where temperatures are higher and the fuel-air mixture is oxidised to specific gas species without nuclei formation [22, 24]. Soot formation mechanics can be primarily based on the initial temperature and type of fuel injected. The tendency for soot formation is determined based on its primary aromatic ring formation, following the increase in the rate of soot inception. The aromatic rings, bound together or with other radicals, determine the rate of formation of a soot nucleus. With the ascension of these aromatics to form PAHs in the presence of radicals and other gas-phase predecessors, a soot nucleus is formed. Whereas, tearing of these rings decreases the process of soot formation, as stated by [28].

Surface growth increases the size and mass of the nucleated particle. As the temperature gradient reduces inside the chamber, nucleated particles ascend in further physical processes to adsorb, desorb, deposit and condense on formed vapour and particulate phase species. Since the residence time for these processes is time-dependent from a few picoseconds to 0.05 ms, the soot volume fraction and soot mass experience its effects significantly. [1, 9, 22, 25]

Coagulation or coalescence takes place further to the surface growth of spherule particulates. The process of coagulation (or coalescence) is two particulates fusing with each other to form a larger spherule. During this process, the particle number reduces depending on the coagulation rate of particulates and does not change the mass of two independent particles. Considering the particles are spherical, the coagulated particle is formed to give an approximately larger sphere. Further to coagulation, these fused particles combine with other coagulated and singular particles forming irregular or spherical structures of particulates. They form chain-like structures comprised of small and large particles, and the process of this formation is called agglomeration. [22, 24, 29]

Diesel exhaust soot comprises primary spherical particles which agglomerate to chain structures, and the initial size of these spherules depends on the engine operating conditions and other fuel injection parameters. In [22] it was reported that 20 to 50 nm as the primary spherule ranges. Whereas, [30-32] reported a different range for primary particle formation using different instrumentation and methodologies. The authors used optical and light scattering techniques reporting 30-70 nm, 30-50 nm and 40-65 nm respectively as the average particle size ranges. To investigate these physico-chemical processes involved, emission models have been previously studied, giving an insight into the changes from particle

nucleation of gas emissions to forming agglomerates, depending on the physical and chemical factors associated with it.

### 2.1.2 Effects of engine operating parameters on PM characteristics

Characterisation of PM depends majorly on the engine operating conditions or the factors that affect the particulate structure. The PM changes can be mainly classified and controlled based on two categories: pre-combustion and post-combustion. Figure 2.5 shows the techniques involved for PM control used before and after combustion. The highlighted points shown are the techniques used in the research carried out by the author in this thesis and the further literature is focussed on the same parameters.

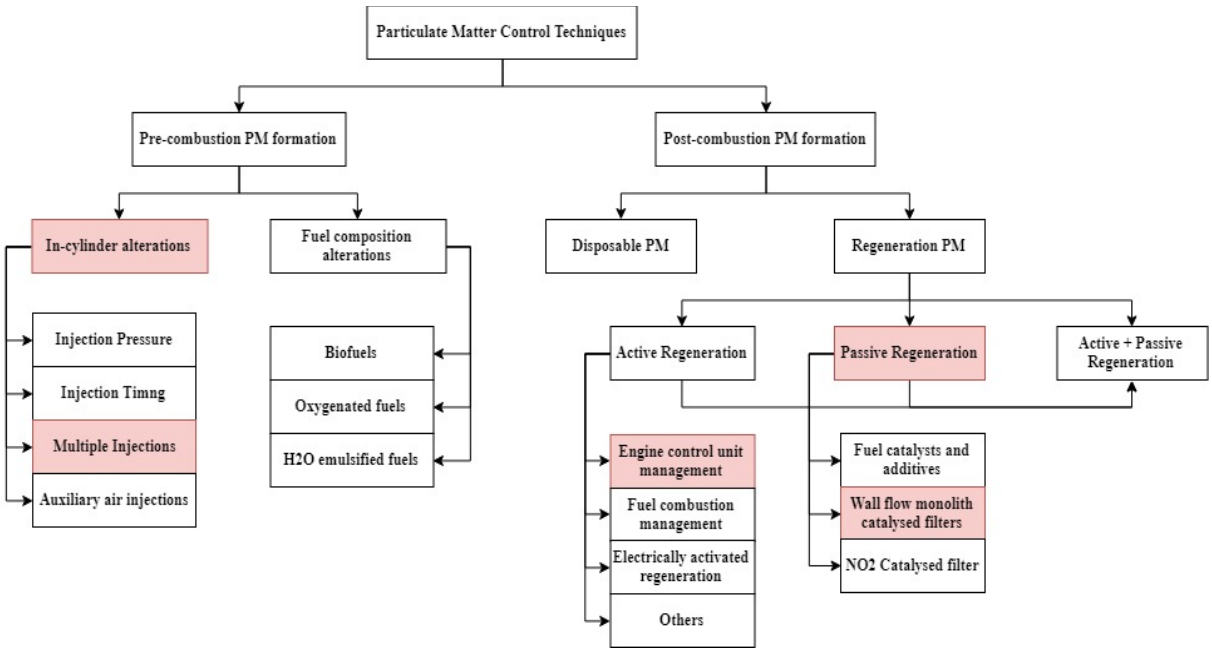


**Figure 2.5 - Particulate matter control techniques' layout [24]**

#### 2.1.2.1 Effect of in-cylinder operations on particulate matter

For pre-combustion PM formation, the control techniques are categorised as in-cylinder and fuel compositions' alterations. These relate chiefly in the discipline of fuel injection strategies and fuel compositions used for the combustion process.

Biodiesel fuels have been widely researched due to their lower aromatics and sulphur content, aiding complete combustion and reducing PM significantly compared to pure diesel. Additionally, biodiesels have also proven to have partially achieved the stringent emissions targets for regulated emissions and still undergoing a continual research for its higher share of applicability. Some of the research for reducing PM using biodiesel was done by [33-36]. Similarly, oxygenated fuels have also shown an effective reduction in PM due to the oxygen content present in their chemical composition. A higher cetane number due to the oxygen present in the fuel improves the ignition quality and substantially reduces the ignition temperatures and PM formation. Using these oxygenated fuel additives has shown a high-grade reduction in PM and was reported by [37-42]. Although these methodologies help in the reduction of PM, there are many other methodologies that relate to altering the engine in-cylinder parameters which are further explained.

##### 2.1.2.1.1 Effect of injection pressure

Fuel injected in the cylinder responds in its output during combustion through its injection timing and pressure. The atomization of fuel closely depends on its injection pressure. An increase in fuel injection pressure contributes to a fine fuel atomisation and reduces the size of the fuel droplets considerably. This leads to a large reduction in PM due to its complete combustion inside the combustion chamber with high injection pressure. Additionally, the nozzle hole is also a critical factor to be considered with increasing injection pressure. The use

of micro-sized nozzle holes and high injection pressures have shown a significant decrease in PM formation. [24, 43, 44]

#### 2.1.2.1.2 Effect of injection timing

A common controlling technique to reduce PM is fuel injection timing. The controlling technique is accompanied by a renowned $NO_X$-PM trade-off. Retarding the injection timing gives an increase in $NO_X$ with a decrease in PM concentration; and contrarily, advancing the injection timing shows a substantial increase in PM with a reduction in $NO_X$. [22, 24]

Retarding the injection timing reduces the ignition delay, and hence reduces the premixed combustion duration and the unconventional mixing of the air-fuel mixture, giving rise to PM formation and decreased $NO_X$. Contrarily, with advancing the injection timing the duration of the premixed combustion is lengthened leading to a more homogeneous mixture preparation prior to combustion and thus increasing the ignition delay. Hence, the PM decreases significantly and $NO_X$ concentration is observed to increase. [1, 9] Also, the rate of vaporisation of the fuel droplets is dependent on the droplet size, distribution, velocity, and in-cylinder temperature and pressure. As observed, due to the $NO_X$-PM trade-off, it is essential to review the advancement in reducing the formation of both gas and particulates.

#### 2.1.2.1.3 Effect of multiple injections

Multiple injections are a widely and commercially used injection strategy for conventional diesel engines in order to reduce $NO_X$ and particulate emissions. It has proved to be effective in reducing these emissions on a common rail direct injection (CRDI) fuel system, providing variable injection timing at shorter durations. Comprised of an electronically

controlled solenoid valve, these multiple injection events aid in controlling the pressure and timing precisely.

Multiple injection events stem from the pilot injection, main injection and finally post-injection event. Pilot injection introduces the fuel inside the combustion chamber before the main injection event, aiding in increasing the in-cylinder temperature before the main injection. This reduces the ignition delay, and helps in reducing the chance of the fuel burn fraction occurring at primary premixed fuel burn at the main injection. Due to this effect, engine knock reduces considerably as the in-cylinder peak pressure also reduces effectively. As mentioned in section 2.1.2.1.1, lower pressure increases the amount of PM formation and hence pilot injection increases the PM in most cases. This effect on the PM increase occurs due to two factors mentioned below:

1. By-products formed at the pilot injection event have a higher temperature and further reduce the oxygen concentration; in turn reducing the oxidation rate after fuel pyrolysis.
2. Due to the initial high in-cylinder temperature during the main injection event, combustion duration is reduced significantly, thus reducing the charge air during the main injection.

On the other hand, post fuel injection is executed after the main injection event; where about 10% of the total fuel is injected into the combustion chamber. Post injection also helps in increasing the exhaust gas temperatures needed for regeneration in particulate filters and wall-flow monoliths addressed in the following section. Several authors have studied and reviewed the effects of multiple injection strategies on gas and particulate emissions. [1, 9, 22, 24, 41, 42]

## 2.2 Diesel particulate filters – filtration and regeneration

The diesel particulate filter (DPF) is a commercially used after-treatment system in light-duty, heavy-duty and also off-highway diesel engines worldwide. An increase in the research of DPFs is seen in the past for filter geometric configurations, filtration efficiencies, minimal pressure drop and its oxidation temperatures for PM burn and gas species conversions. The fundamental objective of a DPF is to provide high mechanical filtration of PM and oxidising soot under low or high temperatures. A considerable issue with the DPF is its increasing backpressure due to soot accumulation on its channel walls and the high oxidation temperatures, decreasing the engine performance significantly. [45-48]

For every geometric design rendered for the DPF, wall-flow monoliths have come across as an appropriate DPF configuration, generally manufactured using silicon carbide (SiC) or cordierite ($Mg_2Al_4Si_5O_{18}$). It is important that the materials used in the manufacturing of DPFs should possess a low thermal expansion, high operating temperatures, thermal and chemical resistance, low-pressure drop and high filtration efficiency characteristics which aid in providing a high performance in filtration and regeneration of substrates. [48-51] They contain a bundle of axially parallel porous channels, plugged alternately at each end, which drives the exhaust gas and particulates to flow through these porous walls to undergo filtration and gas species conversion during regeneration. [51] Some of the important characteristics needed for the optimal performance of DPFs were studied by [52-54] to achieve the maximum performance and robustness of the system. A typical DPF internal structure and a schematic of the channels is shown in Figure 2.6.

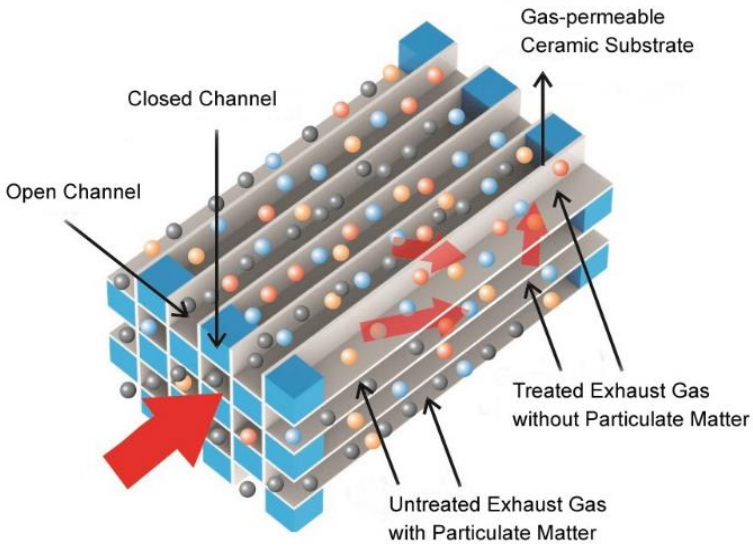


**Figure 2.6 - DPF channel structure [55]**

### 2.2.1 Diesel particulate filter regeneration

An incorporated diesel particulate filter in the exhaust pipe of diesel engines undergoes two types of regeneration mode: active regeneration and passive regeneration. Table 2.1 shows the classified techniques used for active or passive regeneration for any DPF. [48] High-pressure drop and high exothermic temperatures are mainstream causes that affect the performance and failure of DPFs. To compensate for these failure mode problems for DPFs, the regeneration of these substrates is critically important. Regeneration is the process where the soot accumulated inside the filter substrate channels undergoes soot burn and oxidation using different regenerative methodologies. In general, particulate filter regeneration is categorised in active and passive regeneration methodologies. Both are conventionally used together to provide higher filtration and soot reduction/oxidation efficiency. [56]

Active regeneration is proceeded in a DPF using an internal or external method for soot burn by thermal treatment. Some of its common methodologies are carried out using a controlled post-injection fuel intake [57-59], external fuel burning [60] and strategies to inject

hydrocarbons inside the exhaust tailpipe. Whereas, passive regeneration or continuous regeneration requires a catalyst coated on the DPF channels, or fuel additives to improve the soot-catalyst interaction and increase the rate of oxidation without an increase in the exhaust temperatures. [48] A commonly used non-noble commercial catalyst material is platinum (Pt), which generally is accompanied with the DPF as a powder coat on the filter channels. The interaction between the catalyst and the PM increases with increase in the particle surface areas, but depletes the overall porosity factor of the monolith substrate depending on the volume of the catalyst dissipated on the DPF. Also, catalysts are commonly used to increase the oxidation inside the particulate filter channels. Such after-treatment systems commonly undergo a continuous regeneration procedure. The advantages of these systems are that they help in reducing the backpressure of the DPF to a minimal, increasing the filtration efficiency and reducing oxidation temperatures (< 500 ºC).

**Table 2.1 - Diesel particulate filter regeneration modes**

| | **Active Regeneration** | **Passive Regeneration** |
|---|---|---|
| Continuous Regeneration | Microwave regeneration<br>Plasma regeneration (Ozone, OH – radicals, $NO_2$) | CRT System (producing $NO_2$ at DPF upstream) |
| Discontinuous Regeneration | Engine management system (EGR, post-injection or compressor bypass), Exhaust gas burner, Electric heater, Electric oven | Catalyst coating on DPF channels,<br>Fuel additive catalyst |

### 2.2.1.1 Catalysed particulate filter passive regeneration

A diesel particulate filter (DPF) is utilised with an exhaust tailpipe to separate carbonaceous particles by mechanical filtration, and concomitant burning of particulates to avoid pressure build-up by filter plugging. As these materials burn at high temperatures of around 550 °C in the presence of oxygen, and diesel exhaust gas temperatures lie between 100 to 400 °C, an acceptable catalyst is essential to advance the particulate combustion. [61, 62] Thus, it is important to develop an appropriate chemically reactive material that bears sufficient activation energy to ignite and combust the particulates at low temperature. The combustion of soot subject to a lot of species conversion as NO is altered to $NO_2$ and acts as an oxidizer for the soot combustion at low temperatures. [63, 64]

Most studies were conducted on soot samples that were easily accessible. The utilisation of model soot-like C (Printex ® – up by Degussa) [65] can be considered as a substitute for real soot for catalyst testing, as the composition of real soot from a diesel exhaust is heterogeneous. [66] To sporadically regenerate the filter, the loaded soot modifies by

increasing the flue gas temperature (250-400 °C) to reach soot ignition, depicting considerable oxidizing rates at approximately 550-650 °C. Since the temperature increase is achieved using post fuel injection for active regeneration, a catalyst is employed to aid soot combustion at lower temperatures, achieving an overall reduced fuel consumption called passive regeneration. Several soot combustion catalysts are developed and it is also observed that many oxides work as soot combustion catalysts. [67-71] However, ceria based catalysts often exhibits an extensive oxidation reactivity, poor chemical reactivity, and high thermal stability, considering several different ceramic supports and compression ignition emission elements. Due to the excessive oxygen storing capability, ceria and its oxide compound materials have attracted much attention as chemical reaction catalysts. [72, 73] In particular, cerium oxide ($CeO_2$) and praseodymium (Pr)-based oxides are proposed as a low-cost chemical compound with the potential to extend the reaction rates of soot combustion chemically, acknowledging the production of active oxygen. [74-76]

Praseodymium chemical compound is enlisted in the group of the rare-earth oxides, as it forms a homological series with a numerous range of stoichiometric defined oxides: $Pr_nO_{2n-2}$, with n = 4, 7, 9, 10, 11, 12, ∞, [77, 78] and its acute cases are $Pr_2O_3$ and $PrO_2$; $Pr_2O_3$ will acquire a hexangular or a 3-dimensional structure, [79, 80] while $PrO_2$ exhibits a fluorite-like (cubical) structure. Another conjointly stable phase at close temperature and in the atmosphere is $Pr_6O_{11}$, which can be thought of as an associate degree oxygen-deficient mutation of $PrO_2$. The $Pr_6O_{11}$ and the optional phases with a fluorite-like structure in the homological group of oxides that bear metal cations of variable valence states (3+ and 4+). These oxides possess the highest oxygen mobility characteristic in the series of lanthanoid oxides, as a result of the variability of stable phases permitting immediate alterations in the oxidation number of metal. [81] This aspect renders this system and is appealing for catalytic and other applications

requiring eminent oxygen ion mobility. Platinum (Pt) based catalysts are considered to be the major dynamic compounds for diesel residue oxidation in realistic conditions, however, other strong catalysts are being researched to enhance the movement and reduce the cost. Impregnation of cerium oxides and Ce–Pr blended oxides specifically are among the promoted contenders to supplant platinum, on the grounds that they deliver exceptional dynamic oxygen species for oxidation. [82-87] this receptive dynamic oxygen is delivered by oxygen trade between the cerium oxide-based impulses and the oxygen-containing gas atoms (predominantly $O_2$). [71]

## 2.3 Diesel particulate filter numerical model

Although the thesis does not contain any modelling based research of DPFs, it is still critically important to understand the fundamental of pressure drop and soot oxidation inside the filter substrate channels. Hence, with the investigation of dimensional models for a single and multi-channel, it is critical to review the sub-models associated with them. There are three major categories for DPF sub-models:

1. Pressure drop model
2. Filtration model
3. Soot oxidation model

Where, the pressure drop and soot oxidation models are introduced to give a foundation on final results achieved in chapter 6 based on the control of PM, filtration and oxidation. Some authors, such as [45, 46, 88] have studied pressure drop models inclusive of empirical and numerical validations and have investigated without much consideration of other parameters like soot density and permeability. Since the regeneration of the DPF plays an important role

in studying the conversion of gas and PM emissions inside the DPF, it is necessary to define the soot oxidation model precisely to attain robust results for the defined problem. Many researchers have integrated the filtration model in their study but did not precisely calibrate the model to achieve prominent results. To define the problem and increase the precision for various models it has to be defined mathematically, in particular for pressure drop across channel walls due to soot build-up, filtration across the channel, and temperature gradient to achieve higher soot oxidation.

### 2.3.1 Pressure drop model – clean and loaded channels

For pressure drop for a rendered DPF design, it is important to consider the two important parameters, the pressure drop (Δp) and soot oxidation. The design of a DPF depends on its backpressure at upstream, as it is critical to reduce it as low as possible to avoid DPF failures in realistic conditions. Whereas, experimentally the soot oxidation is activated using the engine control unit which takes the backpressure into account for the regeneration process to burn soot mass. A pressure drop model incorporates the overall pressure change due to the channel walls, soot layer displacement, contraction and expansion of exhaust flow. [45] The pressure drop across a DPF channel includes these four factors combining to result in the total pressure drop as shown in equation 12.

$$\Delta p = \Delta p_{wall} + \Delta p_{soot} + \Delta p_{contraction} + \Delta p_{expansion} \quad (8)$$

Each function relating to pressure drop has its specific parameterisation. The pressure drop model for a clean filter channel wall is expressed by the elemental Darcy's Law with the inclusion of the Forchheimer inertial term for differential pressure as:

$$\Delta p = \frac{dp}{dx} = \frac{\mu v(x)}{k_p} + \beta \rho(x) v^2(x) \tag{9}$$

Where $k_p$ is Darcy permeability and $\beta$ represents the Forchheimer coefficient. The terms are inter-related as established in [45, 89] and are dependent on the porosity and pore size of the medium. The Forchheimer term is expressed in equation 14, to define the inter-relativity of these terms. The Darcy losses are very high compared to Forchheimer losses, hence neglecting the term does not affect the total pressure drop across the filter channel. Further, the Darcy permeability term is defined in equation 15.

$$\beta = \frac{constant}{\varepsilon^{1.5}\sqrt{k_p}} \tag{10}$$

$$k_p = f(\varepsilon) \cdot d_{c0}^2 \cdot SCF \tag{11}$$

where $\varepsilon$ is the filter porosity; $f$ (ε) as the porosity factor; $d_{c0}$ is the clean collector diameter; and *SCF* is the Stokes-Cunningham factor for slip flow effect correction. The above model for pressure drop satisfies certain limitations; and reference [89] notes, due to the scarcity of pressure drop data for various DPF designs provided, the above model can be taken into consideration for permeability estimation for porous medium theory.

For a soot-loaded channel of the DPF, the complexity of the pressure drop model increases due to its additional factors such as an increase in the soot layer density and particulate filtration on the channel walls and soot layer. Changes in pressure drop are carried out due to two sequential filtration phases. The initial phase comprises the filtration through the blank channel walls called deep bed filtration, where particulates are filtered from the

porous walls. Depending on the pore size, the channel walls are packed with a large spectrum of differently sized particulates inside these pores. As the particle packing inside the walls reaches its peak, the formation of a soot layer on these channel walls starts to build up. This phase is known as soot cake layer filtration. During this stage, the pressure drop across the DPF starts to increase non-linearly with time until it reaches its peak pressure for regeneration. [59, 89, 90]

Soot layer permeability and density are considered as the integral and important parameters of a pressure drop model. Many authors [59, 91-96] have studied and estimated different values for soot layer density and permeability. The generic range of soot layer density lies between 75 and 200 $kg/m^3$. Whereas, soot permeability falls in the range of 1 to $6*10^{-14}m^2$ which has not been explained by many authors in earlier literature. [89]

### 2.3.2 Soot oxidation model

To investigate the optimal performance of a rendered DPF design, it is essential to achieve maximum filtration and regenerative/oxidation efficiency. Soot oxidation explains the species conversion of gas and particulate emissions inside DPF channels, and it is significantly dependent on the oxidation reactivity of soot particles. As described in earlier sections, the oxidation of aggregated soot inside channels rely on their ignition temperatures which go as high as 600 ºC. An in-depth understanding of soot kinetics, surface chemistry, and exhaust gas composition is needed to provide an efficient strategy for regeneration inside DPFs. The soot oxidation models provided by [88, 93, 95, 97, 98] give a detailed understanding of the global reactions taking place inside the channels, but do not specifically provide the corresponding reactivity values. To investigate these specific reaction relativities to thermic reactions taking

place inside the DPF channels, it is prominently difficult. Due to the consistent changes in the exhaust emissions by transient engine conditions, it is difficult to specify the exhaust composition and achieve robust valuation for reactivity terminology. Some authors have previously presented the parametric values based on non-catalytic reactions as shown in Table 2.2. The soot oxidation is dependent on the generic expression of the Arrhenius equation for investigating reaction rates, as shown below in equation 16. Various Arrhenius expressions are presented with the inclusion of oxygen-dependent parameters for activation energies, reaction orders, and rates.

$$k = Ae^{\left(\frac{-E_A}{RT}\right)} \tag{12}$$

where '*A'* represents the pre-exponential factor; *'$E_A$'* is the activation energy calculated experimentally or theoretically; *'R'* is the gas constant and *'T'* represents temperature.

**Table 2.2 - Soot oxidation rates and parameterisation [88]**

| Author | Rate Expression | Parameters | Remarks |
|---|---|---|---|
| Neeft et al. | $\frac{dm}{dt} = -A \cdot \exp\left(-\frac{E_a}{RT}\right) \cdot [1 - \lambda']^{n_c}\left[P_{O_2}\right]^{n_{O_2}}$ | $A$ = 5.2 * $10^6$ 1/s, $E_a$ = 168 kJ/mol, $n_C$ = 0.73, and $n_{O2}$ = 1 | Derived from surrogate soot, poor fit for diesel soot, temperature: 442 – 527 °C |
| Yezerets et al. | $\frac{dm}{dt} = -A \cdot \exp\left(-\frac{E_a}{RT}\right) \cdot [m]^{n_c}\left[F_{O_2}\right]^{n_{O_2}}$ | $E_a$ = 132 ± 5.1 kJ/mol, $n_C$ = 1, and $n_{O2}$ = 0.71 ± 0.03 | $A$ not given temperature: 375 – 550 °C |
| Darcy et al. | $\frac{dm}{dt} = -A \cdot \exp\left(-\frac{E_a}{RT}\right) \cdot \left[P_{O_2}\right]^{n_{O_2}} m_0 \left(\frac{m}{m_0}\right)^{n_c}$ | $A$ = 8.5 ± 0.4 * $10^7$ 1/s, $E_a$ = 164 kJ/mol, $n_C$ = 0.5, and $n_{O2}$ = 0.9 | Dry diesel soot temperature: 480 – 560 °C |
| Chong et al. | $\frac{dm}{dt} = -A \cdot \exp\left(-\frac{E_a}{RT}\right) \cdot [m]^{n_c}\left[P_{O_2}\right]^{n_{O_2}}$ | $A$ = 0.31/0.05 * $10^7$ 1/s, $E_a$ = 139.6/136.3 kJ/mol, $n_C$ = 0.24/0.74, and $n_{O2}$ = 0.96/0.97 Zone 1/Zone 2, respectively | Dry diesel soot temperature: 500 – 600 °C |
| Kalogirou and Samaras | $\frac{dm}{dt} = -A \cdot \exp\left(-\frac{E_a}{RT}\right) \cdot [m]^{n_c}\left[P_{O_2}\right]^{n_{O_2}}$ | $A$ = 1.72 * $10^9$ 1/min, $E_a$ = 161.2 kJ/mol, $n_C$ = 1, and $n_{O2}$ = 0.75 | Temperature: 550 – 700 °C |

## 2.4 Exhaust emission modelling progression

Tailpipe aerosols have demonstrated the significant impact on human health and climate. To assess the impact of these aerosols from fuel-led engines, it has become crucial to predict and investigate the nature of these gas and particulate emissions. To do so, various modelling methods have been introduced in investigating the physical and chemical science behind these heterogeneous compositions of gas and particulates. As mentioned previously, the formation of exhaust emissions constitutes numerous physical and chemical processes carried out from fuel pyrolysis to formation of agglomerates. Further, when these emissions are forced out of the exhaust port, due to the changing temperature gradient along the exhaust tailpipe the gas emissions form a nucleus by the combination of solid, liquid and gaseous matter and later forming variable size particulates. To investigate the physical impact of temperature gradient and dilution on gas and PM emissions, many authors have investigated different dynamic phases of gas-to-particulate growth.

Emissions' theoretical, numerical and empirical modelling dates back to when the classical nucleation theory was introduced in 1935 by R. Becker. [99] Over the course of the last 30 years, modelling emissions has been an important research area considering the formation of carbon, sulphates and other harmful gas compounds to nuclei and growth of particles due to their individual condensation rates and temperature gradients. Many researchers like [100-106] have performed fundamental case studies on particulate formation; differentiating the dynamical formation of particulates from gas to the particulate phase. The important models differentiated by [107] in their model studies are the empirical Gaussian model, similarity model, probability density function (PDF) model, statistical model, $k - \varepsilon$ model and large-eddy simulation (LES) model for exhaust plume after a tailpipe.

To investigate particle formation, it is also important to consider the sampling conditions from the exhaust tailpipe or plumes. The effects of dilution air on particulate dynamics of particulates can aid in predicting gas to particulate matter (PM) nucleation more precisely. Due to the limitation of instrumentation and sampling devices operating at sampling and dilution temperatures, the engine exhaust is mixed with dry and ambient air for measuring PM sizes and concentrations, considering a pre-determined dilution ratio (PDR). The sample progresses for analysis which determines the characteristics for different modes of particulates (mainly nucleation and accumulation mode). Modelling these parameters makes the predictive model more precise yet complex, due to its variability in initial parameterization.

In 1991, [100] introduced a detailed planar computational model for soot inception, nucleation, and growth. The model described the initial fuel pyrolysis to the formation of PAHs, and further surface growth to increasing spherules and their oxidation. The particle inception follows up due to the coagulation of monomers and dimers (specifically PAHs), and essentially shows the surface growth of particulates affected due to the chemically induced environment. Due to pyrolysis, the initial formation of the aromatic ring can be given for phenyl and benzene using equations 13 and 14.

$$n - C_4H_3 + C_2H_2 \rightarrow phenyl \quad (13)$$

$$n - C_4H_5 + C_2H_2 \rightarrow benzene + H \quad (14)$$

Fuel sulphur is also an important aspect in the formation of particulates, where fuel sulphur content (FSC) is more or less proportional to the conversion and fractional content in the exhaust. A major fraction of fuel sulphur is oxidised to form sulphur dioxides ($SO_2$); some escape in further formation to sulphur trioxide ($SO_3$) that subsequently undergoes

hydrogenation forming sulphuric acid ($H_2SO_4$) and other sulphate compounds. These aid in nuclei formation due to vapour condensation. [25, 103] To predict a more accurate particle size and concentration, use of binary nucleation of $H_2O$–$H_2SO_4$ parameterisation is critically important, as a certain fraction of particle composition also consists of these compounds'; and also crucial for the variations in the nucleation rate among the collective result of particle size and concentrations that aid in a comparative analysis of theoretical and empirical outputs. [102, 103]

Particle formation can be determined precisely considering the dilution of exhaust gases and in regards of other atmospheric conditions. Hence, exhaust gas temperature (T) and relative humidity (RH) add to the conversion and nuclei formation of sulphuric acid and water. The nucleation threshold are dependent on the "T" and "RH" is given by equation 15, where nucleation of sulphuric acid proceeds when $C_{H2SO4} > C_{critical}$ in terms of gas-phase concentration. [108]

$$C_{critical} = 0.16 \exp(0.1T - 3.5RH - 27.7) \quad (15)$$

Many authors mentioned by Vehkamäki [103] have investigated theoretical and experimental studies of dilution effects on ultra-fine particulates, whereby parameterising binary water and sulphuric acid and the inclusion of consequential hydration are observed to provide a reasonable comparison between numerical and experimental studies. Although the nucleation rate from gas species has the highest priority in understanding nucleation of gas compounds, it was observed that singular estimated nucleation of $H_2O$–$H_2SO_4$ provides a lower theoretical nucleation rate, and it is important to consider other gas emissions aiding nuclei formation and ultra-fine particulates.

Relative humidity (RH) and temperature (T) parameters for nucleation rates are calculated as the sampling of PM is done under diluted exhaust and dry air conditions using gas and particulate analyser instrumentation. The initial condensation of gas emissions (PAHs, $H_2O$, and $H_2SO_4$) proceeds with the nucleus formation and it is critical to determine the nucleation rates and also calculating the molecules added in the critical cluster of nuclei, further updating the initial nucleation mode particle size and density. [103] Vehkamäki provided parameterization for a temperature range of 300K to 400K (26.85ºC to 126.85ºC), by mentioning an extrapolation of the numerical method used for temperature above the desired range.

Another parameterisation was also explained by Vehkamäki [109], where the nucleation and thermodynamic computation was valid for temperatures below 305.15K at dilution percentages from 0.01% to 100%. Also, many authors have simulated gas and particulate emissions using computational fluid dynamics (CFD), [105, 110-115] investigating the in-cylinder and the exhaust tailpipe particle growths under dilution and non-dilution conditions. A comprehensive soot model by Sanjin Hong [110] was simulated for a 3D CFD model for soot emission predictions under various engine operating conditions. The simulated model was a combined approach to validate the experimental approach and data acquired, for an increasing range of injection timings with the soot model for an ‘n-heptane’ detailed reaction chemistry.

Erik Herrmann [112-114] provided a merged model, FLUENT based CFD model and fine particle model (FPM), where the numerical approach was established on Euler equations for mass and momentum conservation in FLUENT, and the FPM applied user-defined

functions (UDF) for typical particle formation, growth, coagulation, species transport, deposition and gas and liquid phases. The model used a corrected version of a notable equation of classical nucleation theory shown in equation 11, where the FPM considered 'i' as nucleating species which was single-component nucleation.

$$J_{Becker} = \frac{\left(\rho_g \xi_i\right)^2}{\rho_i w_i} \sqrt{\frac{2\sigma_i}{\pi w_i}} exp\left(-\frac{\Delta G^*}{k_B T}\right)\left(\frac{m_p^*}{w_i}\right)^{2/3} \quad (16)$$

Erik Herrmann mainly studied the inception of particles in $H_2O$-$H_2SO_4$ systems using a CFD approach and FPM for nucleation rates and cluster activation theory. [113] Considering the flow characterisation in a tube or pipe, having low flow velocity significantly changes the particle inception and growth with decreasing growth and increasing residence on chamber walls. Hence, with the decrement in flow velocity, the particle nucleation proceeds closer to the inlet side of the tube and moves away from the inlet with the increment in flow velocity.

Authors [102, 107, 108, 111, 115] used a numerical, computational and empirical approach for the prediction of aerosols. The key aspect of these approaches dealt with the simultaneous growth of particulate matter from the water and sulphuric acid vapour condensation and nucleation and later the effects of temperature and atmospheric conditions on the particle and gas-phase species. The authors also mentioned their other studies considering the dilution and humidity effects of exhaust plumes for light-duty and heavy-duty vehicles. The effects of meteorological conditions have shown a significant change in the number, size and nucleation rate concentrations of particulate and gas-phase species. Considering this wide range of modelling approaches for in-cylinder and tailpipe emissions,

this thesis establishes a compounded model for investigating the particulate characteristics for a long exhaust tailpipe.

## 2.5 Summary

In this chapter the formation, evolution and impacts of gas and particulate matter emissions are discussed. The process of the nucleation of gas emissions to the formation of agglomerates is widely explained. The chapter also explains the impact of different fuel injection strategies for compression ignition engines, and their impact on particulate characteristics. There is also focus on previous emission modelling techniques and case studies to investigate the fundamentals of particulate matter formation and evolution in in-cylinder and plume exhausts. Finally, the chapter explains the functionality of a diesel particulate filter (DPF) from various background literature concerning different morphologies and materials used as catalysts for increasing PM filtration and oxidation. This includes the basis of the numerical understanding of the pressure drop across a DPF and soot oxidation based on different gas emissions and catalytic oxidation.

# CHAPTER 3

# EXPERIMENTAL SYSTEMS AND SETUP

This chapter focuses on the numerical and experimental methods used for the investigation of particulate dynamics, particle growth and an after-treatment system. The initial part of the chapter is focussed on the engine test bench, dynamometer, control systems and on-engine data acquisition systems. The further chapter deals with the introduction of exhaust tailpipe cooling set-up used in chapter 5 for particle dynamics investigation. Additionally, the catalyst preparation and coating methodology on the diesel particulate filter (DPF) is explained in detail that is utilised in chapter 6. The online instrumentation used in the experimentation is also addressed in the later part of the chapter, assisted with the uncertainty and data analysis done for all measurements.

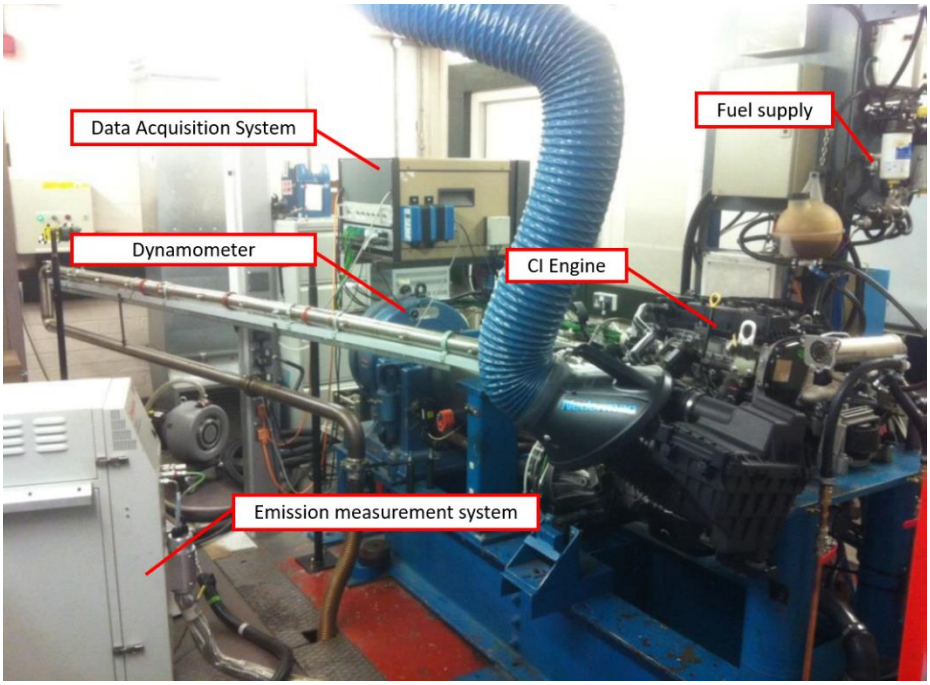


**Figure 3.1 - Diesel engine test bench and data acquisition systems**

## 3.1 Ford Puma direct injection diesel engine

Experiments were performed concerning diesel exhaust emissions on the Ford Puma 2.2 L direct injection diesel engine also referred to as Duratorq L316. The engine is incorporated with a variable geometry turbine (VGT) turbocharger and exhaust gas recirculation (EGR) systems. The in-line 4-cylinder CI engine uses a common rail direct injection (CRDI) system, where solenoid injectors are used for fuel injections providing desirable control of the engine.

Table 3.1 below shows the engine configuration. The engine is coupled with a dynamometer in order to monitor and maintain the engine at consistent speeds (1800 rpm ± 10 rpm). It also has the flexibility of converting an in-line 4-cylinder CI engine to a 3+1-cylinder configuration, allowing the single cylinder of the combined engine to work on different fuel emulsions and the remaining three cylinders on pure diesel. For the single cylinder (3+1) configuration, a separate system for exhaust gas recirculation is incorporated and the fuel injection is done using an external high-pressure injection system equipped with a separate fuel tank. Emission control systems like a DOC and DPF can also be used for emission measurements after the VNT and research of these different emission control systems. Figure 3.2 shows a schematic of the engine and its connected components, to give a clear picture of the engine components and the assisting instrumentation for the engine.

**Table 3.1 - Engine specifications**

| **Specification** | **Value** |
|---|---|
| Engine displacement | 2.198 $cm^3$ (2.2 L) |
| Injection system | Direct injection |
| Compression ratio | 15.5:1 |
| Bore | 86 mm |
| Stroke | 94.6 mm |
| Connecting rod length | 155 mm |
| Fuel | Neat diesel |

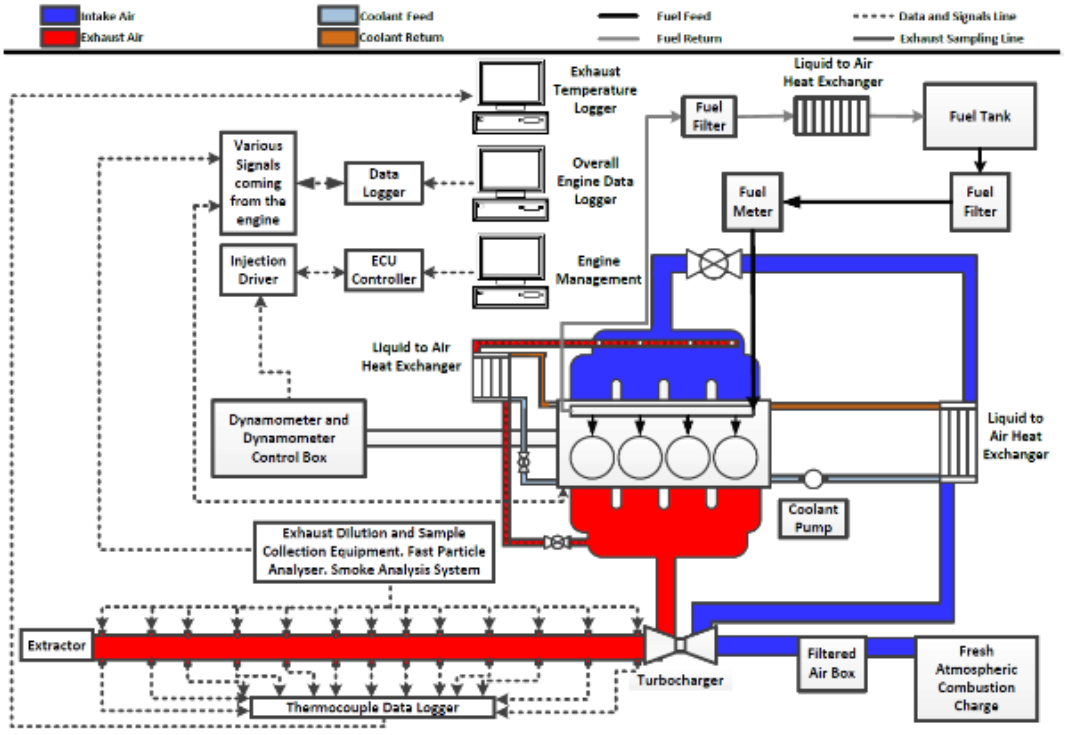


**Figure 3.2 - Schematic for Ford Puma engine**

### 3.1.1 Engine control unit

The engine control unit (ECU) for diesel engine control is an open EC unit that assists the user/ controller to use the engine according to the experimental design requirements with more flexibility. A Pi-innovo manufactured M250 engine control unit is used to control the engine performance, equipped with EGR valve and VNT position control from H-bridges (Axiomatic – manufacturer). The injector controller and open ECU strategic controller are monitored and controlled through a software-based user interface (UI) provided by ATI vision.

The engine control allows the user to control the engine systems for a high performance and high sensitivity engine operation. The user interface (UI) used in the experimentation is given in Figure 3.3, for a better understanding of user control modules. Before the engine is started, the current ECU control strategies are introduced into the UI, where the control strategies are calibrated and optimise the EGR and VNT positions and provide all the enlisted on-board component pressures and temperatures (such as coolant and oil temperatures). Activation of the ECU and calibration/optimisation is done using the 12 V battery power supply when the ignition switch is turned on. This is carried out using a different UI provided by LabVIEW, connected through National Instruments (NI) USB-6218 data acquisition system, allowing the ignition and starter motor to be activated when needed.

Prior to engine cranking, the engine control (fuel quantity and timing, EGR and VNT positions, pressure and temperature) was set to default positions and values that can be overridden with new values once the engine is cranked.

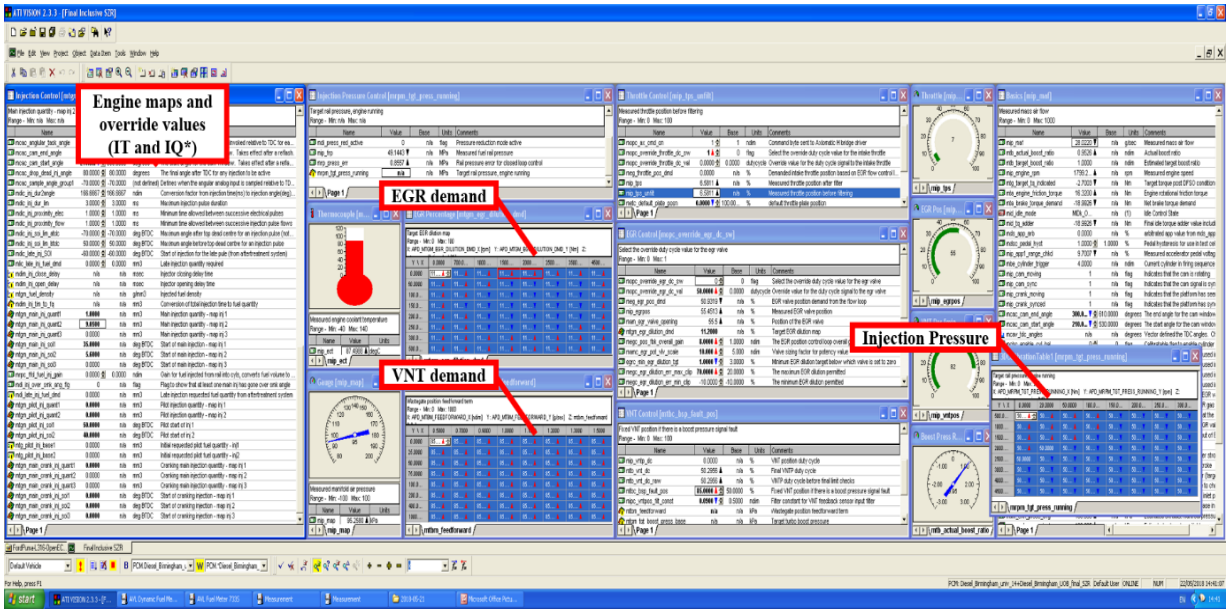


*IT – Injection Timing, IQ – Injection Quantity

**Figure 3.3 - ATI Vision user interface for engine control**

The UI in Figure 3.3 shows the engine operation executed using multiple factors, where the software entitles in the control of the engine depending on the user requirements. Strategic maps provided within the software are used as an important tool for the initial commencement to start the engine. The injection pressure is controlled through the display where, after the engine crank it is increased eventually based on the test plan. Exhaust pressure is monitored using the EGR and VNT demands based on singe values, injection pressure values are generally set from 50 to 120 for the present thesis. The fuel introduced in the cylinders by the CRDI system is controlled by engine maps shown in the figure, and the engine control gives a provision to operate on multiple injections or a single injection which is also dependent on the user test plans.

## 3.2 Eddy current dynamometer

As mentioned previously, the engine is coupled with a dynamometer to control the engine speed and torque. The Frouda Engineering EC38TA – maximum torque 477 Nm, is an eddy current dynamometer used in the engine coupling and for maintaining engine speed. The dyno controller uses a load cell to control engine loads and equipped with a 60-toothed wheel coupled for the assessment of its rotational speed.

The EC38TA is coupled to the Ford Puma (Duratorq L316) which is in turn coupled to a power take-off (PTO) unit, clutch, and dual mass flywheel. Dyno control is done using a control box by Schneck 2000 D/W system, which is comprised of two modules: power supply and control unit. This control unit allows the user to set a specific value for engine speed and torque before the engine is started. In this case, the engine speed is set and fixed to 1800 rpm, whereas the engine torque is controlled through the engine control unit (ECU) by controlling the continuous running engine components. The dyno controls the engine speed and torque but restricts the user in starting the engine; hence, the test cell uses a battery and an OEM starter motor to crank the engine. Section 3.1.1 above explains the ECU system and the bridge between engine cranking and engine control together using the UI.

**Figure 3.4 - Dynamometer controller**

## 3.3 Real-time in-cylinder heat release rate and pressure

### 3.3.1 Kistler 6058A

In-cylinder pressure and heat release rate is measured using a Kistler 6058A non-cooled Peizostar pressure transducer (PT). The PT is equipped at the fourth cylinder of the engine with a 6544Q192 glow plug adapter, allowing the PT to be fitted into the combustion chamber. Previously, the transducer had been sent to Kistler for sensor calibration, where the sensitivity was determined as -17.68 pC/bar, and ≤ ±0.05% of linearity was seen as the full-scale output of the sensor. The calibrated values were introduced in the Kistler manufactured charge amplifier, which assisted the charge amplifier to present accurate and repeated in-cylinder pressure signals. The pressure signals were acquired through the charge amplifier coupled with a NI data acquisition card PCI-6251 connected to the LabVIEW UI, to present the real-time engine in-cylinder data like pressure, heat release rate, mass fraction burn and change in pressure. The data acquisition for in-cylinder pressure and heat release rate was done over 200 cycles. Table 3.2 below shows the data specifics of the pressure transducer.

**Table 3.2 - Pressure sensor specifications**

| Specifications | Value |
|---|---|
| Measuring range | 0 – 250 bar |
| Natural frequency | ≈ 160 kHz |
| Operating temperature range | -20 to 350 ºC |
| Sensitivity | ≈ -17.68 pC/bar |
| Sensitivity shift | ≤ ±0.5% |
| Overload | 300 bar |
| Linearity in all ranges | ≤ 0.3 % FSO |
| Thermal shock (Δp) | < ±0.5 bar |

## 3.4 Real-time pressure and temperature measurements

The pressure measurements were done using absolute pressure transducers. Calibration of these PTs was carried out online before using them during engine operations. It was done by estimating a co-relation between the voltage supply (0 to 5 Volts) and the corresponding pressure (absolute or gauge pressure in bar). These pressure measurements were displayed in real time using PICO data loggers and LabVIEW user interfaces.

For the measurement of temperature at various engine locations K-type thermocouples are used. The thermocouples used during the experimentation provided real-time thermal measurements displayed using a PICO data logger (TC-08) and NI USB-6218. The long exhaust pipe experiments used the TC-08 PICO data logger to measure the exhaust gas temperature for 180 seconds (3 min) simultaneously at 12 consecutively equidistant testing positions. The NI USB-6218 was used to measure on-engine temperatures such as the intake

air, fuel feed, fuel return, oil sump, EGR (before and after) and exhaust gas temperatures before and after VNT.

## 3.5 Particulate dynamics lab (PDL)

The experimentation in Chapter 5 addresses the investigation of particulate dynamics in a long exhaust pipe (3.5 m), under different engine operating conditions. The PDL experimental set-up is shown in Figure 3.5. The experimental approach is done to investigate PM dynamics, with the inclusion of gas phase emissions from a diesel exhaust showing particulate size, mass and concentration effects. Nucleation, condensation, deposition, and agglomeration are all studied.

**Figure 3.5 - Particulate dynamics lab**

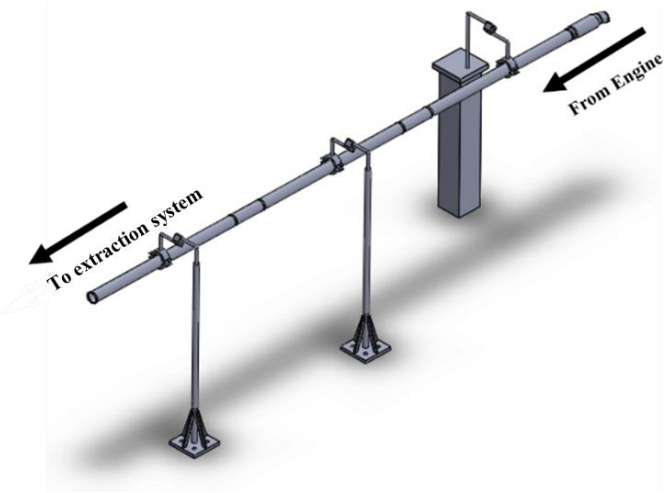


**Figure 3.6 - Design for particulate dynamics lab**

### 3.5.1 Exhaust tail pipe cooling

An exhaust tail pipe cooling set-up is provided to investigate the external cooling effects on particulate matter and particulate number using copper coil windings along the length. The engine equipped with a 3.5-metre exhaust pipe is subjected to an external cooling set-up using copper coil tubing (4 mm OD * 50 m) to wrap the exhaust pipe with a variable decreasing pitch of 5.0 to 0.1 cm along the length with a total of 130 revolutions around the exhaust tail pipe covering the 3.0 m length. Antifreeze and cold water were supplied through these copper coils to reduce the temperature gradient, and further investigate the particulate dynamics inside the tail pipe.

The schematic shown in Figure 3.8 explains the set-up used for the exhaust tail pipe cooling. The set-up is equipped with two 38-plate heat exchangers to reduce the outflow water and antifreeze temperatures, connected to a closed tank filled with the fluid. Heat exchangers use a counter-flow tubing set-up for a substantial reduction in the fluid temperature using high-pressure water-cooling, bypassed from the engine cooling set-up. The high-pressure pump

connected to the ice water + antifreeze mixture in the tank provides a consistent and controlled flow rate of 60 litres per hour inflow and a 9 litres per hour outflow over a length of 50 m of coil windings, aiding in subsequent cooling around the tail pipe.

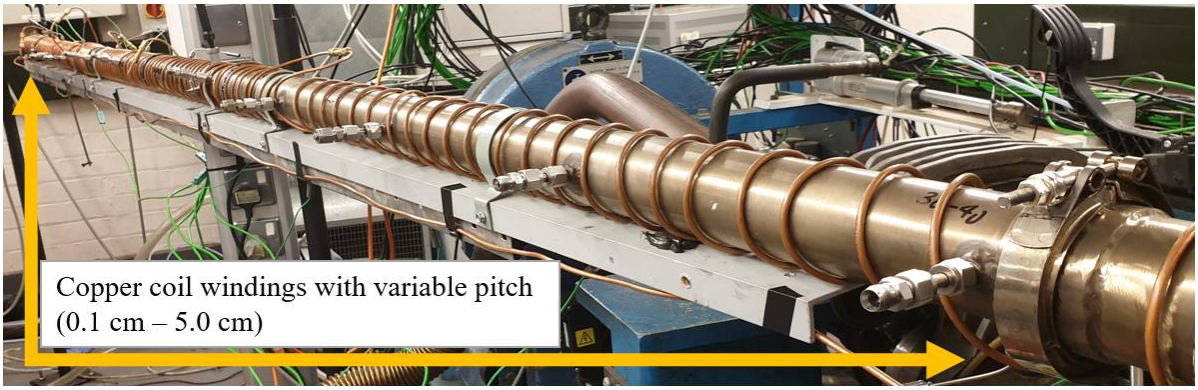


**Figure 3.7 - Copper coils wound around the exhaust tailpipe**

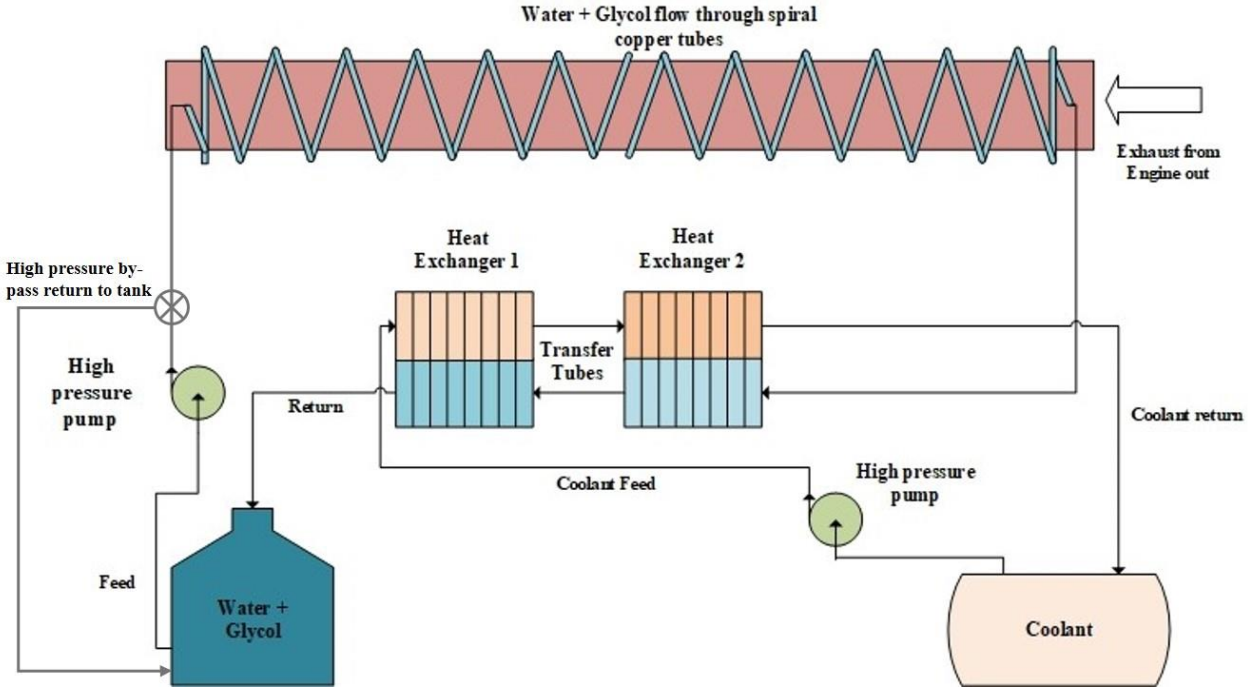


**Figure 3.8 - Exhaust cooling set-up**

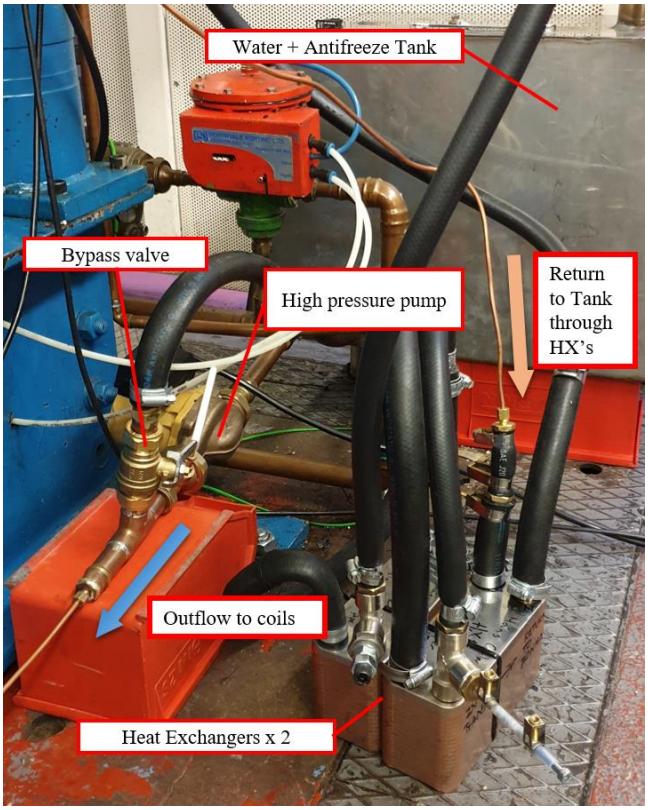


**Figure 3.9 - Inflow and outflow set-up for water and antifreeze mixture**

## 3.6 Diesel particulate filter (DPF)

Chapter 6 describes the investigative analysis of a nanofiber coated catalysed diesel particulate filter (C-DPF). A praseodymium nanofiber catalyst coated on a cordierite ($MgO_2$-$2Al_2O_3$-$5SiO_2$) diesel particulate filter is used in the laboratory and engine test bench experimentation to investigate the effects of catalysed and non-catalysed DPFs on gas and particulate matter emissions. The porous ceramic filter is a 22.86-cm (length) *13.58-cm (diameter) cylindrical filter with a channel density of 200 cpsi (cells per square inch). The channels are alternately batched as shown in Figure 3.10, allowing the exhaust flow through the channel walls and resisting large particle sizes from flowing through, incurring a soot cake

formation on the channel walls. The filter's channels are comprised of porous walls that are irregularly impregnated with holes throughout, and the porosity of the channels ranges between 20 and 30μm. Since the channels are plugged alternately, the DPF filters by 92-95% of fine, ultra-fine and nano-sized particulate matter, depending on the porosity of the filter during the engine operation.

The engine exhaust is comprised of gas and particulate emissions, which reside in or filtered out from the porous walls upstream of the DPF. Exhaust gas temperatures initiate the oxidation/reduction procedures inside the channels and PM and gases react with the oxygenated catalyst coated on the walls reducing particle emissions and toxic gases. The residence of the PM and increase in the soot cake layer reduces the flow of the exhaust emissions through the filter, increasing the pressure drop inside the DPF. With the increase in the pressure drop, engine performance is affected majorly by requesting higher fuel consumption. The wall flow monolith used in the experimentation of the catalysed and non-catalysed DPF is shown in Figure 3.11.

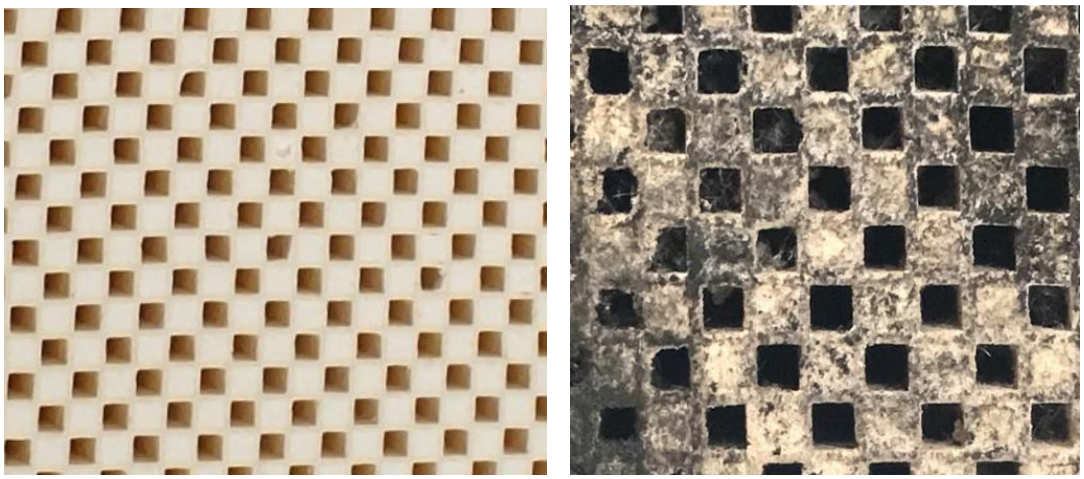

**Figure 3.10 - DPF channel structure and condition before experimentation (left) and after experimentation (right)**

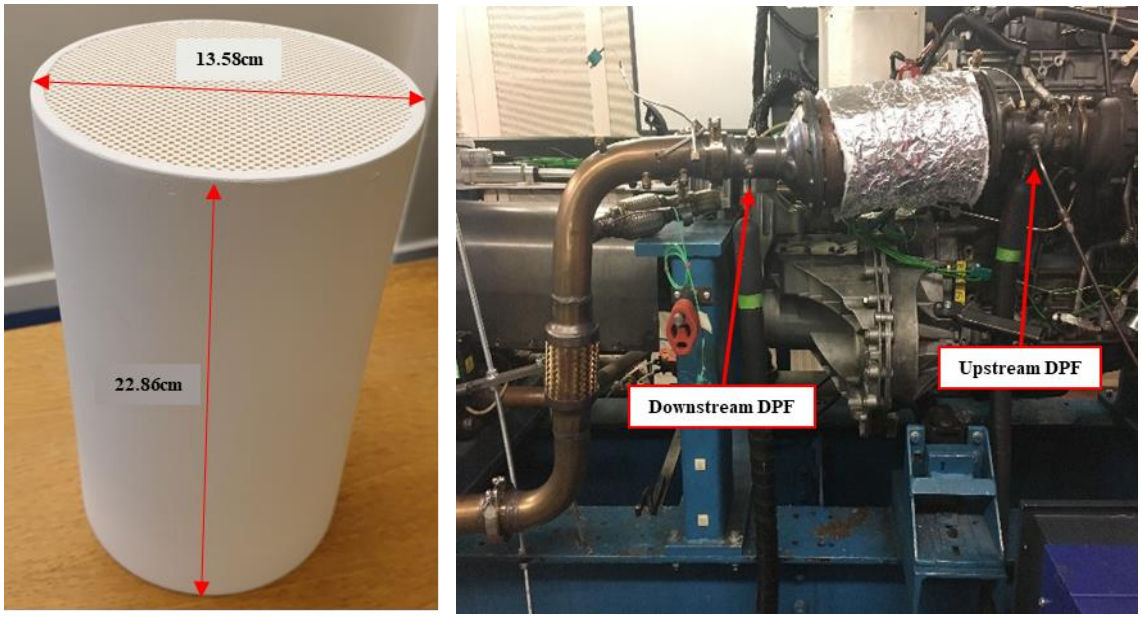


**Figure 3.11 - DPF monolith (left), DPF Canning (right)**

### 3.6.1 Thermogravimetric analysis

Thermal gravimetric analysis or TGA is used in the analysis of chemically and thermally reactive chemical compounds with an increase in temperature (0-1000 ºC). The mass change of the chemical is observed and analysed with respect to altering the temperature. Figure 3.12 shows a chemical compound undergoing TGA, where the mass changes take place with the increase in temperature.

Thermal gravimetric analysis (TGA) can also be analysed with time constraints for the x-axis, keeping the temperature consistent for longer periods and observing the mass change of compounds with increasing time. The technique is ordinarily used to analyse the carbonaceous content for sample (for example diesel exhaust or catalyst reactivity) and also

for composite materials. The mass of the sample is continuously measured with an increase in time or temperature constraints. In the present study the device and method is used for a raw diesel exhaust and metal catalyst characterisation, observing the oxidation of carbon and mass reduction in presence of praseodymium nanofibers and powder catalysts.

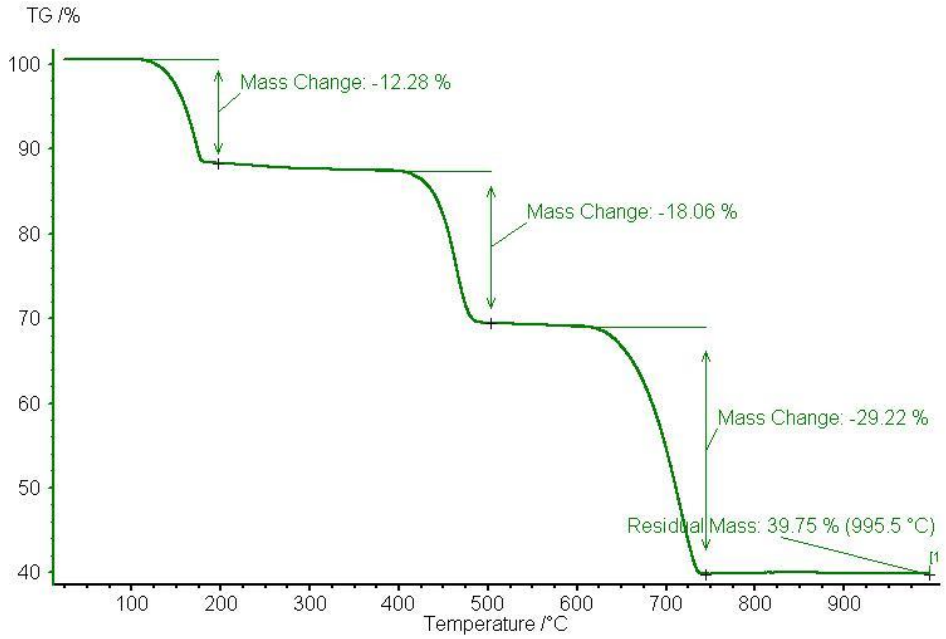


**Figure 3.12 - TGA technique - temperature vs wt. % [116]**

### 3.6.2 Catalyst development and coating

Although the temperature and resistivity of these filters is very high, it is critically important for DPFs to regenerate actively or passively over time. As mentioned in the review of DPF regeneration in Chapter 2, passive regeneration is established to be effective during a consistent engine run at variable conditions. The requirement for the active regeneration temperature of DPFs is very high, which also increases the additional fuel consumption during the engine run. Hence, to achieve low regeneration temperatures for the diesel particulate

filters, passive regeneration (continuous or non-continuous) methods are preferred. Fuel additives (injection system) or metal catalyst coating on the DPF (exhaust after-treatment) are the most commonly used methodologies for passive regeneration. Hence, a coating of a new metal oxide catalyst is introduced in these wall flow filters.

### 3.6.2.1 Catalyst synthesis

The $Pr_6O_{11}$ and $Pr_2O_3$ mixed fibres were synthesized by the co-precipitation/ripening method. [117] A solution of $Pr(NO_3)_3.6H_2O$ (Aldrich, 99%) of 0.1 molars each was prepared by dissolving it in distilled water; a 0.8-mole ratio of KOH/citric acid (Aldrich) solution was prepared in another beaker. Both solutions were mixed together in a separate beaker and then aged at 90 °C for 24 hours until the complete precipitates were obtained. Then, the formed precipitates were filtered and washed with distilled water, followed by drying and calcination at different temperatures, 100 °C and 550 °C for 2 hours in the air. Thus, the slurry prepared is ready for coating on the DPF channel walls.

### 3.6.2.2 Full-scale catalysed DPF prototype development

The $Pr_6O_{11}$ and $Pr_2O_3$ mixed fibres showing the most effective catalytic activity towards particulate combustion reaction were supported on a DPF. The cordierite wall-flow filter that was used for this purpose had the subsequent geometrical characteristics: 9.4 cm long, 5.4 cm in aspect (square section) 200cpsi. The deposition of $Pr_6O_{11}$ and $Pr_2O_3$ mixed fibres on the surface of the filter inner channels was performed through the following method: the $Pr_6O_{11}$ and $Pr_2O_3$ mixed fibres prepared by co-precipitation/ripening (KOH/citric acid molar quantitative relation equal to 0.8, calcination temperature of 100 $^oC$ for 2 hours in the air) were dispersed in a $2HNO_3$ solution, acting as a binder between the $Pr_6O_{11}$ and $Pr_2O_3$ mixed fibres

and the cordierite surface. This suspension solution was then ball-milled for 4 hours. Grinding was used to get sufficiently small particles to facilitate deposition on the support. The DPF was, in turn, inserted into the resulting suspension that adhered to the inner surface of the channels. The excess of suspension remaining within the channels was forced out by processing a controlled air flux through the filter. A final calcination step was performed at 550 $^{o}$C for 2 h in the air. A load of catalyst deposit was assessed by quantitative analysis. This procedure was continual until the amount of deposit of $Pr_6O_{11}$ and $Pr_2O_3$ mixed fibres' catalyst was 10-14 wt. %, referred to the blank filter weight.

## 3.7 Cambustion DMS500 MKII fast particulate analyser

This instrument is used for measurements in real time for particulate matter size, number and mass distributions, using spectrometry and a double dilution system. Particle measurements range from 4.87 nm to 1.0 µm in size and can be used to investigate the particle number (PN), size ($D_P$) and particle mass (PM) for before and after after-treatment systems like a DPF/GPF. Figure 3.13 shows the particle measurement procedure using dual dilution systems. The exhaust gas sampling is controlled at a maximum of 191 $^{o}$C and undergoes two-stage dilution through the high efficiency particulate air (HEPA) filter. During sampling, the exhaust emission is diluted with dry air, which goes through a local cyclone to allow the intake pressure to a limited pressure of 250 mbar and further proceeding to the HEPA filter.

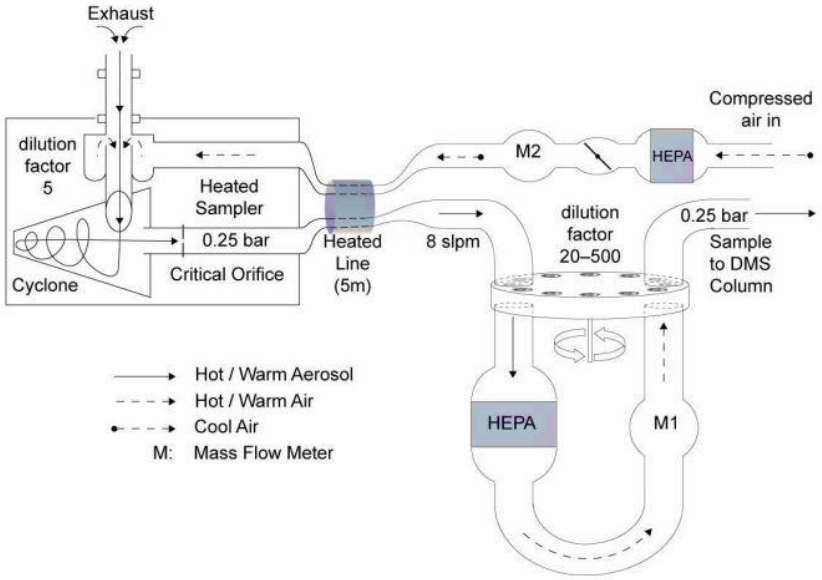


**Figure 3.13 - DMS500 MKII sampling schematic [118]**

The sample is then supplied to the DMS column, where it collides with a unipolar corona charger which produces many positive ions, and the particles are charged. The particle charge is roughly proportional to its surface area. These charged particles are transported to the classifier column that is surrounded by the sheath flow air filtered by HEPA. Positively charged particles are repelled by the column to flow towards the electrode and hence the particulate detection is carried out at different distances from the column based on the mobility of the electrons. Small and large particles have differential mobility. The particle size/number spectrum is determined according to the outputs from the 22 electrometers. [118]

Due to differences in particle size and number for diesel/gasoline, the DMS500 measures instances with a fixed first and differential second dilution ratios and projects particle modes in real time: Nucleation, accumulation and discrete spectrum mode particulate emissions; where the particle sizes from 4.87 to 50 nm in diameter are displayed as nucleation

mode and 50 to 1000 nm as accumulation mode. The user interface displays real-time particulate size distributions for the PM exhaust, which provides transient PM data while sampling. The user interface is shown in Figure 3.14 providing nucleation, accumulation and total spectrum mode.

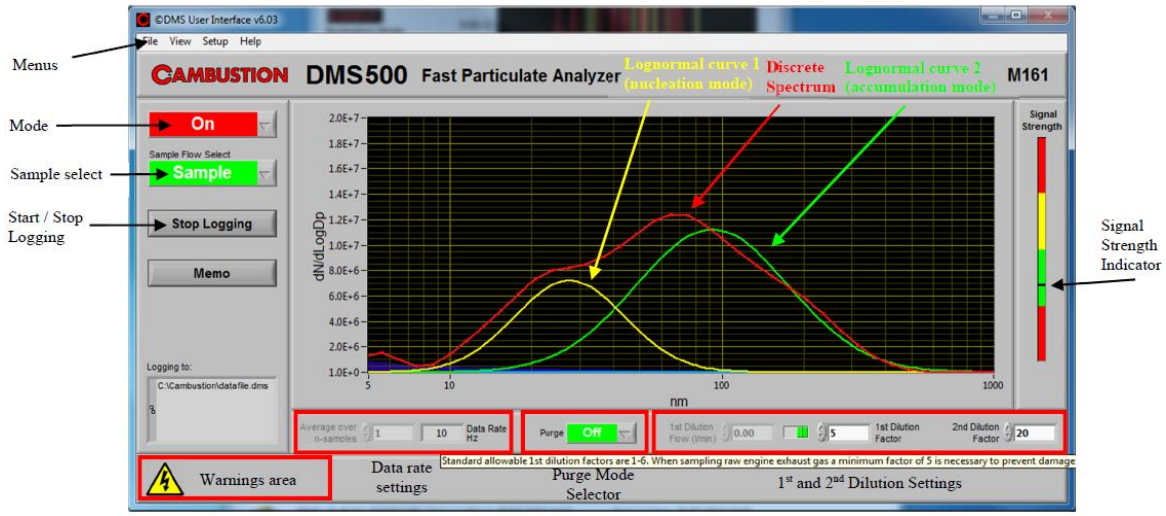


**Figure 3.14 - Cambustion DMS500 fast particulate analyser user interface [118]**

### 3.7.1 PM data analysis

The acquired data in real time from the DMS500 is transient and depends on each sampling time. The aerosol statistics displayed are calculated for total number (N/cc), geometric mean diameter (GMD), standard deviation for GMD and count median diameter (CMD), particle concentration and particle mass (PM: µg/cc), Particle number for different particle diameters. The particle diameter is discretized into 38 sections ranging from 4.87 nm to 1 µm and each section displays its individual particle number at each instance. The

measurement and data acquisition for each testing position in present work is done for 180 seconds.

The DMS500 is provided with a calibration file by the manufacturer that permits the user to set up the software for calculating the mass data for gasoline or diesel exhaust emissions depending on the engine test bench used. The mass calculation for a specific particle is done using:

$$Mass\ (\mu g) = D_p^{Power\ factor} \times Density\ Factor$$

## 3.8 Horiba MEXA-7100-DEGR gas analyser

The HORIBA MEXA-7100-DEGR is a gas analyser, which was used to provide exhaust gas concentrations of CO, $CO_2$, NO, $NO_X$, $O_2$, THC, Lambda (λ) and EGR percentage in real time during engine operation. The CO and $CO_2$ are calculated using a non-dispersive infrared (NDIR) methodology. It uses an optical chopper to determine the concentrations and displays in parts per million (ppm) and percentage (%). Chemi-luminescence detection (CLD) methodology is used to provide the gas concentration of NO and $NO_X$ during engine operation. Gas concentration between 10 to 10,000 ppm is calculated for the same. Using a $NO_X$ converter by chemical reaction, $NO_2$ is reacted with carbon to provide NO which further reacts with ozone gas ($O_3$).

The $O_2$ measurements were taken using the magneto-pneumatic detection (MPD) method with a single magnetic pole and differential condenser microphone. The $O_2$ was determined in percentage factor. Flame ionization detection (FID) was used to estimate total

hydrocarbons (THC) in exhaust gases by using a hydrogen flame to burn the HC and further using a high-voltage supply to detect the HC on a metallic detector. The process is slower (1-2 seconds) for detection. Lambda (λ) or air-fuel ratio is determined by calculating the intake and exhaust gas constituents in the sample extraction during engine operation. Each sample for gas emission analysis is taken for 180 seconds giving an averaged value over a time period. The EGR valve operating percentage is also determined during the process by investigating the $O_2$ % for intake and exhaust gas concentration. Although, the EGR% can be monitored by manual input variation of engine parameters, which is controlled through the open ECU control UI. The HORIBA system uses a two-way sampling line, having a manual switch over functionality, to assist in the investigation of gas emission conversion/variation rate for before and after exhaust after-treatment systems. Figure 3.15 shows the apparatus for gas concentration detection and analysis.

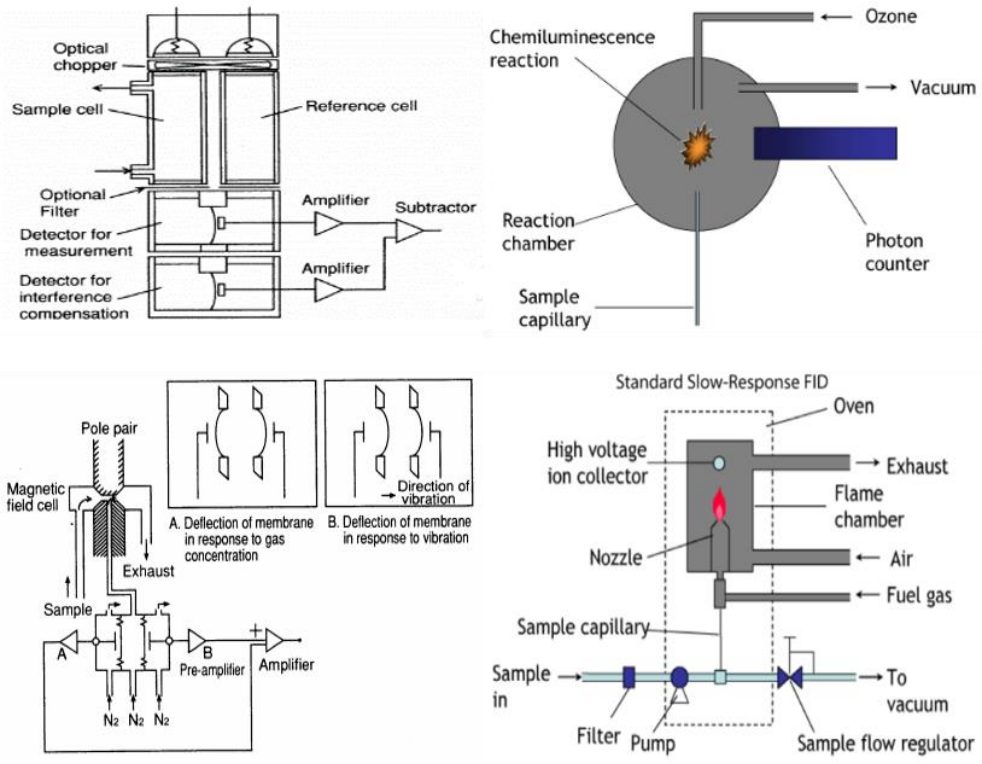


**Figure 3.15 - Horiba gas analysers' schematic**

## 3.9 Uncertainty and data analysis

The following section provides an insight into the uncertainty of the experimental data acquired from the empirical work done in the further chapters. The error information provided below includes the dynamometer, gaseous and particulate matter emissions' measuring devices and the data analysis done for all measured data.

The Schnek system was employed for the control of the EC38TA eddy current dynamometer. At zero speed, the engine torque should display a value of 0 ± 1 Nm. If there is an increased deviation for the given value, then using the key for calibration equipped on the system it can be eliminated to ±1% at full-scale range at zero speed.

The HORIBA MEXA 7100 DEGR was used for the gas emission measurements. The manufacturers' specifications were provided, all having a gas error deviation of ±1% full scale. After the initial warming up auto-calibration is carried out in the system to deduce all the gas supply errors at zero, span and measure controls. The particulate matter emissions were measured using the Cambustion DMS500 MKII, where the software allows the auto-calibration of the instrument after the device warm-up stage and before any measurement is logged in. An average set of high period, the sensitivity is raised and therefore a longer sample of offset data is obtained with a more precise zero. If the zero noise floor ends with errors, necessary measures to rectify the noise problems are initiated.

The temperature measurements are taken using a K-type thermocouple by thermal detection and accompanied with a logging system by PicoLog. The screening and calibration

values for the temperatures by thermocouples was within a deviation of ±1.5 ºC; whereas the data logger resolution was 20-bit or 1.993 x $10^{-4}$ ºC/sample step. The calibration of the pressure transducers equipped in the experimental set-up was done using a calibration table, with a linear and systematic co-relation between the voltage and the pressure range. The logger in the data acquisition used National Instruments USB-6218 with an ADC resolution of 16 bits.

The results acquired from the simulation and experimental work are analysed and plotted based on repetition for two or three sets of data. For each data acquisition done, the measurement is averaged based on the repetition and the averaged value is considered in the final process of analysis. To provide accuracy for similar recurring results, standard deviation for every set of raw data acquired is included in the process and plotted on the graph for investigating the high and low deviations. Figure 3.19 shows the process of raw data to final analysed data.

The raw data is acquired from the instrumentation equipped during the experimentation and post processed with the methods mentioned earlier. For temperature measurements, multiple thermocouples are used to investigate the changes along the length of pipe or at the aftertreatment systems used in the experimentation. Furthermore, the particulate matter analysis done using the DMS500 fast particulate analyser, provided with raw data of 180 seconds for each measurement logged and further the raw data is processed using an add-in provided by the manufacturer to assess each measurement characterised in nucleation, accumulation modes for their specific particle size, number concentrations, total concentrations and mass of particle. The averaged values are collated together based on its requirements and further conclusions are made to the results. The gas emission values are measured for 180 seconds at each testing position as shown in Figure 3.2. Gaseous emissions measured is a single

averaged value logged for the specific time period and provide the raw data to be post processed further.

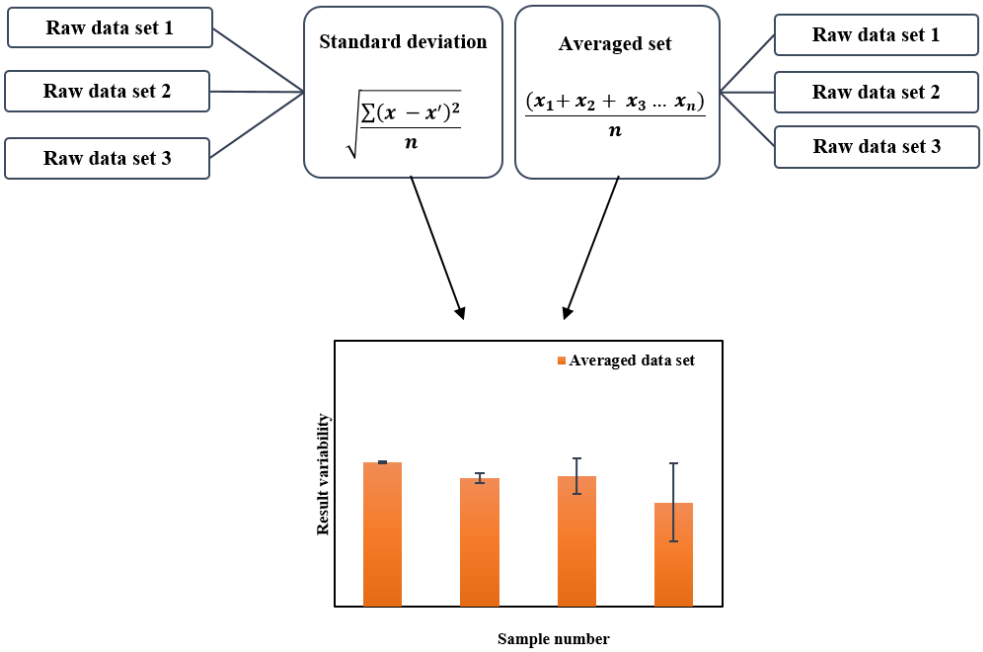


**Figure 3.16 - Data analysis and method**

## 3.10 Summary

This chapter summarises the engine test bench, modelling method, experimental set-up and instrumentation used in the further research work undertaken. The diesel engine test bench and chassis dynamometer used for the experimentation are thoroughly explained. In addition, the model used for particulate matter characterisation is represented in detail with numerical equations, and referenced extrapolation is given in the appendices of the thesis. The online instrumentation used during the experimentation is described in depth with its functional purpose and working procedure.

# CHAPTER 4

# SIMULATION OF PARTICLE INCEPTION AND GROWTH USING PARTICLE GROWTH MODEL

## 4.1 Introduction

This chapter establishes the developed numerical model for particulate matter (PM) growth inside an exhaust pipe of a diesel engine. The developed model is implemented for the predictive and investigative analysis of particulate matter dynamics inside the chamber, where gas and particulate matter emissions undergo physical processes involved in the inception and growth of a particle. The combusted fuel by-products undergo multiple physically and chemically driven reactions that incur into gas and particle phases. The pseudocritical temperatures of gas phase components differs from each other and thermally react in phase transitions (from solid, liquid or gas to other phases). The nucleation rate change is dependent on multiple factors like the binary nucleation of $H_2O$-$H_2SO_4$, PAHs that contribute chiefly in the particle inception at initial stages during phase transitions.

Soot modelling is depicted in many research areas, which includes particle inception and formation of nucleated particles, along with the inception of larger particle sizes due to surface growth and condensation of nucleates. The work in [100] provided the initial detailed model for soot particle nucleation and particle surface growth in premixed hydrocarbon laminar flames. It defined the post fuel pyrolysis particle inception, showing three stages as initial PAHs' formation due to chemical kinetics of pyrolysis and oxidation, surface growth, and condensation of PAHs giving rise to partly-spherical and larger particles. The model

anticipated the traditional structure of soot particles where density at the centre was lower than the shell and coagulated PAHs were irregularly placed. Authors in [106, 119] have closely investigated the PM formation and soot characteristics for pool combustion of diesel fuel on an open flame. The incomplete combustion flame was established to rise in large particle sizes (> 50 nm); whereas nucleation mode particles decreased radically. Experimentation with dual-flame types, open and closed flame, was carried out testing different fuels: $C_6 - C_{16}$ inclusive of diesel fuel with and without lubricant and PM characterisation was done with respect to soot emitting properties.

The detailed model development and study carried out for this thesis is reviewed in this chapter with an insight into the sub-models used in the investigation of particle growth inside the exhaust tailpipe. The collated model uses the sub-models to give an output of particle size, concentration and nucleation rates with overall particle size distributions along the length of the tailpipe. The particle growth model (PGM) is comprised of interlinked sub-models for nucleation [100]; condensation [120]; deposition [102, 107]; and coagulation [101, 121]. The subsequent models are parameterized, executed and combined the effects of physical and chemical parameters together, showing the linearity and non-linearity of particulate matter variations. The model is calibrated and optimised to provide a replication of near-realistic conditions observed in a vehicle accommodated with an exhaust tailpipe experiencing ambient condition varieties.

## 4.2 Research objectives

The objectives mentioned below will be used to investigate the robustness of the particle growth model (PGM) for primary and secondary particulate formation.

1. Numerical modelling and analysis of gas phase constituents' contribution ($H_2O$, $H_2SO_4$ and PAH) to the overall particulate matter (PM) mode concentrations inside the exhaust tailpipe, under the influence of exhaust temperatures and dilution factors.
2. Investigating the nucleation rates, particle size and number concentration from 0.0m to 3.5m at variating engine exhaust temperatures by achieving a global simulation output of the particle growth model (PGM).
3. Investigating the particle to particle interaction inside the spatial tube for characterising the concentration changes, residence of material on chamber walls and the coalescence of particles under variating exhaust flow velocities.

## 4.3 Baseline testing – initial boundary conditions

The baseline experimentation is done for a 2.2L diesel engine equipped with an exhaust tailpipe of 3.5 m. The engine is tested for an engine load varying at three levels from 1.4 bar to 6.0 bar BMEP. These tests are executed to acquire the initial particle size distributions at 0.0m length for each load test, with combustion by-product gases, temperature, and pressure. The data acquired from the instrumentation is used during the tests, where the predetermined dilution ratios are also acquired. The selection of these tests was done for increasing engine loads and a split-injection strategy at 20% pilot and 80% main fuel injection quantities, to generate nucleation and accumulation mode particles and measure them near the exhaust port.

The temperature gradient of the exhaust emission reduces with the increase in length; the acquired temperature reduction is shown in Figure 4.1 as an initial background. It can be observed below that for a certain engine condition, the temperature from the exhaust port decreases nonlinearly as the length increases. This is due to the heat dissipation or heat transfer to ambient conditions from the stainless steel exhaust pipe chamber. Gas and PM emissions can be significantly affected due to the thermic changes occurring inside and outside the exhaust pipe. A detailed comparative analysis of experimental and modelling results is given in the further sections, providing a detailed study and discussion of the formulation executed.

The instrumentation used in acquiring the initial boundary conditions for numerical simulation are: Cambustion DMS500 for online PM data analysis; HORIBA MEXA 7000 series for primary exhaust gas composition analysis; and NI LabVIEW, Pico data logger for online temperature and pressure measurements.

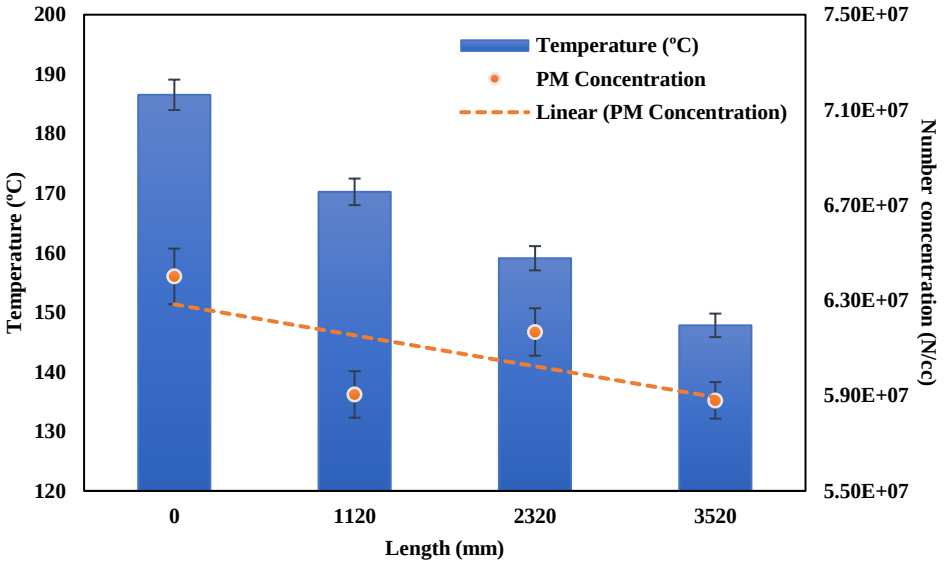


**Figure 4.1 - Temperature and PM concentration variations along the length of the exhaust tailpipe**

## 4.4 Simulation models for particulate matter inception and evolution

The model used in Chapter 4 deals with the primary process of particle inception and growth. The particle growth model (PGM) used, processes the initial boundary conditions and numerically estimates the variations in particulate matter occurring at consecutive instances of length given during initialisation. The changes are characterised into particle size, mass, and concentrations; which give a valued understanding of particulate matter (PM) behaviour.

The first stage of the model is initiated using the initial boundary conditions acquired from the experimental investigation (baseline testing) for different engine operating conditions. The primary boundary conditions to be used are the exhaust temperatures, regulated gas emissions and particulate matter characteristics such as the number, size, and concentration. The size concentration distribution is done for 38 particulate size partitions which are used in the model and its sub-models. The second stage of the model uses the model simulator for the parameter conversion, used in the first stage. The conversion of parameters is done for the calculation of $H_2SO_4$ (g), $H_2O$ (g) mass fraction, fuel sulphur content and its conversion percent, absolute humidity and diluted gas properties (a mixture of exhaust gas and PM with dilution air inclusive of pre-dilution ratios (PDR)).

### 4.4.1 Nucleation model

The nucleation model is based on the classic nucleation theory (CNT) formulation [99] to calculate the nucleation rate using:

$$R_n = \frac{(\rho_g \xi_i)^2}{\rho_i w_i} \sqrt{\frac{2\sigma_i}{\pi \omega_i}} \exp\left(-\frac{\Delta G^*}{k_B T}\right) \left(\frac{m_p^*}{w_i}\right)^{\frac{2}{3}} \qquad \text{(the nucleation rate)} \qquad (17)$$

$$\Delta G^{*} = \frac{4}{3}\pi r^{*2}\sigma \quad \text{(the nucleation barrier)} \tag{18}$$

$$r^{*} = \frac{2\sigma}{k_g T \ln S} \quad \text{(the radius of the critical nucleus)} \tag{19}$$

where 'i' represents the number of nucleating species; ξ represents the mass fraction of each gaseous species; $\rho_g$ is the density of the gas; $\rho_i$ is liquid density for 'i' species; $w_i$ is the molecular weight; σ is the surface tension coefficient; $k_B$ is the Boltzmann constant; T is the gas temperature; $m_p^*$ is the mass of the critical cluster; S is the vapor super saturation ratio (S = p/p*).

The third stage uses numerous sub-models to execute the nucleation process based on the initial PM data. Expressions 21 and 22 calculate the surface tension for the $H_2SO_4$ molar fraction ($J/m^2$) given by [103]. Furthermore, the sub-model divides to calculate the nucleation rates ($1/cm^3.s$) proposed by [109] given in expression 24.

$$\begin{aligned} Z^{*} = {} & 0.740977 - 2.66379 * 10^{-3} * T_{abs} + 5.0422 * 10^{-5} * T_{abs} * \ln(SA_{conc}) \\ & - 3.49998 * 10^{-3} * \ln(SA_{conc}) + 2.01048 * 10^{-3} * \ln\left(\frac{RH}{100}\right) \\ & - 1.83289 * 10^{-4} * T_{abs} * \ln\left(\frac{RH}{100}\right) + 1.57407 * 10^{-3} \\ & * \left[\ln\left(\frac{RH}{100}\right)\right]^2 - 1.79059 * 10^{-5} * T_{abs} * \left[\ln\left(\frac{RH}{100}\right)\right]^2 + 1.84403 \\ & * 10^{-4} * \left[\ln\left(\frac{RH}{100}\right)\right]^3 - 1.50345 * 10^{-6} * T_{abs} * \left[\ln\left(\frac{RH}{100}\right)\right]^3 \end{aligned} \tag{20}$$

Where, $Z^*$ represents the mole fraction of $H_2SO_4$ in the critical cluster; $SA_{conc}$ as the $H_2SO_4$ total gas phase concentration ($1/cm^3$); RH represents the relative humidity; and $T_{abs}$ as absolute temperature. Surface tension can be calculated by:

$$A(Z) = 0.2358 - 0.529 * Z^* + 4.073 * (Z^*)^2 - 12.6707 * (Z^*)^3 + 15.3552 * (Z^*)^4 - 6.3138 * (Z^*)^5 \quad (21)$$

$$B(Z) = -0.14738 + 0.6253 * Z^* - 5.4808 * (Z^*)^2 - 17.2366 * (Z^*)^3 - 21.0487 * (Z^*)^4 + 8.719 * (Z^*)^5 \quad (22)$$

$T_{pc}$ represents the pseudocritical temperature of the binary solution for liquefaction. The coefficients 647.15K and 900K represent the critical temperature of $H_2O$ and $H_2SO_4$, respectively.

$$T_{pc}(Z) = 647.15 * (1 - Z^*)^2 + 900 * (Z^*)^2 + 3156.186 * Z^* * (1 - Z^*) \quad (23)$$

The sub-model calculates the nucleation rates considering the polynomial of the third order of ln ($SA_{conc}$) and ln (RH/100), where "a (T, $Z^*$)" to "j (T, $Z^*$)" represent the function of temperature and mole fraction of critical cluster which is calculated earlier in expression 20.

$$J = \exp\left\{a\,(T, Z^*) + b(T, Z^*) * \ln\left(\frac{RH}{100}\right) + c(T, Z^*) * \left[\ln\left(\frac{RH}{100}\right)\right]^2 + d(T, Z^*) * \left[\log\left(\frac{RH}{100}\right)\right]^3 + e(T, Z^*) * \ln(SA_{conc}) + f(T, Z^*) * \ln\left(\frac{RH}{100}\right) * \ln(SA_{conc}) + g(T, Z^*) * \left[\ln\left(\frac{RH}{100}\right)\right]^2 * \ln(SA_{conc}) + h(T, Z^*) * [\ln(SA_{conc})]^2 + i(T, Z^*) * \ln\left(\frac{RH}{100}\right) * [\ln(SA_{conc})]^2 + j(T, Z^*) * [\ln(SA_{conc})]^3\right\} \quad (24)$$

The extrapolation of nucleation rates for each function from "a (T, $Z^*$) to j (T, $Z^*$)" represents the function of temperature and mole fraction of critical cluster given as, [103, 109]

$$a(T, Z^*) = 0.14309 + 2.21956 * T_{abs} - 0.0273911 * T_{abs}^2 + 7.22811 * 10^{-5} * T_{abs}^3 + \frac{5.91822}{Z^*} \quad (25)$$

$$b(T, Z^*) = 0.117489 + 0.462532 * T_{abs} - 1.18059 * 10^{-2} * (T_{abs})^2 + 4.04196 * 10^{-5} * (T_{abs})^3 + \frac{15.7963}{Z_*} \quad (26)$$

$$c\,(T, Z^*) = -0.215554 - 0.0810269 * T_{abs} + 1.43581 * 10^{-3} * T_{abs}^2 - 4.7758 * 10^{-6} * T_{abs}^3 - \frac{2.91297}{Z^*} \quad (27)$$

$$d(T, Z^*) = -3.58856 + 0.049508 * T_{abs} - 0.00021382 * T_{abs}^2 + 3.10801 * 10^{-7} * T_{abs}^3 - \frac{0.0293333}{Z^*} \quad (28)$$

$$e(T, Z^*) = 1.14598 - 0.600796 * T_{abs} + 8.64245 * 10^{-3} * T_{abs}^2 - 2.28947 * 10^{-5} * T_{abs}^3 - \frac{8.44985}{Z^*} \quad (29)$$

$$f(T,Z^*) = 2.15855 + 0.0808121 * T_{abs} - 4.07382 * 10^{-4} * T_{abs}^2 - 4.01957 * 10^{-7} * T_{abs}^3 + \frac{0.721326}{Z^*} \quad (30)$$

$$g(T,Z^*) = 1.6241 - 1.60106 * 10^{-2} * T_{abs} + 3.77124 * 10^{-5} * T_{abs}^2 + 3.21794 * 10^{-8} * T_{abs}^3 - \frac{1.13255 * 10^{-2}}{Z^*} \quad (31)$$

$$h(T,Z^*) = 9.71682 - 0.115048 * T_{abs} + 1.57098 * 10^{-4} * T_{abs}^2 + 4.00914 * 10^{-7} * T_{abs}^3 + \frac{0.71186}{Z^*} \quad (32)$$

$$i(T,Z^*) = -1.05611 + 9.03378 * 10^{-3} * T_{abs} - 1.98417 * 10^{-5} * T_{abs}^2 + 2.46048 * 10^{-8} * T_{abs}^3 - \frac{5.79087 * 10^{-2}}{Z^*} \quad (33)$$

$$j(T,Z^*) = -0.148712 + 2.83508 * 10^{-3} * T_{abs} - 9.24619 * 10^{-6} * T_{abs}^2 + 5.00427 * 10^{-9} * T_{abs}^3 - \frac{1.27081 * 10^{-2}}{Z^*} \quad (34)$$

The sub-model also allows the calculation of the total number of molecules in the critical cluster given in the expression below, where the coefficients are dependent on the mole fraction of the critical cluster and temperature as given in expression 35.

$$N_{total} = \exp\left\{a_2\,(T,Z^*) + b_2(T,Z^*) * \ln\left(\frac{RH}{100}\right) + c_2(T,Z^*) * \left[\ln\left(\frac{RH}{100}\right)\right]^2 + d_2(T,Z^*) * \left[\log\left(\frac{RH}{100}\right)\right]^3 + e_2(T,Z^*) * \ln(SA_{conc}) + f_2(T,Z^*) * \ln\left(\frac{RH}{100}\right) * \ln(SA_{conc}) + g_2(T,Z^*) * \left[\ln\left(\frac{RH}{100}\right)\right]^2 * \ln(SA_{conc}) + h_2(T,Z^*) * [\ln(SA_{conc})]^2 + i(T,Z^*) * \ln\left(\frac{RH}{100}\right) * [\ln(SA_{conc})]^2 + j_2(T,Z^*) * [\ln(SA_{conc})]^3\right\} \quad (35)$$

The extrapolation for each function from $a_2(T,Z^*)$ to $j_2(T,Z^*)$ is given as, [109]

$$a_2(T,Z^*) = -2.95413 * 10^{-3} - 9.76834 * 10^{-2} * T_{abs} + 1.02485 * 10^{-3} * T_{abs}^2 - 2.18646 * 10^{-6} * T_{abs}^3 - \frac{0.101717}{Z^*} \quad (36)$$

$$b_2(T,Z^*) = -2.05064 * 10^{-3} - 7.58504 * 10^{-3} * T_{abs} + 1.92654 * 10^{-4} * T_{abs}^2 - 6.7043 * 10^{-7} * T_{abs}^3 - \frac{0.255774}{Z^*} \quad (37)$$

$$c_2\,(T,Z^*) = 3.22308 * 10^{-3} + 8.52637 * 10^{-4} * T_{abs} - 1.54757 * 10^{-5} * T_{abs}^2 + 5.66661 * 10^{-8} * T_{abs}^3 + \frac{0.0338444}{Z^*} \quad (38)$$

$$d_2(T,Z^*) = 4.74323 * 10^{-2} - 6.25104 * 10^{-4} * T_{abs} + 2.65066 * 10^{-6} * T_{abs}^2 - 3.67471 * 10^{-9} * T_{abs}^3 - \frac{0.000267251}{Z^*} \quad (39)$$

$$e_2(T,Z^*) = -1.25211 * 10^{-2} + 5.80655 * 10^{-3} * T_{abs} - 1.01674 * 10^{-4} * T_{abs}^2 + 2.88195 * 10^{-7} * T_{abs}^3 + \frac{0.0942243}{Z^*} \quad (40)$$

$$f_2(T,Z^*) = -3.8546 * 10^{-2} - 6.72316 * 10^{-4} * T_{abs} + 2.60288 * 10^{-6} * T_{abs}^2 + 1.19416 * 10^{-8} * T_{abs}^3 - \frac{0.008.51515}{Z^*} \quad (41)$$

$$g_2(T,Z^*) = -1.83749 * 10^{-2} + 1.72072 * 10^{-4} * T_{abs} - 3.71766 * 10^{-7} * T_{abs}^2 - 5.14875 * 10^{-10} * T_{abs}^3 + \frac{2.6866 * 10^{-4}}{Z^*} \quad (42)$$

$$h_2(T,Z^*) = -0.0619974 + 9.06958 * 10^{-4} * T_{abs} - 9.11728 * 10^{-7} * T_{abs}^2 - 5.36796 * 10^{-9} * T_{abs}^3 - \frac{0.00774234}{Z^*} \quad (43)$$

$$i_2(T,Z^*) = 0.0121827 - 1.0665 * 10^{-4} * T_{abs} + 2.5346 * 10^{-7} * T_{abs}^2 - 3.63519 * 10^{-10} * T_{abs}^3 + \frac{0.000610065}{Z^*} \quad (44)$$

$$\mathrm{j_2(T,Z^*)} = 3.20184 * 10^{-4} - 1.74762 * 10^{-5} * \mathrm{T_{abs}} + 6.06504 * 10^{-8} * \mathrm{T_{abs}^2} - 1.142177 * 10^{-11} * \mathrm{T_l^3} + \frac{0.000135751}{\mathrm{Z^*}} \quad (45)$$

This extrapolation was used in the model for specifying each function of the mole fraction and the number of molecules in the critical cluster and simulate the nucleation model based on these sub-models.

Afterwards, the radius, diameter and equivalent density of the critical clusters are calculated and updated within the sub-model using expressions 26 and 27. [109]

$$\mathrm{r_{nucleation}} = \exp[-1.6524245 + 0.42316402 * \mathrm{Z^*} + 0.3346648 * \ln(\mathrm{N_{total}})] \quad (46)$$

$$\mathrm{d_{nucleation}} = 2 * \mathrm{r_{nucleation}} \quad (47)$$

### 4.4.2 Condensation model

The fourth stage combines the sub-models to calculate the condensation process of the $H_2O/H_2SO_4$ vapour, and the substitutes of the fuel combusted and released after-exhaust as high temperature exhaust gas molecules. The condensation process calculates the condensed vapour molecules that have exceeded the pseudocritical temperature, over the nucleation mode particles and updates the number concentration for nucleation mode particles. Hence, the rate of condensation of $H_2O/H_2SO_4$ vapour on the nucleation mode particles can be given by the (Fuchs–Sutugin expression)

$$R_{H_2O/H_2SO_4} = 2\pi\overline{D}_{pj}\beta_{M,ij}D_i\left[N_i - \Gamma_{ij}N_{ie}\exp\left(\frac{4\sigma_i\mu_i}{k_B T_{pj}\rho_j\overline{D}_{pj}}\right)\right]N_j \quad (48)$$

$$\beta_{M,ij} = \frac{0.75\left(1 + Kn_{ij}\right)}{Kn_{ij}^2 + Kn_{ij} + 0.283Kn_{ij} + 0.75} \quad (49)$$

where $N_{ie}$ is the equilibrium molecular concentration over a flat surface; $\beta_{M,ij}$ are the correction factors; $C_{diffusion}$ is the i-vapor diffusion coefficient; $\overline{D}_{pj}$ is the mean diameter of each particle zone; Γ is the activity coefficients; $Kn_{i,j}$ refers to the Knudsen number given for $H_2O$ and $H_2SO_4$ are given in equation 50 and 51:

$$Kn_{H_2O} = \frac{\lambda_{H2O}}{R} \quad \text{(Knudsen number of } H_2O \text{ vapour)} \quad (50)$$

$$Kn_{H_2SO_4} = \frac{\lambda_{H_2SO_4}}{R} \quad \text{(Knudsen number of } H_2SO_4 \text{ vapour)} \quad (51)$$

$$\lambda_{H2O} = 3 * \sqrt{\frac{\pi * H_2O_{mass}}{8 * k_{boltzmann} * T_{abs}}} * C_{diffusion} \quad (52)$$

$$\lambda_{H_2SO_4} = 3 * \sqrt{\frac{\pi * H_2SO_{4mass}}{8 * k_{boltzmann} * T_{abs}}} * C_{diffusion} \quad (53)$$

Where $\lambda_{H2O}$ and $\lambda_{H2SO4}$ are the mean free path for vapour molecules; $H_2O_{mass}$ and $H_2SO_{4mass}$ represent the condensing vapour molecular mass; $k_{boltzmann}$ is the Boltzmann coefficient; and $C_{diffusion}$ is the diffusion coefficient which can be approximated using an empirical formulation. Furthermore, the saturation vapour pressure of water is given in expression 54 for subsequent condensation of particles.

$$P_{water} = \exp\left[77.34491296 - \frac{7235.424651}{T_{abs}} - 8.2 * \ln(T_{abs}) + 5.7113 * 10^{-3} * T_{abs}\right] \quad (54)$$

To calculate the condensation rate of $H_2SO_4$, it is essential to formulate and estimate the vapour pressure of sulphuric acid given by [122] which was corrected for lower temperatures by [120, 123]. The vapour pressure of $H_2SO_4$ required for the condensation to nucleation mode particles is calculated in expression 55.

$$P_{SA} = 101325 * \exp\left\{-11.695 + 10156 * \left[\frac{1}{360.15} - \frac{1}{T_{abs}} + \frac{0.38}{545} * \left(1 + \ln\left(\frac{360.15}{T_{abs}}\right) - \frac{360.15}{T_{abs}}\right)\right]\right\} \quad (55)$$

The condensation model process also takes the substitutes of dodecane, butanol, and benzene (combusted HC vapour) into consideration if their calculating models are initiated, and calculates the condensation rates of hydrocarbon vapour on nucleation mode particles.

### 4.4.3 Loss of material on chamber walls

The effects of particulate losses on the chamber walls is also a critical consideration point as it aids in understanding the total number concentration from upstream to downstream of the exhaust pipe. To investigate the loss of material, it is important to detect the rate of deposition of particles by formulating the particle velocities. The model is adapted from [124] as the particle velocity deposition.

$$k = 0.042 * Re * \sqrt[2]{\left(\frac{0.0791}{Re^{1/4}}\right)} * \sqrt[3]{Sc} * \left(\frac{D}{d}\right) \quad (56)$$

$$Re = \rho_{ex} * U_{ex} * \mu_{ex} \quad \text{(Reynolds Number)} \quad (57)$$

$$Sc = \frac{\mu_{ex}}{\rho_{ex} * D_{ex}} \quad \text{(Schmidt Number)} \quad (58)$$

$$Sh = 2 + 0.552 * Re^{0.5} * Sc^{0.33333} \quad \text{(Sherwood Number)} \quad (59)$$

The loss of material on the chamber walls is calculated for $H_2O$ and $H_2SO_4$ and takes updated number concentrations of $H_2O$ and $H_2SO_4$, flow velocity, chamber diameter, and particle diameter into account to estimate the deposition rate. Hence, the loss of material on the chamber walls can be defined by the formulation given by:

$$R_{loss_{H_2O}} = 4 * d_{H_2O} * \left(N_{H_2O} * 10^{-15}\right) * \frac{Sh}{D^2_{chamber}} \quad (60)$$

$$R_{loss_{H_2SO_4}} = 4 * d_{H_2SO_4} * \left(N_{H_2SO_4} * 10^{-9}\right) * \frac{Sh}{D^2_{chamber}} \quad (61)$$

Where **Re** is the Reynolds number for the conditions in the exhaust pipe; **Sc** is the Schmidt number; D is the chamber diameter and 'd' is the mean droplet diameter.

### 4.4.4 Coagulation model

The assumption for the particles is that they are orbicular in shape and in a free system. Hence, the coagulation between two particles is represented as Fuchs interpolation formulation, [121]. The change in the rate of particle concentration is defined by the expression:

$$\frac{dN}{dt} = -\frac{1}{2}\beta(v_1, v_2)N^2 \quad (62)$$

where β is the collision frequency by Fuchs interpolation formula given by:

$$\beta = \frac{2\pi\left(d_{p_i} + d_{p_j}\right)\left(D_i + D_j\right)}{\left[\frac{d_{p_i} + d_{p_j}}{d_{p_i} + d_{p_j} + 2g_{ij}} + \frac{8\left(D_i + D_j\right)}{c_{ij}\left(d_{p_i} + d_{p_j}\right)}\right]} \quad (63)$$

$$c_{ij} = \sqrt{\bar{c}_i^2 + \bar{c}_j^2} \quad (64)$$

$$g_{ij} = \sqrt{g_i^2 + g_j^2} \quad (65)$$

$$g_i = \frac{1}{3d_{p_i}\lambda_{p_i}}\left[\left(d_{p_i} + \lambda_{p_i}\right)^3 - \left(d_{p_i}^2 + \lambda_{p_i}^2\right)^{3/2}\right] - d_{p_i} \quad (66)$$

Where, the particle velocity, particle mean free path and its diffusivity is given by the expressions given below

$$\text{Particle velocity: } \bar{c}_i = \sqrt{\frac{8k_B T}{\pi m_i}} \tag{67}$$

$$\text{Particle mean free path: } \lambda_{p_i} = \frac{8D_i}{\pi \bar{c}_i} \tag{68}$$

$$\text{Particle diffusivity: } P_d = \frac{k_B T}{3\pi\mu d_{p_i}} C_{ci} = \frac{k_B T}{3\pi\mu d_{p_i}} \left[1 + \frac{2\lambda_{p_i}}{d_{p_i}} \left(A_1 + A_2 \exp\left(-\frac{A_3 d_{p_i}}{\lambda_{p_i}}\right)\right)\right] \tag{69}$$

The PGM simulates all the models mentioned above simultaneously depending on the input of the boundary conditions and presents the results for different particulate matter characteristics, as shown in Figures 4.2 and 4.3.

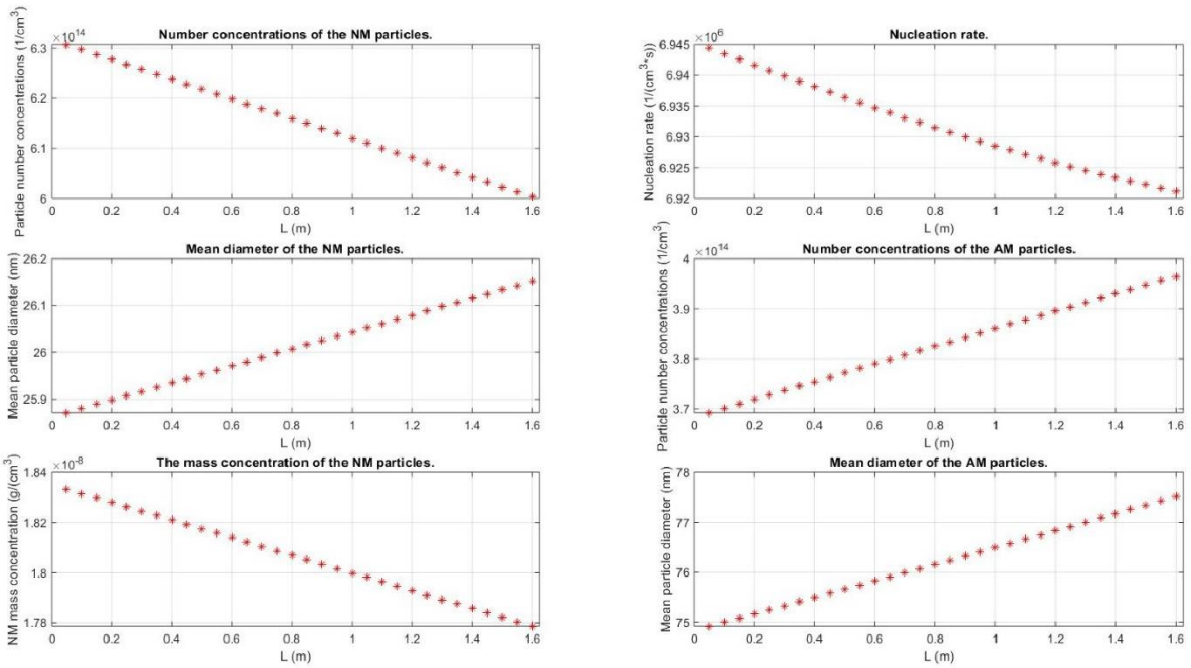


**Figure 4.2 - Particulate characteristics based on PGM**

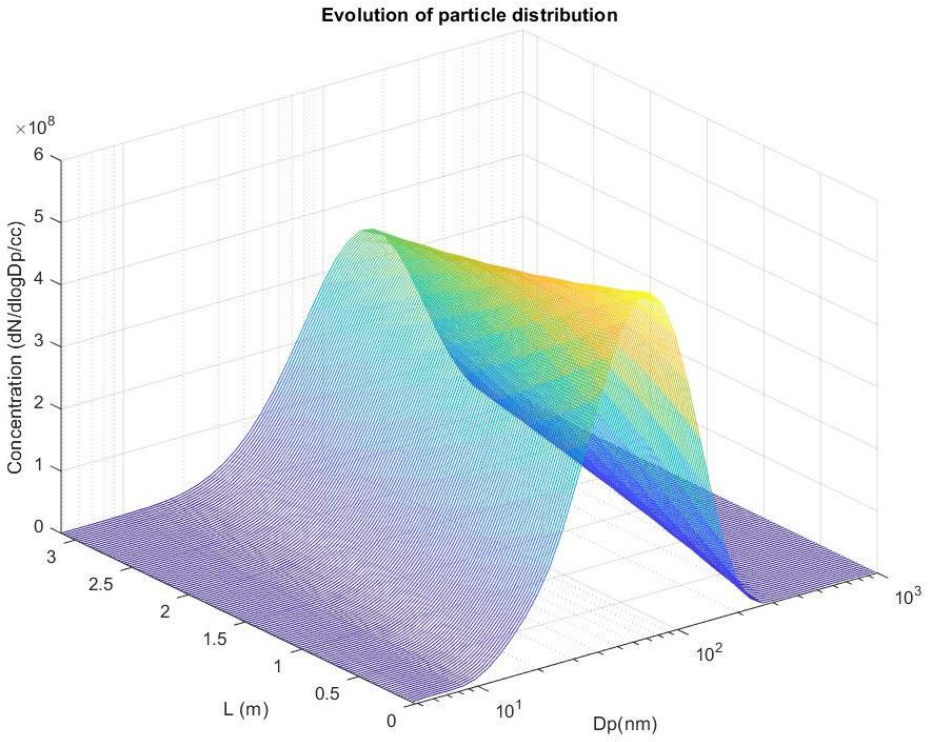


**Figure 4.3 - Particle evolution based on PGM**

## 4.5 Simulation procedure

The complexity of the PGM is dependent on the number of variables and parameters it considers during the simulation of the developed codes. With a higher number of variables and parameters the complexity of the model increases, and also increments the probability of achieving an appropriate solution. Thus, the simulated model is parameterised and characterised to consider multiple inputs that provide with a solution, which can be validated with a comparative analysis of the experimental and modelling approach.

The model's initiation is carried out using the initial boundary conditions', where the physical and chemical parameters involved in the model implementation are installed; and then further, these parameters are used to calculate the demand outputs. The initial boundary conditions are acquired from test bench experimentation and instrumentation as mentioned

earlier, that involve physical factors like dimensions of the exhaust pipe, exhaust gas temperature and pressure, predetermined dilution ratios (PDR) and lambda (actual/stoichiometric). Whereas, the chemical-based boundary conditions are those such as fuel sulphur content (provided by company supplier), fuel sulphur conversion ratio, and exhaust gas composition fractions (THC, CO, and $NO_X$). The discretisation of the particle size distribution (PSD) is carried out initially from 4.87 nm to 1000 nm, with 38 partitions of each particulate size concentration monitored. The initial PSD is measured from the particulate measurement system taken from the closest testing position after the exhaust port.

The model's execution is carried out with a continuous and simultaneous run of the sub-models for nucleation of gas vapours; vapour condensate formation; condensates residing or adjoining nucleates or gas vapours forming large particles; and finally achieving a local solution based on the length demanded from the particle modes. The results from the model's execution provide information on the PSD at each given time step and nucleation rate, size, concentration and accumulation size and concentration along the length of the pipe. Figure 4.2 shows the schematic table of the model's execution. The model simulated for the three baseline engine test bench conditions is provided in Table 4.1. Calibration of the model is proceeded using a condensation factor that ranges from 0.95 to 1.25. The factor is used as one of the fundamental parameter that connects and cascades the rate change of nucleation and coagulation of ultra-fine and fine particulates.

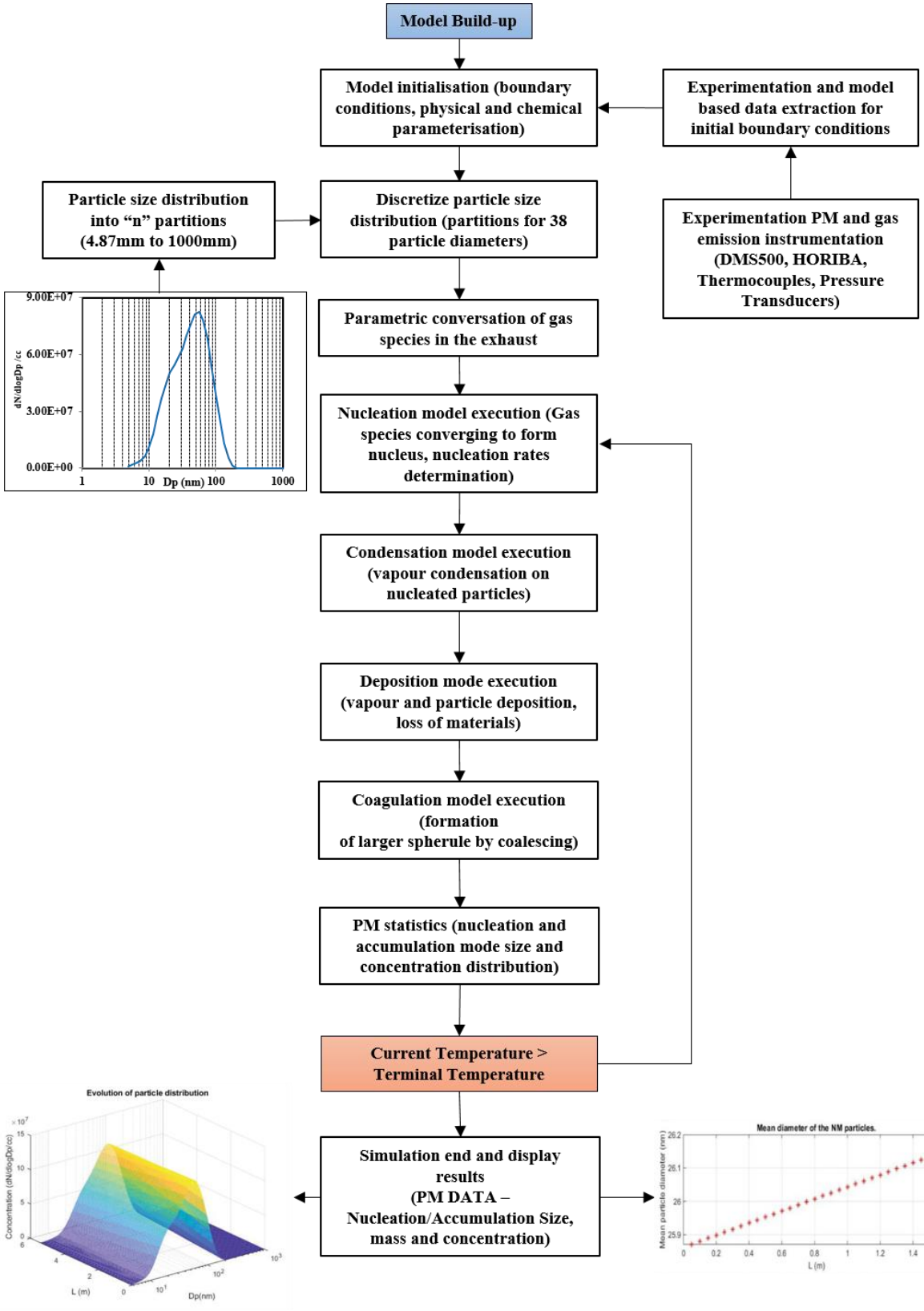


**Figure 4.4 - Model process for particle growth estimation**

**Table 4.1 – Experimentally acquired boundary conditions for PGM simulations**

| **Parameters** | **1.4 bar BMEP** | **3.0 bar BMEP** | **6.0 bar BMEP** |
|---|---|---|---|
| Length of the exhaust pipe | 3.5 metres | 3.5 metres | 3.5 metres |
| Diameter of exhaust pipe | 0.065 m | 0.065 m | 0.065 m |
| Pressure in chamber | 1.01e5 Pa | 1.01e5 Pa | 1.01e5 Pa |
| Exhaust gas temperature | 187 ºC(upstream) | 250 ºC(upstream) | 377 ºC(upstream) |
| Particle size range | 4.87 to 1000 nm | 4.87 to 1000 nm | 4.87 to 1000 nm |
| Number of partitions of PM | 38 | 38 | 38 |
| Minimum partition size of PM | 0.688 | 0.688 | 0.688 |
| Maximum partition size of PM | 3.0 | 3.0 | 3.0 |
| PM Coagulation coefficient (correction factor) | 1.01 | 1.01 | 1.01 |
| Dilution ratio | 9 | 9 | 12 |

## 4.6 Comparison of experimental and simulation results

The results presented in the following section are a combination of a series of optimised simulations done for the exhaust out from the engine at different engine load operations from 1.4 bar to 6.0 bar BMEP. The simulation results are compared to the results acquired from the test bench experimentation. Particulate data analysed from the model's results are provided in terms of the particle size of each mode (nucleation and accumulation mode), number concentration and size spectral density.

Results of the test bench experimentation on the 3.5-m exhaust tailpipe for increasing engine load conditions are shown in Table 4.2 and Figure 4.3 and 4.4. The results shown are discretised in specific outputs for nucleation and accumulation modes' number concentrations.

**Table 4.2 - Mode concentrations at 1.4 bar, 3.0 bar and 6.0 bar BMEP**

| Length (mm) | NMC* 1.4 bar BMEP | AMC* 1.4 bar BMEP | NMC* 3.0 bar BMEP | AMC* 3.0 bar BMEP | NMC* 6.0 bar BMEP | AMC* 6.0 bar BMEP |
|---|---|---|---|---|---|---|
| 0 | 3.22E+07 | 2.34E+07 | 4.48E+07 | 4.04E+07 | 2.41E+07 | 2.35E+07 |
| 1120 | 3.25E+07 | 2.13E+07 | 4.49E+07 | 3.76E+07 | 2.24E+07 | 2.22E+07 |
| 2320 | 3.14E+07 | 2.44E+07 | 4.40E+07 | 3.73E+07 | 2.31E+07 | 2.14E+07 |
| 3520 | 2.70E+07 | 2.46E+07 | 4.11E+07 | 3.77E+07 | 2.07E+07 | 2.02E+07 |

*NMC – Nucleation mode concentration (N/cc), *AMC – Accumulation mode concentration (N/cc)

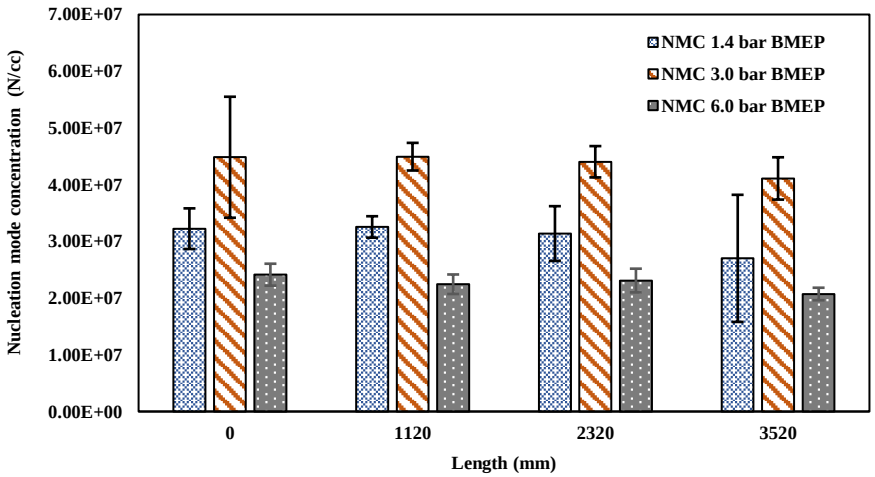


**Figure 4.5 - Experimental nucleation mode concentration for 1.4 bar, 3.0 bar and 6.0 bar BMEP**

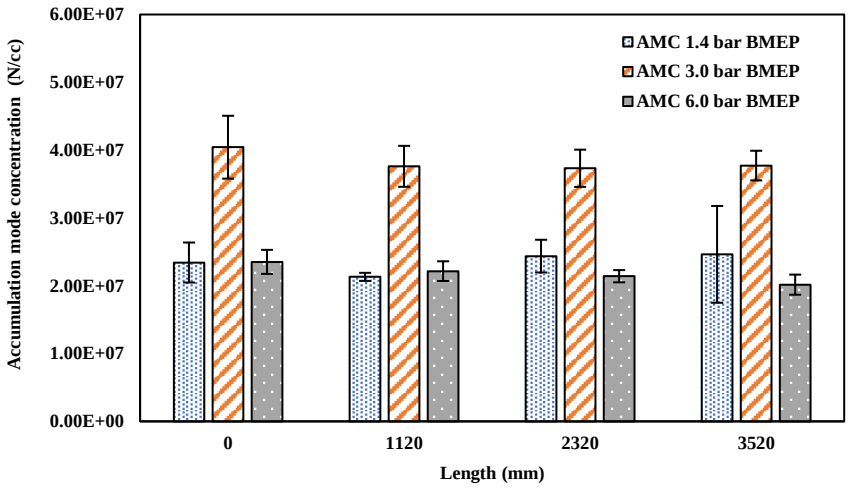


**Figure 4.6 - Experimental accumulation mode concentration for 1.4 bar, 3.0 bar and 6.0 bar BMEP**

### 4.6.1 Nucleation rates at 1.4 bar, 3.0 bar, and 6.0 bar BMEP

The nucleation rates are dependent on the relative humidity, sulphuric acid concentrations (fuel sulphur conversions), and mole fractions in the critical cluster with temperature functions. The calculation coefficients are mentioned the equations mentioned from [109] and their extrapolations are also mentioned in the earlier part of the chapter.

Figure 4.5 shows the nucleation rate changes along the length from 0.0m to 3.5m, for the simulation conditions mentioned from 1.4 bar to 6.0 bar BMEP. A linear non-substantial decrease is observed in all simulation cases for the nucleation rates, with a visible trend of a decreasing nucleation rate with the increasing engine load conditions. The relativity of the decreasing trend is the inclusion of parameters such as the pre-determined dilution ratio and temperature and the calculated exhaust gas properties included at the initial stages before model execution. The changes in the exhaust gas and particle compositions substantially affect the

formation of clusters and nuclei. At high exhaust temperatures nuclei formation is assumed to be lower than at low exhaust temperatures, as the vapour phase condensation of gas components do not achieve pseudocritical temperatures for condensation and forming nuclei outside the exhaust port.

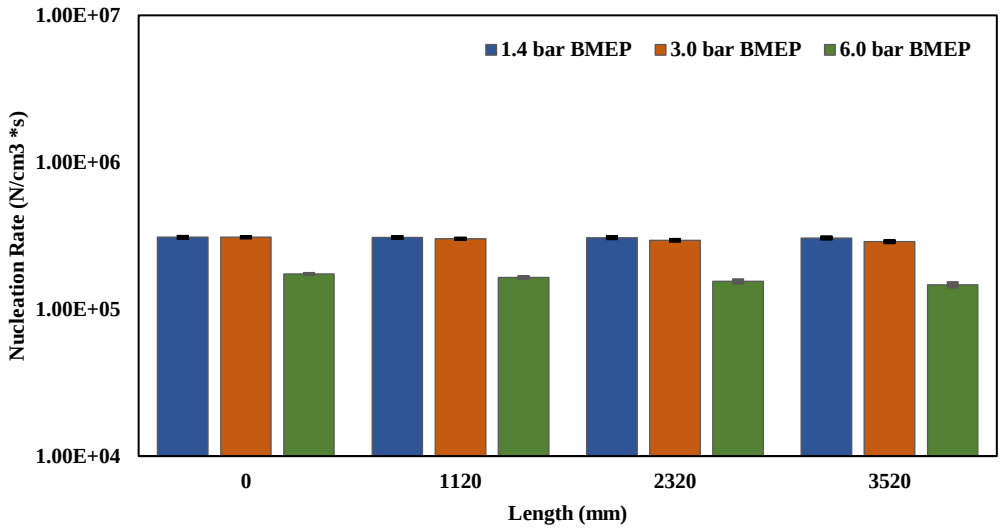


**Figure 4.7 - Nucleation rates from numerical modelling for increasing engine load conditions**

### 4.6.2 Comparative analysis of numerical simulations and test bench experimentation at 1.4 bar BMEP

Results of experimentation conducted at 1.4 bar BMEP, are given in Figure 4.8 to 4.11 compared with the model results acquired from optimised simulations with similar initial boundary conditions. The temperature profile shown in Figure 4.8 depicts the continuous decrease of temperature due to heat transfer in ambient conditions. From the figure, the conditions used for numerical simulation at low engine load show a significant and comparable change along the length of the exhaust tailpipe for test bench and simulations.

A linear decrease in the temperature gradient along the exhaust pipe is observed in Figure 4.8 and 4.9. The temperature difference between the initial and final points is approximately 40 ºC with a consistent pressure of 1.05 bar along the pipe, showing an average 10 ºC drop between every consecutive sampling position. Temperature and pressure are important parameters that affect the soot formation inside the chamber. For both cases, the NM size shows a significant increase in the particle diameter along the length lying in the range of 20 to 30 nm, which satisfies the conclusive statement for primary particle formation given by [22, 30]. The experimental NM particle diameter increased by 3.5%; whereas the NM particle diameter from the simulations shows an increase of 2.6% from the initial test position to the final position. The AM particle diameter for the numerical simulation increased by 7.6% along the length; whereas a 3.0% non-significant decrease was observed during the experimental analysis. The computational method gives a precisely calculated output, ignoring the human error percentage and considering a perfected experimentation approach. Hence, the difference of 8.1% between experimentation and modelling results is observed during comparative analysis. A maximum deviated variability observed in particle size was 2.1 nm and 11.2 nm for nucleation and accumulation modes respectively.

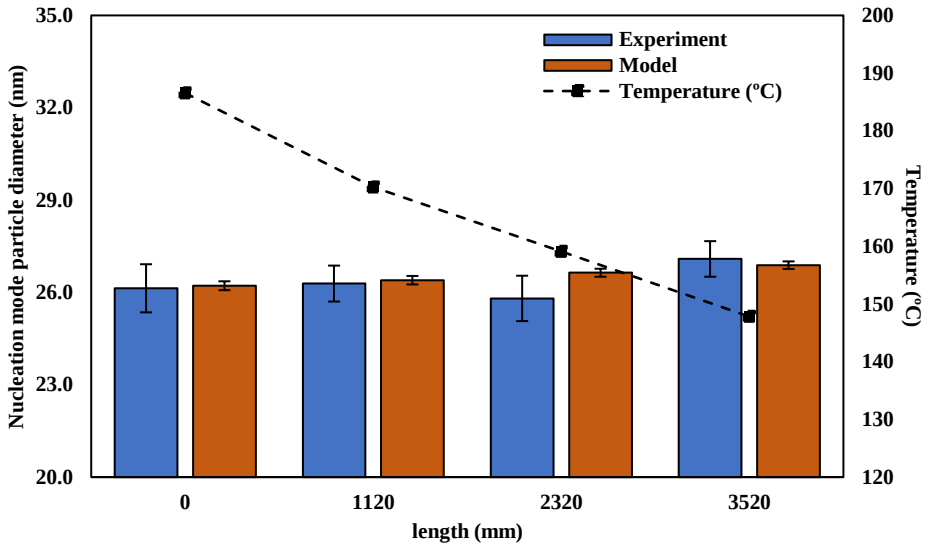


**Figure 4.8 - Nucleation mode particle diameter at 1.4 bar BMEP**

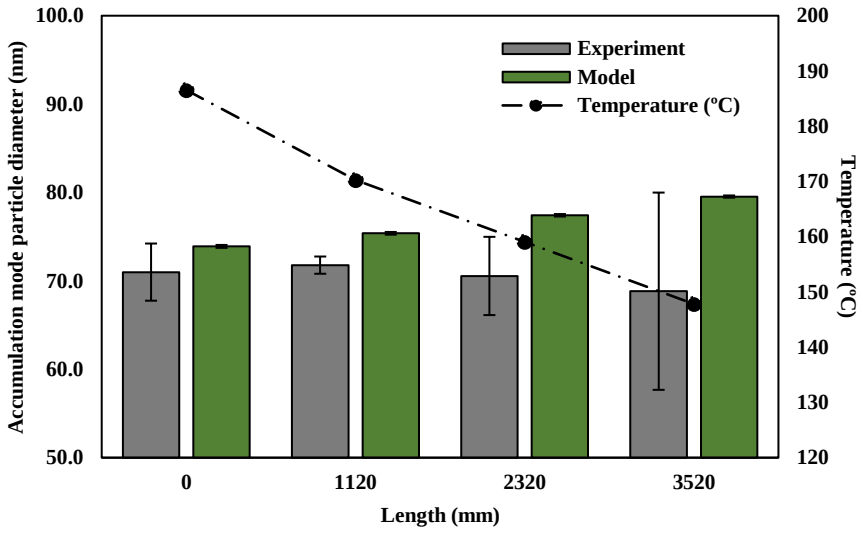


**Figure 4.9 - Accumulation mode particle diameter at 1.4 bar BMEP**

Figures 4.10 and 4.11 depict the variations in number concentrations in NM and AM. Numerical analysis of NM concentration shows a significant drop along the length of the pipe, with an overall decrease of 11.5% and 16.2% from the experimentation. The reduction in NM concentration is due to the compounding of nucleated particles together or adsorption and deposition of NM particles on other particulates, forming heavier spherules and overall

reducing its concentration at advancing lengths. Particle losses due to residence on chamber walls is also a strong hypothesis that can be proven through the decreasing NM particle concentration. On the contrary, the AM concentration with increasing length increases in number as well. A substantial increase of 13.6% and 5.1% is observed in numerical and experimental particulate analysis, respectively. A complete conversion of nucleation to accumulation mode particles is uncertain, as it is critical to consider the particle losses on the chamber walls. Hence, the significant difference between the simulation and experimentation results is observed.

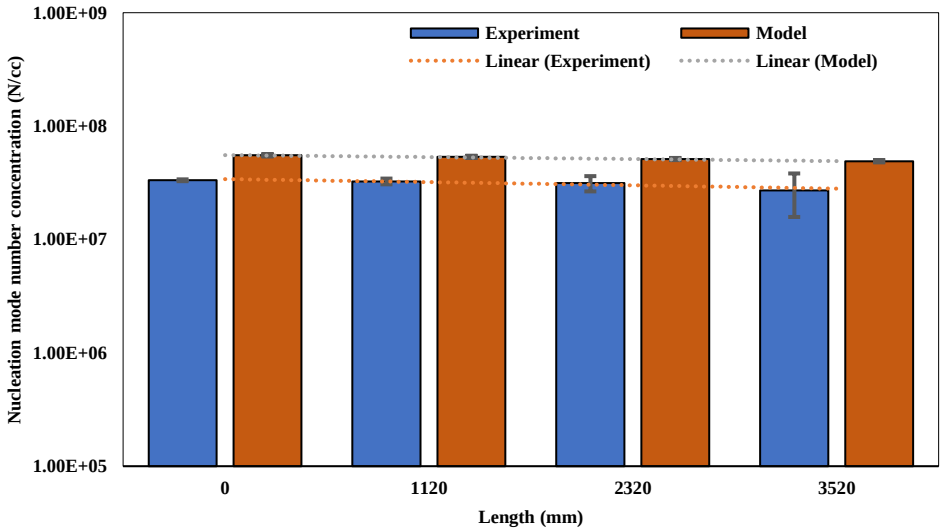


**Figure 4.10 - Nucleation mode number concentration at 1.4 bar BMEP**

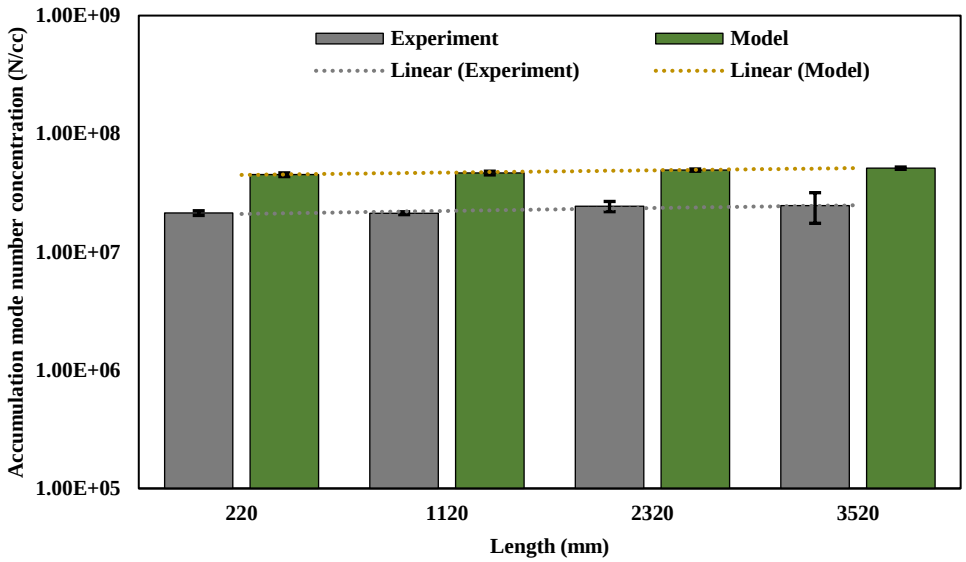


**Figure 4.11 – Accumulation mode number concentration at 1.4 bar BMEP**

The particle size distribution for the experimental and simulation results are shown in Figures 4.12 and 4.13. Results acquired from test bench experimentation show a higher variability in the PSD along the length of the exhaust tailpipe; whereas, for the simulation results, there is higher stability and a higher approximation in determining the size distributions at each time step. The high particulate concentration is observed mainly between 27.4 nm and 70 nm particle sizes. The phase transitions from the nucleation to the accumulation modes can be observed more significantly in the PSD for the simulation results.

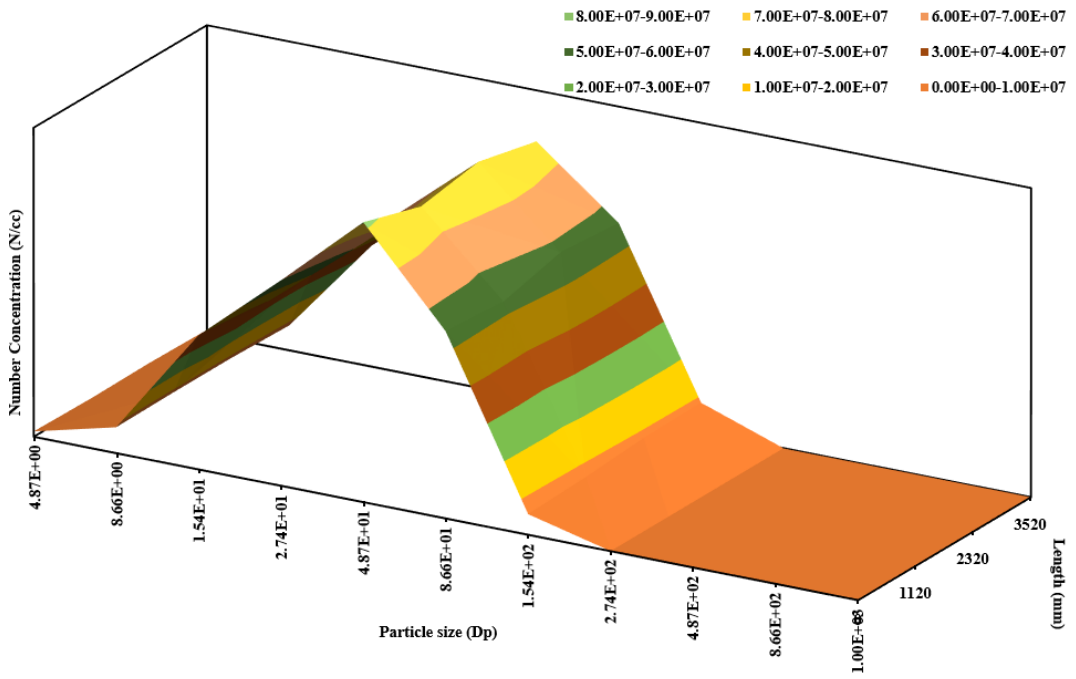


**Figure 4.12 - Experimental analysis of particle size distribution along the length at 1.4bar BMEP**

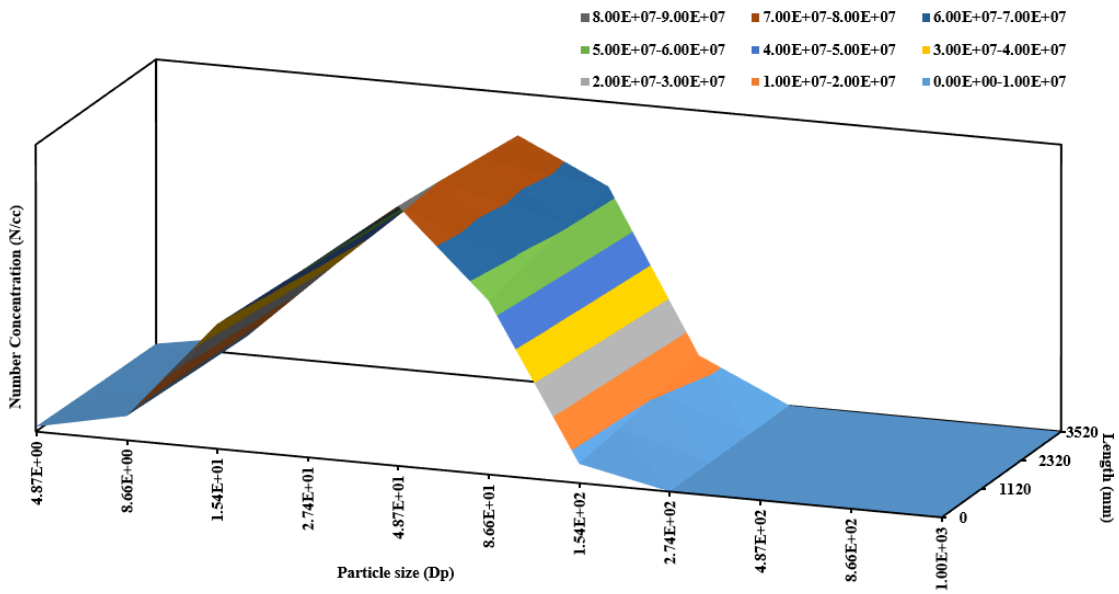


**Figure 4.13 - Model based particle size distribution along the length at 1.4bar BMEP**

### 4.6.3 Comparative analysis of numerical simulations and test bench experimentation at 3.0 bar BMEP

With the increase in exhaust temperatures, at 3.0 bar BMEP the variations in the particulate size and number concentrations have a substantial increase compared to 1.4 bar BMEP. Due to higher exhaust temperatures, the nuclei formation rate from vapour condensation is assumed to decrease by a certain degree, nevertheless, they undergo particle growth along the length of the exhaust tailpipe. The temperature along the exhaust tailpipe significantly dropped by 69 ºC.

The particle diameter along the length of the exhaust tailpipe is observed to increase linearly from the numerical simulations; whereas with experimental investigation the particle diameter shows an insignificant increase of 0.1 nm, but has variations along the length. The NM particle diameter shows an increase of 3.3% overall, from multiple numerical simulation assessments. The AM particles show a consistent increase of overall 4.3% (3.1 nm) and 11.9% (14.46 nm) for experimental and simulation analysis, respectively.

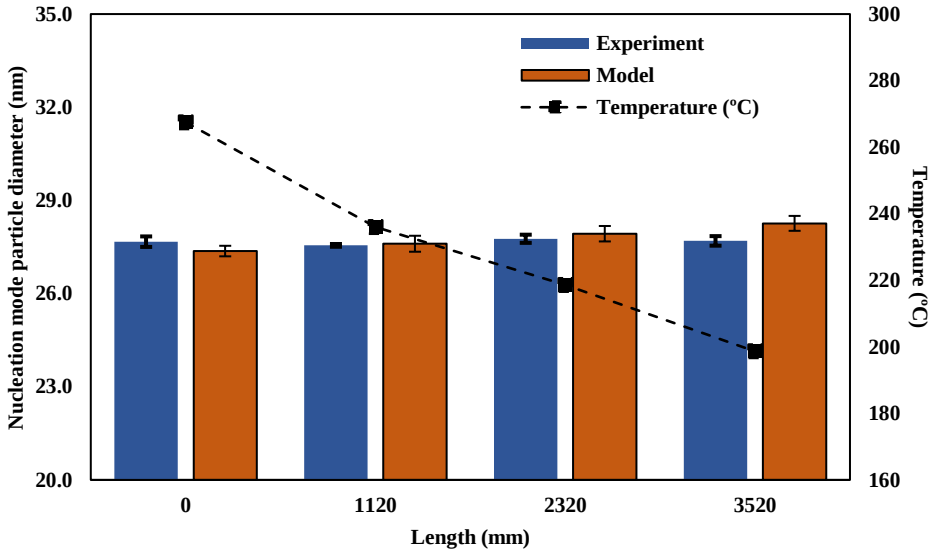


**Figure 4.14 - Nucleation mode particle diameter at 3.0 bar BMEP**

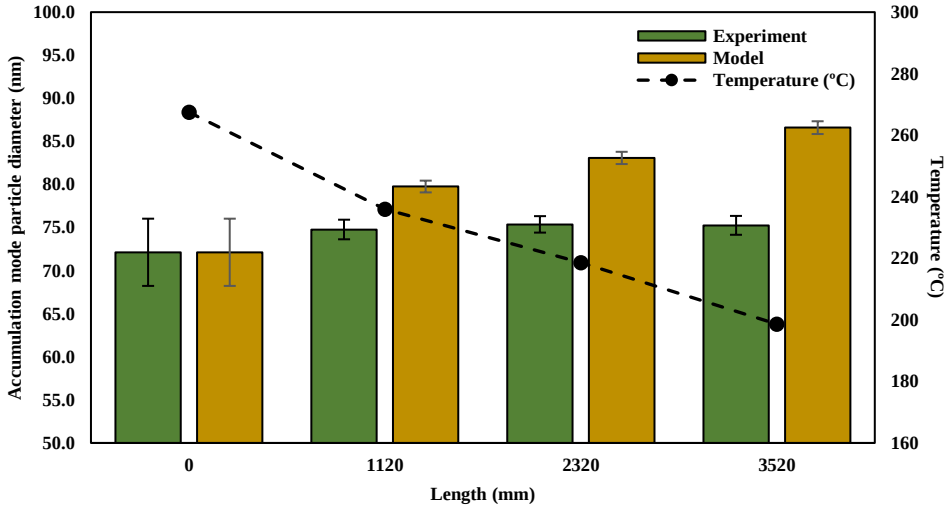


**Figure 4.15 - Accumulation mode particle diameter at 3.0 bar BMEP**

On the other hand, the nucleation mode concentration (NMC) and accumulation mode concentration (AMC) show a decrease of 8.3% and 6.7% experimentally, exposing no gain in particle concentration for either particle modes. Whereas, based on the numerical model analysis of NMC and AMC, there is a concentration loss of 18.1% in NMC and a significant gain of 12.6% observed for AMC.

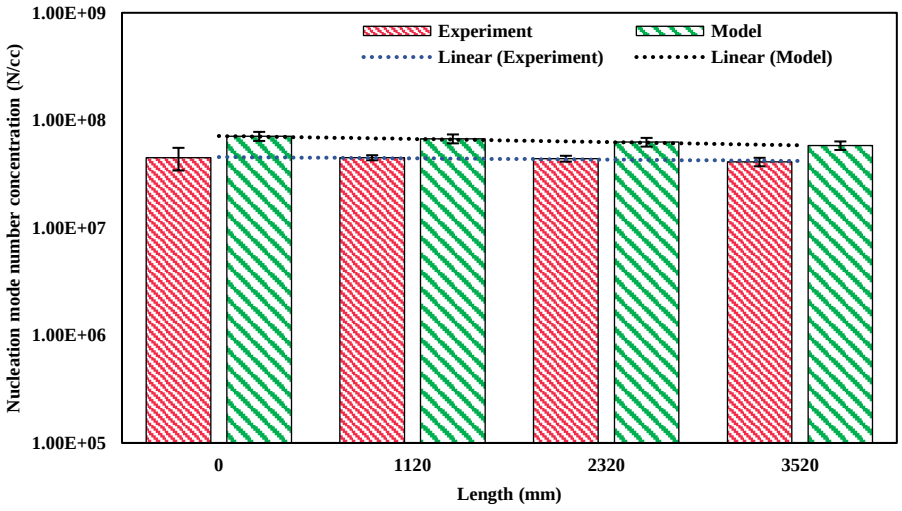


**Figure 4.16 - Nucleation mode number concentration at 3.0 bar BMEP**

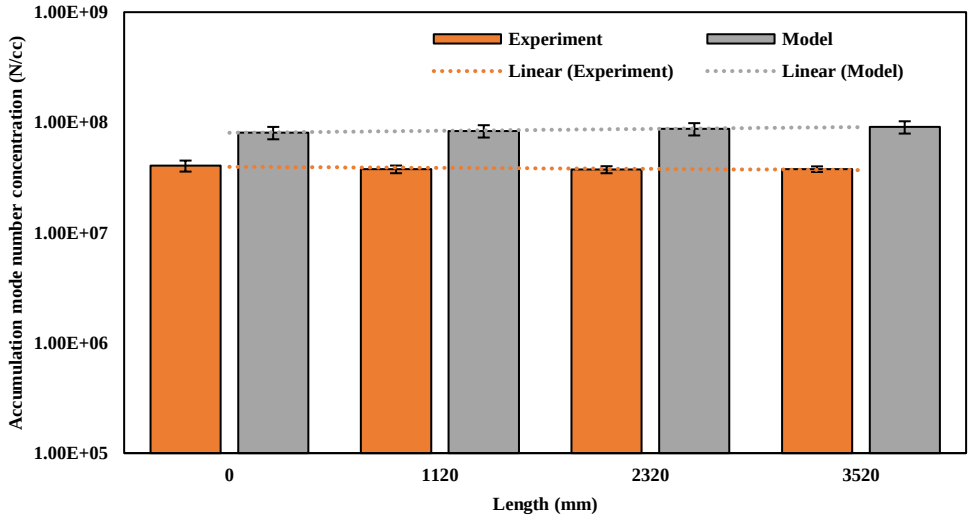


**Figure 4.17 - Accumulation mode number concentration at 3.0 bar BMEP**

The particle size distribution along the length of the exhaust tailpipe has shown a substantial decrease in experimental and simulation analysis. An average reduction in overall number concentration for all discretised particle size number concentrations is observed between 4% and 20%, where the analysed gain and loss of particles can be compared with the above NM and AM results. Concentration gains in the experiments and modelling are both noticed due to surface growth, adsorption and absorption in both NM and AM particulates. Whereas, losses seen in the particle concentrations are the results of the formation of larger particulates from ultra-fine particles and chamber wall depositions of PM during exhaust flow. Figures 4.16 and 4.17 evidently show the changes in particle size distribution (PSD) from 0.0 m (first sampling position) to 3.52 m (final sampling position), compared between experimental and modelling analysis. It is discovered that the PSD deviation from initial to final sampling, particles tends to increase in size more than 50nm with minor changes in the number concentrations.

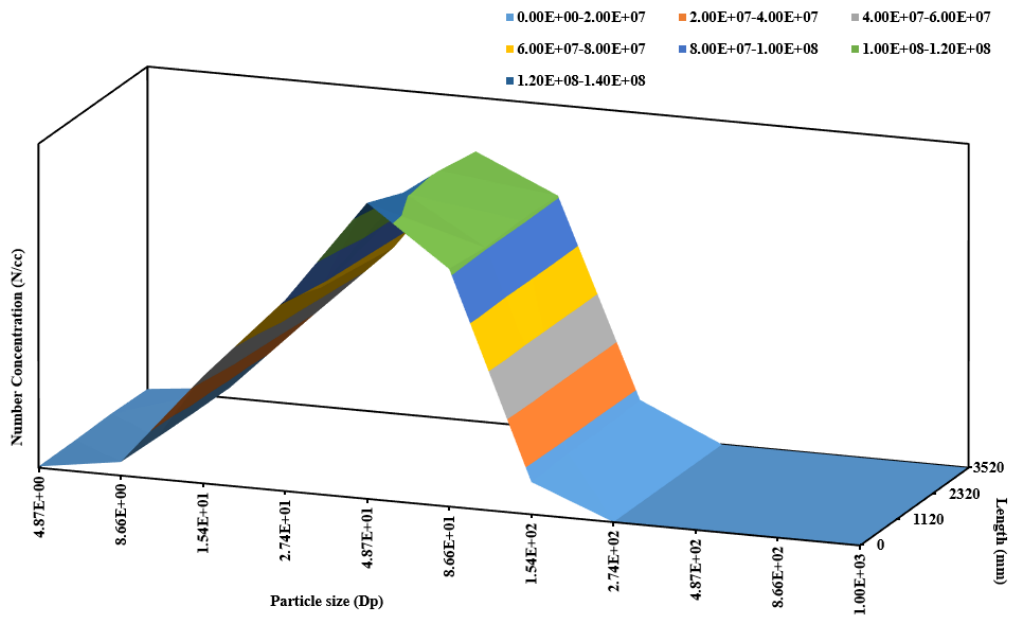


**Figure 4.18 - Experimental analysis of particle size distribution along the length at 3.0 bar BMEP**

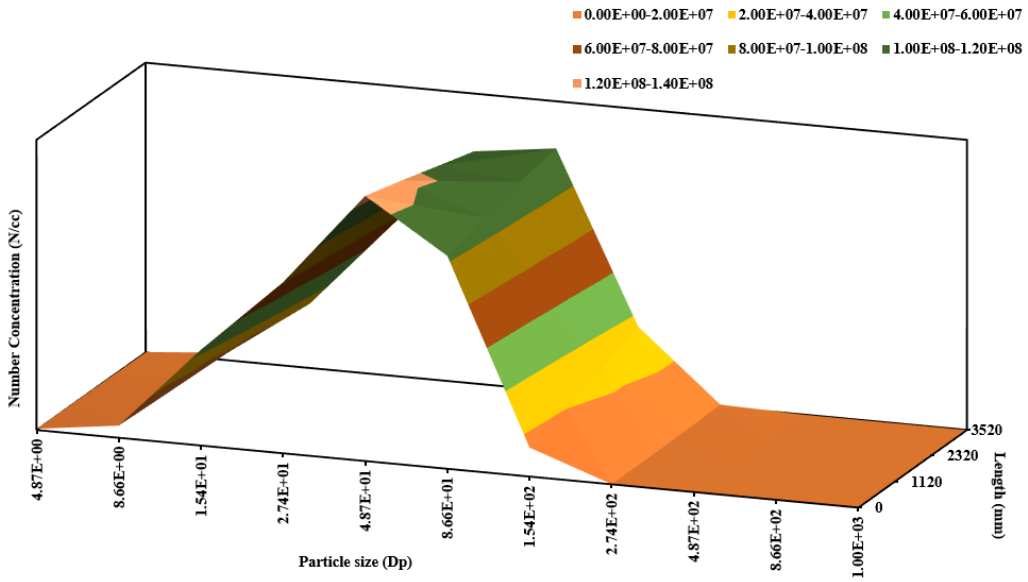


**Figure 4.19 - Modelling analysis of particle size distribution along the length at 3.0 bar BMEP**

### 4.6.4 Comparative analysis of numerical simulations and test bench experimentation at 6.0 bar BMEP

Particle inception and growth analysis carried out for 6.0 bar BMEP engine operation are shown from Figure 4.20 to 4.25. The exhaust gas temperature was noted at 350 ºC and decreased to a measured temperature of 272 ºC along the length of the exhaust tailpipe. The air dilution increased during sampling experimentally, which was amended in the model to achieve precise values for nucleation and accumulation modes. The amending of the dilution ratio for high-temperature exhaust gases can aid in an in-depth understanding of nucleation of vapour phases gas constituents and vapour condensation on particulates.

Due to high exhaust temperatures, the particle size for NM does not vary to a great degree, but has small overall gain in the particle diameters for experimental and modelling approaches. Due to high exhaust temperatures, the nucleation of PAHs, $H_2SO_4$ and $H_2O$ does not have a higher rate and hence fewer nucleation mode secondary particles are produced. Existing nuclei from in-cylinder combustion progress to increasing particle sizes by surface growth, vapour deposition and particle-to-particle (P2P) interactions. The NM particle diameters for experimental and simulations lie between 26 and 28 nm, showing a decrease of 4% and an increase of 1.5% for experiments and simulations, respectively. Contrastingly, the AM particle size is observed to increase by 1.7% and there is a consistent overall increase of 4.3% from experimental and simulation result analysis.

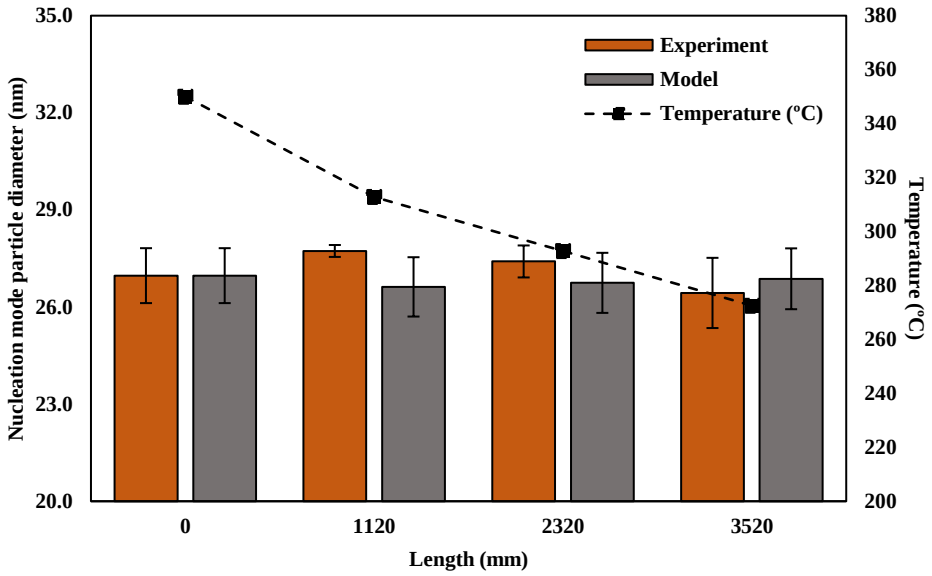


**Figure 4.20 - Nucleation mode particle diameter at 6.0 bar BMEP**

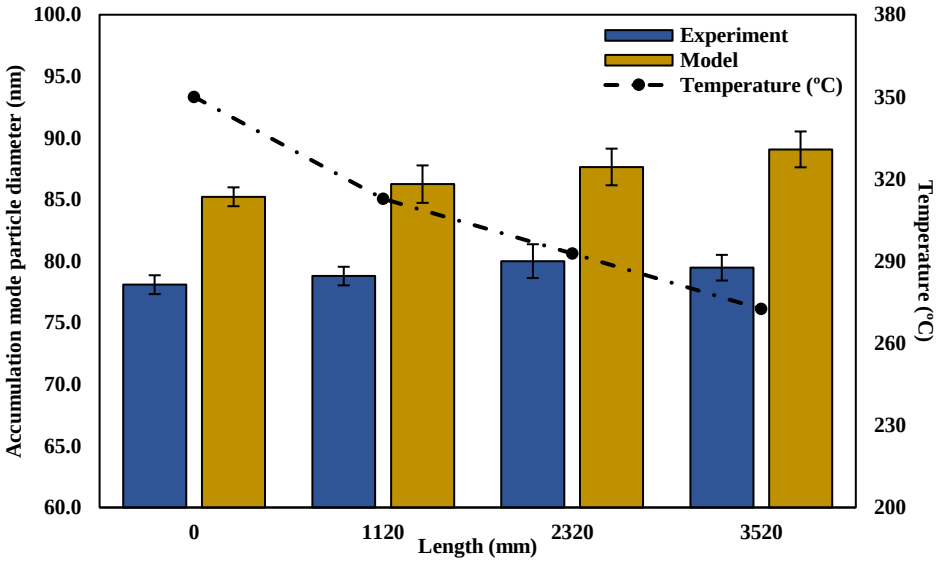


**Figure 4.21 - Accumulation mode particle diameter at 6.0 bar BMEP**

Surface growth increases the particle potential to collide and coalesce, and hence, a gain and some losses in particle concentration are observed during the exhaust gases travelling through a chamber. The NM concentration is observed to reduce significantly by 13% during

experimentation and similarly based on the boundary conditions input in the model, the simulation results show a reduction in NM number concentration by 7.2%. On the other hand, the AM concentrations show an increment of approximately 5% based on numerical modelling and analysis, but contrarily an insignificant decrease of 5.5% is shown in experimental AM concentration.

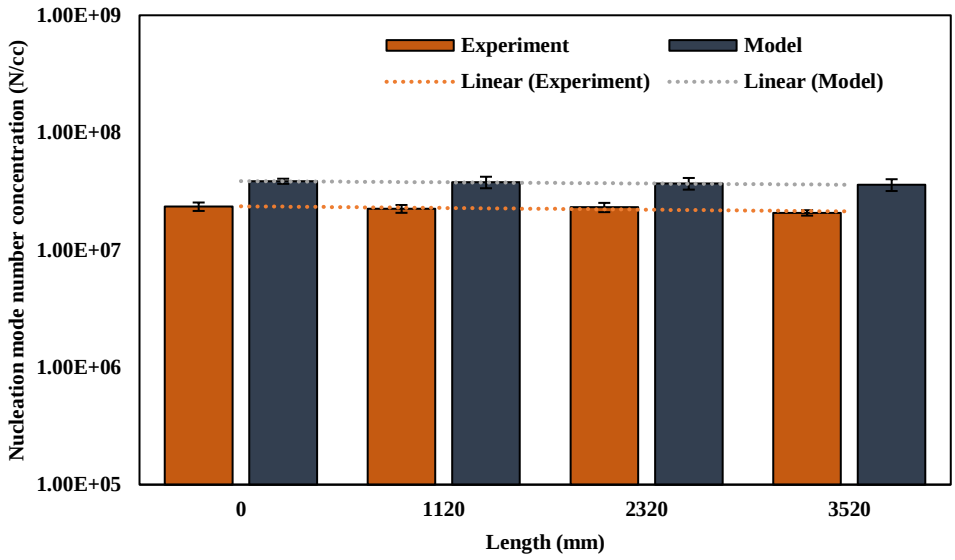


**Figure 4.22 - Nucleation mode number concentration at 6.0 bar BMEP**

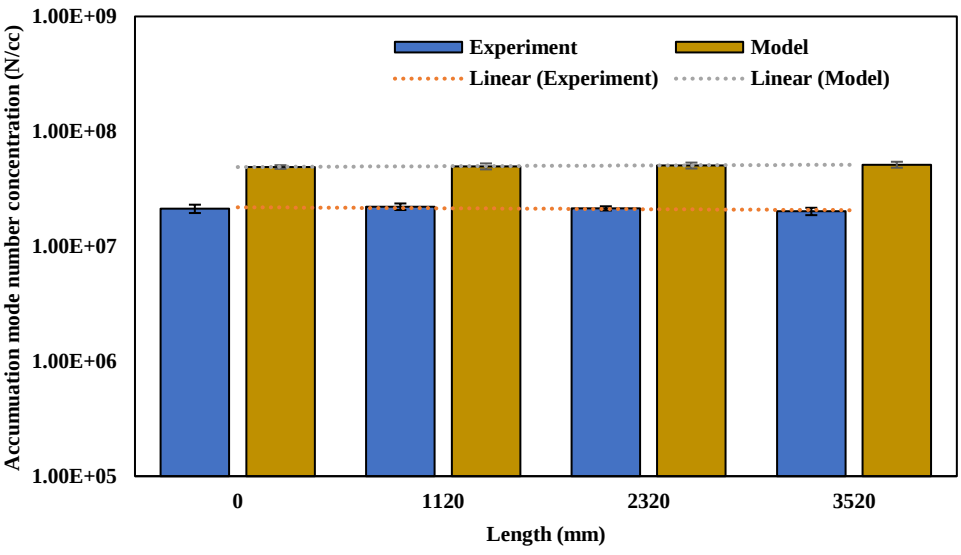


**Figure 4.23 - Accumulation mode number concentration at 6.0 bar BMEP**

Particle size distribution (PSD) for 6.0 bar BMEP testing conditions have shown an initial concentration distribution in both nucleation (0-50 nm) and accumulation (50-1000 nm) modes, as the engine conditions were achieved using the pilot and main injection combined. Further particle distribution and growth does not depend on the engine conditions but is inter-dependent between the length of the exhaust tailpipe and the pressure and dilution parameters. The PSD numerical simulations have shown a higher accuracy in the phase transition trend of the particulates. Changes in particulate matter (PM) characteristics are supported by particle inception and growth at the initial stages, and are followed by vapour condensation, adsorption, and agglomeration by particle to particle interactions.

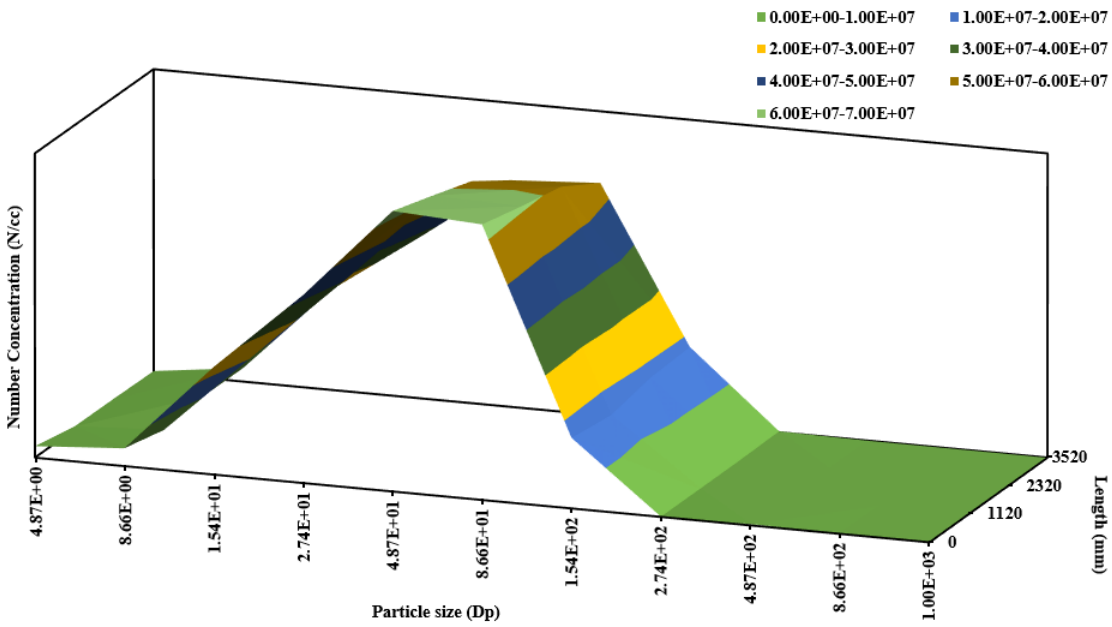


**Figure 4.24 - Experimental analysis of particle size distribution along the length at 6.0 bar BMEP**

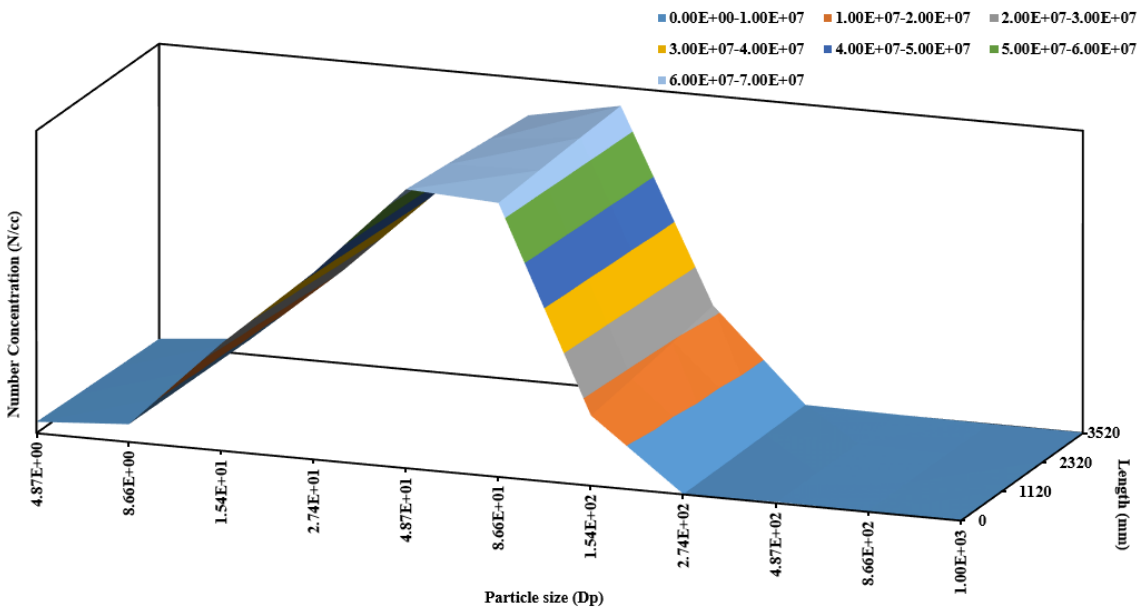


**Figure 4.25 - Simulation analysis of particle size distribution along the length at 6.0 bar BMEP**

## 4.7 Summary

The particle growth model (PGM) contains a multilevel simulation model, which determines the particulate characteristics depending on various input parameters. The focus of the model is to observe the effect of temperature gradient and the input parameters in understanding the particulate evolution along the length of a 3.5-metre exhaust tailpipe. The following primary conclusions can be made for the research work carried out above. In the model, $H_2O$-$H_2SO_4$ vapour nucleation is the prime factor considered in predicting the nucleation mode particle variation. Particulate growth in diameter, surface area and mass is dependent on these three factors: $H_2O$, $H_2SO_4$ and $C_nH_n$ vapour nucleation and condensation in the primary stages. Although the combined particulate growth is largely dependent on the water and sulphuric acid vapour, fuel combusted substitute, hydrocarbon molar fraction can also affect the nucleation mode particle growth.

Particle number concentration for each phase follows a similar trend line at each engine load condition from 1.4 to 6.0 bar BMEP, with a considerable difference of size, concentration

or distribution between two consecutive testing positions. The model's results provide the following conclusions:

1. Model predictive analysis shows the global solution of PM data based on the fixed physical parametric changes which occur/can occur inside the chamber. Experimental analysis shows the local solution of PM data which can vary due to minor fluctuations in the engine conditions. Hence, the difference between the modelling and experimental results are observed with comparability.
2. Theoretically, and based on physical and chemical variation assumptions, the changes in the nucleation and accumulation modes' number concentration should contrast with each other. The model's results partially agree with this hypothesis: as the nucleation mode PN decreases along the length of the chamber; and the accumulation mode PN has a gradual increase up to a peak at the end of the chamber. This variation is observed as small-sized particles are adsorbed, condensed and combined to form larger size particles, hence, decreasing the PN for the smaller particles and increasing in accumulation mode.
3. The contribution of $H_2O$-$H_2SO_4$ nucleation and adsorption does not have a significant effect on the PN concentration since low fuel sulphur content gasoline (<5 ppm) is used during the experimentation. Hence, the fuel sulphur conversion percentage reduces and overall decreases the involvement of water and sulphuric acid vapours on the nucleated particulates. Combusted fuel substitutes' (hydrocarbon) vapour and other gas emissions' mass fraction supports higher adsorption on nucleation mode particulates, and hence increases the rate of nucleation and condensation.

# CHAPTER 5

# PARTICULATE AND GAS EMISSION DYNAMICS IN COOLED EXHAUST TAILPIPE

## 5.1 Introduction

As studied in the previous chapter, gas and particulate emissions produced during diesel fuel combustion comprise complex and toxic compounds that are pushed out from the exhaust valve through to the exhaust tail pipe. The effect of these harmful emissions is already mentioned previously in earlier chapters of the thesis. Particle formation, nucleation to agglomerates processes inside the exhaust tail pipe, depends on multiple factors which are studied in the particle growth model (PGM) like the exhaust temperature; particulate and gas concentration; nucleation rates; length of the exhaust pipe; exhaust flow velocity; particle residence time; and ambient conditions. This chapter is focused to give a better understanding and investigating the particle dynamics by reducing exhaust gas temperatures by the external cooling treatment of a diesel engine exhaust tail pipe using copper coil tubing wrapped around the tailpipe, when the engine is run at steady-state conditions for increasing engine loads. The analysed results can aid in the design considerations for an after-treatment system based on the gas and particulate emissions' results, and also contribute to the knowledge of particulate matter behaviour under various temperature conditions and give a better insight of gaseous emissions contribution to total particulate number concentrations.

## 5.2 Research Objectives

The empirical study carried out in this chapter deals with the particulate matter (PM) dynamics inside an exhaust tail pipe (ETP). Two experimental set-ups are implemented for investigating the evolution of particulates and the gas and particulate matter dynamics involved inside a 3.5-metre-long exhaust pipe. The copper coil tubing wrapped around the ETP is supplied with ice water and antifreeze to provide a variable cooling effect. The comparative analysis is done to observe a near-realistic condition of an ETP for an on-road vehicle where the temperature of ETP reduces with their lengths.

The engine is run at three steady state conditions from 1.4 bar BMEP to 4.5 bar BMEP, keeping the fuel injection quantity percentage consistent at 20% pilot injection quantity and 80% main injection quantity. The increasing exhaust temperatures and the external cooling effects are compared with similar engine operations as baseline experimentation. The PM characteristics are studied based on their number concentrations, individual size diameters and mass using particulate analyser.

The physical parameters and particulate matter results acquired from the cooling of the ETP, is also used as an initial boundary condition for the validation, applicability and robustness of the particle growth model (PGM), which was used similarly in chapter 4. It will be an interesting study to perform to explain the particulate behaviour under different physical conditions affecting the PM characteristics and also establishing the application of PGM.

## 5.3 Experimental and exhaust cooling set-up

The external cooling set-up used copper coil tubing (4 mm OD * 50 m) for wrapping the exhaust pipe, covering 3.0 m of length with a variable decreasing pitch of 5.0 to 0.1 cm and 130 revolutions around the pipe. Antifreeze (30%) and cold water (70%) was supplied through these copper coil windings to reduce the temperature gradient.

The schematic shown in Figure 3.8 (chapter 3) earlier, explains the set-up used for the exhaust tail pipe cooling. The set-up is equipped with two 38-plate heat exchangers to reduce the outflow water and antifreeze temperature, further fitted to a closed tank filled with the fluid. The heat exchangers use a counter-flow tubing set-up for a substantial reduction in the fluid temperature with high-pressure water-cooling, bypassed from the engine cooling set-up. The high-pressure pump connected to the water and antifreeze mixture tank flowing through the copper coils provided a continuous controlled flow rate of 60 litres/hour aiding in subsequent cooling around the tail pipe.

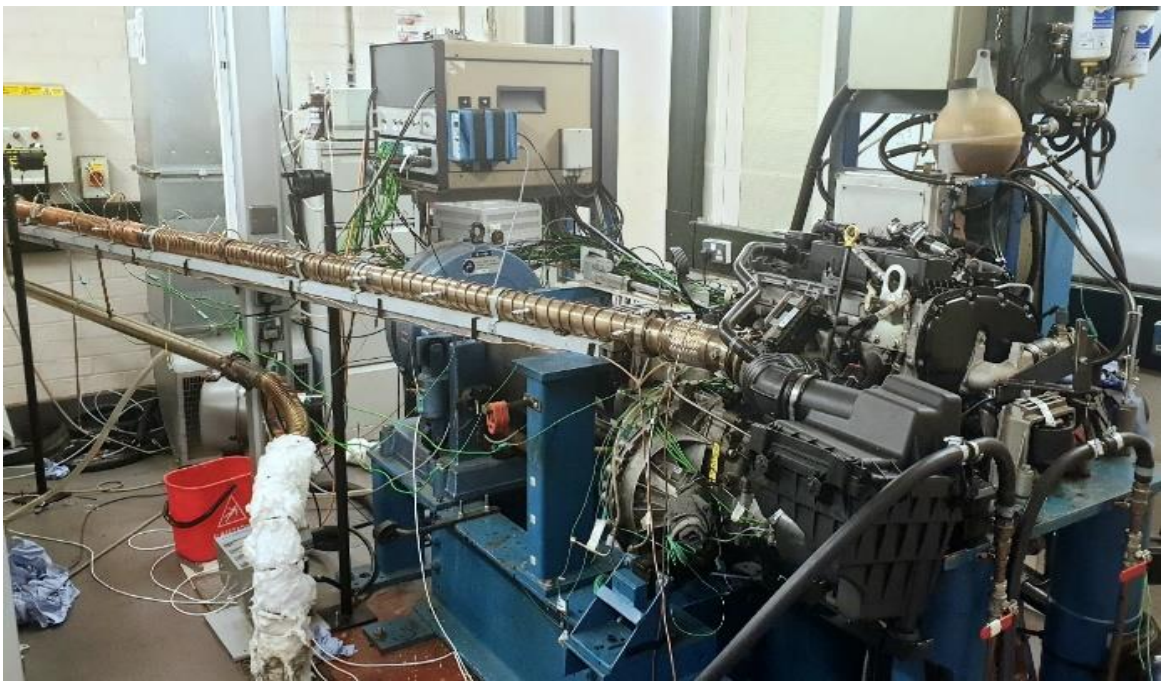

**Figure 5.1 – Cold exhaust experimental set-up (left)**

## 5.4 Experimental instrumentation

The exhaust pipe is equipped with K-type thermocouples, equidistant with each other and measured in real-time using two PicoLog thermocouple data loggers TC-08 for 12 test points that can measure temperatures from -270 to +1820 ºC. The experiment set-up above displays the data acquisition systems and measurement instruments used during the PM experimentation. As mentioned above, the experiment is performed for a 3.5-m exhaust tail pipe used for 13 sample test points and 12 K-type thermocouples placed after the turbocharger to the end of the exhaust pipe. The test points are equidistant at 26 cm (±3 cm). The test points are used for emission measurements by employing particle and gas emission analysers shown in Figure 3.2 of chapter 3.

## 5.5 Experimental method

An experimental method for hot and cooled exhaust conditions is demonstrated in Table 5.3. Engine load conditions at low (1.4 bar BMEP), intermediate (3.0 bar BMEP), high (4.5 bar BMEP) are monitored with a split injection of pilot and main injections, with different amounts of EGR flow.

The engine is warmed up to reach its optimum oil and coolant temperatures at 90 °C and 89 °C respectively. During the warming up stage, the engine is kept at a steady-state condition of 1800 rpm and an engine load of 1.4 bar BMEP (24.5 Nm). The EGR percentage is increased in small levels after a 50 °C coolant temperature is achieved. The split injection strategy was fixed at 25% pilot injection volume and 75% main injection volume. Using ATI Vision the injection timing and volume were fixed before data acquisition.

The baseline testing for particulate dynamics is done at 7 equidistant consecutive testing points along the length of the exhaust pipe. The analysis was done for low, intermediate and high loads, acquiring data for PM, gas emissions and temperature gradients. As mentioned previously, the exhaust pipe is subjected to external cooling using copper tubes supplied with low temperature water and antifreeze. A similar testing procedure is carried out for exhaust cooling with data acquisition at 7 testing positions for 1.4 bar BMEP to 6.0 bar BMEP engine loads. All experimentation is done for a similar split-injection strategy as mentioned in Table 5.2 below.

**Table 5.1 - Experimental methods for hot and cold exhaust**

| Parameters | Baseline Experimentation | | | External Cooling | | |
|---|---|---|---|---|---|---|
| | **Test 1** | **Test 2** | **Test 3** | **Test 1** | **Test 2** | **Test 3** |
| BMEP (bar) | 1.4 | 3.0 | 4.5 | 1.4 | 3.0 | 4.5 |
| Speed (rpm) | 1800 | 1800 | 1800 | 1800 | 1800 | 1800 |
| EGR (%) – Cold EGR | 30 | 25 | 20 | 30 | 25 | 15 |
| VNT (%) | 100 | 40 | 30 | 100 | 40 | 30 |
| Intake manifold pressure (kPa) | 90 | 95 | 100 | 90 | 95 | 100 |
| Injection pressure (MPa) | 60 | 75 | 105 | 60 | 75 | 105 |
| Injection timing (CA BTDC) | Pilot: 20º Main: 2.5º | Pilot: 20º Main: 2º | Pilot: 20º Main: 3º | Pilot: 20º Main: 2.5º | Pilot: 20º Main: 2º | Pilot: 20º Main: 3º |
| Injection volume ($mm^3$) | $1^{st}$: 0.999 Main: 4.25 | $1^{st}$: 1.65 Main: 6.4 | $1^{st}$: 2.3 Main: 9.1 | $1^{st}$: 0.999 Main: 4.25 | $1^{st}$: 1.75 Main: 6.7 | $1^{st}$: 2.3 Main: 9 |
| Coolant temperature (ºC) | 89 | 89 | 89 | 89 | 89 | 89 |
| Ambient temperature (ºC) | 25.5 | 29 | 32 | 25.5 | 32 | 32 |

## 5.6 Results

### 5.6.1 Temperature distribution for engine load conditions

The temperature of the water and antifreeze solution flowing through the copper coil windings increases at a higher temperature as the engine exhaust temperature increases. Copper has a higher thermal conductivity coefficient than stainless steel, hence it acts as a natural heat exchanger and reduces the temperature inside the ETP by some degrees. The decreasing copper coil winding pitch, as shown in Figure 3.7 of chapter 3, increases the probability of temperature gradient reduction by a significant number and develops various temperature profiles along the exhaust tailpipe (ETP), as shown in Figures 5.3 to 5.5.

The exhaust gas temperatures vary based on the engine BMEP conditions and other engine operating conditions like EGR, VNT, injection quantity, injection pressure, and injection timings. Exhaust gas temperatures vary for engine loads from 1.4 bar to 4.5 bar BMEP with and without the exhaust tail pipe cooling effects, but both show a monotonous decreasing trend for each condition. The engine-out temperature was measured along the length of the exhaust tailpipe for 7 testing positions, with approximately 50 cm to 60 cm difference between each consecutive point. Table 5.2 shows the upstream and downstream temperature differences for individual engine condition with and without the exhaust cooling implementation.

**Table 5.2 - Temperature drop in the exhaust tailpipe**

| Engine Conditions | Upstream temperature (0 m) | Downstream temperature (3.5 m) | Temperature drop (ºC) |
|---|---|---|---|
| 1.4 bar BMEP – Hot | 239 | 179 | 60 |
| 1.4 bar BMEP – Cold | 235 | 160 | 75 |
| | | | |
| 3.0 bar BMEP – Hot | 312 | 227 | 85 |
| 3.0 bar BMEP – Cold | 309 | 219 | 90 |
| | | | |
| 4.5 bar BMEP – Hot | 388 | 279 | 109 |
| 4.5 bar BMEP – Cold | 387 | 275 | 112 |

The temperature drop observed in each condition is due to the variating changes in the cooling of the exhaust assisted by copper coil windings along the length of the exhaust tail pipe. At high engine loads, the cooling does not have a substantial effect and does not depict any changes in the temperatures for hot and cooled exhaust conditions, as the heat convection at high temperature exhaust gases reduces the effect of assisted coil cooling at higher rates. The comparative analysis is specifically done without the exhaust cooling, to prove the heat convection from both copper coils and the stainless-steel exhaust tube has a prominent effect on exhaust emissions. Figures 5.3 to 5.5 show the temperature profiles for cooled and non-cooled exhaust tail pipe temperatures, and also the water and antifreeze solution temperatures during cooling of ETP.

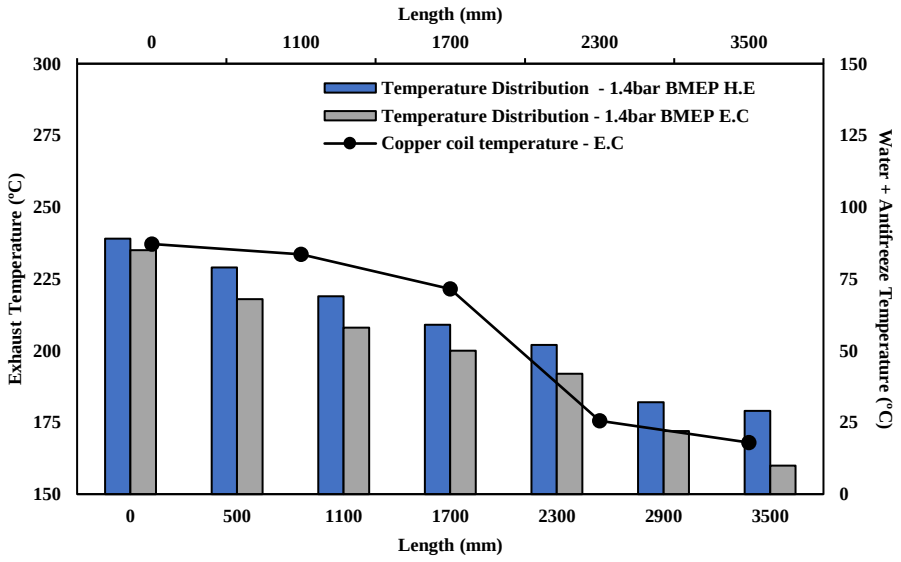


**Figure 5.2 - Exhaust temperature distribution at 1.4 bar BMEP**

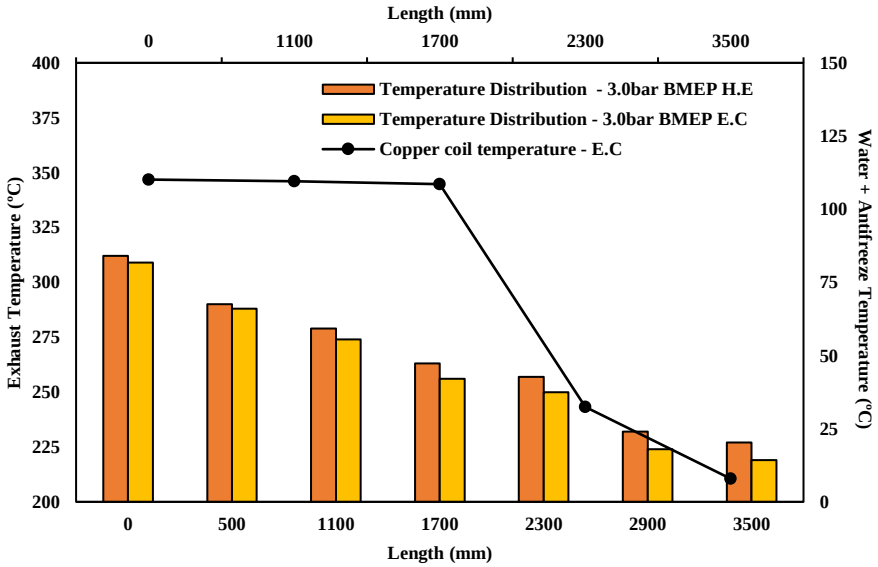


**Figure 5.3 - Exhaust temperature distribution at 3.0 bar BMEP**

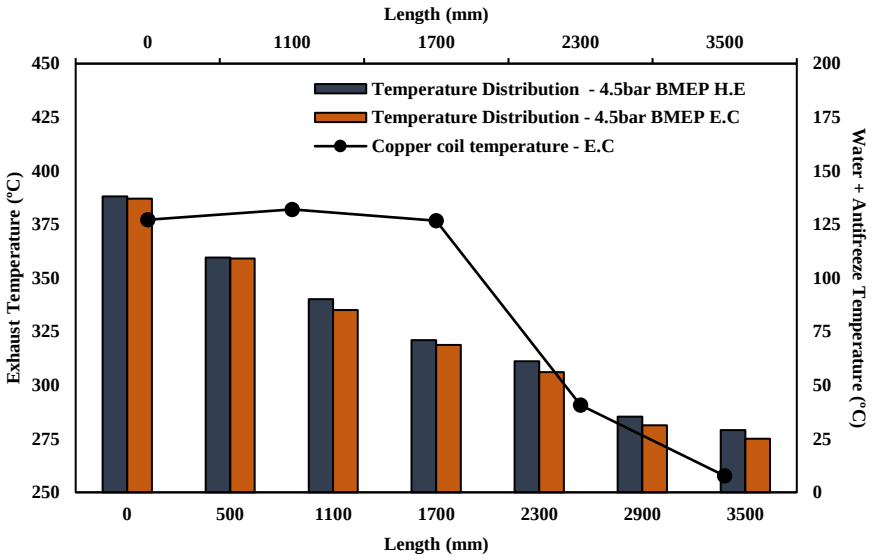


**Figure 5.4 - Exhaust temperature distribution at 4.5 bar BMEP**

### 5.6.2 Particulate matter (PM) dynamics at 1.4 bar BMEP

The PM dynamics along the exhaust tailpipe (ETP) have shown a significant change with hot and cool conditioning under approximately similar engine operating conditions at 30% EGR and 100% VNT positions, assisted with 20% pilot and 80% main fuel injection settings. The focus is not completely on the engine operating conditions, but on the combined interaction of particulate matter and gas species inside the ETP. Table 5.3 depicts the upstream and downstream particulate matter total number concentration (TNC) measurements for low engine loading conditions. The PM TNC overall reduced by 13% and increased by 2.6%, for the hot and cool conditioned exhaust respectively. The particulate decrease in the TNC is a resultant can be because of continuous PM residence on chamber walls and particulate-to-particulate agglomeration along the ETP. On the other hand, due to the cooling of the exhaust pipe and a substantial decrease in temperature gradient compared to no external cooling, the minor increase in total number is due to the gas species condensation that reached pseudocritical

temperatures and formed nano-sized particulates by the combination of vapour phase molecules and nanoparticles; this is an established phenomenon addressed by [22, 24]. The increase in species conversion and TNC is not significant however, as the exhaust temperatures are higher than the temperature expected to aid condensation and particle formation. This increase in TNC is further analysed and supported with particle modes' (nucleation and accumulation) size, concentration and mass.

**Table 5.3 - Total number concentration variations at 1.4 bar BMEP**

| Engine condition | Upstream PM – TNC (N/cc) | Downstream PM - TNC (N/cc) |
|---|---|---|
| | | |
| 1.4 bar BMEP – Hot | 7.10 $e^7$ | 6.27 $e^7$ |
| 1.4 bar BMEP – Cold | 6.27 $e^7$ | 6.43 $e^7$ |

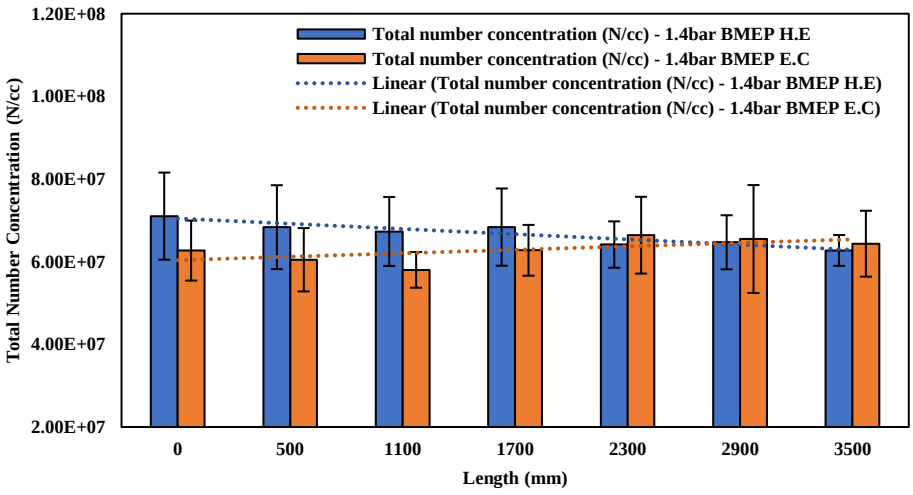


**Figure 5.5 - Total number concentration at 1.4 bar BMEP**

Table 5.4 and Figures 5.7 to 5.8 show the nucleation mode concentration (NMC) and accumulation mode concentration (AMC), and also the nucleation mode count mean diameter (NMCMD) and accumulation mode count mean diameter (AMCMD) at upstream and downstream for both ETP conditions. From the analysis and evaluation of both ETP conditions, it can be observed that the changes in the NMC and AMC decrease significantly in the hot ETP and show different the changes in the cold ETP, where the NMC decreases by a small fraction of 4.05% and AMC increases by 3.32%. For NMCMD, the particle size showed a prominent increase in both conditions, but a significant increase of approximately 4.0 nm particle diameter in cold ETP conditions was observed compared to the hot ETP condition. Similarly, the AMCMD has shown an increase for the hot and the cold ETP, but there was a higher increase of particle diameter by approximately 9.0 nm during cold conditioning.

The AMCMD increase in the cold conditioning can be supported by the increase in the coagulation rate of particulates that are transported from 0 m to 3.5 m, where a higher particle to particle interaction is carried out inside the ETP. Also, the increase in NMCMD is observed due to small particles (< 50 nm) agglomerating together to form an overall larger nucleated particle, progressing to a decreasing shift in the NMC and increasing the NMCMD. The particle sizes and concentrations for each mode (NM and AM) are also dependent on the particle masses which are explained further. Particle masses are the quantification in determining the temperature gradient effects on overall PM characteristics. These changes in NM and AM modes for concentrations are an overall quantification to the variations in TNC of hot and cold ETP conditions. Also, the flow velocity of engine exhaust is lower which gives an advantage for particulates to interact or reside dramatically inside the ETP, and much variations and instability in particulate behaviour can be observed.

**Table 5.4 - Particle mode concentration and size variations at 1.4 bar BMEP**

| **Particulate mode characterisation** | **Upstream (0 m)** | **Downstream (3.5 m)** | **Percentage (increase (+)/decrease(-))** |
|---|---|---|---|
| **Hot ETP** | | | |
| Nucleation mode concentration (NMC) | 2.69 $e^7$ | 2.19 $e^7$ | -23.22 |
| Accumulation mode concentration (AMC) | 3.69 $e^7$ | 3.39 $e^7$ | -8.66 |
| | | | |
| Nucleation mode count mean diameter (NMCMD) | 24.64 | 26.54 | 7.13 |
| Accumulation mode count mean diameter (AMCMD) | 72.43 | 74.95 | 3.35 |
| **Cold ETP** | | | |
| Nucleation mode concentration (NMC) | 2.3 $e^7$ | 2.21 $e^7$ | -4.05 |
| Accumulation mode concentration (AMC) | 3.35 $e^7$ | 3.46 $e^7$ | 3.32 |
| | | | |
| Nucleation mode count mean diameter (NMCMD) | 22.607 | 26.37 | 14.27 |
| Accumulation mode count mean diameter (AMCMD) | 69.75 | 78.1 | 10.69 |

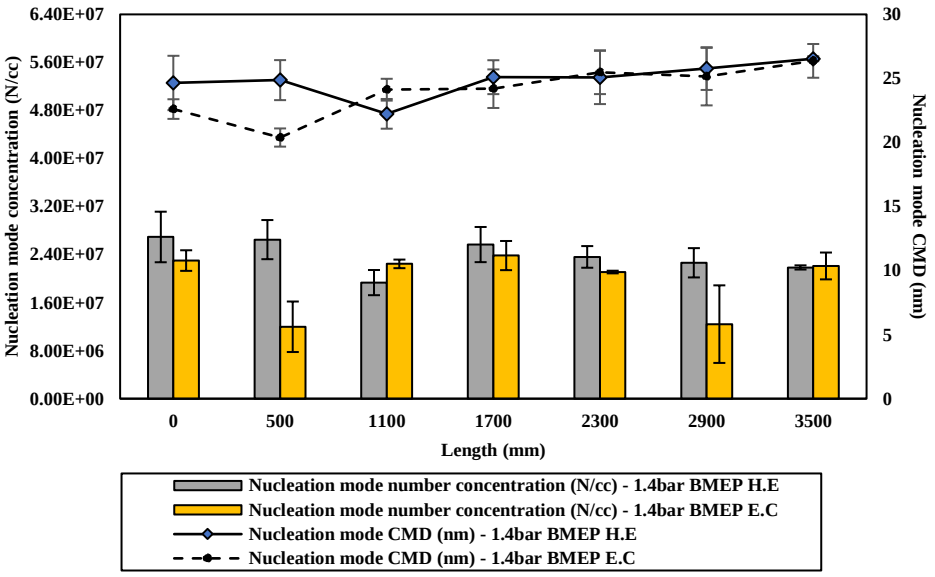


**Figure 5.6 - Nucleation mode concentration and size at 1.4 bar BMEP**

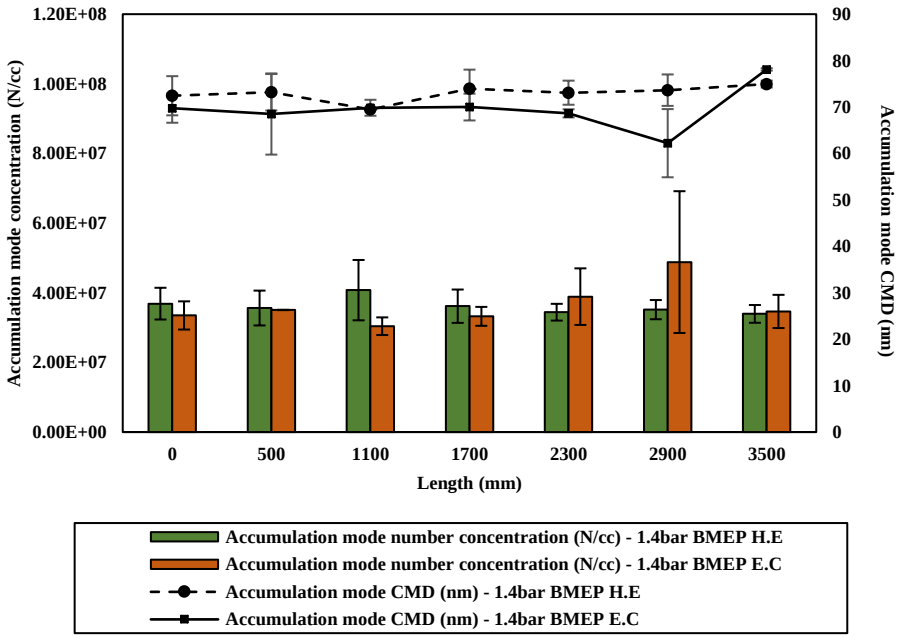


**Figure 5.7 - Accumulation mode concentration and size at 1.4 bar BMEP**

The particle masses for both ETP conditions have shown comparable and visible changes along the length. As mentioned previously, the NMCMD and AMCMD for both ETP conditions have shown an increasing trend line, and that is comparable to the particle masses of these conditions. The nucleation mode mass (NMM) and accumulation mode mass (AMM), for hot conditions show a reduction in NMM by 4.1% but do not have any overall change in the AMM. However, the NMM and AMM for cold ETP conditions have been shown to have a massive effect on the particle mass by 33.5% and 25.6% respectively. The increment in particle masses quantifies the increasing diametrical sizes for particle modes (NM and AM). An increase in particle mass can also be assisted by the condensation of gaseous species and VOFs on particulates. Particle mass increase is a resultant of surface area growth when gas molecule morphology is transited to liquid or solid phase and increases the overall mass by the combination of similar morphed particles.

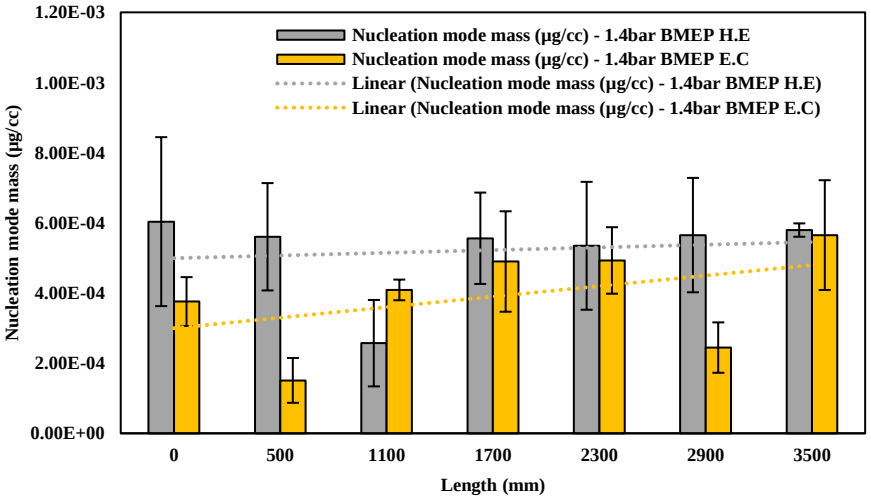


**Figure 5.8 - Nucleation mode mass at 1.4 bar BMEP**

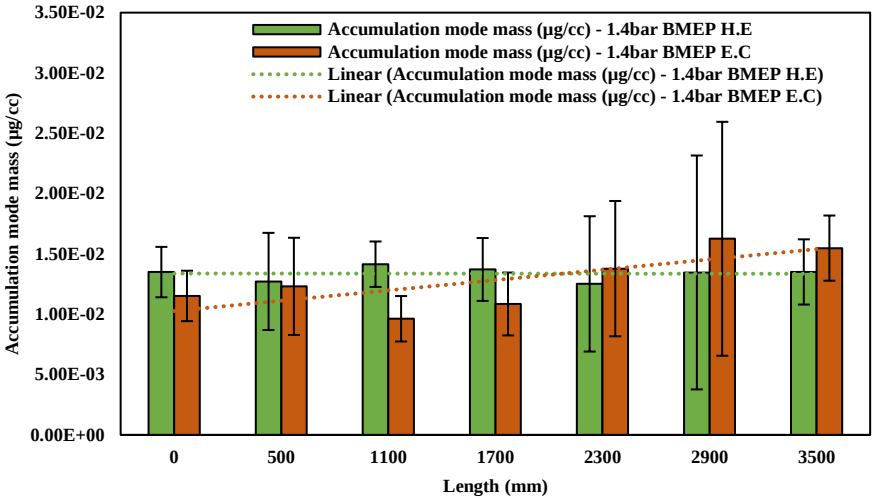


**Figure 5.9 - Accumulation mode mass at 1.4 bar BMEP**

The instability observed in PM, for a low engine load condition of 1.4 bar BMEP is due to the low exhaust flow rates inside the ETP that are strongly affected by the PM size, concentration, and mass. The heterogeneous mixture of gas and particulates interact and undergo numerous physical phenomena as mentioned in Chapter 2 of this thesis; where at critical and low temperatures have shown gas species' condensation has been shown to have a significant effect on PM characteristics.

### 5.6.3 Particulate matter (PM) dynamics at 3.0 bar BMEP

Figure 5.11 shows the TNC for an intermediate load of 3.0 bar BMEP. As observed during the experimentation, the changes in TNC show a similar decreasing trend line for both ETP conditions. However, the comparative variations between these conditions are substantially different from one another. Figure 5.5 shows the changes in PM TNC for upstream (0.0 m) and downstream (3.5 m), noting the overall measured decreased concentration. The TNC for the hot ETP condition, shows a reduction by 3.34% from upstream

to downstream with minor variations along the length; whereas, an overall reduction by 10.2% is observed for cold ETP conditions.

The TNC decrease observed for both conditions is due to a number of physical factors, such as increased exhaust flow rates, absorption, adsorption and coagulation of particulates (NM ↔ NM, NM ↔ AM, AM ↔ AM) and also loss of particulates on chamber walls during transport. These factors can be further explained based on the discretised analysis of particle mode concentration, size, and mass.

**Table 5.5 - Total number concentration variations at 3.0 bar BMEP**

| Engine condition | Upstream PM-TNC (N/cc) | Downstream PM-TNC (N/cc) |
|---|---|---|
| 3.0 bar BMEP – Hot | 6.21 $e^7$ | 6.01 $e^7$ |
| 3.0 bar BMEP – Cold | 5.65 $e^7$ | 5.13 $e^7$ |

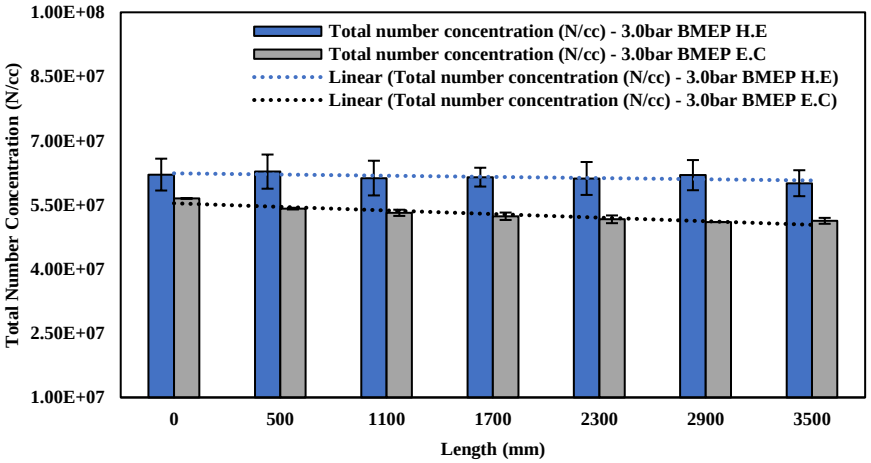


**Figure 5.10 - Total number concentration at 3.0 bar BMEP**

Figures 5.12 and 5.13 depict the variations in NMC, AMC, NMCMD, and AMCMD along the length of the ETP. The changes do not appear to be significant based on the graphical representation, hence Table 5.6 shows the numerical values of the overall changes occurring inside the ETP. The results for an intermediate engine load condition have shown contradictory results for cold ETP compared to low engine load conditions. The NMC shows a dynamical decrease of 15.3% with an increase in NMCMD of 7.53% for the hot ETP condition. The bonding or coagulation of NM particles together can reduce the concentration number of nucleated particles and increase the average counted mean diameter. This can be observed in the particle size change showing the increasing particle diameter along the length. However, for the cold ETP condition, the NMC has a non-significant reduction of 2.35%, but shows an 8.2% increase in the averaged count mean diameter. For both conditions, the NMCMD does appear to be significantly affected compared to the AMC and AMCMD.

The AMC for hot ETP shows an unimportant increase with the length but shows an overall 5.4% increase in the particle count mean diameter from 0.0m to 3.5m. The NM

particulates, collating together and forming larger particulates (> 50 nm) can aid in the overall increase in particle size and a minor increase in concentration. However, for AMC with cold ETP conditions, the concentration showed a substantial decrease by approximately 15% with an overall increase in AMCMD by 6.05%. Aggregation of particles in the accumulation mode is observed in this case, which can be justified by the decrease in particle number concentration in the accumulation mode and an increase in particle size and mass. These overall variations can be justified by the alterations in particle masses for both ETP conditions and quantifying the overall dynamics due to minor temperature gradient changes and external cooling.

**Table 5.6 - Particle mode concentration and size variations at 3.0 bar BMEP**

| **Particulate mode characterisation** | **Upstream (0 m)** | **Downstream (3.5 m)** | **Percentage (increase (+)/decrease(-))** |
|---|---|---|---|
| **Hot ETP** | | | |
| Nucleation mode concentration (NMC) | 2.6 $e^7$ | 2.25 $e^7$ | -15.3 |
| Accumulation mode concentration (AMC) | 3.09 $e^7$ | 3.19 $e^7$ | 3.12 |
| | | | |
| Nucleation mode count mean diameter (NMCMD) | 25.9 | 28 | 7.53 |
| Accumulation mode count mean diameter (AMCMD) | 72.36 | 76.52 | 5.4 |
| **Cold ETP** | | | |
| Nucleation mode concentration (NMC) | 2.2 $e^7$ | 2.15 $e^7$ | -2.35 |
| Accumulation mode concentration (AMC) | 2.91 $e^7$ | 2.54 $e^7$ | -14.7 |
| | | | |
| Nucleation mode count mean diameter (NMCMD) | 25.2 | 27.44 | 8.2 |
| Accumulation mode count mean diameter (AMCMD) | 69.58 | 74.06 | 6.05 |

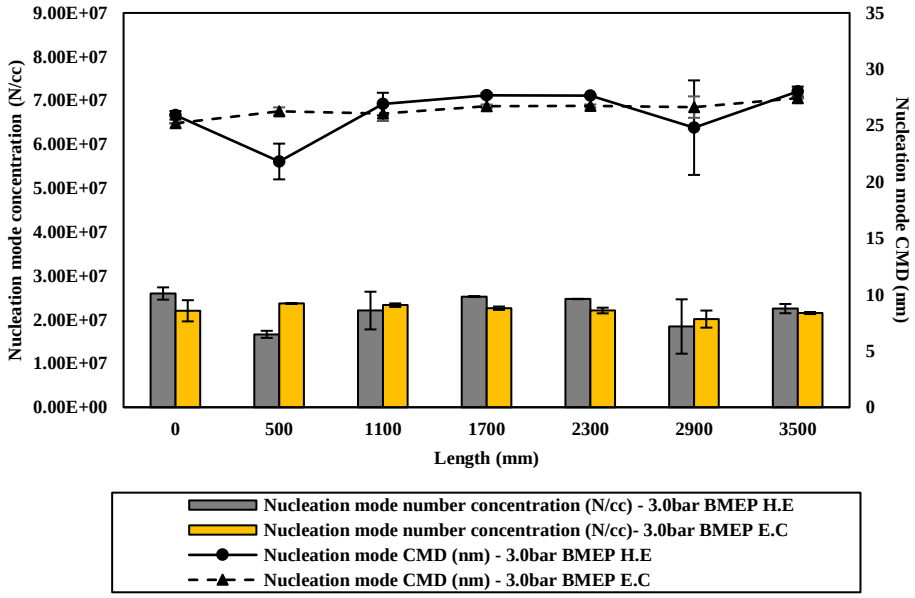


**Figure 5.11 - Nucleation mode concentration and size at 3.0 bar BMEP**

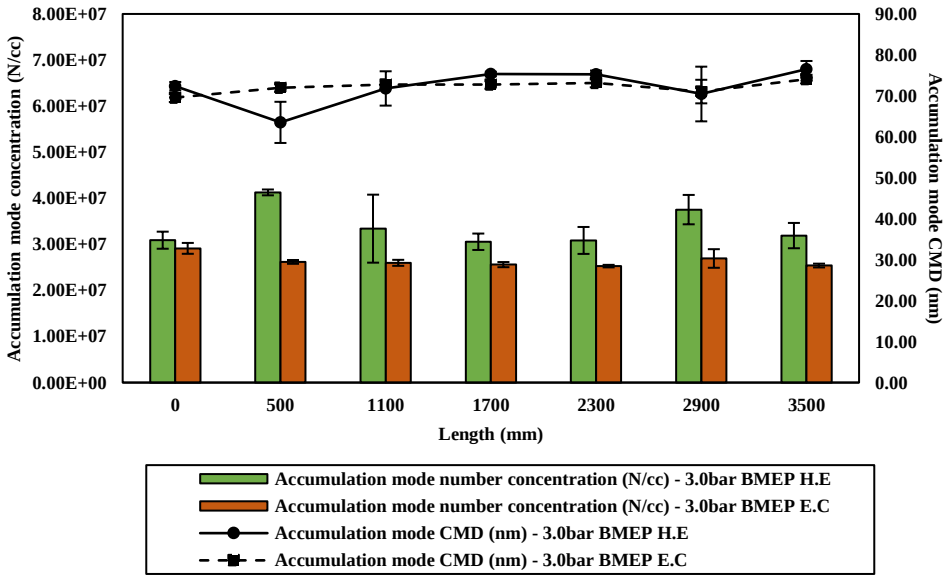


**Figure 5.12 - Accumulation mode concentration and size at 3.0 bar BMEP**

Particle mass for both conditions of the ETP shows an increasing trend for NMM. The increase in NMM for hot ETP is observed to be 5.51% and for cold ETP it has a significant increase of 29.4%. Adsorption and coalescence of stochastic particles, increases the overall density of the collated new particle that shows a mass increment for individual particles. Specific gas species that achieve their critical phase change temperatures can also aid in the deposition and adsorption on other particles which can affect in uplifting the particle masses. However, the AMM for both conditions shows an interesting result, where the AMM for hot ETP increased by 16% and no change was observed for the cold ETP condition. Coagulation of particulates in the case of hot ETP is more dominant and not observed for cold ETP, even with the increase in AMCMD. These null effects on AMM can be a consequence of condensed gas species of AM particulates that do not contribute much to the overall mass of the particle. For an intermediate load of 3.0 bar BMEP, the changes in concentration, size, and mass for both conditions have a lower effect due to increased copper coil temperatures and heightened exhaust temperatures.

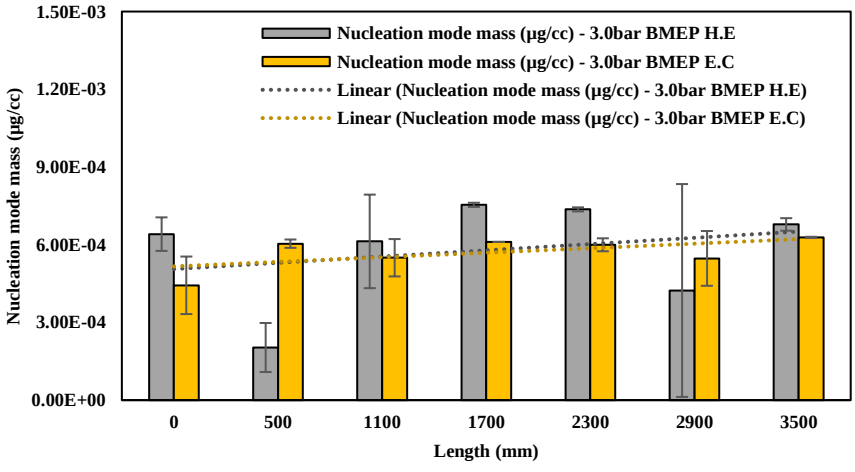


**Figure 5.13 - Nucleation mode mass at 3.0 bar BMEP**

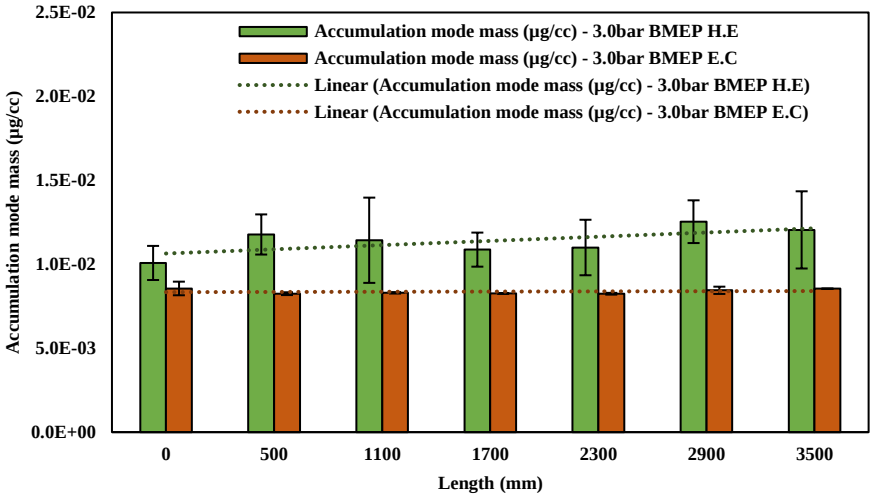


**Figure 5.14 – Accumulation mode mass at 3.0 bar BMEP**

### 5.6.4 Particulate matter (PM) dynamics at 4.5 bar BMEP

The engine for a high load condition was set with a high injection pressure of 105 MPa, assisted with a 15% EGR and VNT at 40%, keeping the intake manifold pressure at 100 kPa. The fuel injection was kept consistent with increased values for 20% and 80% pilot and main injections. The initial particulate size and concentration decreased due to the high injection pressure and low EGR supply. Figure 5.16 depicts the total number concentration acquired along the length of the ETP for both conditions and shows consistent and similar trend lines. The copper coil temperatures at this load increased to a much higher degree due to a large amount of heat absorption from the heat dissipated from the stainless steel pipe. The initial temperature from the tank is observed to be the same as with previous conditions.

The TNC for hot and cold ETP conditions are in the same order of magnitude as given in Figure 5.16, with unimportant changes along the length of the 3.5 m. It can be observed that compared to the previous experimentation of similar methodology, as the load and initial

exhaust temperatures increase, the changes in particulate characteristics reduce substantially, even while using external cooling. The temperature gradient for both the conditions is similar to a change of ±3 ºC. For hot and cold ETP, the TNC is observed to decrease by 13% and 11% respectively. With a clear picture of no changes in TNC, it cannot be concluded that the changes in NMC, AMC, NMCMD, AMCMD, NMM, and AMM are non-significant. Hence, to further examine the dynamics of PM for high load conditions, Figure 5.17 to 5.20 and Table 5.7 show the numerical and graphical representations of these parameters.

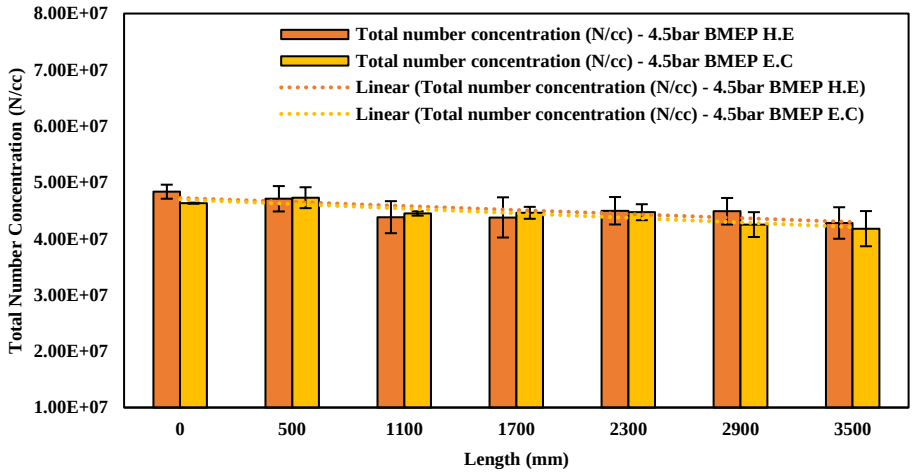


**Figure 5.15 - Total number concentration at 4.5 bar BMEP**

With the increasing length, the NMC and AMC for both conditions have shown a similar trend, where the decrease in concentrations is evident due to physical processes and factors, such as an increase in particle to particle interaction, which aids in heightening particle size and mass; particle residence on the chamber walls during particulate and gas species transport; and temperature gradient providing no effects on gas species to condense on particulates or the formation of new particulates by condensation of gas molecules.

The unimportant increase in particulate sizes is due to the NM, AM and other volatile particulate coagulation with consideration of the conceptualisation of Brownian motion inside the ETP. These variations can be further supported by particulate masses for NM and AM. Although, [125] addressed that the TNC and NMC increases with increasing lengths and decreasing temperatures, the effect on high engine loads do not show a convincing trend for PM data analysed.

**Table 5.7 - Particle mode concentration and size variations at 4.5 bar BMEP**

| **Particulate mode characterisation** | **Upstream (0 m)** | **Downstream (3.5 m)** | **Percentage (increase (+)/decrease(-))** |
|---|---|---|---|
| **Hot ETP** | | | |
| Nucleation mode concentration (NMC) | 1.83 $e^7$ | 1.47 $e^7$ | -24.6 |
| Accumulation mode concentration (AMC) | 2.45 $e^7$ | 2.25 $e^7$ | -8.8 |
| | | | |
| Nucleation mode count mean diameter (NMCMD) | 27.2 | 29.4 | 7.4 |
| Accumulation mode count mean diameter (AMCMD) | 77.9 | 79.3 | 1.85 |
| **Cold ETP** | | | |
| Nucleation mode concentration (NMC) | 1.8 $e^7$ | 1.51 $e^7$ | -18.72 |
| Accumulation mode concentration (AMC) | 2.32 $e^7$ | 2.18 $e^7$ | -2.18 |
| | | | |
| Nucleation mode count mean diameter (NMCMD) | 25.2 | 27.44 | 8.2 |
| Accumulation mode count mean diameter (AMCMD) | 78.7 | 79.9 | 1.45 |

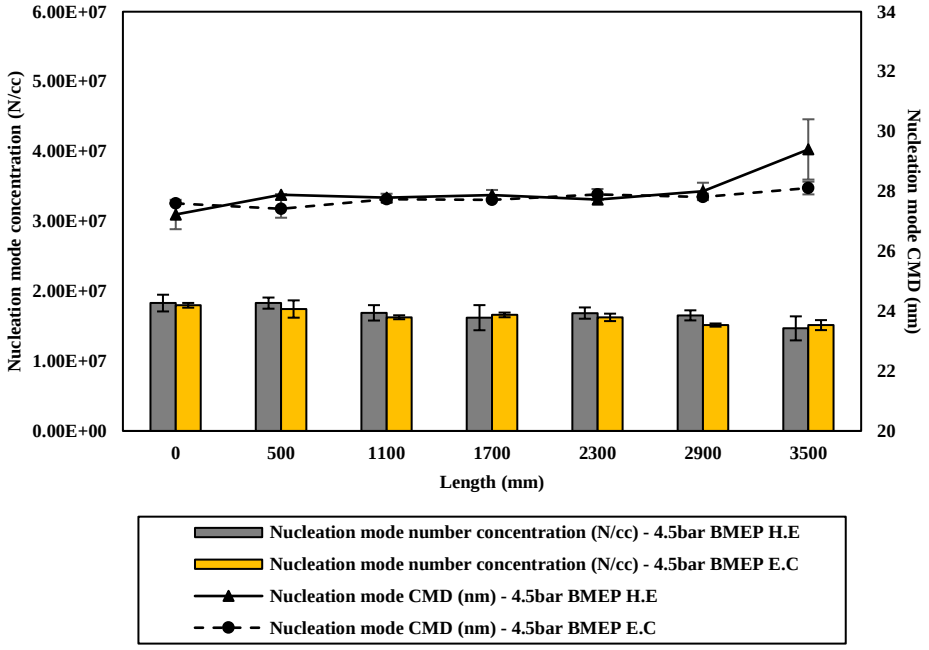


**Figure 5.16 - Nucleation mode concentration and size at 4.5 bar BMEP**

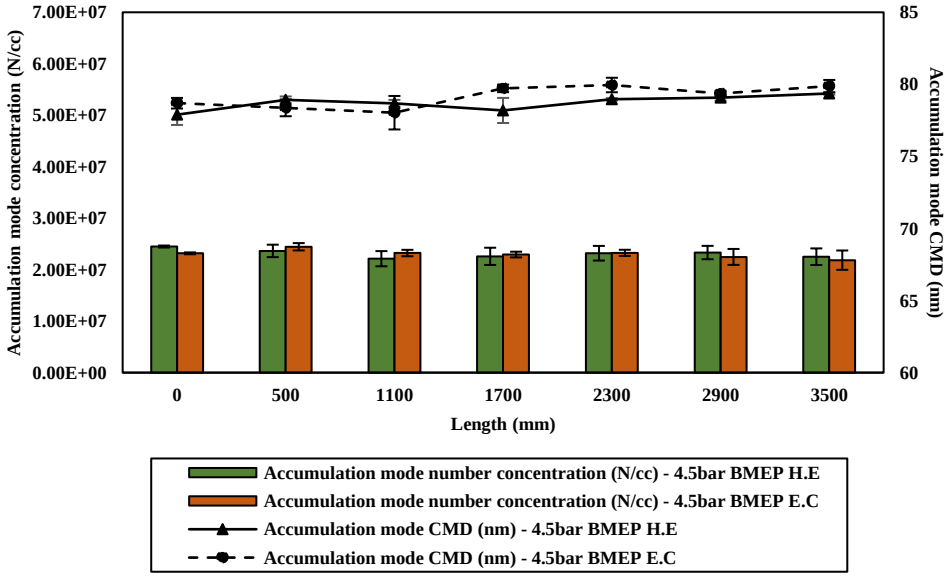


**Figure 5.17 - Accumulation mode concentration and size at 4.5 bar BMEP**

Particle mass along the length of the ETP, shows a decrease in both NMM and AMM for hot and cold ETP conditions. For the hot ETP condition, the NMM shows a reduction by 23% and the AMM by 4.63%. On the other hand, for the cold ETP, a 16% decrease in the particulate mass of the NM is observed with a non-significant decrease of 2.66% in the AMM. Particles undergo desorption and fracture at high temperatures, as a particulate is comprised of a combination of VOFs, THC, ash, sulphates and other gas species. At higher temperatures and for every regulated and unregulated gas species the pseudocritical temperatures differ, hence the gas phase transitions impact the change in particle masses and concentrations along the length even with different temperatures. The amount of particle mass reduced for NMM and AMM, does not affect the particle size and concentrations massively, hence, the consideration and justification of mass contribution at elevated exhaust temperatures cannot be determined based on experimental investigations completely.

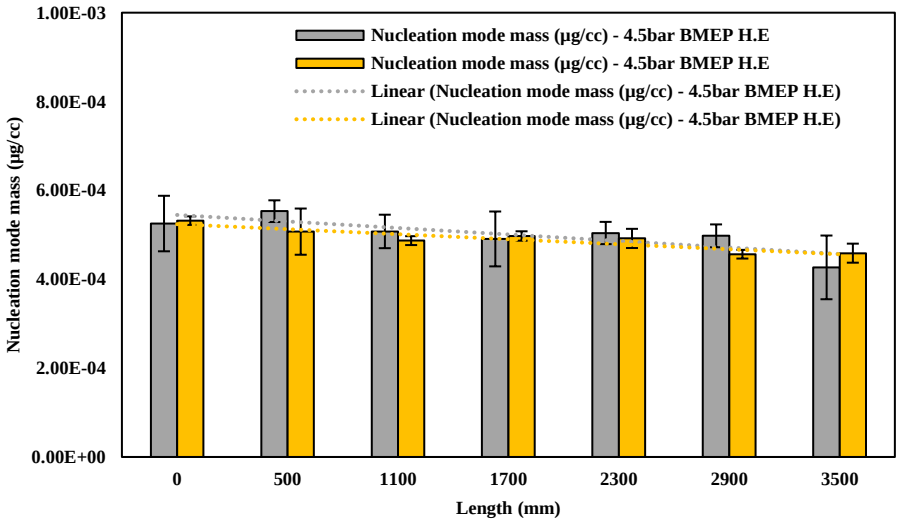


**Figure 5.18 -Nucleation mode mass at 4.5 bar BMEP**

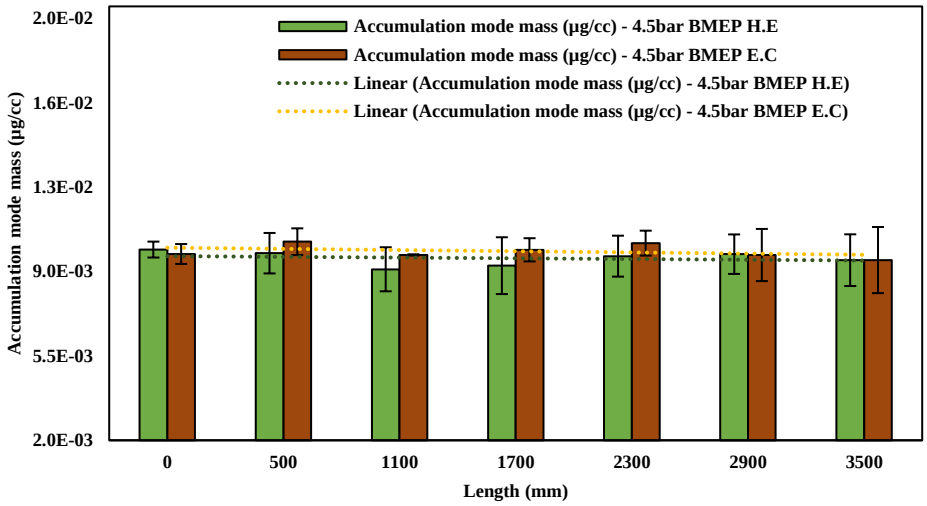


**Figure 5.19 - Accumulation mode mass at 4.5 bar BMEP**

## 5.7 Validation of exhaust cooled particulate matter evolution using the particle growth model (PGM)

The developed numerical model, the particle growth model (PGM), introduced previously in Chapter 3, is applied to the empirical case study carried out in this chapter. To investigate the particulate behaviour and the robustness of the numerical model, the following simulations are carried out based on the initial boundary conditions acquired from the experimental technique.

Since the exhaust cooling effect on intermediate (3.0 bar BMEP) and high (4.5 bar BMEP) engine load was not observed to be significant in terms of temperature profile, it is initially assumed that the behaviour of the particulate matter (PM) during simulations will depict a similar trend line. However, for low (1.4 bar BMEP) engine load the ETP cooling has shown contrasting results in consideration to the baseline experimentation. Including the boundary conditions of three engine load conditions into the model provided the estimated nucleation rates, particle size distribution and the individual particle mode characteristics for

an ETP length of 3.5 metres. The initial temperature condition entered in the model is based on the experimental data acquisition assisted by the total temperature drop along the length of the ETP, as mentioned below in the equation.

$$T_{length} = T_{initial} - \Delta T \quad (70)$$

### 5.7.1 Comparison of PM emissions at 1.4 bar BMEP

The changes observed in the experimental investigation for ETP cooling are noted above, but to perform a validation in establishing the robustness of these PM emission results is also imperative. For a low engine load condition with an exhaust temperature below 300 ºC, the PM behaviour is marginally different between a cooled and non-cooled ETP.

The model-based validation is performed for a cooled ETP, where the coagulation and condensation of particulates is arguable. The empirical changes in the cooled ETP are significant in the total number concentration, with minor variations in the nucleation and accumulation mode concentrations. The temperature profile exhibited in Figures 5.21 and 5.22 show a monotonous and continual reduction in temperature from 0 to 3.5 metres. As the temperature reduction is observed, the particulate matter behaviour for size and concentration show a similar trend line in nucleation and accumulation modes. Based on the numerical model, the calculated mean diameter of the nucleation and accumulation mode particles are 25.8 nm and 73 nm respectively. Whereas, the empirical data acquired show 23.0 nm and 68.5 nm for nucleation and accumulation modes. These 11% and 6% particle size differences and calculative comparisons can be supported with the instrumentation error percentages. Factors that affect the changes in particulate sizes can mainly incline towards human error,

instrumentation sensitivity and the experimental set-up environment. Figures 5.21 and 5.22 show the particle size comparisons for simulation and experimentation, where both follow a similar increasing trend, with the increase in the length of the ETP.

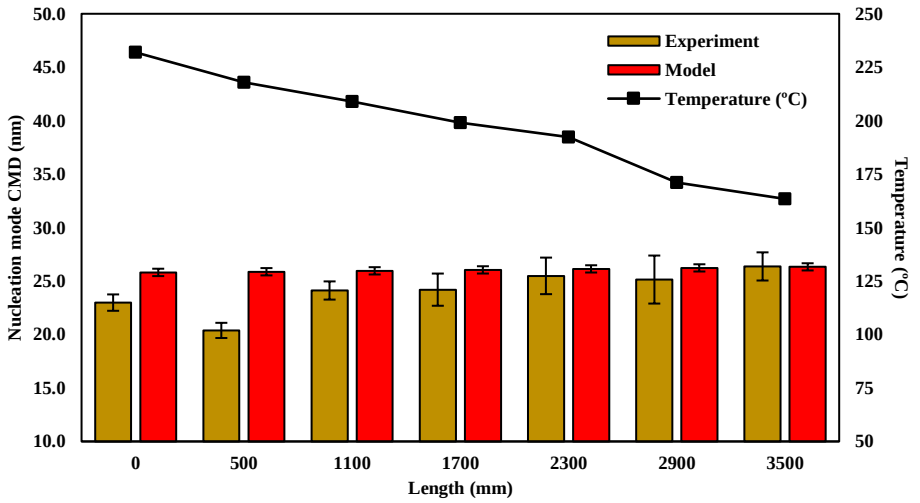


**Figure 5.20 - Nucleation mode CMD at 1.4 bar BMEP**

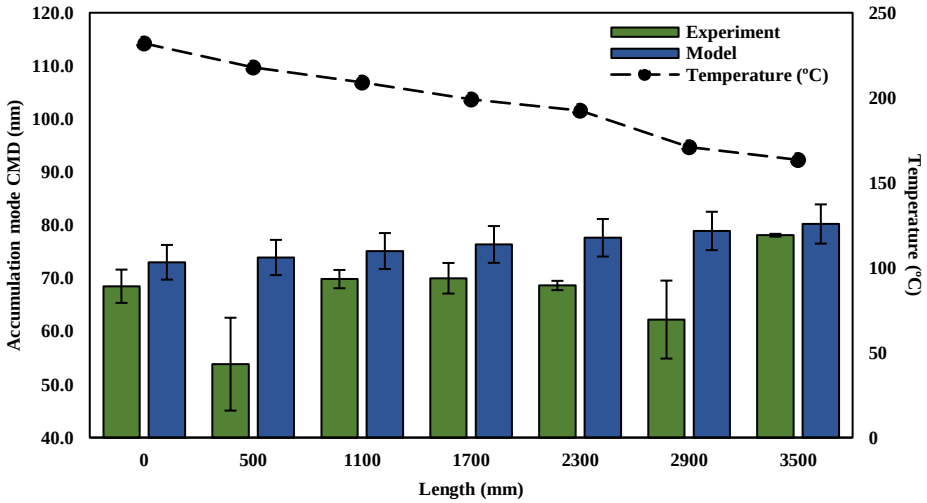


**Figure 5.21 - Accumulation mode CMD at 1.4 bar BMEP**

Similarly, NMC and AMC for simulation and experimentation conditions in Figures 5.23 and 5.24 have a fall in the same logarithmic scale from $1e^7$ to $1e^8$ with a difference of -9.6% and 5.7% from 0 to 3.5 metres. Particle losses under this condition are observed more in the case of NMC, and a small gain is seen in AMC. Particles < 50 nm (nucleation mode), have shown a coalescence effect in the formation of particles > 50 nm (accumulation mode), where the mode transition is dominant from nucleation to accumulation mode. This can be understood in detail based on the size spectral densities for both numerical and experimental results in Figures 5.25 and 5.26.

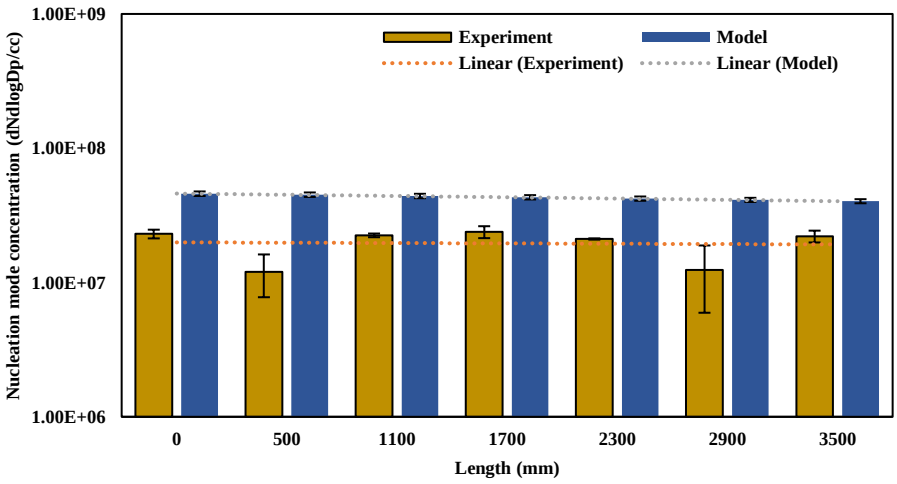


**Figure 5.22 - Nucleation mode concentration at 1.4 bar BMEP**

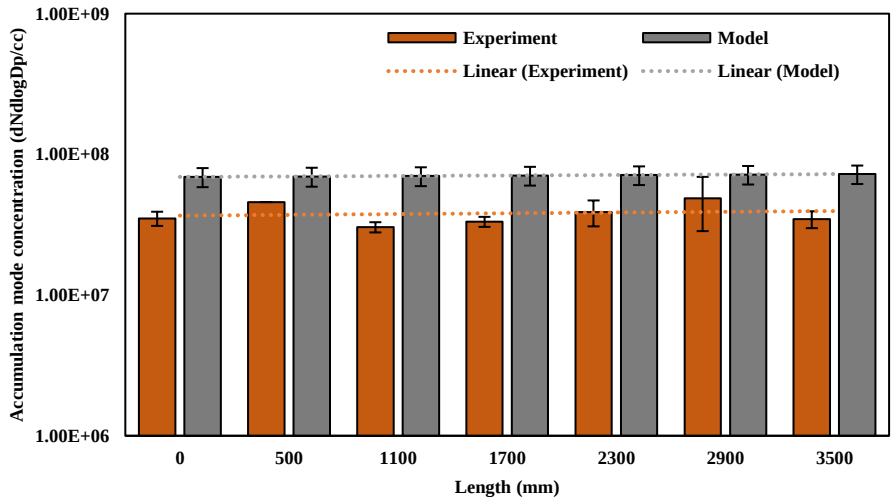


**Figure 5.23 - Accumulation mode concentration at 1.4 bar BMEP**

Size spectral densities provide a clear picture of the incremental changes in total particle concentration based on its size spectrum from 4.87 nm to 1000 nm. Decrementing changes from 4.87 nm to 48.7 nm are observed with higher variability in particles < 10 nm as they ought to have a higher probability of particulate to particulate coagulation and have higher residence time for a particle loss. This shows a significant decrease in particulate concentration at nucleation modes. The changes from particles > 50 nm to < 200 nm have shown incrementing changes, where the particulate to particulate coagulation between nucleation and accumulation particles increases as the particles are travelling towards the end of the ETP. These changes can be studied in detail based on the changes in size and concentration of individual modes.

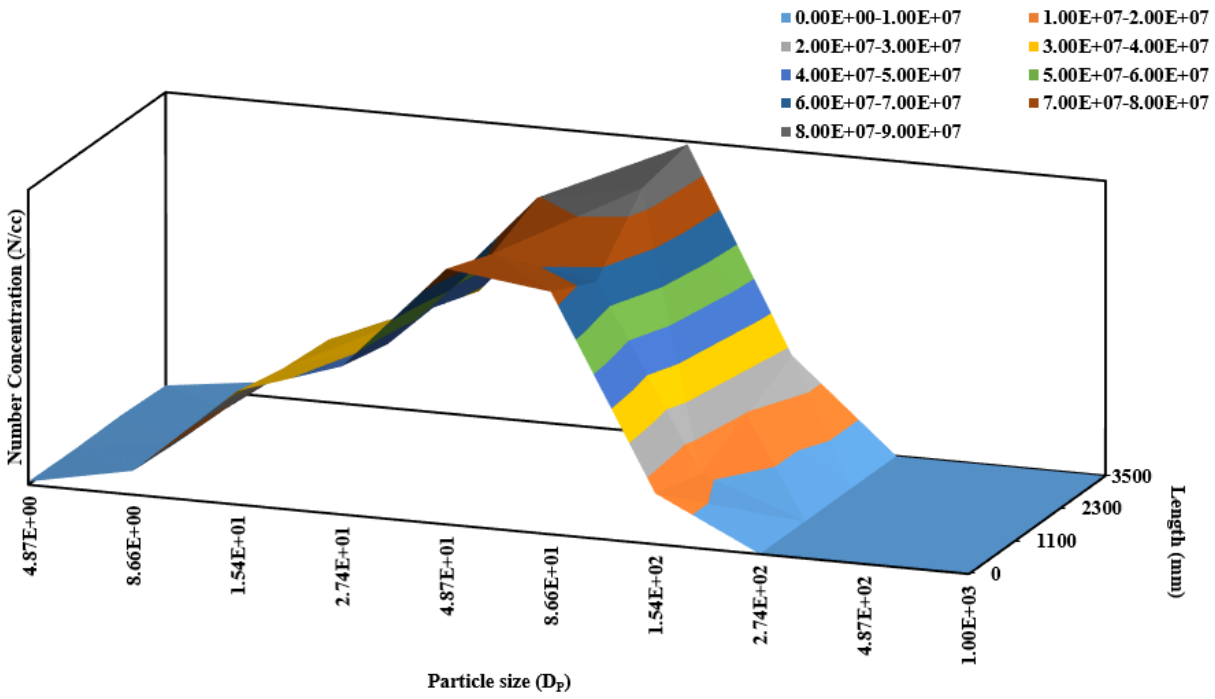


**Figure 5.24 – Experimental size spectral density at 1.4 bar BMEP**

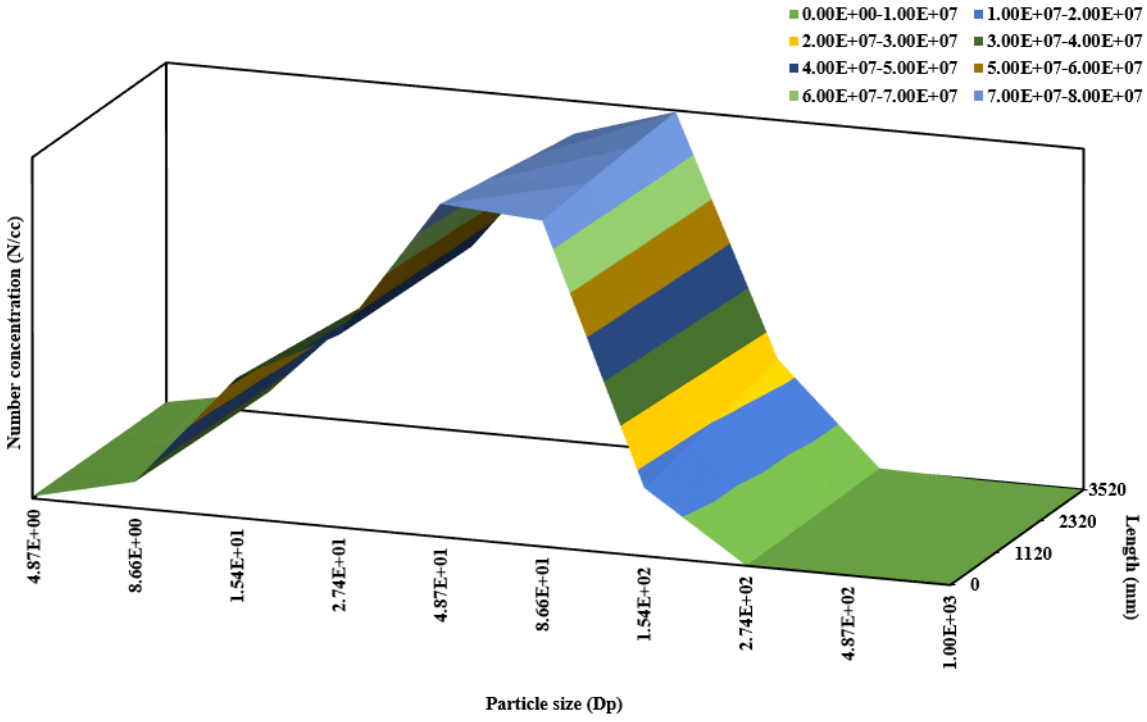


**Figure 5.25 - Simulation size spectral density at 1.4 bar BMEP**

### 5.7.2 Comparison of PM emissions at 3.0 bar BMEP

The initial exhaust temperature at the intermediate engine load increased by approximately 30 ºC compared to low engine load of 1.4 bar BMEP, with a similar decreasing trend line from 309 ºC to 219 ºC. The subsequent changes in NMCMD, AMCMD, NMC and AMC are shown from Figures 5.27 to 5.30.

Inputting the initial boundary conditions where the alteration in the model was done for lambda, size spectral concentration distribution, and condensation factor and temperature difference. The NMCMD for the simulation and experimental results is observed to have a difference of 6.6% where the initial model mean diameter is 24.7 nm and 25.2 nm for the experimental mean diameter. Both the cases have shown an overall increment in the size, 8.1%, for the experimental and 1.6% for the numerical case. Similar to the previous low engine load case, the number concentration for the numerical simulation showed an approximate 10% loss for nucleation mode concentration and an approximately 6% gain in the accumulation mode concentration. The losses are comparable to the experimental results at the same engine loads, as it is expected the nucleation mode particles will undergo physical processes of increase in surface areas and bonding with other gas and particulate emissions. Due to the Brownian motion of particulates in the confined space of the tube, the residence of particles on chamber walls also has potential. These changes can also be well defined and understood based on the analysis of the size spectral densities of the experimental and numerical simulation cases shown in Figure 5.31 and 5.32.

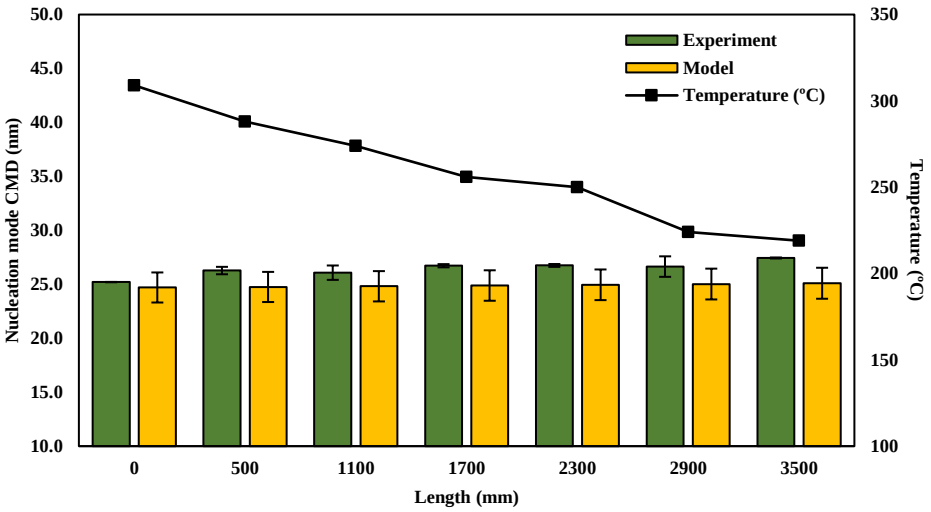


**Figure 5.26 - Nucleation mode CMD at 3.0 bar BMEP**

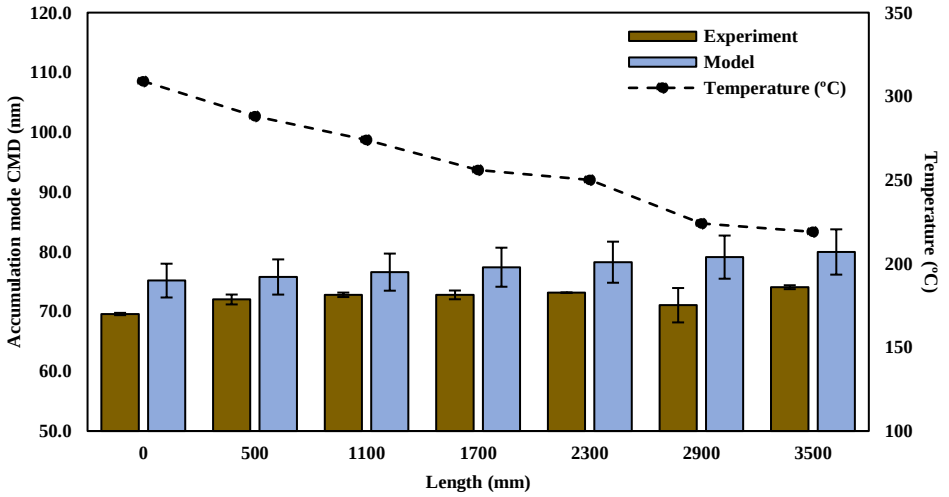


**Figure 5.27 – Accumulation mode CMD at 3.0 bar BMEP**

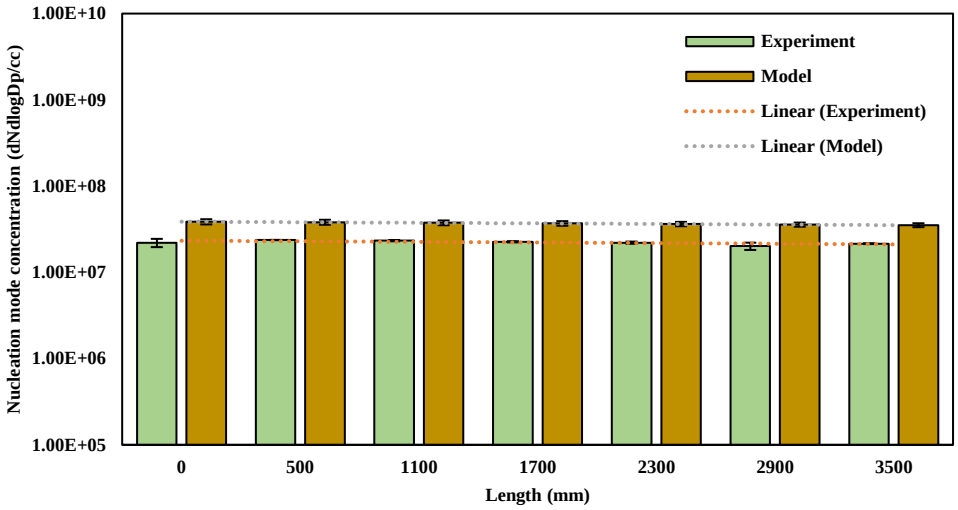


**Figure 5.28- Nucleation mode concentration at 3.0 bar BMEP**

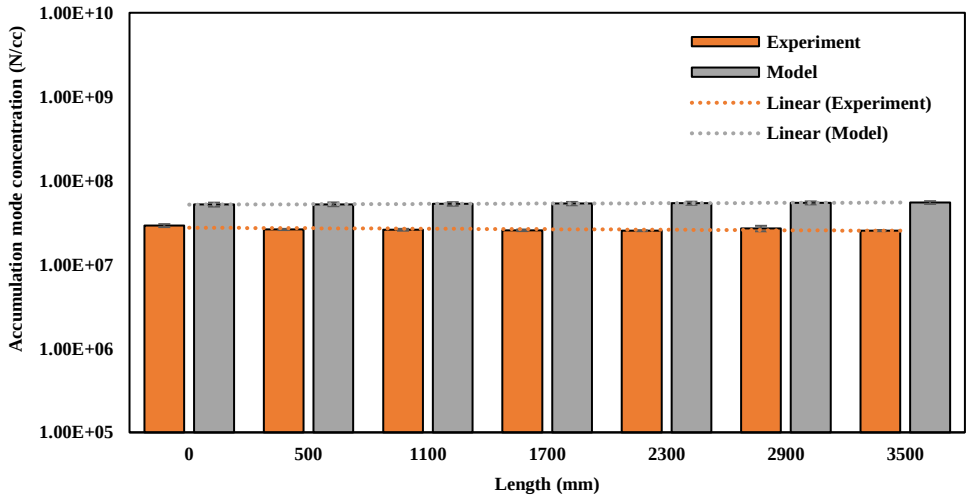


**Figure 5.29- Accumulation mode concentration at 3.0 bar BMEP**

The size spectral densities for numerical and experimental results show more dominant variations for particulate sizes > 50 nm along the length of the ETP. Particle sizes from 56.2 nm to 177.8 nm show substantial changes as the concentration and size increases with the increase in length where the peak concentration change is observed between 100 nm to 200 nm. The larger particulate sizes have shown a higher potential for surrounding particles to adsorb on

their surface, increasing the overall particle surface area and concentration between these particle size ranges. With higher exhaust temperatures taken into consideration, the gaseous emission condensation does not contribute a significant percentage to the particle concentration and size. Hence, the significance of particulate to particulate physical processes are more prevalent. Also, the nucleation mode particulates < 50 nm increase in size with the concrescence of multiple size nanoparticles ranging between 4.87 nm and 50 nm.

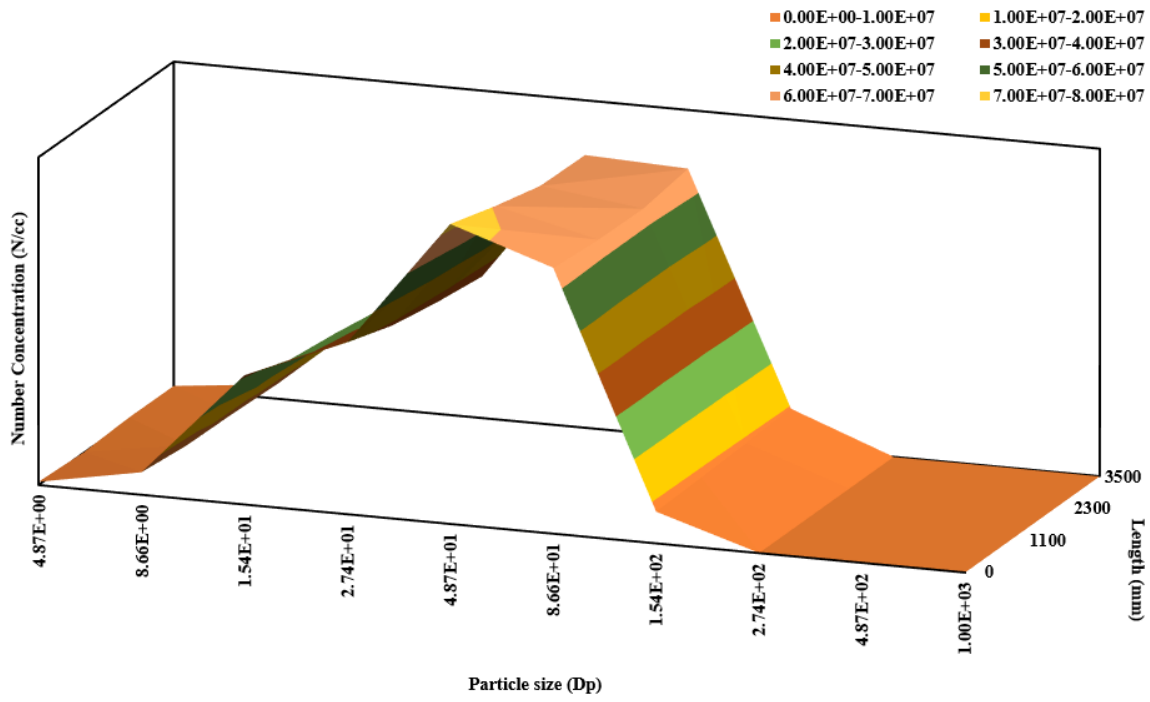


**Figure 5.30 - Experimental PSD at 3.0 bar BMEP**

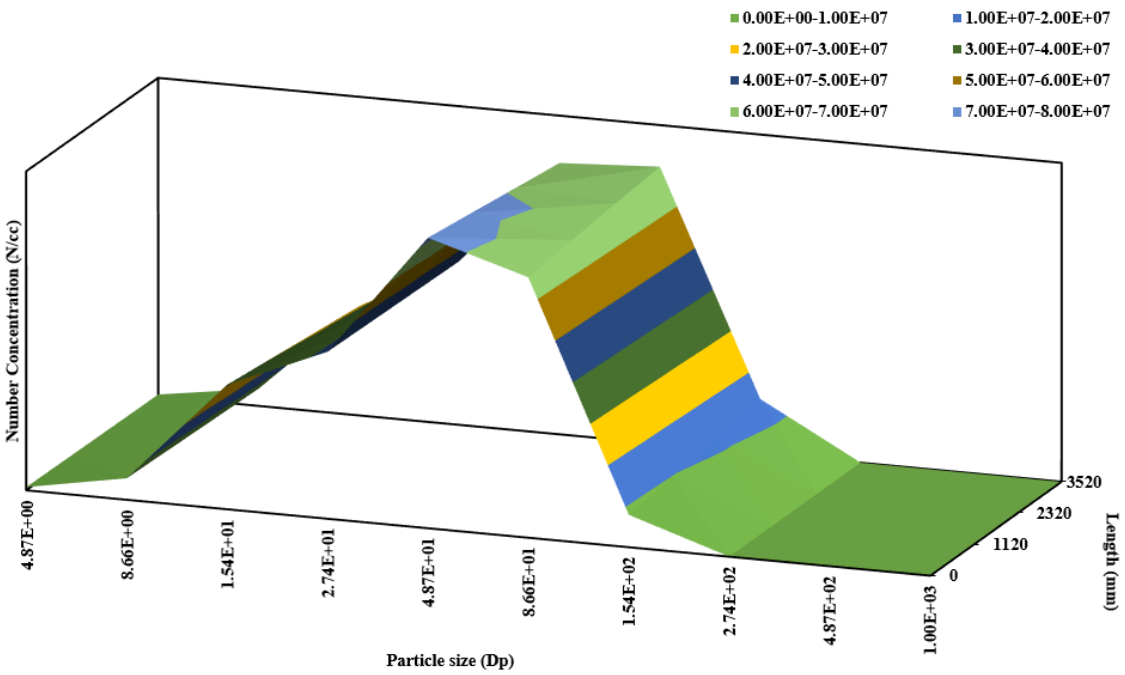


**Figure 5.31 - Simulation PSD at 3.0 bar BMEP**

### 5.7.3 Comparison of PM emissions at 4.5 bar BMEP

For a high engine load of 4.5 bar BMEP, particulate behaviour does not show a substantial change as the flow rate of the exhaust gas is higher and hence leading to a small period of observable changes. Figures 5.33 to 5.36 depict the variations and comparisons between simulation and experimental PM characteristics.

The initial NMCMD for experimental and numerical analysis have shown an approximate 10% difference between them at 27.6 nm (experiment) and 25.1 nm (simulation). Whereas, for AMCMD the particle size differs by less than 1%. The NMC and AMC for the experiment and simulation have shown the same decreasing trend and reside in the same logarithmic scale between 1.0E+07 to 1.0E+08. The high concentration observed in the case of the numerical simulations is due to its calculative method used in the model, and provides a higher number concentration than the experimentally acquired data. These differences can be

neglected if there are overall important changes observed in the PM characteristics in terms of mean diameter size.

In theory and in the model, the particle size will increase along the length of the ETP depending on multiple internal and external factors. The model considers the initial boundary condition as a steady flow through the ETP; whereas based on the experimentation, the particle size distributions change with high or low variability depending on their engine parameters. Although the engine condition during experimentation is kept at a steady state, there are minute variations during an engine's operation and instrumentation sensitivities can result in a cascade of changes in the particulate matter in real-time measurements.

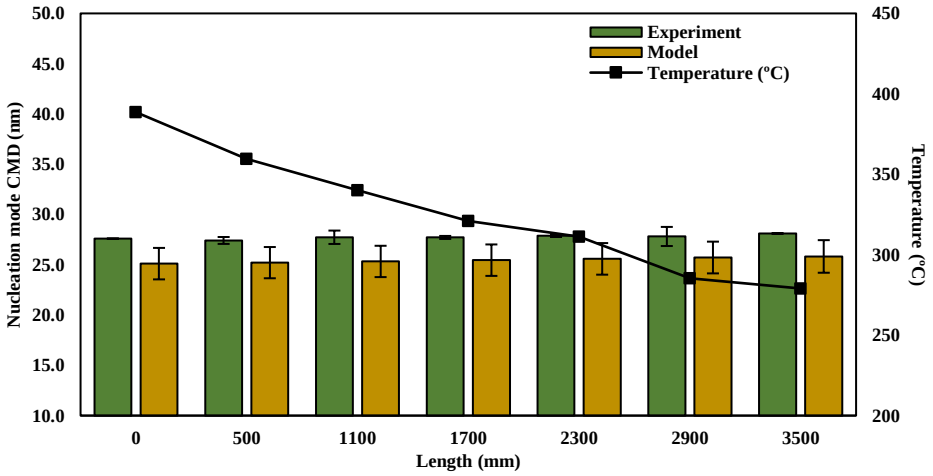


**Figure 5.32 - Nucleation mode CMD at 4.5 bar BMEP**

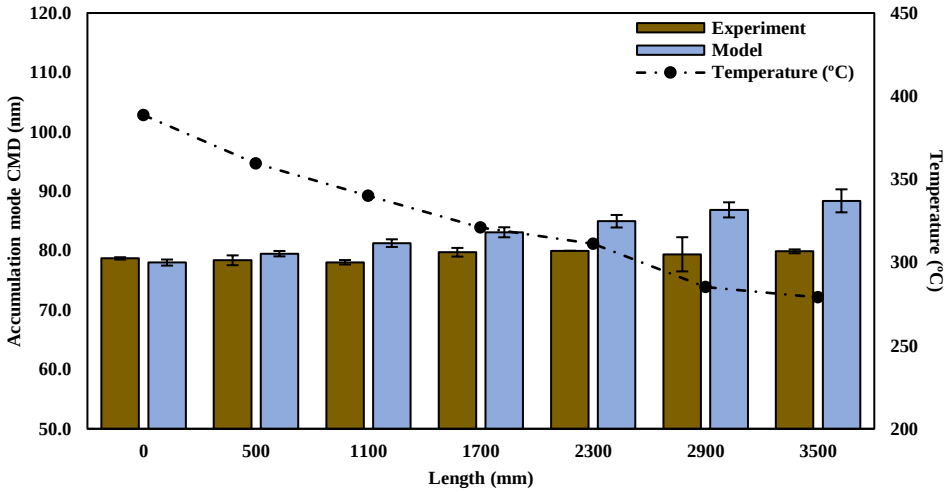


**Figure 5.33 - Accumulation mode CMD at 4.5 bar BMEP**

The number concentrations for nucleation mode have shown a linear reduction, with a decrease of 18.7% for experimental and 19.8% for simulation analysis. This decrease is evident due to only particulate to particulate interaction along the length of the ETP. Due to high exhaust temperatures inside the ETP, the nucleation of water and sulphuric acid does not contribute to the overall particle formation. The physical process of particle formation from gaseous emissions can only be achieved when the temperature of gas condensation is below its critical temperature. The overall size spectral variations can be understood in detail from Figures 5.37 and 5.38.

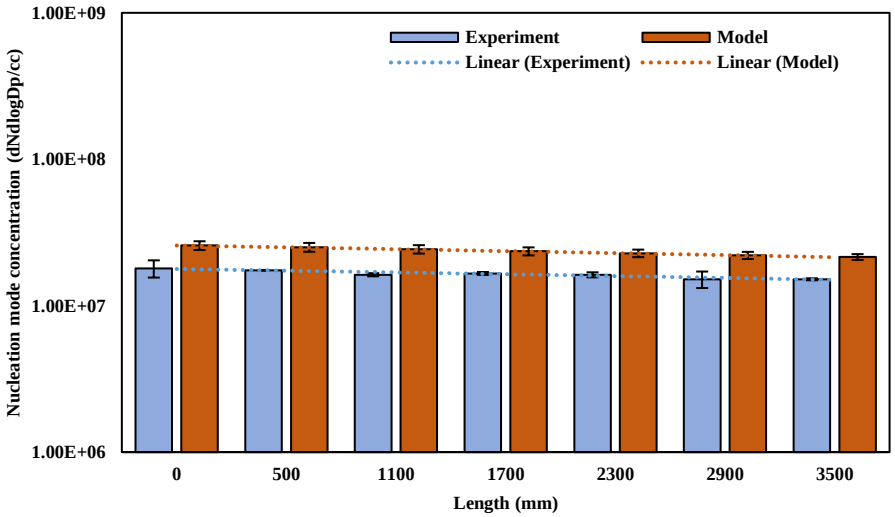


**Figure 5.34 - Nucleation mode concentration at 4.5 bar BMEP**

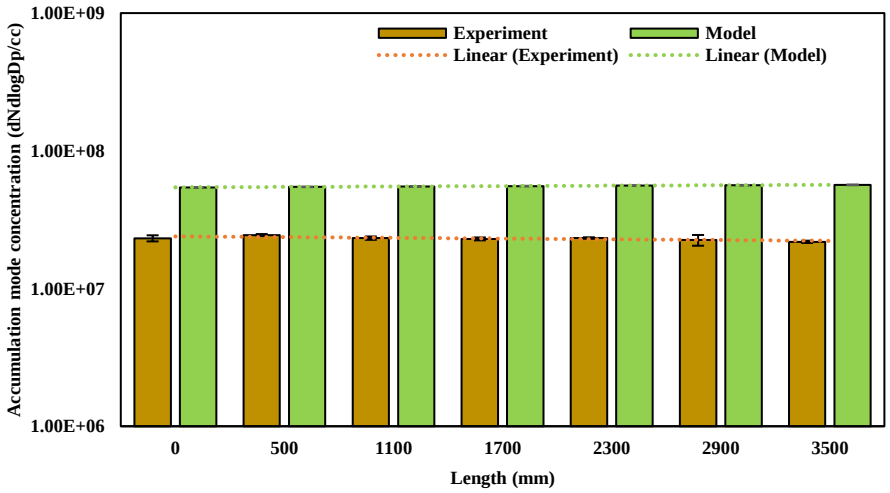


**Figure 5.35 - Accumulation mode concentration at 4.5 bar BMEP**

The size spectral densities of the experimental and numerical analysis have shown a comparable result; where the concentration changes with increasing lengths, and larger particle to particle interaction is observed. Particle sizes between 4.87 nm to 48.7 nm show minor losses which are compensated with particle sizes > 60 nm. The concentration gain for particles between 50 nm to 200 nm is more dominant, where the overall concentration change between these size spectrums is about 95% at its peak. These changes can be supported based on the

accumulation mode CMD changes from 0 to 3.5 metres. Also, the nucleation concentration decrease of about 20% for numerical and experimental results can be supported with the increase in particle number concentration for the size spectrum of 50nm to 1000nm.

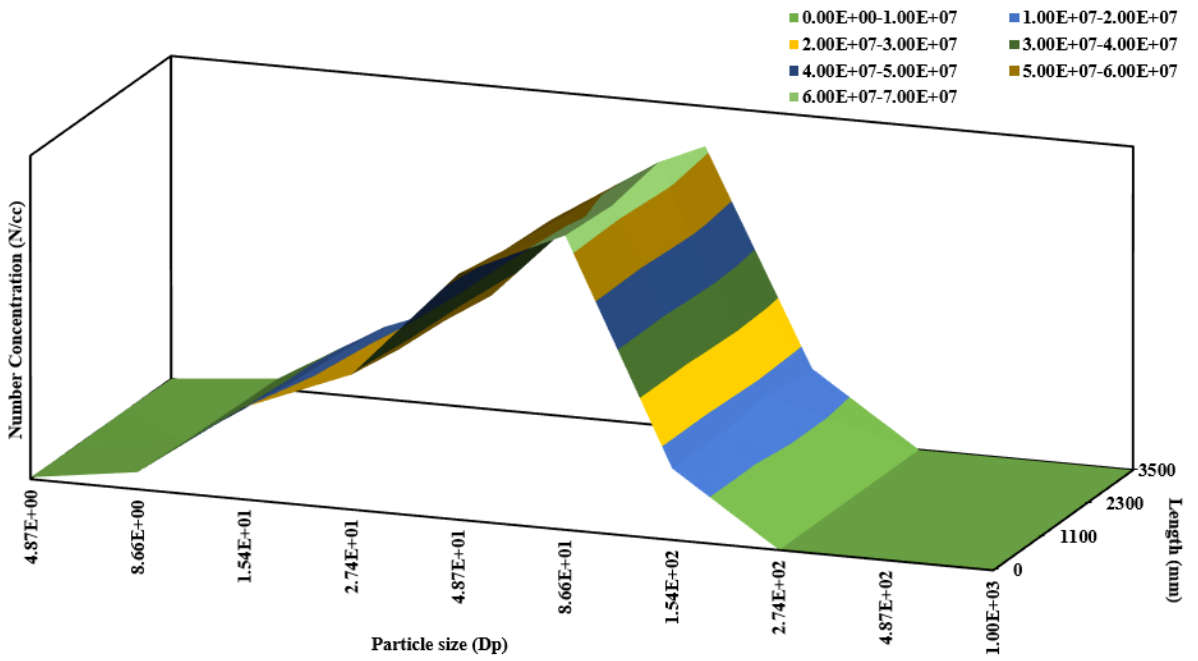


**Figure 5.36 - Experimental size spectral density at 4.5 bar BMEP**

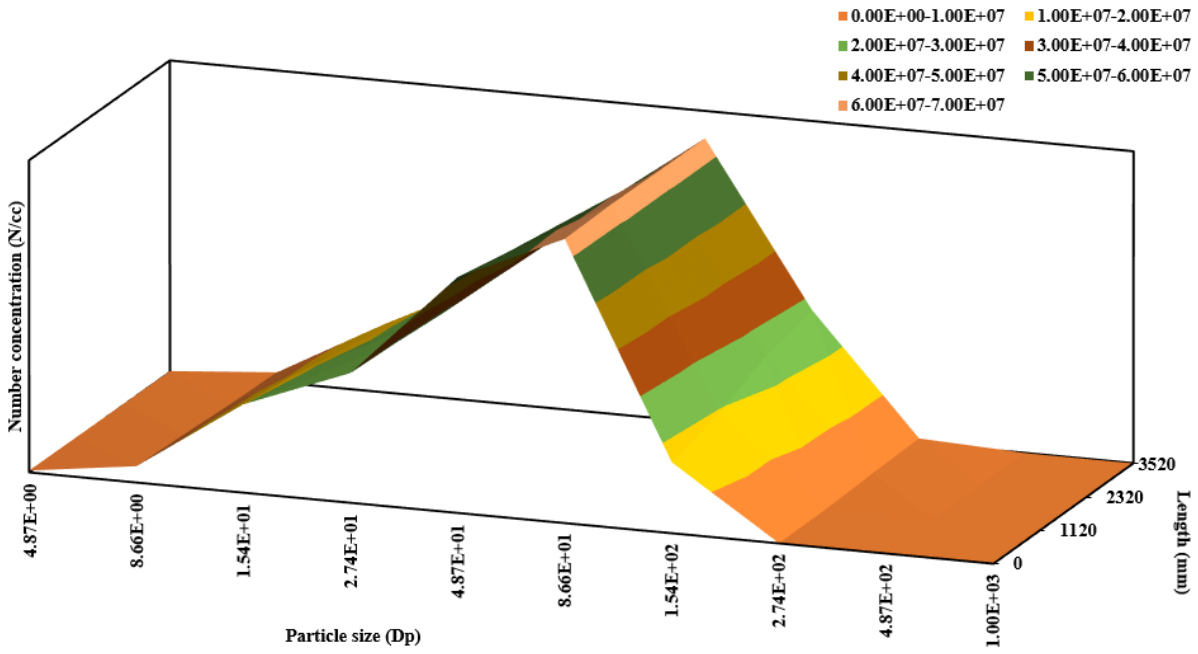


**Figure 5.37 - Modelling size spectral density at 4.5 bar BMEP**

## 5.8 Summary

The research work done in this chapter deals with the empirical and numerical study of particulate behaviour in an exhaust tail pipe under different engine operating conditions. The figure given below shows the trends on changes in the total number concentration of PM emissions with respect to the temperature. The study was primarily focused on the understanding of gaseous and particulate emissions' behaviour from a diesel engine exhaust at different exhaust temperatures by varying the engine operating conditions. The primary conclusions that can be noted from it are:

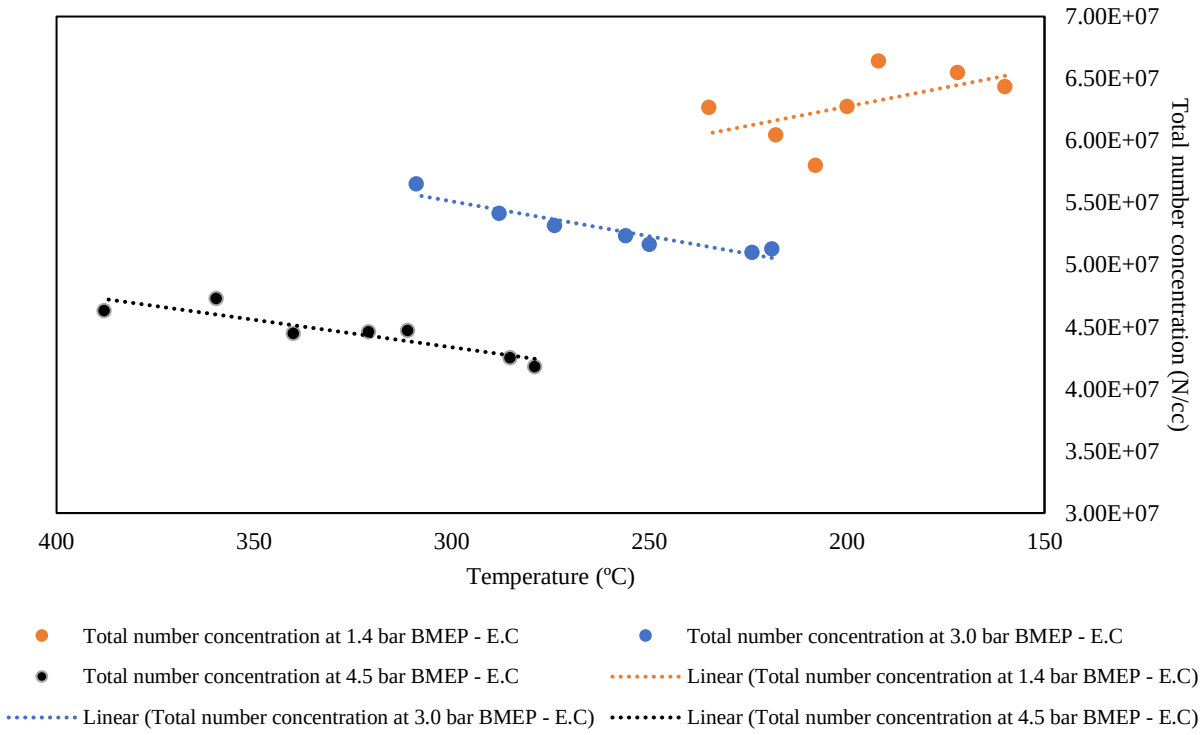


**Figure 5.38 - Temperature based particulate matter trends**

1. The exhaust tail pipe cooling using copper coil windings with variable coil pitch was successfully used as an external cooling source, employing the solution of antifreeze and ice water through the coils. Copper coils having endothermic properties help to decrease the exhaust temperature by a certain number of degrees which then depicted

the changes in particulates at low engine load conditions. The results for cooled and non-cooled exhaust tail pipes have contrasting conclusions, where the changes in particulate behaviour can be precisely depicted in low engine load conditions. These also help in showing that the temperature inside the exhaust pipe can be altered and can be used in research and commercial applications by improvising changes in the current experimental set-up.

2. The robustness, applicability and repeatability of these experiments are validated using the particle growth model (PGM) and altering the initial boundary conditions as acquired from the experimental data analysis for all three cases. The results are agreeable and applicable, and can be used for future PM characteristics' analysis. Based on the comparative analysis of the numerical and experimental data, it is important to mention the minor variability in these cases is due to the instrumentation and the sensitivity of it during the experimentation. Having said that, the results acquired from both the experimental and numerical procedures have a marginal difference of not more than 20%.

3. With the increasing engine loads and split injection strategies used in the experimentation, the changes in particulate size and concentration are independent of these factors; and the physical process and the dynamics of particulates are wholly dependent on the after-exhaust factors such as temperature, cooling coefficients, initial size spectral densities and the length of the tail pipe.

# CHAPTER 6

# DESIGN CONSIDERATIONS OF EXHAUST TAIL PIPES FOR COMPRESSION IGNITION ENGINES

The chapter provides an insight to design an exhaust system based on the particle growth model (PGM), and the following chapter 7 which represents the exhaust aftertreatment system aiding in the particle filtration and low temperature oxidation using a catalysed diesel particulate filter. The chapter bridges the particulate matter dynamics, exhaust temperatures and flow velocities to the design considerations to be made for a high efficiency aftertreatment system for oxidation.

## 6.1 Introduction

Particulate matter emissions dynamics from engine out are primarily dependent on three major factors: exhaust temperature, flow velocities and gas-particulate interaction. These factors accommodate in the recognition of particle size distributions at different exhaust pipe lengths as shown in the previous chapters. These simulation and experimental investigations help in design considerations to be made for an exhaust system for the positioning of filter substrates.

Due to the important role in the design and optimisation of exhaust aftertreatment systems, the heat transfer conditions in the automotive exhaust pipes are being studied in depth [8, 126, 127]. The complex exhaust flow geometry and the flow conditions complicate the question of the estimation of particulate matter emissions characteristics and the influence of physical factors on them. The positioning of a particulate filter in an exhaust system is investigated using previously established PGM and the temperature variations at different

positions of exhaust tailpipe. In this context, due to the consistent failures of diesel particulate filter substrates due to soot loading and high backpressures, the design of exhaust systems is critically important.

## 6.2 Research objectives

The objectives stated are used to investigate the exhaust temperatures and the resulting particulate characteristics using simulation techniques. Investigating the particulate matter emissions dynamics for 250mm fixed length of exhaust tail pipe (turbocharger to aftertreatment system inlet), also used for experimentation further in this thesis, before the particulate filter substrate under the influence of variant engine operating conditions and flow velocities. The particulate size and concentration for nucleation and accumulation modes are thoroughly discussed to provide further optimisations and use of catalysts in particulate filter substrates.

## 6.3 Methodology

The simulation carried out for steady state engine conditions output, is done from 3.0 bar to 4.5 bar BMEP primarily to establish a relation of exhaust temperatures and the placement of diesel aftertreatment system be fitted from a fixed length. The particulate filter is selected at 0.25 metres length from the turbocharger and PM characteristics and other physical entities are acquired using the boundary conditions from the experimental data. Table 6.1 below shows the boundary conditions that are used in the simulation of PM dynamics.

The simulation considers the initial parameters like exhaust temperatures, geometrical specifications of the exhaust pipe and the instrumentation acquired particulate matter characteristics, with certain gaseous emissions involved in the model for accurate formulation.

**Table 6.1 - Boundary conditions for exhaust tailpipe conditions**

| **Parameters** | **Values** | |
|---|---|---|
| | **1** | **2** |
| Engine load | 3.0 bar BMEP | 4.5 bar BMEP |
| Exhaust temperature | 312 ºC | 388 ºC |
| Lambda | 2.8 | 1.75 |
| Exhaust pressure (absolute) | 1.01e5 Pa | 1.01e5 Pa |
| Length of the exhaust pipe | 0.25 metres | 0.25 metres |
| Diameter of the exhaust pipe | 0.065 m | |
| Particle size range | 4.87nm to 1000 nm | |
| PM size partitions | 38 | |
| Minimum partition size of PM | 0.688 | |
| Maximum partition size of PM | 3.0 | |
| PM Coagulation coefficient | 1.01 | |
| Dilution ratio | 10 | |

## 6.4 Results

The results acquired from the simulation of PGM are shown based on two primary factors, exhaust gas temperatures, and length of the tail pipe. It is imperative to consider these factors as they aid in the optimisation and management of an exhaust tail pipe aftertreatment system. Hence, the engine exhaust data at 3.0 bar BMEP and 4.5 bar BMEP are considered in these cases. The data is extracted for the initial boundary conditions for PGM, from PM characteristics of hot exhaust from Chapter 5.

The results are shown from Figure 6.1 to 6.4 depicting the changes in PM characteristics at 0.25m length exhaust pipe, showing nucleation and accumulation mode characteristics and particle size distributions for an exhaust pipe length of 0.25m. Due to the changes in the engine load conditions, the exhaust temperatures vary significantly in comparison.

From figure 6.1 and 6.2 the logarithmic particle size distributions show minor changes with reducing concentrations. These changes are negligible for the particulate characteristics with respect to the heat loss of approximately 15ºC and 10ºC in exhaust temperature at 3.0 bar BMEP and 4.5 bar BMEP, respectively. Also, in figure 6.3 and 6.4, the changes in particulate size variation with reference to the changes in temperature are shown. It is evident that the particulate size is not dramatically affected due to the changes in temperature gradient for a length of 0.25m exhaust pipe. These effects cannot be seen for both nucleation and accumulation mode PM size.

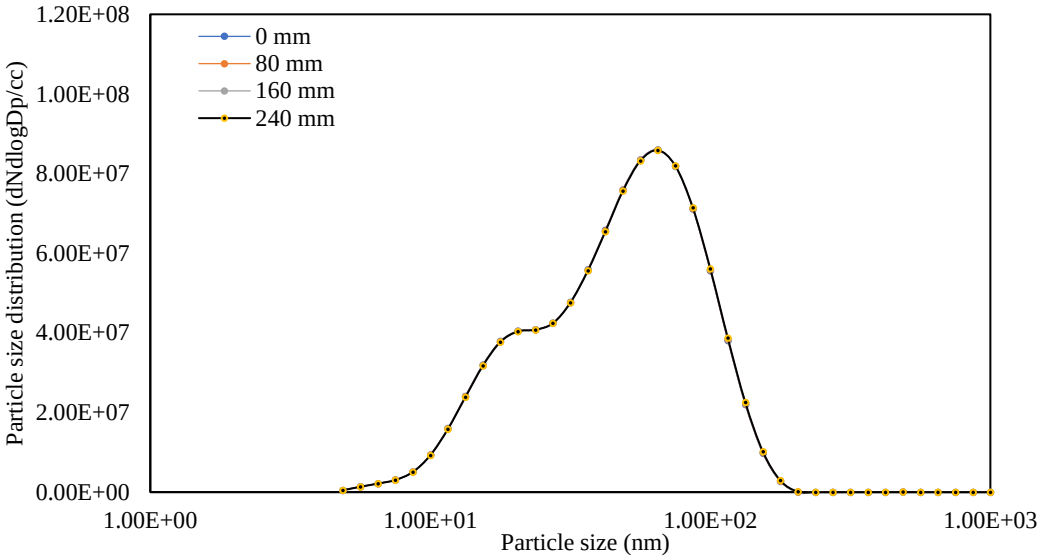


**Figure 6.1 - Particle size distributions at 3.0 bar BMEP**

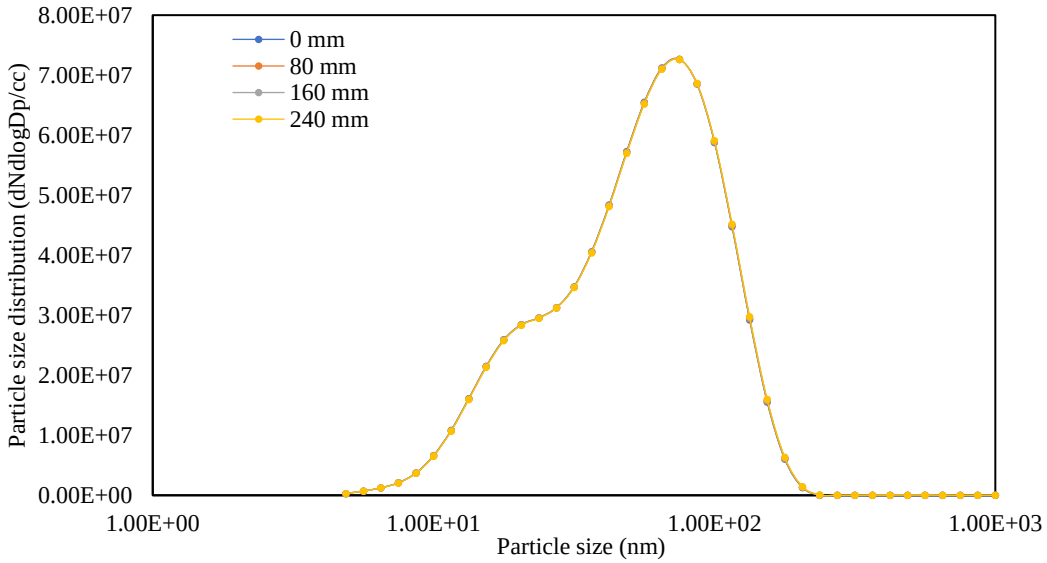


**Figure 6.2 - Particle size distributions at 4.5 bar BMEP**

The particle size distributions have depicted no significant changes in the concentrations as shown in the above figure. Due to the flow velocities, high exhaust temperature and short distance for PM transiting from 0.0m to 0.25m, the vapour condensation, aggregation of PM and residence of PM does not take place. The specific PM mode changes;

nucleation and accumulation modes, also have no substantial effects on the characteristics as the variations are observed to be less than 1%.

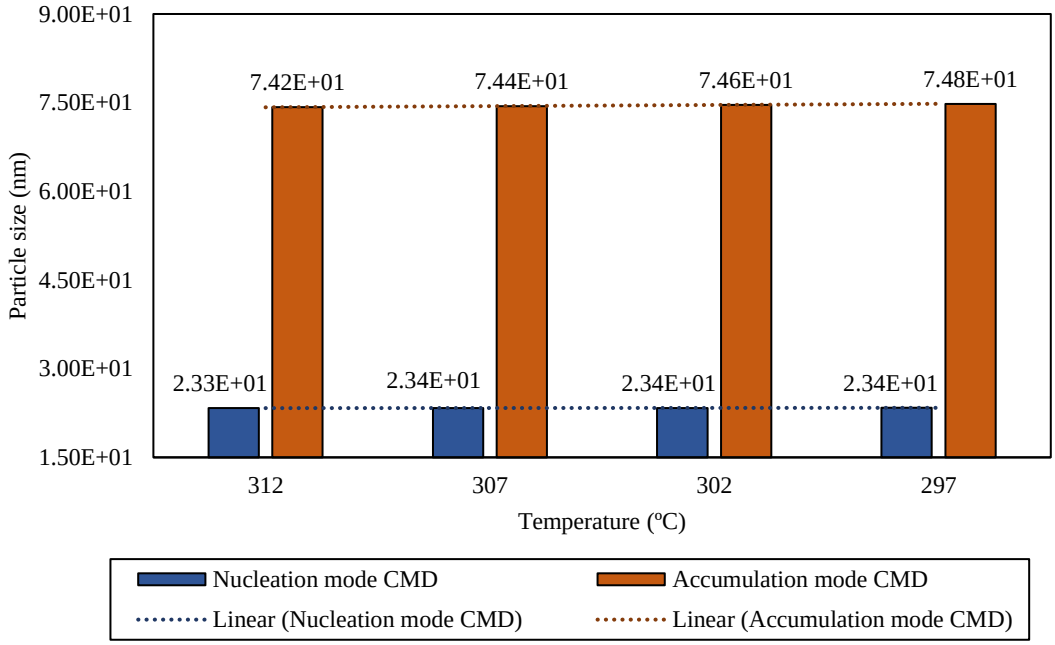


**Figure 6.3 - Particulate mode characteristics at 3.0 bar BMEP**

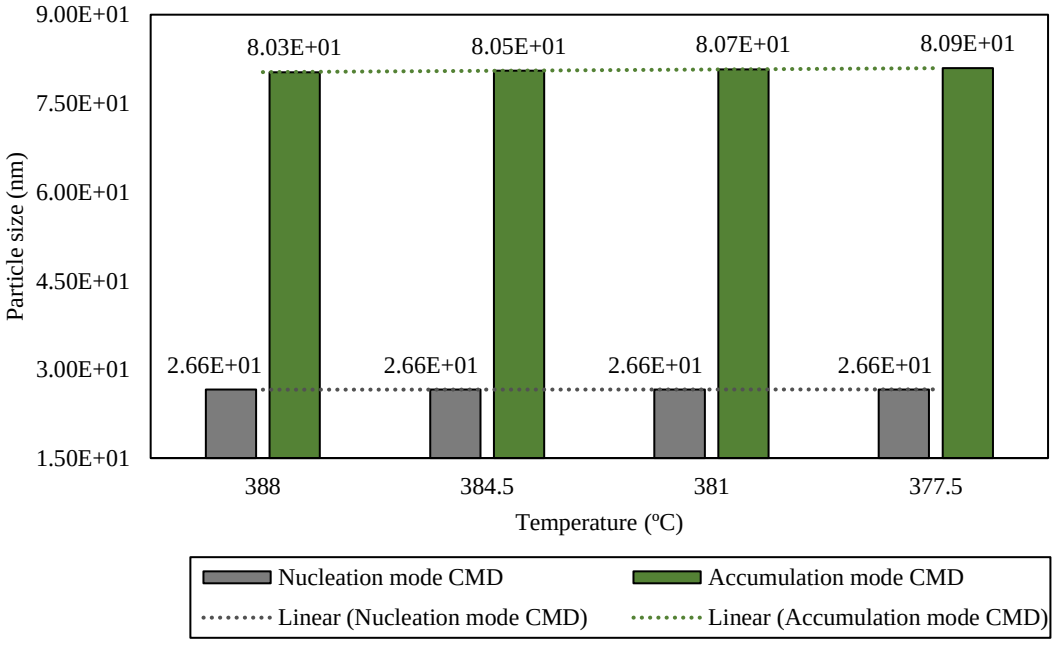


**Figure 6.4 - Particulate mode characteristics at 4.5 bar BMEP**

Since the heat loss decreases with the increasing engine loads, it is imperative that the engine operations should be progressed to high engine loads which will increase the exhaust temperatures and balance the heat losses to minimal within the length of 0.25m. But, it is also important to consider the effects of high engine loads that can affect the engine performance as well if not balanced appropriately.

## 6.5 Summary

It is observed from the recent simulation findings, that the changes in particulate characteristics are not significant in terms of particle size and concentration, with respect to the exhaust temperatures and fixed length of the exhaust pipe.

The simulation results have shown that the changes in particulate size for nucleation and accumulation mode lie between 20 to 30nm and 65 to 75nm, respectively. As the concentrations do not change significantly, the observed variations in the particulate sizes, exhaust gas temperatures and the length of exhaust pipe are optimised to retrofit an exhaust aftertreatment system to control and regenerate the particulate matter emissions transiting towards the end of the exhaust pipe.

The selection of any exhaust system is critical for the engine performance as well since the backpressures inside the exhaust system can recoil on the engine. Impact of thermal losses also affects the performance of aftertreatment systems like DOC, DPF and SCR. The thermal losses are higher with the decrease in exhaust flow rates, engine torque and the exhaust temperature itself which are all interrelated. Ambient temperatures also effect thermal losses in these cases including the orientation of the aftertreatment system and flow rates. The aftertreatment system requires a high temperature for PM burn, hence the following

recommendations are important to be attended in to optimise and provide better performance of the DPF aftertreatment system:

1. Increasing the engine torque to increase the exhaust temperatures required for PM burn in aftertreatment systems. This method can aid in the early oxidation of trapped PM in DPF channels and have less effect on the engine performance due to increasing DPF backpressure.
2. Reducing the thermal losses by the insulation of exhaust pipes, to contain the exhaust temperature without any hindrance due to ambient conditions. Also, retrofitting the aftertreatment systems closer to the variable nozzle turbine to reduce the significant heat losses caused due to length between them.
3. Secondarily, an increase in high exhaust temperatures is aided with the help of higher in-cylinder pressure and temperatures. This arises the probability of engine performance issues during steady state or transient conditions. Hence, reducing the oxidation temperatures by using metal catalyst coating can aid in a continuous regeneration of PM trapped inside DPF channels.
4. The use of a nanofibrous morphology catalyst can aid in the PM trap better since the average PM size range from 20nm to 100nm, and this will provide a high PM trap, surface contact points with higher filtration efficiency. It is also essential that the catalyst coated requires the capability of storing oxygen radicals which help in the gas species conversions during continuous or passive regeneration. Hence, a metal catalyst from the lanthanoid series which is a commonly selected metal catalyst series for passive regeneration can be used in reducing the oxidation temperatures and rather minor increase in the exhaust temperatures will balance and add in the oxidation procedures.

# CHAPTER 7

# EXPERIMENTAL INVESTIGATION OF NANOFIBER CATALYST ON DIESEL PARTICULATE FILTER

## 7.1 Introduction

Aftertreatment systems for combustion engines are equipped to reduce, control and convert harmful gaseous and particulate matter emissions to a minimal. To do so, particulate filters are commonly equipped to every engine that utilises fossil fuels. Particulate matter (PM) emissions are trapped and oxidised using this filter substrate and an increasing concern in filter substrate breakdown failures due to clogging and required high oxidation temperatures for soot burn has motivated in performing this research addressed in the following chapter.

In the following chapter, the application and the results acquired from lab-scale and full-scale nanofiber-based catalysed diesel particulate filter (C-DPF) tests are presented, to investigate the reduction of the oxidation temperature for passive regeneration and soot removal from DPF with minimal backpressure. The effects of pressure drop and temperature on diesel particulate matter and gaseous emissions are investigated thoroughly. To achieve optimal results and establishing the proof of concept, a series of lab-scale and test-bench scale DPF tests were performed. The lab-scale tests are performed on TGA-MS providing valuable results on the effects of nanofiber catalysts on gas and particulate emissions. Investigation of the pressure drop effect and further examination of continuous passive regeneration was carried out on a light-duty CRDI diesel engine.

## 7.2 Research objective

This study performed for a diesel after-treatment system aims to investigate the effect of a non-noble metal catalyst using refined morphology and providing higher particulate to catalyst interaction and low temperature (< 550ºC) oxidation for soot burn and removal. Results acquired are for pressure drop and passive regeneration temperature, with an in-depth analysis of gaseous and particulate matter emissions for investigating filtration and conversion efficiencies of a catalysed DPF.

## 7.3 Catalyst activity testing

Lab-scale experimentation was done using thermal gravimetric analysis–mass spectrometry (TGA–MS); where the thermal degradation temperature of particulate matter is measured using a mass spectrometer. A generic TGA-MS comprises of a precise mass balance recording the instantaneous and instant mass of the sample, with a furnace equipped to increment the temperature in linearity to time, with a temperature range from 35 ºC to 700 ºC. The instrument was set up with approximately 60 mg of a sample in the required position, and the temperature was increased with a consistency of 10 ºC/minute. In addition, nitrogen ($N_2$) and oxygen ($O_2$) were supplied at 55 ml/min and 25 ml/min purge rate.

The collection of a sample of diesel soot was done from the exhaust tailpipe of the diesel engine to produce a mixture of soot and catalyst together and to investigate the oxidation regime. The catalyst-to-soot mixture was formed physically using a spatula, with subsequent homogenisation for 5 to 10 minutes. The mixture consisted of the catalyst-to-soot ratio of 95:5 and was further introduced to the sampling instrument with a consistent temperature increment of 10 ºC/min from 35 to 700 ºC in the presence of oxygen. This sample mixture depicts a highly

realistic condition since the bonding of soot to catalyst is comparatively poor. For soot combustion under non-catalysed conditions, the temperature of soot burn purely depends on its exhaust constituency, adsorbed hydrocarbon compounds, and experimental methodology. The composition of the DPM is sensitive to engine operations, hence, providing consistently collected batches of soot with unvarying properties can be difficult. It is known from previous studies [94, 128] that soot burn or oxidation usually requires temperature in the range of 500 ºC to 600 ºC; hence, a raw sample of soot is a comparative baseline to investigate the soot burn temperatures in the presence of loose contact catalyst mixed with soot.

### 7.3.1 Nanofiber catalyst reactivity

The $Pr_6O_{11}$ nanofibers were synthesized by a co-precipitation/ripening method by controlling the pH using a different KOH/citric acid mole ratio and was confirmed by SEM images. A SEM image is shown for a sample of nanofibers that was prepared using repining method in figure 7.1. Further to calcination at temperatures higher than 550 °C, the material is composed of nanometre-sized domains with distinctive diameters in the range of some 60 to 70 nm. The clearly visible lattice fringes display that the nano size domains are crystalline.

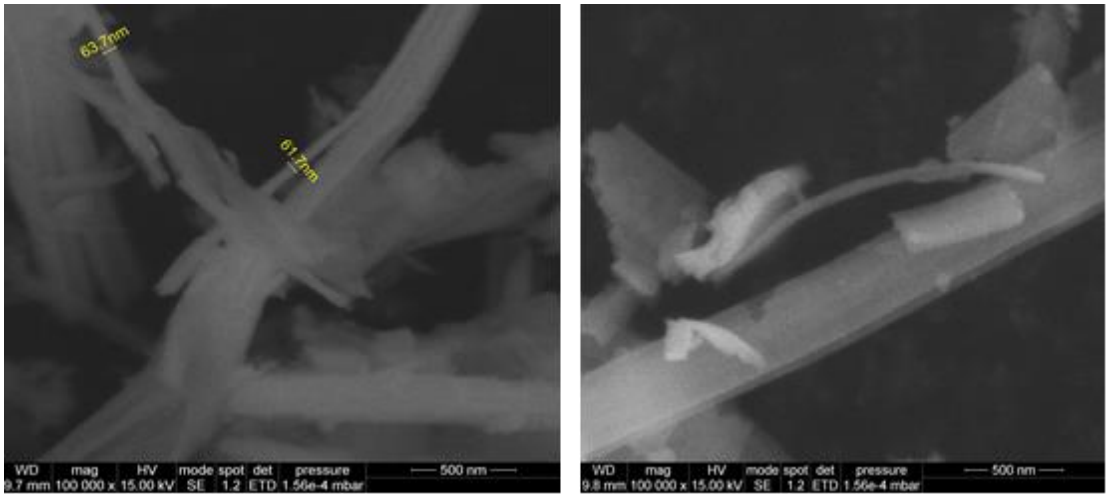


**Figure 7.1 - SEM images of praseodymium oxide nanofibers**

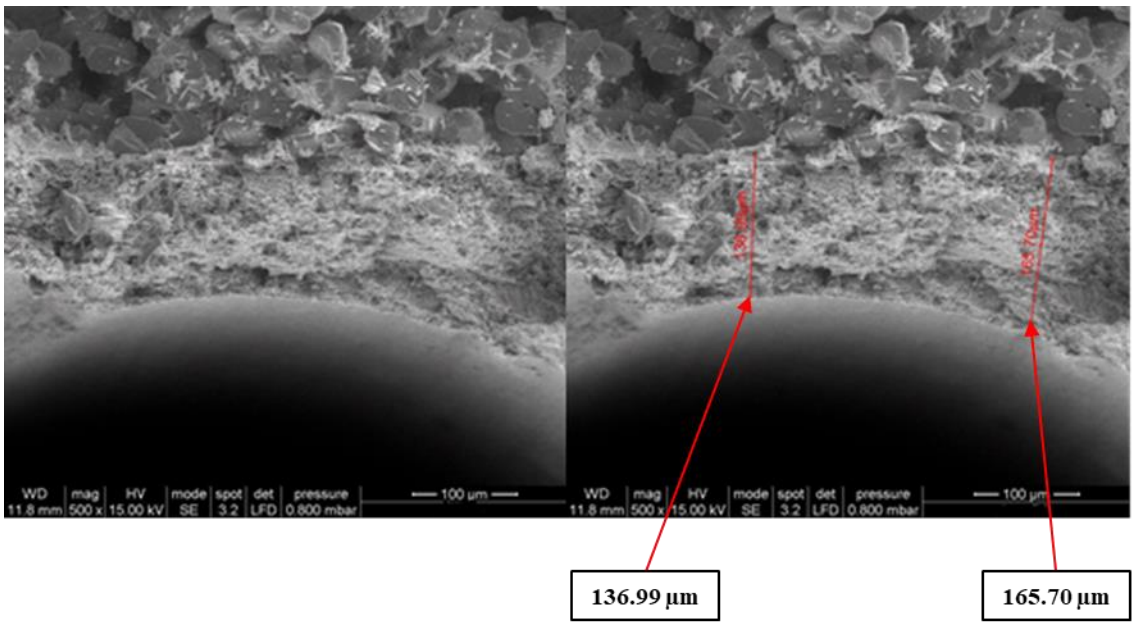


**Figure 7.2 - Catalyst coated DPF SEM images**

### 7.3.2 Laboratory scale activity result

Figures 7.3 to 7.5, show the PM/carbon oxidation evaluation (TGA-MS) results. These figures give temperature values $T_i$ (start of the combustion) and $T_f$ (complete combustion). The value $\Delta T = T_i - T_f$ determines the reaction velocity. The reactivity of diverse catalysts

were evaluated by the comparative analysis of these values with and without catalysts under similar experimental conditions. Loose contact provides a more realistic conditions as compared to that of tight contact and therefore this method has been used in the present study. There is a substantial difference observed between the non-catalysed and catalysed reaction of carbon and oxygen.

The reaction gradually increased at a rate over a temperature range of 400-600 °C and during this stage the reaction inclined to become highly exothermic. The PM oxidation process was observed and analysed from the weight loss pattern; while the derivative plots suggested any disturbance occurring during the analysis, associated to a very noisy curve.

The oxidation activity for the $Pr_6O_{11}$ fibre catalyst was carried out under flowing air from 30-800 °C and then analysed to obtain the combustion temperatures. Figure 7.4 shows the loss in weight of PM from the initial 60 mg (95 mg catalyst + 5 mg PM) or no weight loss (0%), without the catalyst the complete combustion of PM took place at around 650 °C (75%). A steady mass loss was observed due to combustion, at its peak between 500 to 600 °C that determined the rate of PM oxidation. A minor amount of weight loss observed from the catalyst that contributed to the weight loss beyond 23%. The plots shown in Figure 7.4 depicts the combustion activity. The results showed that the $Pr_6O_{11}$ fibre catalyst reduced the temperatures from the reaction temperatures, compared to non-catalysed PM oxidation ($T_i$ - 320 °C, $T_f$ - 460 °C). This suggested that the fibre morphology provides more PM and catalysts' interaction; and to provide the lattice oxygen stored within it for the PM oxidation, on coming in contact with PM it had sufficient contact points, allowing sufficient mobility of the oxygen through this structure.

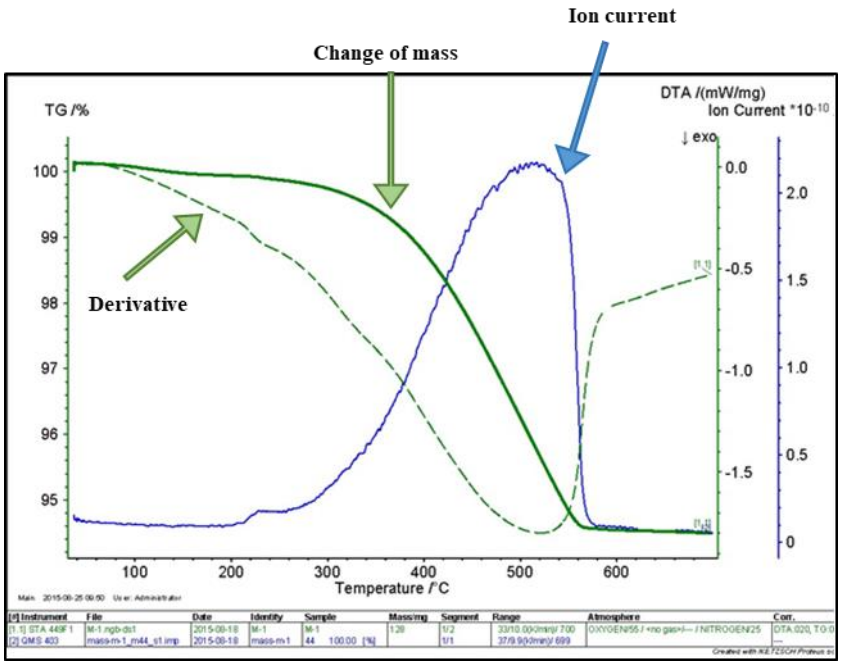


**Figure 7.3 - Thermal gravimetric analysis of diesel soot**

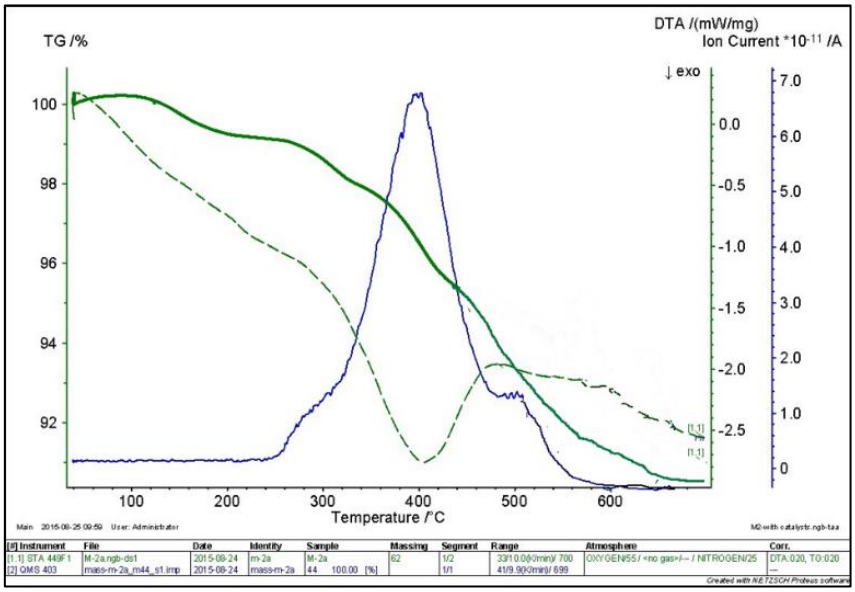


**Figure 7.4 - Thermal gravimetric analysis of diesel soot mixed with $Pr_6O_{11}$ fibre catalyst**

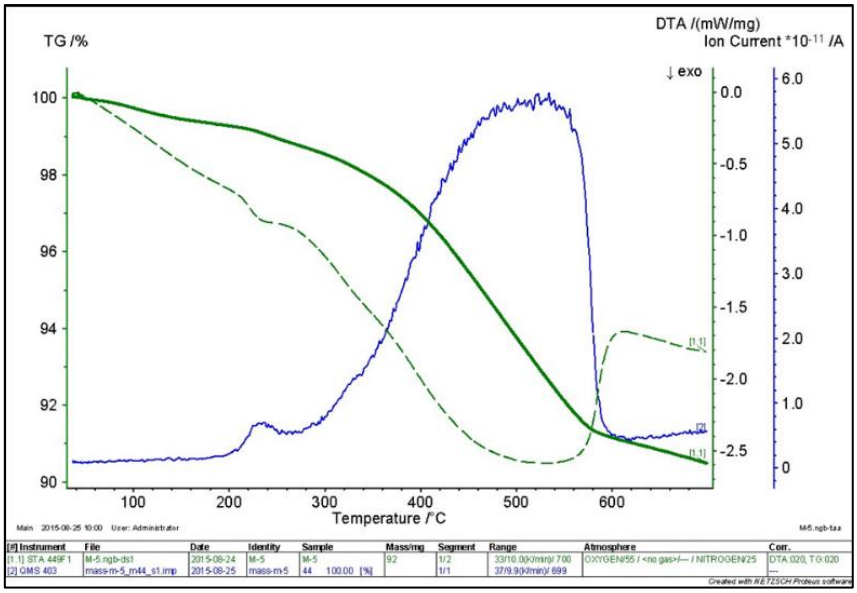


**Figure 7.5 - Thermal gravimetric analysis of $Pr_6O_{11}$ powder catalyst**

## 7.4 Engine test bench – catalyst activity and passive regeneration

The full-scale C-DPF experimentation was carried out on a 2.2 L in-line 4-cylinder CRDI turbocharged diesel engine as mentioned in the research methodology. The engine is run at steady-state high engine load conditions to investigate the effect of a catalyst coated on the channel walls of the DPF by the co-precipitation/ripening method.

The Horiba MEXA 7100 DEGR is used in the experimentation to investigate the gaseous emissions' (CO, $CO_2$, $O_2$, NO, $NO_X$ and THC) conversion efficiency by the catalyst coated substrate during soot loading and regeneration at upstream and downstream testing positions. The Cambustion DMS500 MKII was used for PM measurements at upstream and downstream, to investigate the filtration efficiency of the C-DPF. It also provided a detailed report on particle size (range: 4.87 nm to 1000 nm), concentration and mass of particles at both ends, which gave an in-depth understanding of PM behaviour inside the DPF channels.

### 7.4.1 Test procedure

The C-DPF testing done at steady state conditions was initiated after the engine warm-up, increasing the engine conditions to high engine loads and exhaust gas temperatures using a split injection strategy and introducing EGR in the combustion system. The engine testing is done for soot loading a C-DPF and non-catalysed DPF under similar engine operations. Table 7.1 shows the experimental method used for C-DPF soot loading and regeneration. The engine test results were acquired over a course of 4 days that included engine testing of a catalysed and non-catalysed DPF. Non-catalysed DPF baseline testing was done to investigate the passive regeneration temperature and pressure drop; and was compared to the testing done for a catalysed DPF. With results acquired for gas emissions, particulate matter, upstream and downstream pressure and temperature, the comparative analysis and concluding statements are provided.

**Table 7.1 - Experimental strategy for DPF and CDPF tests**

| **Engine Parameters** | **Catalysed DPF** | **Non-catalysed DPF** |
|---|---|---|
| Speed (rpm) | 1800 | 1800 |
| IMEP (bar) | 8.2 | 8.1 |
| Injection pressure (MPa) | 80 | 80 |
| EGR (%) | 25 | 28 |
| MFB50 (deg BTDC) | 12 | 12 |

### 7.4.2 Experimental analysis of full-scale catalysed and non-catalysed DPF

A $Pr_6O_{11}$ nanofibre catalyst-based full-scale DPF was used in the investigation of filtration, regeneration, and species conversion (oxidation) efficiencies. The coated oxide fibres showed a significant difference in the oxidation temperatures by providing a DPF efficiency of 97 to 99%. The following results in the further sections are shown for particulate matter, normalized gas emissions, temperature, and pressure before and after the C-DPF.

#### 7.4.2.1 Pressure drop and regeneration temperature

As mentioned earlier in the test procedure, the experiment is carried out on a 2.2-L turbocharged diesel engine under steady state engine operations. The exhaust gas temperature during the engine soot loading was measured at 407 ºC. The pressure drop across the substrate increased significantly from 35 mbar to 80 mbar after an engine warm-up of 25 minutes. The increase in pressure drop is observed due to the filtration of engine exhaust with subsequent soot loading inside of filter substrate channel walls. Results acquired for PM filtration during this stage show a filtration efficiency of 99.7% for a prolonged period.

The pressure drop is measured after every 550 seconds (approx. 9 minutes) to monitor the upstream and downstream pressure changes. Figure 7.6 shows the continuous increase in pressure drop across the filter. For every measurement taken with respect to time, the instrumentation is used to measure the temperatures for upstream and downstream of the DPF, including on-engine PM and gas emission measurements. Before passive regeneration is activated, the elevation in pressure drop ($\Delta p$) was observed to reach its peak at 166 mbar. The activation of passive regeneration mode started approximately after 17,500 seconds (approx. 4.8 hours) of soot loading.

During the regeneration process, the substrate achieved its break-even temperature (BET) where the maximum temperature difference was noted at 21 ºC (483 ºC - upstream and 462 ºC - downstream) reducing to 11 ºC shown in Figure 7.6; which also depicted a substantial decrease in total backpressure by 60 mbar during regeneration. The regeneration process was carried out for approximately 20 minutes during which the coagulated channel walls with soot were oxidised and the remaining ash was coagulated on the channel walls. After the regeneration, the measured temperature and pressure drop showed a decrease in the maximum BET to 11 ºC (434 ºC – upstream, 423 ºC – downstream) and Δp – 117 mbar. Due to the catalyst coating on the DPF, the porosity of the filter decreased; which concluded in a higher amount of unremoved ash being deposited on the channel walls, incrementing the filter pressure drop significantly after regeneration. Loose contact catalyst nanofibers coated on the channel walls restricted larger particulates and ash deposits from flowing out of the filter after regeneration; hence, this increased the pressure drop again over time. The importance of investigating the break-even temperature and pressure drop is to differentiate the soot reactivity of a C-DPF. It is not completely dependent on these factors, as the involvement of the physical composition of the exhaust emissions also needs to be considered and has been addressed in the following section below.

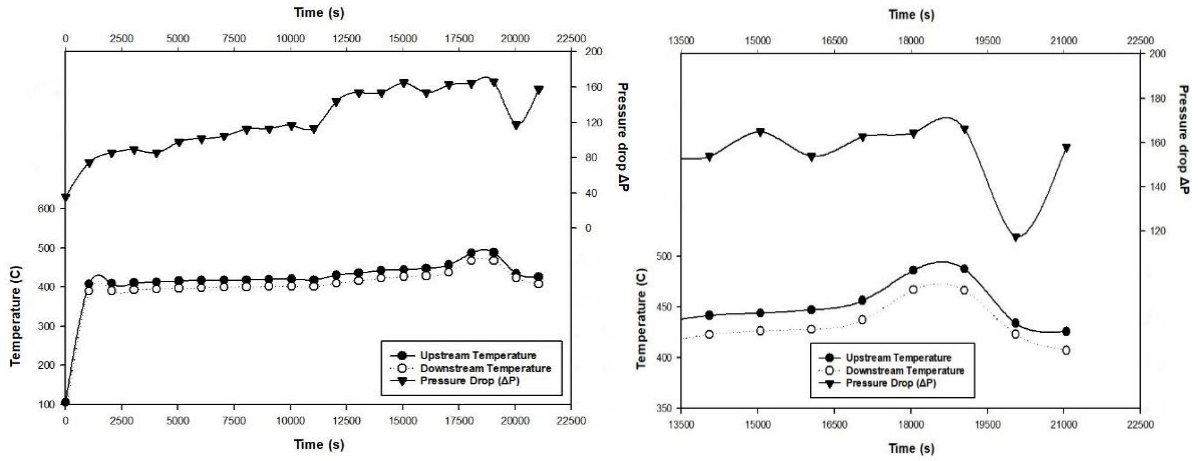


**Figure 7.6 - Pressure drop for DPF (Left), upstream and downstream temperatures for DPF regeneration (Right)**

### 7.4.2.2 Particulate matter and gas emissions' results

Particulate matter (PM) results are acquired using a Cambustion DMS500 particulate analyser that shows results for PM size spectral densities, number concentrations and particle mode sizes before, during and after regeneration. Particle filtration from the C-DPF shows an increasing filtration efficiency from 99.3% to 99.7% during soot loading and regeneration conditions. Figure 7.7 shows the upstream and downstream particle size distributions from the C-DPF. The decrease in the particulate number is the result of the mechanical filtration of PM emissions. The PM filtration results can be justified by the increasing pressure drop (Fig. 6.6) inside the C-DPF and reducing number concentrations. A significant decrease of PM number concentration is observed during the soot loading stage, which further reduces by approximately 97% after regeneration.

Particle sizes for nucleation and accumulation modes vary significantly at soot loading and regeneration modes. The results shown are based on the count median diameter (CMD) of individual particle mode. The nucleation and accumulation mode particles before the C-DPF

during soot loading have particles ranging from 20 nm to 30 nm and 50 nm to 70 nm, respectively. In clean filter conditions, pores and openings in the C-DPF channel walls and catalyst remove small particulates from the outlets, and large particulates tend to reside on the channel walls and catalyst, impregnate the holes creating a soot cake layer on the porous walls. Hence, a higher fraction of nucleation mode concentration is observed initially from the outlet at the early stages; which further reduces as the PM capture increases inside the channels. The resident nucleation and accumulation mode particles on the channel walls adsorb and combine with other ultra-fine and fine particles, increasing the surface area of the spherules and providing more contact points to the catalyst for oxidation and forming larger particles. The PM burn during the regeneration mode removes the nucleated and accumulated PM from the outlet, resulting in a larger accumulation mode particle size (Dp > 50 nm) and number concentrations (N/cc) with a smaller fraction of nucleation mode particulates, as shown in Figure 7.7.

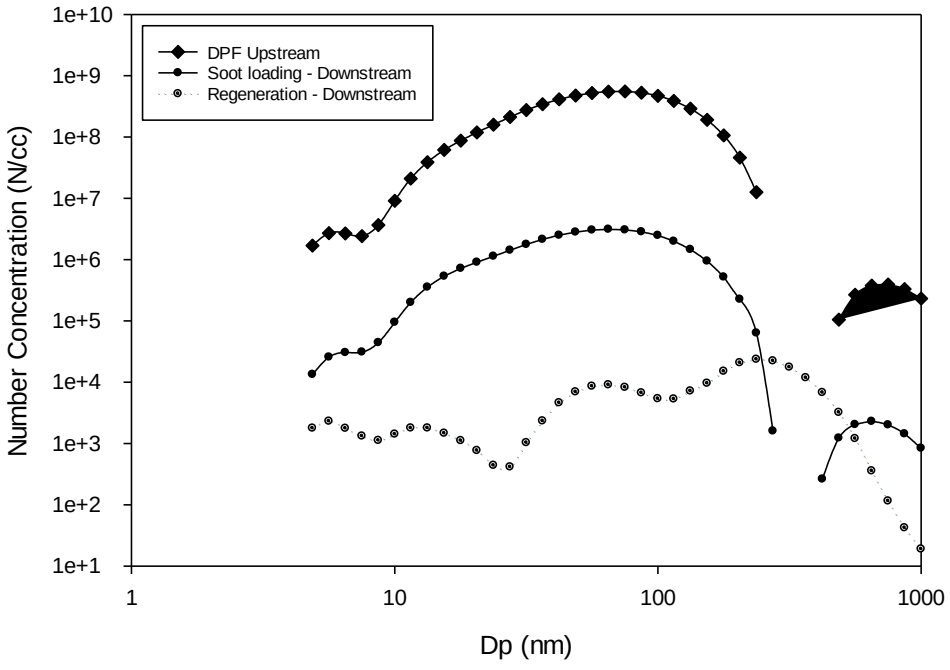

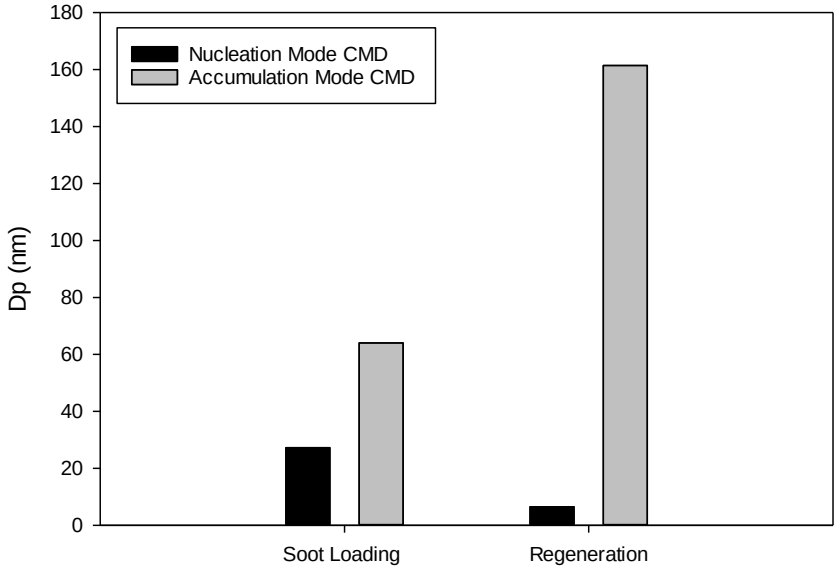


**Figure 7.7 - Particle size distribution at upstream and downstream of DPF (top); nucleation and accumulation mode CMD during soot loading and regeneration (bottom)**

As mentioned earlier, the changes in pressure drop and break-even temperatures depend partially on exhaust gases and their composition in the exhaust. Wherein, many authors have previously established the major involvement of $NO_2$ and $O_2$ in oxidation reactivity and soot burn but at different temperatures. For passive regeneration, $NO_2$ assisted soot burn at low temperatures (300-400 ºC) is used as $O_2$ assisted soot burn, and oxidation temperatures require more than 500 ºC. [66, 67, 128-131]

Figure 7.9, enlisted are the gaseous emissions (THC, CO, $CO_2$, NO, $NO_2$, $NO_X$, and $O_2$) and the displayed graphs are taken after the DPF during soot loading and regeneration modes. Compared to the exhaust temperatures, soot oxidation is carried out at temperatures between 450 and 500 ºC. At various catalytic sites, nitrogen oxide (NO) reacts with oxygen ($O_2$) to give

a reversible reaction for the by-product of $NO_2$. The $NO_2$ generated at these catalytic sites is absorbed and reacts at optimal temperatures with trapped soot, producing other gaseous emissions such as $CO_2$, CO, $N_2$ and $N_2O$. For the DPF regeneration process, the oxidation reactions taking place inside the inlet channels are given below [51, 131]:

**Table 7.2 - Generic chemical reactions inside the DPF [129]**

| No. | Reactions $k_f = AT^b \exp(-E/RT)$ | A | b | E | Remarks |
|---|---|---|---|---|---|
| R1 | $C + NO_2 = CO + NO$ | 3.90E+13 | 0 | 177 | Reaction mechanism of C and NOx |
| R2 | $C + N_2O = CN + NO$ | 4.10E+13 | 0 | 258 | |
| R3 | $C + NO = CO + N$ | 2.90E+13 | 0 | 322 | |
| R4 | $NO_2 + CO = NO + CO_2$ | 2.19E+13 | 0 | 29200 | Reaction mechanism of CO and NOx |
| R5 | $N_2O + CO = N_2 + CO_2$ | 2.70E+13 | 0 | 740 | |
| R6 | $NO + CO = N + CO_2$ | 1.90E+11 | 0 | 3400 | |
| R7 | $NO + O_2 = NO_2 + O$ | 1.00E+13 | 0 | 600 | Conversion reaction between NOx |
| R8 | $NO_2 + NO_2 = NO + NO + O_2$ | 2.00E+12 | 0 | 26825 | |
| R9 | $NO_2 + NO = N_2O + O_2$ | 1.00E+12 | 0 | 60000 | |
| R10 | $N_2O + OH = N_2 + HO_2$ | 2.00E+12 | 0 | 40000 | |
| R11 | $N_2O + O = N_2 + O_2$ | 1.40E+12 | 0 | 10800 | |
| R12 | $N_2O + O = NO + NO$ | 2.90E+13 | 0 | 23150 | |
| R13 | $N_2O + N = N_2 + NO$ | 1.00E+13 | 0 | 19870 | |
| R14 | $CO + O_2 = CO_2 + O$ | 2.50E+12 | 0 | 47800 | Reaction mechanism of C, CO and 02 |
| R15 | $C + O_2 = CO + 0$ | 2.00E+13 | 0 | 576 | |
| R16 | $N + N = N_2$ | 2.90E+10 | 0 | 133 | |

At approximately 450 ºC, the regeneration mode is initiated where the high reactivity of the soot begins. It is observed, from soot loading to regeneration mode, the total hydrocarbons (THC) are reduced by 64%. Breakdown of hydrocarbon chains and further carbon particles form carbon monoxide and dioxide (CO and $CO_2$) in the presence of oxygen radicals and catalyst sites. An increase of 3% in the $CO_2$ concentration is seen during regeneration, compared to soot loading conditions; whereas, a decrease in CO and $O_2$ is observed by 7% and 47% respectively. The catalytic reactivity of the soot-catalyst in loose contact conditions provides a significant absorption of oxygen radicals inside the channels, due to an increased surface area of particulates and later reacting to the increased concentrations of NO and $NO_X$ by approximately 10%. The catalyst filled with oxygen sites possibly undergoes several exothermic reactions for NO, $NO_X$, CO and $O_2$, which increase the regeneration temperatures to 487 ºC at the peak temperature. A series of reversible and irreversible exothermic reactions take place inside the DPF depending on the catalyst sites spread through the channels. Due to decreased soot porosity inside the channels, a continuous regeneration does not provide a substantial rise in $CO_2$ and $H_2O$ gas concentrations.

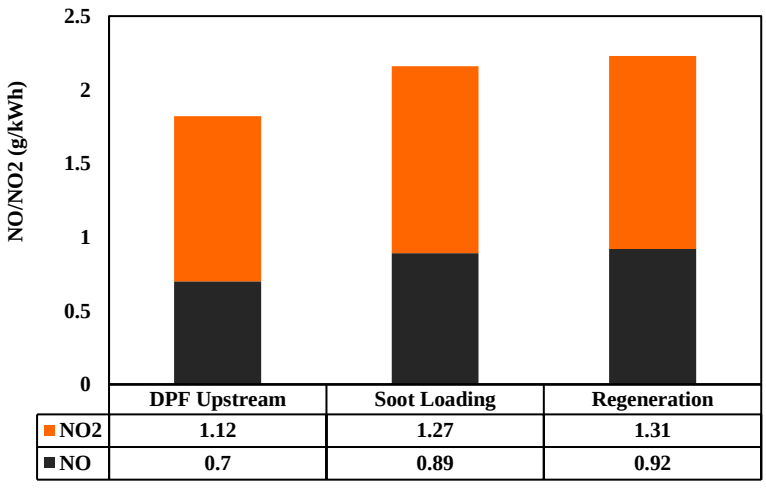


| | DPF Upstream | Soot Loading | Regeneration |
|---|---|---|---|
| NO2 | 1.12 | 1.27 | 1.31 |
| NO | 0.7 | 0.89 | 0.92 |

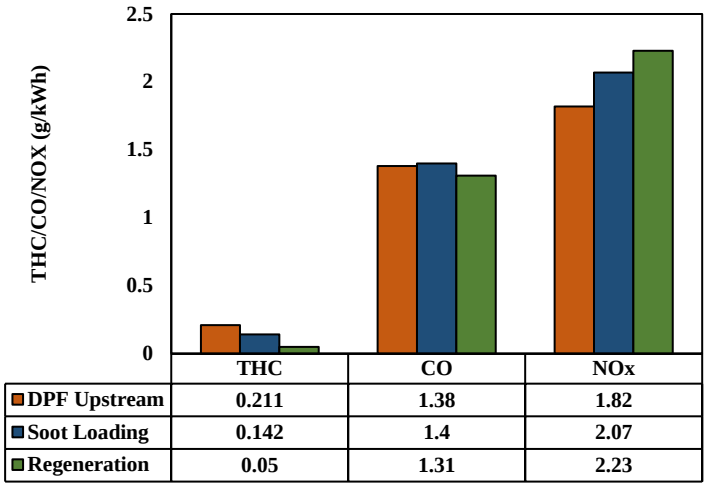


| | THC | CO | NOx |
|---|---|---|---|
| DPF Upstream | 0.211 | 1.38 | 1.82 |
| Soot Loading | 0.142 | 1.4 | 2.07 |
| Regeneration | 0.05 | 1.31 | 2.23 |

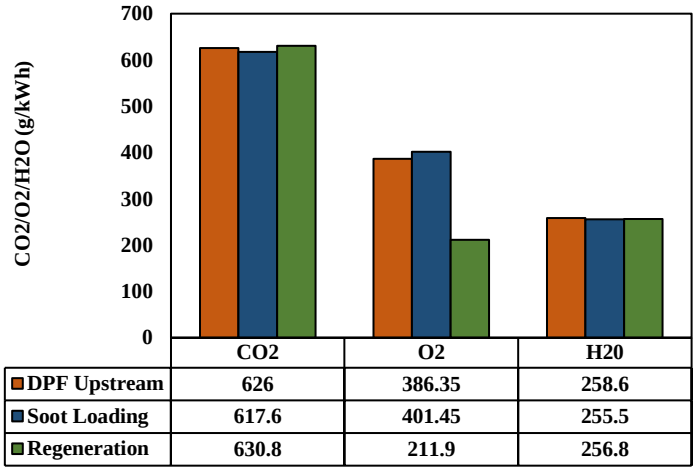


| | CO2 | O2 | H20 |
|---|---|---|---|
| DPF Upstream | 626 | 386.35 | 258.6 |
| Soot Loading | 617.6 | 401.45 | 255.5 |
| Regeneration | 630.8 | 211.9 | 256.8 |

**Figure 7.8 - Gas emissions at the DPF outlet (soot loading and regeneration)**

### 7.4.3 Diesel particulate filter – proof of concept

For proving of the novelty and robustness of a catalysed diesel particulate filter, modelling or experimental approach is widely used. The validation test is performed to show the effects of significant changes in particulate matter (PM), gas emissions, pressure drop (Δp) and exhaust temperatures on a catalysed and a non-catalysed DPF. The engine operating

conditions are shown earlier in Table 6.1 for the experimental approach carried out in this validation. Further, the results comparison of C-DPF and DPF is shown in this section.

#### 7.4.3.1 Comparative analysis for pressure drop and exhaust temperatures

The investigation of the pressure drop and the upstream/downstream temperatures is done using a comparative analysis of a non-catalysed and a nanofibre catalysed DPF. The engine operation on the DPF was kept at a steady state for both the experiments, to provide a clear comparison for the catalysed DPF validation and proving its novelty.

The overall efficiency of the non-catalysed DPF was noted between 86% and 95% during the experimentation. The initial soot loading on the DPF observed a 25 mbar of pressure drop across it, and subsequently, with the consistent increase in soot loading on the filter channels, the pressure drop increased with respect to time at an exhaust temperature of approximately 460 ºC. The increase in the pressure drop kept rising until it reached its peak pressure drop of 230 mbar across. This increase showed a significant change in the engine operation where the back pressure on the engine started to rise. This significant rise in pressure is not observed in the catalysed DPF under similar engine operating conditions. The pressure rise difference at the final stage of experimentation for the non-catalysed DPF was noted to have increased by 27% without showing any changes in pressure release from downstream of the DPF.

The exhaust temperatures during the experimentation were observed to reach a peak temperature of 485 ºC without any particulate matter oxidation or reduction. The experimentation ended with the maximum pressure drop of 225 mbar, which took the similar

amount of time for a C-DPF with reduced and regenerated pressure drop. The initiation of passive regeneration of C-DPF was noted at the exhaust temperature of 483 ºC, whereas for a non-catalysed DPF the exhaust temperature was approximately the same without any initiation of regeneration and decreasing pressure drop.

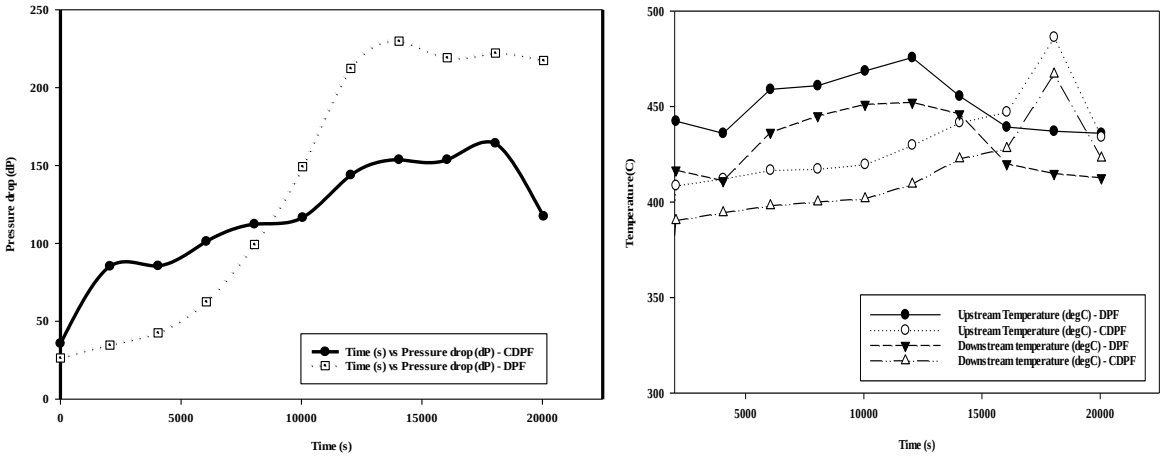


**Figure 7.9 - Pressure drop and temperatures across DPF filters**

### 7.4.3.2 Comparative analysis for particulate matter (PM) emissions

With significant differences between the two particulate filters, the changes in the particulate matter emissions were also observed to be significant. The PM data was analysed to investigate and provide a comparison of mechanical filtration and particulate sizes for the DPFs. The nucleation and accumulation mode particle diameters ($D_P$) were observed to have a similar trend for both experimentations on the DPFs, but with varying initial and final diameters. A difference of 42% in the nucleation mode count mean diameter (CMD) of the non-catalysed DPF was observed compared to the C-DPF; whereas for the accumulation mode CMD there was a significant decrease of 41% compared to the C-DPF, as shown in Figure 7.11.

The pore size for the C-DPF has a smaller escape pathway, as the channel walls are coated with oxidising catalysts. Whereas for a non-catalysed DPF the pore sizes are larger and hence only the larger particulates fill the pores during soot loading. The smaller particulates are removed from the particulate filter with minor hindrance and hence, the particulate size for nucleation modes does not change substantially. With the increase in pressure drop, it can be understood that the channel walls are aggressively filled with PM of higher order particulate diameters that further restrict the flow from the outlet of the channels. The robustness of these statements can be analysed based on the number concentration of these PM modes.

Theoretically, as the soot build-up and pressure drop increases inside the filter, the particle number concentration will decrease downstream compared to the upstream number concentration. This decrease successfully satisfies the theoretical and empirical conceptualisation of mechanical filtration of particulate matter inside a DPF. From Figure 7.12 it can be observed the nucleation mode concentration does not decrease significantly for a non-catalysed DPF as compared to the C-DPF. Based on the analysis there is a significant difference of 54% in the nucleation mode particle filtration in the C-DPF compared to the non-catalysed filter. Even with the increase in the pressure drop of the DPF, some ultra-fine particulates are assumed to escape from the pores and channel walls of the filter and provide a reduced efficiency in the filtration of ultra-fine particles. On the other hand, the accumulation mode concentration from downstream of the DPF shows a significant filtration efficiency of 98%. This filtration of accumulation mode particles aids in the increase of soot building inside the filter channels; and furthermore, is an important factor in the substantial rise of the pressure drop across the filter.

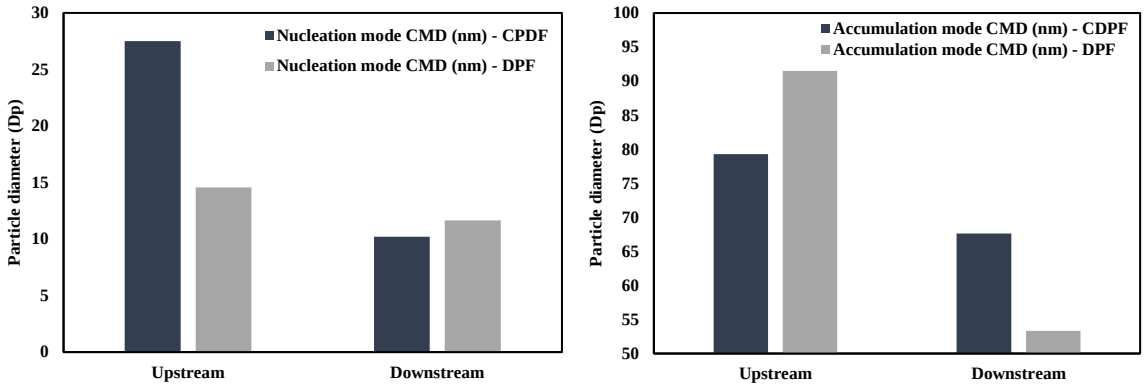


**Figure 7.10 - Nucleation mode CMD for C-DPF and DPF (left); accumulation mode CMD for C-DPF and DPF (right)**

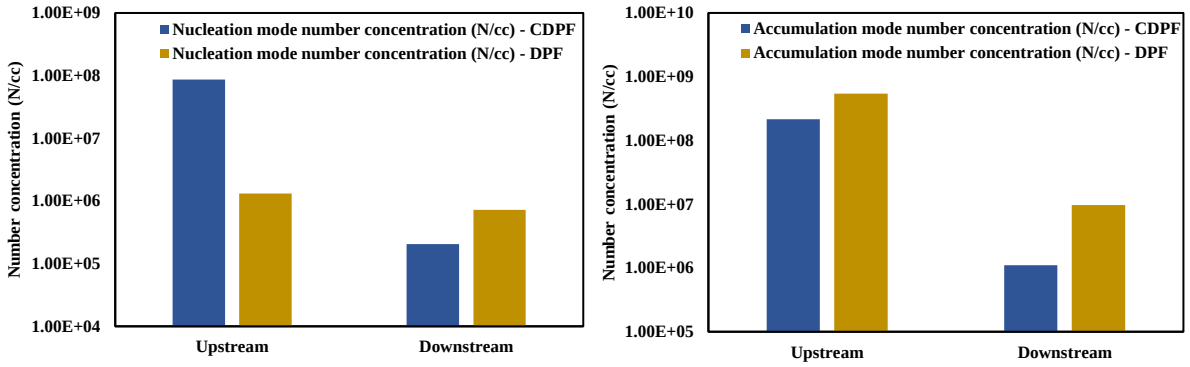


**Figure 7.11 - Nucleation mode concentration for C-DPF and DPF (left); accumulation mode concentration for C-DPF and DPF (right)**

Figures 6.13 and 6.14 represent the size spectral density from both filter substrate experimentations. With the significant decrease of the porosity, the substrate undergoes mechanical filtration which aids in the reduction of the number concentration as mentioned above. The overall reduction in particulate size densities is also observed. Equating the results from the C-DPF to a non-catalysed DPF, the filtration efficiency of a C-DPF is observed to have achieved a higher filtration of 95% to 98% during the experimentation. On the other hand, an efficiency of 85% to 95% was observed in the non-catalysed filter. These results are already demonstrated and established based on the previous particulate mode analysis. The particulate

concentration for the non-catalysed DPF is distributed more than 50% in the logarithmic order of $1e^6$ to $1e^7$ N/cc; whereas the distribution is less for the C-DPF in the logarithmic order for the size distribution of these particulates downstream. This can be supported with the facts and results analysed for particle mode concentration as explained previously.

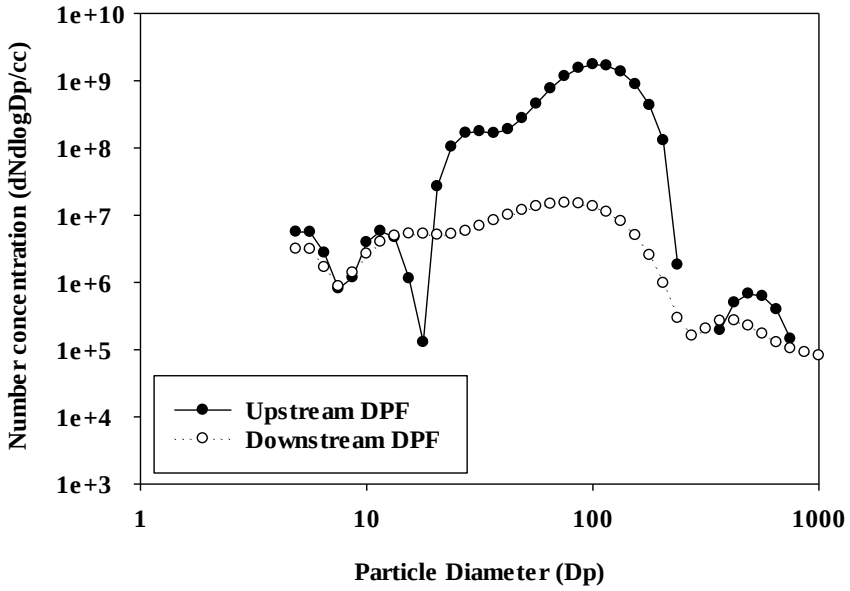


**Figure 7.12 - Non-catalysed DPF size spectral distribution**

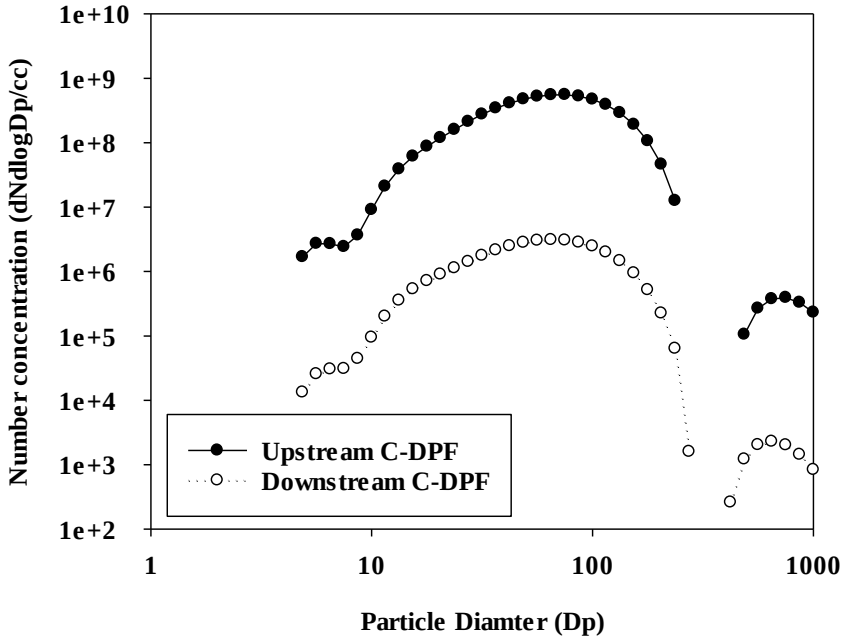


**Figure 7.13 - Catalysed DPF size spectral distribution**

## 7.5 Summary

The peculiar morphology of $Pr_6O_{11}$ and $Pr_2O_3$ nanofibre was tested in laboratory and test bench experimentation. The oxides of praseodymium coated on the DPF have been shown to have a significant effect on filtration and reactivity of particulate matter and gaseous emissions; proving the applicability of these catalysts as high grade oxidising agents for combustion engine exhausts. The primary conclusions drawn from this study are as follows:

1) Using $Pr_6O_{11}$ and $Pr_2O_3$ novel morphology, it has shown that the catalyst maximizes the contact between the PM and the catalyst at increasing degrees; giving aid to higher filtration efficiency, with consistency which is observed based on the increasing pressure drop ($\Delta p$) from upstream to downstream.
2) The DPF's performance is dependent on its filtration efficiency, and oxidation temperatures for continuous regeneration and low back pressures. Increased back pressure can cause a cascade of permanent faults on the DPF and also reduce the engine performance. The catalysed DPF used in the study showed the activation of a regeneration mode at low temperatures compared to a non-catalysed DPF, which in turn helped in reducing the overall pressure drop across the filter.
3) Absorption of oxygen radicals from the catalyst have shown a substantial variation in the regulated gaseous species' conversion. Results have shown changes in gaseous species from upstream to downstream, establishing the effect of the catalyst coated on the DPF and the absorption of these oxygen radicals helping in the formation of converted gas compounds.

# CHAPTER 8

# CONCLUSIONS AND FUTURE WORK

The following empirical and modelling work carried out in this thesis is primarily focussed on investigating gas and particulate matter evolution using novel experimental methodologies and developed models. The thesis also provides a high-grade catalyst for low temperature particle filtration and oxidation. The conclusions mentioned below are separated and focussed on each research chapter.

## 8.1 Simulation of particle inception and growth using particle growth model

The establishment of the particle growth model (PGM) is described in this chapter. Particle inception due to binary nucleation of water and sulphuric acid, with hydrocarbon compounds aiding particle inception and growth is closely studied. Additionally, condensation of vapour phase species on particulate modes (nucleation and accumulation) is parameterised and simulated, to estimate particle size distributions, nucleation, and accumulation mode concentrations and sizes. The effects on particulate characteristics due to exhaust gas temperatures, exhaust tailpipe lengths, relative humidity, specific pseudocritical temperatures of gas components and dilution ratio are extensively validated using the numerical model. The following conclusions for the nucleation mode ($D_P$ < 50 nm) and accumulation mode ($D_P$ > 50 nm) particles are stated below.

1. Nuclei formation or rate of nucleation from the vapour phase are chiefly dependent on the relative humidity and dilution ratio used for data extraction from an exhaust

emission sampling system. An increase in relative humidity of exhaust gases reduces the nucleation rates significantly, explaining the binary nucleation of $H_2O$-$H_2SO_4$.

2. An increase in the nucleation mode particle size is observed in each simulation case (using 1.4, 3.0 and 6.0 bar BMEP boundary conditions). The average particle size range of the nucleation mode resides between 20 and 30 nm for each condition along the length of the exhaust tailpipe. The variations in particle size are a result of thermophoresis and agglomeration, which increase the rate of condensation and adsorption of gas-phase species like VOF, $H_2O$, $H_2SO_4$ and PAHs; forming a nucleus and subsequently conjoining with agglomerated particles to form particulates $D_P$ < 50 nm. Nucleation mode particles are more responsive to physical stimuli than accumulation mode particles with increase in exhaust pipe length.
3. Decreasing nucleation mode concentration is dependent on many factors involved in particle formation and growth. With the observed particle size increase in the nucleation mode, the concentration decreases by forming larger particles ($D_P$ > 50 nm) through coagulating, colliding and coalescing with other particle-phase and gas-phase species. The increase in surface growth and density of particles, increases the mass of the particle inclining number concentration deviating to accumulation mode particulates. Heavier particle formation with increasing length also resides on the chamber walls, where the deposition of particulates can show a decrease in the number concentration of PM.
4. For accumulation mode ($D_P$ > 50 nm), the average particle size range is between 60 and 90 nm, showing a high variability in particle sizes with the changes in exhaust gas temperatures, dilution ratios, initial particle size distributions and length of the exhaust pipe. Hydrocarbon condensation, adsorption, and condensation of other gas-phase species aid in the incrementing of the accumulation mode particles. An increase in

particle colloidal and fracturing processes between nucleated particles with a decrease in temperature, increase the coagulation rate, increasing the particle concentrations as well for the accumulation mode.

5. The particle growth model (PGM) has shown a high degree of robustness and increased precision in the prediction of particulate matter (PM) characteristics and provides an precise parameterisation validated using initial boundary conditions from test bench experimentation.

Due to a consistent monotonous decrease in exhaust temperature at increasing lengths, gas-phase species like $H_2O$, $H_2SO_4$, PAHs and others incline to condense and give rise to initial particle inception. A small fraction of water and sulphates aids in the particle inception at reduced temperatures. The nucleated particles formed can vary in sizes depending on the nucleation rate of gas emissions and form new particulates with high variability in particle masses. [22, 24, 25]

## 8.2 Particulate matter evolution and dynamics in diesel exhaust tailpipe

This chapter provides an insight into PM characteristics due to the effect of exhaust tailpipe length, engine operating conditions, exhaust gas temperatures, and external cooling. Physical processes like nucleation, condensation, deposition, surface growth and agglomeration are involved in the PM dynamics and their characteristics. The following conclusions are made based on the empirical investigative analysis.

1. At low exhaust temperatures, the particle-to-particle interaction has a higher dominance as the length of exhaust pipe increases. Due to low exhaust flow rates and higher gas condensation probability, the particulate measurements at each testing position have

increased standard deviations showing high variability. Nucleation mode concentration is not significantly affected as it has an unimportant decrease; whereas for particle size and mass, the changes are significant due to the coalescence of nucleated particles. The particle mass at low exhaust temperatures has shown elevated changes by 33% and 26% for nucleation and accumulation modes. The Brownian motion effect on the particulates increases the particle sizes due to impact, and in turn, increases the mass.

2. At intermediate engine load and higher exhaust temperatures, the variations in the particulate matter characteristics follow a similar trend line for number concentration with a cooled, conditioned exhaust having more decrement than a no-cooling effect. A copper coil having higher thermal conductivity increases the absorption of heat and further balances the temperature gradient the same as the no-cooling effect. The increase in exhaust temperatures and exhaust flow rates also reduces the Brownian motion effect on particulates increasing its Reynolds number nearing to laminar flows. Hence, changes in the particle size and mass are concluded to be non-significant at high exhaust temperatures.
3. It can be stated that for low exhaust gas temperatures, vapour condensation and nucleation processes are more dominant and mass of particles increase significantly; and for high exhaust gas temperatures particle-to-particle interactions are prevalent. Overall, the increase of engine load from 1.4 bar BMEP to 4.5 bar BMEP shows more variability in PM < 50 nm (nucleation mode) and supports the further increasing/decreasing changes from PM > 50 nm (accumulation mode). Particle dynamics along the exhaust tail pipe at different engine operating conditions and the effects of exhaust gas temperatures and cooling provide in-depth information on particle evolution.

## 8.3 Design considerations of exhaust tail pipes for compression ignition engines

This chapter provides a brief investigation and discussion of the design and development of exhaust aftertreatment systems, considering engine operations, exhaust temperatures and the particulate characteristics. The chapter provided the following conclusions and recommendations:

1. Particulate matter characteristic variations are negligible due to the short distance of exhaust pipe (from the turbocharger to the aftertreatment system inlet). Thermal losses are prominently observed with the increasing length of the exhaust pipe.
2. The nucleation of gas phase species is negligible due to high flow velocities and shorter lengths of the exhaust pipe. This provides minor variations in the nucleation and accumulation particle mode concentration and size, and hence giving a low percentage of PM characteristic variations.
3. Aftertreatment systems require high temperature for PM burn, and due to the thermal losses, this process cannot be carried out with high efficiency. Hence, the recommendations were provided to operate the engine at high engine loads that increase the exhaust temperatures. Also, reduce thermal losses by containment of heat transfer from the exhaust valve to the inlet of the aftertreatment system.
4. The final recommendation is to develop a method to introduce passive regeneration by using oxygen rich catalysts that can be coated of the aftertreatment system and reduce the oxidation temperatures below 500ºC.

## 8.4 Experimental investigation of nanofiber catalyst on diesel particulate filter

The lab-scale and test-bench scale experimentation was done to introduce a novel material and morphology of a catalyst coated on a diesel particulate filter (DPF). The experimentation provided a series of results, presenting a wider perspective towards utilising these catalysts to increase oxidation of accumulated soot particles inside the DPF at low temperatures. The following conclusions can be noted:

1. The synthesized nanofibre catalyst showed increased catalytic activity in the combustion of soot inside the filter, with a significant reduction in oxidising and combustion temperatures by approximately 100 ºC, comparable to a non-catalysed particulate filter. Due to the complex morphology of these nanofibers, the catalyst-soot contact points are elevated to a higher degree and thus provide higher mechanical filtration and increased surface points for particle oxidation.
2. Test-bench experimental investigation supports the results from lab-scale experimentation; showing an increased oxidation reactivity of the catalyst, higher mechanical filtration efficiency, and a significantly reduced oxidation temperature of less than 500 ºC. The regeneration mode was achieved at below 200 mbar of pressure drop, and also provided a consistent particulate filtration efficiency of more than 95%.
3. The authenticity of the novel catalyst morphology used on the DPF was established by comparative experimentation with a catalysed and non-catalysed filter substrate. The DPF's experimentation was under similar engine operations along with the method of soot loading and regeneration. The non-catalysed filter shows a 92% filtration efficiency, with a continuous increase in pressure drop ascending more than the catalysed threshold pressure drop to more than 200 mbar. With a higher exhaust temperature than the catalysed DPF, the regeneration mode did not

activate during the same period and pressure, but showed comparable particulate matter (PM) data.

## 8.5 Thesis conclusion

The thesis depicts the characterisation, physical processes, exhaust system design and the control of particulate matter (PM) emissions in an exhaust pipe and aftertreatment system, using simulation and experimental methodologies for a conventional diesel engine at variant engine operating conditions. The primary stage of PM characterisation is done using simulation methods, where a particle growth model (PGM) is established to combine the physical processes; nucleation, condensation, deposition, surface growth, and coagulation carried in an exhaust pipe under the influence of exhaust temperature, length of pipe and flow velocities. The model satisfies the objectives established initially and is comparable with the experimental methods used. The nucleation of gas phase exhaust constituents, water (H2O) and sulphuric acid (H2SO4) are observed to have less contribution to the overall PM concentration, size and mass, as due to limitations of vapour condensation to nuclei formation is not carried out with the given exhaust temperatures, length and flow velocities. The simulation results have shown low nucleation rates as the exhaust temperature and length increases, and it is comparable to the experimental results obtained at different engine operating conditions.

As the effect of exhaust temperature and length is considered in the simulation procedure, the demand to characterise particulate-to-particulate and gas-to-particulate interactions were crucial. Hence, experimentally characterising the PM processes along the length of exhaust pipe has shown definitive changes for an externally cooled exhaust

pipe, aided by antifreeze and ice water. The cooling effect is more prominent at low exhaust temperatures (<200ºC) compared to high exhaust temperatures (>200ºC). This temperature effect bridges the characteristics of PM, which is observed to show significant changes in particle concentration, size and mass along the exhaust pipe length. As the PM characteristics are determined based on these factors, the abatement of them is also an integral part to be addressed. Hence, abatement and oxidising these PM emissions require a design of an exhaust system that uses particulate filter substrate. Use of catalysts coated on a diesel particulate filter (DPF) substrate aids in low or high temperature oxidation and particulate trap. As addressed in background knowledge, the oxidation and burn of PM emissions carry out at temperatures above 550ºC. Whereas, the optimal exhaust temperature of a conventional diesel engine falls below this range.

To improve the particle filtration and achieving low temperature oxidation (<550ºC), it is carried using an oxygen rich catalyst nanofiber, coated on the DPF channels for this purpose. The low temperature oxidation is characterised using laboratory experimentation and test bench experimentation for approving a robust response of the catalyst used. The nanofiber catalyst coated on the DPF channels has provided with low backpressure with above 95% filtration efficiency and reduced oxidation temperature below 500ºC with species conversion/PM burn. The comparative analysis and to prove the concept of nanofiber catalyst is performed using a conventional cordierite DPF without an external coating of catalyst. The backpressure has shown to increase much higher than a nanofiber catalysed DPF, as the PM trap for a conventional DPF has a higher porosity than catalysed DPF. The novel morphology provides higher contact points with PM during filtration/PM trap which assists PM to burn with oxygen radicals stored in the catalyst in a more beneficial manner.

The thesis concludes with the establishment of the research novelty addressed earlier, to design, develop, characterise, analyse and contribute to the knowledge of particulate matter dynamics and control supported by background knowledge, simulations and experimentations. The applicability of the research addressed has an eminent scope in the design and development of an exhaust system for CI and SI engine technology.

## 8.6 Future Work

The present study can be extended in the understanding of gas and particulate matter emissions:

### 8.6.1 Computational fluid dynamics model

The model-based study performed in the present thesis can be extended in the investigation of particulate matter behaviour and temperature gradient changes for cooled conditioning of exhaust tailpipes. The combination of chemical and physical kinetics incorporated in a singular model, can provide a better insight into particle tracking and gas emission condensations. Thus, to improve the present model by incorporating various gas emissions, three-dimensional CFD model development is recommended.

### 8.6.2 Spark ignition exhaust emission dynamics

The present study was performed on the particle dynamics of a compression ignition engine, having high particle size and mass. The particle size and mass differ by a lower magnitude having increased dominance in nucleation mode particulate size and mass.

Investigating the particulate dynamics under various engine operating conditions with different positions of the exhaust tail pipe, and furthermore, the impact of gas emissions from the exhaust on the particulate matter are recommended.

### 8.6.3 Particulate evolution using after-treatment systems

The present exhaust tail pipe and after-treatment systems have been through experimentation separately under different engine operating conditions. The objectives were different in these cases; and hence, incorporating an exhaust after-treatment system with the exhaust tail pipe is recommended, to investigate the particulate growth, gas species conversions and the cooling effects of the exhaust tail pipe, creating a realistic condition of on-road vehicle exhaust plumes.

# References


1. Heywood, J.B., *Internal combustion engine fundamentals*. McGraw-Hill automotive technology series. 1988.
2. Kagawa, J., *Health effects of diesel exhaust emissions—a mixture of air pollutants of worldwide concern.* Toxicology, 2002. **181-182**: p. 349-353.
3. Ristovski, Z.D., et al., *Respiratory health effects of diesel particulate matter.* Respirology, 2012. **17**(2): p. 201-212.
4. Johansen, K., et al., *Integration of Vanadium and Zeolite Type SCR Functionality into DPF in Exhaust Aftertreatment Systems - Advantages and Challenges*. 2014, SAE International.
5. Sydbom, A., et al., *Health effects of diesel exhaust emissions.* European Respiratory Journal, 2001. **17**(4): p. 733-746.
6. Qian, Y., et al., *Review of the state-of-the-art of particulate matter emissions from modern gasoline fueled engines.* Applied Energy, 2019. **238**: p. 1269-1298.
7. Nevers, N.D., *Air Pollution Control Engineering*. 2nd Edition ed. 1995, Singapore: McGraw-Hill
8. Eastwood, P., *Critical Topics in Exhaust gas Aftertreatment*. 2000: Research Studies Press Ltd. .
9. Heywood, J.B., *Internal combustion engine fundamentals*. 2018.
10. Heywood, J.B.a., *Internal combustion engine fundamentals / John B. Heywood*. 2018, OH McGraw Hill Education: OH.
11. Mendez, S. and B. Thirouard, *Using Multiple Injection Strategies in Diesel Combustion: Potential to Improve Emissions, Noise and Fuel Economy Trade-Off in Low CR Engines*. 2008, SAE International.

12. Agarwal, A.K., A.P. Singh, and R.K. Maurya, *Evolution, challenges and path forward for low temperature combustion engines.* Progress in Energy and Combustion Science, 2017. **61**: p. 1-56.

13. Kimura, S., et al., *New Combustion Concept for Ultra-Clean and High-Efficiency Small DI Diesel Engines*. 1999, SAE International.

14. How, H.G., et al., *Influence of injection timing and split injection strategies on performance, emissions, and combustion characteristics of diesel engine fueled with biodiesel blended fuels.* Fuel, 2018. **213**: p. 106-114.

15. Wei, L., C.S. Cheung, and Z. Ning, *Effects of biodiesel-ethanol and biodiesel-butanol blends on the combustion, performance and emissions of a diesel engine.* Energy, 2018. **155**: p. 957-970.

16. Gharehghani, A., M. Mirsalim, and R. Hosseini, *Effects of waste fish oil biodiesel on diesel engine combustion characteristics and emission.* Renewable Energy, 2017. **101**: p. 930-936.

17. Mirhashemi, F.S. and H. Sadrnia, *NOX emissions of compression ignition engines fueled with various biodiesel blends: A review.* Journal of the Energy Institute, 2019.

18. Thipse, S.S., *Alternative Fuels - Concepts, Technologies and Developments*. 2011: JAICO Publishing House.

19. Chan, C.C., *The state of the art of electric and hybrid vehicles.* 2002. **90**(2): p. 247-275.

20. Fuad Un-Noor, S.P., Lucian Mihet-Popa, Mohammad Nurunnabi Mollah and Eklas Hossain, *A Comprehensive Study of Key Electric Vehicle (EV) Components, Technologies, Challenges, Impacts, and Future Direction of Development.* 2017.

21. Yimin, G. and M. Ehsani, *Design and Control Methodology of Plug-in Hybrid Electric Vehicles.* 2010. **57**(2): p. 633-640.

22. Tree, D.R. and K.I. Svensson, *Soot processes in compression ignition engines.* Progress in Energy and Combustion Science, 2007. **33**(3): p. 272-309.

23. Zhang, J., *PARTICLE MATTER EMISSION CONTROL AND RELATED ISSUES FOR DIESEL ENGINES*. 2010, University of Birmingham. p. 220.

24. Mohankumar, S. and P. Senthilkumar, *Particulate matter formation and its control methodologies for diesel engine: A comprehensive review.* Renewable and Sustainable Energy Reviews, 2017. **80**: p. 1227-1238.

25. Kittelson, D.B., *Engines and nanoparticles.* Journal of Aerosol Science, 1998. **29**(5-6): p. 575-588.

26. Bockhorn, H., A. D'Anna, and A. F. Sarofim, *Combustion generated fine carbonaceous particles*. 2007.

27. Glassman, I., *Soot formation in combustion processes.* Symposium (International) on Combustion, 1989. **22**(1): p. 295-311.

28. Haynes, B.S. and H.G. Wagner, *Soot formation.* Progress in Energy and Combustion Science, 1981. **7**(4): p. 229-273.

29. Smith, O.I., *Fundamentals of soot formation in flames with application to diesel engine particulate emissions.* Progress in Energy and Combustion Science, 1981. **7**(4): p. 275-291.

30. Bruce, C.W., et al., *Trans-spectral absorption and scattering of electromagnetic radiation by diesel soot.* Applied Optics, 1991. **30**(12): p. 1537-1546.

31. Tree, D.R. and D.E. Foster, *Optical Soot Particle Size And Number Density Measurements In A Direct Injection Diesel Engine.* Combustion Science and Technology, 1993. **95**(1-6): p. 313-331.

32. Pinson, J.A., T. Ni, and T.A. Litzinger, *Quantitative Imaging Study of the Effects of Intake Air Temperature on Soot Evolution in an Optically-Accessible D. I. Diesel Engine.* SAE Transactions, 1994. **103**: p. 1773-1788.

33. Gill, S.S., et al., *Diesel emissions improvements through the use of biodiesel or oxygenated blending components.* 2012. **95**: p. 578-586.

34. Zhang, Z.-H. and R. Balasubramanian, *Influence of butanol addition to diesel–biodiesel blend on engine performance and particulate emissions of a stationary diesel engine.* 2014. **119**: p. 530-536.

35. Tan, P.-Q., et al., *Particle number emissions from a light-duty diesel engine with biodiesel fuels under transient-state operating conditions.* Applied Energy, 2014. **113**: p. 22-31.

36. Barrios, C.C., et al., *Effects of animal fat based biodiesel on a TDI diesel engine performance, combustion characteristics and particle number and size distribution emissions.* 2014. **117**: p. 618-623.

37. Burshaid, K.I. and M.A. Hamdan, *The reduction of soot formation from fuels using oxygenates additives.* 2013. **65**: p. 751-754.

38. Sirignano, M., M. Salamanca, and A. D'Anna, *The role of dimethyl ether as substituent to ethylene on particulate formation in premixed and counter-flow diffusion flames.* 2014. **126**: p. 256-262.

39. Guarieiro, L.L.N., et al., *Assessment of the use of oxygenated fuels on emissions and performance of a diesel engine.* 2014. **117**: p. 94-99.

40. Zhang, Z.-H. and R. Balasubramanian, *Effects of oxygenated fuel blends on carbonaceous particulate composition and particle size distributions from a stationary diesel engine.* 2015. **141**: p. 1-8.

41. Choi, C.Y. and R.D. Reitz, *An experimental study on the effects of oxygenated fuel blends and multiple injection strategies on DI diesel engine emissions.* 1999. **78**(11): p. 1303-1317.

42. Benajes, J., et al., *Influence of injection conditions and exhaust gas recirculation in a high-speed direct-injection diesel engine operating with a late split injection.* 2008. **222**(4): p. 629-641.

43. Xu, Z., et al., *Effects of Injection Pressure on Diesel Engine Particle Physico-Chemical Properties.* 2014. **48**(2): p. 128-138.

44. Agarwal, A.K., et al., *Effect of fuel injection pressure on diesel particulate size and number distribution in a CRDI single cylinder research engine.* 2013. **107**: p. 84-89.

45. Haralampous, O.A., et al., *Diesel particulate filter pressure drop Part 1: modelling and experimental validation.* 2004. **5**(2): p. 149-162.

46. Haralampous, O.A., et al., *Diesel particulate filter pressure drop Part 2: On-board calculation of soot loading.* International Journal of Engine Research, 2004. **5**(2): p. 163-173.

47. Stratakis, G.A., D.L. Psarianos, and A.M. Stamatelos, *Experimental investigation of the pressure drop in porous ceramic diesel particulate filters.* Proceedings of the Institution of Mechanical Engineers, Part D: Journal of Automobile Engineering, 2002. **216**(9): p. 773-784.

48. Stamatellou, A.-M. and A. Stamatelos, *Overview of Diesel particulate filter systems sizing approaches.* Applied Thermal Engineering, 2017. **121**: p. 537-546.

49. Schaefer-Sindlinger, A., et al., *Efficient material design for diesel particulate filters.* Topics in Catalysis, 2007. **42-43**(1-4): p. 307-317.

50. Benaqqa, C., et al., *Morphology, physical, thermal and mechanical properties of the constitutive materials of diesel particulate filters.* Applied Thermal Engineering, 2014. **62**(2): p. 599-606.

51. Guan, B., et al., *Review of the state-of-the-art of exhaust particulate filter technology in internal combustion engines.* 2015. **154**: p. 225-258.

52. Khair, M.K., *A Review of Diesel Particulate Filter Technologies*. 2003, SAE International.

53. Iwasaki, S., et al., *New Design Concept for Diesel Particulate Filter*. 2011, SAE International.

54. Seo, J.M., W.S. Park, and M.J. Lee, *The Best Choice of Gasoline/Diesel Particulate Filter to Meet Future Particulate Matter Regulation*. 2012, SAE International.

55. GmbH, E.-A. *Diesel particulate filters*. 2019; Available from: https://www.ernst-hagen.de/en/products/diesel-particulate-filters/.

56. Konstandopoulos, A.G. and M. Kostoglou, *Reciprocating flow regeneration of soot filters.* Combustion and Flame, 2000. **121**(3): p. 488-500.

57. Chen, P., U. Ibrahim, and J. Wang, *Experimental investigation of diesel and biodiesel post injections during active diesel particulate filter regenerations.* 2014. **130**: p. 286-295.

58. Lapuerta, M., J.J. Hernandez, and F. Oliva, *Strategies for active diesel particulate filter regeneration based on late injection and exhaust recirculation with different fuels.* 2014. **15**(2): p. 209-221.

59. Bensaid, S., D.L. Marchisio, and D. Fino, *Numerical simulation of soot filtration and combustion within diesel particulate filters.* 2010. **65**(1): p. 357-363.

60. Kong, Y., et al., *Active DPF Regeneration for 2007 Diesel Engines*. 2005, SAE International.

61. Fino, D., et al., *La–Li–Cr perovskite catalysts for diesel particulate combustion.* Catalysis Today, 2006. **114**(1): p. 31-39.

62. Setiabudi, A., M. Makkee, and J.A. Moulijn, *The role of NO2 and O2 in the accelerated combustion of soot in diesel exhaust gases.* Applied Catalysis B: Environmental, 2004. **50**(3): p. 185-194.

63. Atribak, I., A. Buenolopez, and A. Garciagarcia, *Combined removal of diesel soot particulates and NOx over CeO2–ZrO2 mixed oxides.* Journal of Catalysis, 2008. **259**(1): p. 123-132.

64. López-Suárez, F.E., A. Bueno-López, and M.J. Illán-Gómez, *Cu/Al2O3 catalysts for soot oxidation: Copper loading effect.* Applied Catalysis B: Environmental, 2008. **84**(3-4): p. 651-658.

65. Palmisano, P., et al., *High catalytic activity of SCS-synthesized ceria towards diesel soot combustion.* Applied Catalysis B: Environmental, 2006. **69**(1-2): p. 85-92.

66. Nejar, N., M. Makkee, and M. Illangomez, *Catalytic removal of NOx and soot from diesel exhaust: Oxidation behaviour of carbon materials used as model soot.* Applied Catalysis B: Environmental, 2007. **75**(1-2): p. 11-16.

67. Nejar, N., et al., *Bimetallic catalysts for the simultaneous removal of NOx and soot from diesel engine exhaust: A preliminary study using intrinsic catalysts.* Catalysis Communications, 2005. **6**(4): p. 263-267.

68. Neeft, J.P.A., et al., *Feasibility study towards a Cu/K/Mo/(Cl) soot oxidation catalyst for application in diesel exhaust gases.* Applied Catalysis B: Environmental, 1997. **11**(3-4): p. 365-382.

69. Ciambelli, P., *Redox properties of a TiO2 supported Cu-V-K-Cl catalyst in low temperature soot oxidation.* Journal of Molecular Catalysis A: Chemical, 2003. **204-205**: p. 673-681.

70. Van Setten, B.A.A.L., et al., *Molten salts are promising catalysts. How to apply in practice?* Topics in Catalysis, 2001. **16/17**(1/4): p. 275-278.

71. Van Setten, B.A.A.L., et al., *Realistic contact for soot with an oxidation catalyst for laboratory studies.* Applied Catalysis B: Environmental, 2000. **28**(3-4): p. 253-257.

72. Shan, W., *Reduction property and catalytic activity of Ce1−XNiXO2 mixed oxide catalysts for CH4 oxidation.* Applied Catalysis A: General, 2003. **246**(1): p. 1-9.

73. Cui, Q., et al., *Direct fabrication of cerium oxide hollow nanofibers by electrospinning.* Journal of Rare Earths, 2008. **26**(5): p. 664-669.

74. Boaro, M., et al., *The use of temperature-programmed and dynamic/transient methods in catalysis: characterization of ceria-based, model three-way catalysts.* Catalysis Today, 2003. **77**(4): p. 407-417.

75. Setiabudi, A., et al., *CeO2 catalysed soot oxidation.* Applied Catalysis B: Environmental, 2004. **51**(1): p. 9-19.

76. Kirchnerova, J., M. Alifanti, and B. Delmon, *Evidence of phase cooperation in the LaCoO3–CeO2–Co3O4 catalytic system in relation to activity in methane combustion.* Applied Catalysis A: General, 2002. **231**(1-2): p. 65-80.

77. Rajendran, M., K.K. Mallick, and A.K. Bhattacharya, *Preparation and characterization of LnPrO3+y (Ln=Y and lanthanide)—a series of mixed lanthanide oxides.* Materials Letters, 1998. **37**(1-2): p. 10-16.

78. Thangadurai, V., R.A. Huggins, and W. Weppner, *Mixed ionic-electronic conductivity in phases in the praseodymium oxide system.* Journal of Solid State Electrochemistry, 2001. **5**(7-8): p. 531-537.

79. Popa, M. and M. Kakihana, *Praseodymium oxide formation by thermal decomposition of a praseodymium complex.* Solid State Ionics, 2001. **141-142**: p. 265-272.

80. Hussein, G.A.M., *Rare earth metal oxides: formation, characterization and catalytic activity Thermoanalytical and applied pyrolysis review.* Journal of Analytical and Applied Pyrolysis, 1996. **37**(2): p. 111-149.

81. Antoshin, G.V., K.M. Minachev, and R.V. Dmitriev, *Mobility of oxygen and catalytic properties of rare earth oxides with respect to oxidation of hydrogen.* Bulletin of the Academy of Sciences of the USSR Division of Chemical Science, 1967. **16**(8): p. 1793-1795.

82. Krishna, K., et al., *Potential rare earth modified CeO2 catalysts for soot oxidation.* Applied Catalysis B: Environmental, 2007. **75**(3-4): p. 189-200.

83. Aneggi, E., et al., *Promotional effect of rare earths and transition metals in the combustion of diesel soot over CeO2 and CeO2–ZrO2.* Catalysis Today, 2006. **114**(1): p. 40-47.

84. Pisarello, M.L., et al., *Simultaneous removal of soot and nitrogen oxides from diesel engine exhausts.* Catalysis Today, 2002. **75**(1-4): p. 465-470.

85. Katta, L., et al., *Doped nanosized ceria solid solutions for low temperature soot oxidation: Zirconium versus lanthanum promoters.* Applied Catalysis B: Environmental, 2010. **101**(1-2): p. 101-108.

86. Kockrick, E., et al., *Platinum induced crosslinking of polycarbosilanes for the formation of highly porous CeO2/silicon oxycarbide catalysts.* Journal of Materials Chemistry, 2009. **19**(11): p. 1543.

87. Guillén-Hurtado, N., A. García-García, and A. Bueno-López, *Isotopic study of ceria-catalyzed soot oxidation in the presence of NOx.* Journal of Catalysis, 2013. **299**: p. 181-187.

88. Zhang, Z., S.L. Yang, and J.H. Johnson, *Modeling and Numerical Simulation of Diesel Particulate Trap Performance During Loading and Regeneration*. 2002, SAE International.

89. Yang, S., et al., *Diesel particulate filter design simulation: A review.* Advances in Mechanical Engineering, 2016. **8**(3): p. 168781401663732.

90. Villata, G., et al., *Pollutants Emissions During Mild Catalytic DPF Regeneration In Light-Duty Vehicles*. 2009, SAE International.

91. Konstandopoulos, A.G., *Flow Resistance Descriptors for Diesel Particulate Filters: Definitions, Measurements and Testing*. 2003, SAE International.

92. Bissett, E.J., *Mathematical model of the thermal regeneration of a wall-flow monolith diesel particulate filter.* Chemical Engineering Science, 1984. **39**(7-8): p. 1233-1244.

93. Depcik, C. and D. Assanis, *Simulating Area Conservation and the Gas-Wall Interface for One-Dimensional Based Diesel Particulate Filter Models.* Journal of Engineering for Gas Turbines and Power, 2008. **130**(6): p. 062807.

94. Konstandopoulos, A.G., et al., *Fundamental Studies of Diesel Particulate Filters: Transient Loading, Regeneration and Aging*. 2000, SAE International.

95. Opris, C.N. and J.H. Johnson, *A 2-D Computational Model Describing the Heat Transfer, Reaction Kinetics and Regeneration Characteristics of a Ceramic Diesel Particulate Trap*. 1998, SAE International.

96. Lee, H. and K.O. Lee, *Multi-layered mesh generation and user subroutine development based on an Eulerian-Eulerian approach for soot filtration visualization in a three-dimensional particulate filter model.* 2014. **15**(8): p. 980-992.

97. Haralampous, O. and G.C. Koltsakis, *Intra-layer temperature gradients during regeneration of diesel particulate filters.* Chemical Engineering Science, 2002. **57**(13): p. 2345-2355.

98. Haralampous, O.A. and G.C. Koltsakis, *Oxygen diffusion modeling in diesel particulate filter regeneration.* AIChE Journal, 2004. **50**(9): p. 2008-2019.

99. Becker, R. and W. Döring, *Kinetische Behandlung der Keimbildung in übersättigten Dämpfen.* 1935. **416**(8): p. 719-752.

100. Frenklach, M. and H. Wang, *Detailed modeling of soot particle nucleation and growth.* Symposium (International) on Combustion, 1991. **23**(1): p. 1559-1566.

101. Pirjola, L. and M. Kulmala, *Development of particle size and composition distributions with a novel aerosol dynamics model.* Tellus B: Chemical and Physical Meteorology, 2001. **53**(4): p. 491-509.

102. Kim, D.-H., M. Gautam, and D. Gera, *Modeling Nucleation and Coagulation Modes in the Formation of Particulate Matter inside a Turbulent Exhaust Plume of a Diesel Engine.* Journal of Colloid and Interface Science, 2002. **249**(1): p. 96-103.

103. Vehkamäki, H., et al., *Modelling Binary Homogeneous Nucleation of Water−Sulfuric Acid Vapours: Parameterisation for High Temperature Emissions.* Environmental Science & Technology, 2003. **37**(15): p. 3392-3398.

104. Vouitsis, E., L. Ntziachristos, and Z. Samaras, *Modelling of diesel exhaust aerosol during laboratory sampling.* Atmospheric Environment, 2005. **39**(7): p. 1335-1345.

105. Herrmann, E., et al., *Nucleation Simulations Using the Fluid Dynamics Software FLUENT with the Fine Particle Model FPM.* The Journal of Physical Chemistry A, 2006. **110**(45): p. 12448-12455.

106. Sako, T., T. Furuhata, and M. Arai, *Nano-size PM Emission from Laminar Diffusion Flame of Diesel Fuel*. 2007, SAE International.

107. Kim, D.-H., M. Gautam, and D. Gera, *On the prediction of concentration variations in a dispersing heavy-duty truck exhaust plume using k–ε turbulent closure.* Atmospheric Environment, 2001. **35**(31): p. 5267-5275.

108. Bessagnet, B. and R. Rosset, *Fractal modelling of carbonaceous aerosols—application to car exhaust plumes.* Atmospheric Environment, 2001. **35**(28): p. 4751-4762.

109. Vehkamäki, H., *An improved parameterization for sulfuric acid–water nucleation rates for tropospheric and stratospheric conditions.* Journal of Geophysical Research, 2002. **107**(D22).

110. Hong, S., et al., *Development and application of a comprehensive soot model for 3D CFD reacting flow studies in a diesel engine.* Combustion and Flame, 2005. **143**(1-2): p. 11-26.

111. Uhrner, U., et al., *Dilution and aerosol dynamics within a diesel car exhaust plume—CFD simulations of on-road measurement conditions.* 2007. **41**(35): p. 7440-7461.

112. Herrmann, E., et al., *CFD AND NUCLEATION IN THE WATER-SULFURIC ACID-SYSTEM*. 2010.

113. Herrmann, E., et al., *A Computational Fluid Dynamics Approach to Nucleation in the Water−Sulfuric Acid System.* 2010. **114**(31): p. 8033-8042.

114. Herrmann, E., *Computational fluid dynamics simulations in aerosol and nucleation studies*. 2010.

115. Olin, M., T. Rönkkö, and M. Dal Maso, *CFD modeling of a vehicle exhaust laboratory sampling system: sulfur-driven nucleation and growth in diluting diesel exhaust.* Atmospheric Chemistry and Physics, 2015. **15**(9): p. 5305-5323.

116. Madhusha, *Difference Between TGA DTA and DSC*. 2017, PEDIAA.

117. Je-Yan Yu, W.-C.J.W., Sung-En Lin, Jia-Ming Sung, *Synthesis and characterization of cerium dioxide fibers.* Materials Chemistry and Physics, 2009: p. 410-416.

118. Cambustion. *Cambustion DMS500 MKII*. Available from: https://www.cambustion.com/sites/default/files/instruments/DMS500/DMS500engine.pdf.

119. Sako, T., et al., *Study on Nano-PM Formed from Laminar Diffusion Flame of Diesel Fuel*. Vol. 72. 2006. 3121-3127.

120. Kulmala, M., A. Laaksonen, and L. Pirjola, *Parameterizations for sulfuric acid/water nucleation rates.* Journal of Geophysical Research: Atmospheres, 1998. **103**(D7): p. 8301-8307.

121. Seinfeld, J.H. and S.N. Pandis, *Atmospheric Chemistry and Physics : From Air Pollution to Climate Change*. 2016, New York, UNITED STATES: John Wiley & Sons, Incorporated.

122. Ayers, G.P., R.W. Gillett, and J.L. Gras, *On the vapor pressure of sulfuric acid.* Geophysical Research Letters, 1980. **7**(6): p. 433-436.

123. Kulmala, M. and A. Laaksonen, *Binary nucleation of water–sulfuric acid system: Comparison of classical theories with different H2SO4 saturation vapor pressures.* 1990. **93**(1): p. 696.

124. Williams, M.M.R. and S.K. Loyalka, *Aerosol science: theory and practice*. 1991, United Kingdom: Pergamon Press.

125. Dou, Z., et al., *Experimental study of the effect of engine parameters on ultrafine particle in diesel/methanol dual fuel engine.* Fuel, 2017. **192**: p. 45-52.

126. Qianfan, X., *Diesel aftertreatment integration and matching*, in *Diesel Engine System Design*. 2011, Woodhead publishing.

127. Eastwood, P., *Exhaust gas aftertreatment for light-duty diesel engines*, in *Advanced Direct Injection Combustion Engine Technologies and Development*. 2010, Woodhead Publishing. p. 562-594.

128. Ebrahimnataj, M.R., et al., *Numerical and experimental study on the gaseous emission and back pressure during regeneration of diesel particulate filters.* Transportation Research Part D: Transport and Environment, 2018. **62**: p. 11-26.

129. Konstandopoulos, A.G. and M. Kostoglou, *Periodically Reversed Flow Regeneration of Diesel Particulate Traps*. 1999, SAE International.

130. Kaminaga, T. and J. Kusaka, *Improvement of Combustion and Exhaust Gas Emissions in a Passenger Car Diesel Engine by Modification of Combustion Chamber Design*. 2006, SAE International.

131. Jiao, P., et al., *Research of DPF regeneration with NOx-PM coupled chemical reaction.* Applied Thermal Engineering, 2017. **110**: p. 737-745.